# Spintronics with Terahertz Radiation: Probing and driving spins at highest frequencies

**Dissertation**

zur Erlangung des Grades eines
Doktors (Dr. rer. nat.)

am Fachbereich Physik
der Freien Universität Berlin

**Tom S. Seifert**

Berlin, Dezember 2017

This work was done between April 2014 and December 2017 in the Terahertz Physics Group (Prof. Dr. Tobias Kampfrath) of the Department of Physical Chemistry (Prof. Dr. Martin Wolf) at the Fritz-Haber-Institute of the Max-Planck-Society.

Erstgutachter: Prof. Dr. Tobias Kampfrath

Zweitgutachter: Prof. Dr. Martin Wolf

Drittgutachter: Prof. Dr. Jairo Sinova

Datum der Disputation: 04.06.2018

# Abstract

Electron spins are envisioned to play a key role in future information technologies. Apart from complementing charge-based functionalities, spin-based electronics (spintronics) offers entirely new possibilities. They emerge particularly from spintronic effects allowing for the mutual conversion of charge (or heat) and spin currents. Consequently, widespread applications already exist, including the magnetic random-access memory, which became commercially available only recently. On the other hand, field-effect transistors reaching cut-off frequencies of up to 1 THz have been demonstrated. This strongly suggests that future spintronic devices eventually need to operate at terahertz (THz) speeds.

Consequently, the following questions will be studied in this thesis: Are central spintronic effects operative up to highest THz frequencies? What are the initial elementary processes in their formation? How can we exploit new functionalities? Thereby, intriguing, new phenomena may be found since many fundamental excitations in solids resonate with THz radiation. Most importantly, the spin-orbit interaction, one of the cornerstones of spintronics, typically falls into the THz energy range. Apart from these exciting fundamental motivations, innovative spintronic concepts might advance other application fields, in particular THz photonics.

In this work, we first demonstrate the anomalous Hall effect at highest THz frequencies in technologically relevant metals. Remarkably, we find an anomalous Hall angle ~2 %, nearly constant from 1-40 THz. This result is understood in terms of the largely disordered materials, strongly blurring any spectral features.

Second, we exploit spintronic effects at THz frequencies to build an efficient and ultrabroadband THz spintronic emitter, based on nanometer-thin magnetic and strongly spin-orbit-coupled metals. It relies on ultrashort photoexcitation and the combination of the ultrafast spin-dependent Seebeck effect with the inverse spin Hall effect, and outperforms standard emitters in terms of bandwidth, ease of use, low cost, and scalability. By upscaling, we develop a THz spintronic high-field source allowing for nonlinear THz spectroscopy. Furthermore, we use THz-emission spectroscopy to characterize spintronic materials all-optically.

Third, we aim at revealing the fundamental processes in the ultrafast conversion of heat gradients into spin currents. Therefore, we measure the spin Seebeck effect at THz frequencies in prototypical magnetic-insulator/normal-metal bilayers. We find an ultrafast rise time of ~100 fs, which is ascribed to carrier multiplication during the thermalization of the photo-excited metal electrons. Our findings are relevant for all processes involving photo-induced spin transfer.

In conclusion, this work demonstrates the synergies released upon combining two vibrant fields of research: spintronics and THz spectroscopy.

# Kurzfassung

Elektronenspins wird eine Schlüsselrolle in der zukünftigen Informationstechnologie vorhergesagt. Neben der Ergänzung ladungsbasierter Funktionen bietet die spinbasierte Elektronik (Spintronik) zahlreiche Chancen, die einer Fülle von spintronischen Effekten zur gegenseitigen Umwandlung von Ladungs- (oder Wärme-) und Spinströmen entspringen. Dementsprechend existieren breite Anwendungen, wie z. B. der seit kurzem verfügbare magnetische Arbeitsspeicher. Andererseits wurden bereits Feldeffekttransistoren mit THz-Bandbreiten demonstriert. Dadurch wird es wahrscheinlich, dass zukünftige spintronische Anwendungen bei THz-Frequenzen arbeiten.

Diese Arbeit geht folgenden Fragen nach: Funktionieren spintronische Effekte noch bei THz-Frequenzen? Welche grundlegenden Schritte führen zu ihrem Auftreten? Wie können wir neue Funktionen nutzen? Dabei werden spannende neue physikalische Phänomene erwartet, da viele elementare Festkörperanregungen in den THz-Frequenzbereich fallen. Speziell gilt dies auch für die Spin-Bahn-Wechselwirkung, die grundlegend für die Spintronik ist. Neben diesen grundlegenden Einsichten können wir auf neue Anwendungen spintronischer Effekte im Hochfrequenzbereich hoffen, wie etwa in der THz-Photonik.

In dieser Arbeit wird zuerst der anomale Hall-Effekt in technologisch relevanten Materialien bei THz-Frequenzen untersucht. Die stark störstellenbehafteten Proben bewirken eine extreme Verschmierung der Frequenzabhängigkeit, wodurch wir einen fast konstanten anomalen Hall-Winkel von ~2 % zwischen 1 und 40 THz vorfinden.

Darauf aufbauend nutzen wir spintronische Effekte bei THz-Frequenzen, um eine effiziente und breitbandige THz-Quelle zu entwickeln, die aus nanometerdicken magnetischen und Metallen mit starker Spin-Bahn-Kopplung besteht. Dieser THz-Emitter basiert auf ultrakurzer Fotoanregung und der Kombination des ultraschnellen spinabhängigen Seebeck-Effektes mit dem inversen Spin-Hall-Effekt. Er übertrifft Standardemitter hinsichtlich Bandbreite, Nutzerfreundlichkeit, Bezahlbarkeit und Skalierbarkeit. Durch Größenskalierung entwickeln wir einen spintronischen THz-Hochfeldemitter, der im Stande ist, nichtlineare Prozesse anzutreiben. Wir nutzen die THz-Emission zudem zur Charakterisierung spintronischer Materialien mit optischen Mitteln.

Schließlich untersuchen wir den Ursprung der ultraschnellen Umwandlung eines Temperaturgradienten in einen Spinstrom. Dazu messen wir den Spin-Seebeck-Effekt im THz-Bereich in prototypischen magnetischen Isolator-Metall-Doppellagen und finden eine Anstiegszeit von 100 fs, die auf die Vervielfachung der Elektron-Loch-Paare während der Thermalisierung der fotoangeregten Ladungsträger zurückgeführt wird. Unsere Einblicke sind hinsichtlich einer Vielzahl optisch induzierter Spintransferprozesse relevant.

Zusammenfassend zeigt diese Arbeit die Vielzahl der Synergien auf, die durch die Kombination zweier dynamischer Forschungsfelder, Spintronik und THz-Photonik, freigesetzt werden können.

# Contents

# 1. Introduction

The 21st century is an era of unprecedented rate of progress in nearly all parts of our society. Fueled by innovative fundamental research, new technologies emerge and profoundly transform our everyday life. For future developments, the electron spin is envisioned to be a major player due to its rich physics and its enormous potential for applications.

## 1.1. Spintronics

As conventional charge-based electronics approaches its physical limits regarding miniaturization and heat management, the search is on for new concepts that meet the projected requirements for increased computational speed and data-storage density [Wol01].

The electron spin offers a large potential for future information technology. It is foreseen to complement conventional electronics, which relies on the charge degree of freedom to encode information [San17, Joh85, Pri95]. This field of spin-based electronics (short spintronics) holds the promise for reduced heat dissipation, potentially simpler device architecture, and faster operation [Wol01, Jun16]. To make spintronics competitive with electronics, the overarching goal is to efficiently manipulate, transport and process spin information [Sve15].

An important prerequisite is the generation and detection of spin currents. In this regard, recent progress led to the discovery of the spin (-dependent) Seebeck and Hall effects, allowing for the mutual conversion of charge (and heat) into spin currents [Sin15, Bau12]. Two distinct carriers are particularly important for the flow of spin angular momentum: charges and spin waves (magnons). The latter lay the foundation for magnonics in which electron flow is unnecessary, thereby minimizing Ohmic losses [Chu15].

These possibilities enabled broad spintronic applications for instance in the field of computation and data storage. A prime example is the magnetic random-access memory. The next generation of such magnetic data-storage device will most likely rely on the spin-orbit torque used to switch a magnetic layer [Wal16, Liu12a]. Future developments aiming at even higher density and reliability in magnetic recording are envisioned to be driven by the field of antiferromagnetic spintronics [Jun16].

However, it remains a challenge to accomplish spintronic operations entirely without any charge flow [San17]. Moreover, the spin is locally not a conserved quantity, and typically an efficient spin-to-charge conversion requires large spin-orbit coupling which, however, increases the rate of spin relaxation [Žut04]. These issues make the field of spintronics a complex but exciting field of research.

As modern information technology is inherently demanding ever higher speeds, spintronic concepts must keep pace with other technologies. Recently, field-effect transistors with cut-off frequencies of about 1 THz have been demonstrated [DA11]. Moreover, fiber-based telecommunication as well as wireless local area networks are about to reach terahertz bandwidths [KO11]. This demonstrates the urgent need to transfer spintronic functionalities from the gigahertz into the terahertz frequency range, thereby paving the way towards future spin-based applications at highest speeds.

## 1.2. Terahertz spectroscopy

The terahertz (THz) spectral window, with frequencies from about 0.3 to 30 THz and wavelengths from 10 to 1000 µm, bridges microwave-based electronics with laser-based photonics [Brü12].

As THz photon energies (4 meV at 1 THz) are resonant with many elementary modes in all phases of matter, THz pulses can excite and probe them on the ultrafast time scale. Such THz resonances include vibrational and rotational motions of molecules in gases and liquids [Saj17] as well as many fundamental excitations in solids: lattice vibrations, spin waves in antiferromagnets, internal excitation energies of electron-hole pairs, binding energies of Cooper pairs and many more [Hwa15]. Importantly, also the energy scale of the spin-orbit interaction, central for the field of spintronics, often coincides with the THz spectral range [Wal16].

Based on this high spectral selectivity, many applications have emerged. These include imaging, e. g. in security scanners at airports or in biologically relevant environments exploiting the sensitivity of THz radiation to water [Dhi17]), quality control through nondestructive testing of food [Mit99], or monitoring the drying process of paints [Yas05].

State-of-the-art THz time-domain spectroscopy allows for a direct and simultaneous measurement of the amplitude as well as the phase of the THz electric field. This feature greatly facilitates the interpretation of experiments and requires no challenging reconstruction methods such as the Kramers-Kronig relations [Pei12].

Despite all these remarkable prospects, a profound exploration of the THz spectral window has been impeded by the lack of efficient THz sources and detectors. Even though considerable progress has been made, certain THz spectral ranges have remained challenging. Thus, new efficient and broadband schemes are needed for THz generation and detection, optimally combining ease of use, durability, flexibility, low cost and scalability [Dhi17].

So far, THz spectroscopy has mostly addressed the electronic or ionic charge, resulting in spectacular new findings in a multitude of physical systems [Ton07, Kam13b, Ulb11]. These include the THz-selective driving of chemical reactions on surfaces [LaR15], controlling the Cooper-pair binding energy in a superconductor with THz pulses [Mat14], and tracking the ultrafast motion of single molecules with nanometer spatial and femtosecond temporal resolution [Coc16].

However, the electron spin degree of freedom has been widely neglected. To fill this gap, new schemes are required to explore spin-dependent phenomena in the THz range. In particular, THz-emission spectroscopy has proven useful for studying ultrafast spin and charge dynamics [Lei99b, Kam13a]. However, it has been used only by a few groups worldwide thus being far from routinely reaching a femtosecond time resolution.

## 1.3. Spintronics with terahertz radiation

As seen above, future spintronic devices are likely to operate at THz speeds. Thus, the question arises if central spintronic effects allowing for spin-current generation are still operative at THz frequencies. An advanced understanding might open highly unexploited fields such as the resonant [Mae17a] and off-resonant [Nov16] coupling of the spin to the phononic or magnonic subsystems of a solid. Moreover, the switching dynamics of antiferromagnets supposedly proceed at the sub-picosecond time scale [Jun16], which however remains to be shown.

For all these exciting examples, we expect new physics, due to the multitude of THz resonances [Shi11]. Pressing questions immediately arise: What happens if spin-to-charge conversion schemes are driven at typical quasiparticle scattering rates? Do THz resonances provide a means for advanced spintronic control? Which impact does the ultrafast coupling of the spin to other degrees of freedom have? Can we exploit highly nonequilibrium states in future high-speed spin-based devices?

To target these intriguing open points with THz radiation, new, all-optical schemes need to be employed since electrical circuitry is largely limited to frequencies below 1 THz [Wal16]. In this regard, also the field of THz photonics might benefit from innovative spintronic approaches.

Most recently, several studies demonstrated the potential of combining spintronics with THz radiation. Jin and coworkers used linear THz spectroscopy to investigate the giant magneto-resistance [Jin15], in which the resistance of a heterostructure depends on the magnetization state of the individual constituents. They found that Mott's two-current model remains valid up to THz frequencies. Moreover, Shimano and coworkers were the first to demonstrate that the anomalous Hall effect remains operative up to 1.5 THz [Shi11] followed by works in the mid-infrared [Kim07, Kim10, Kim13] and below 5 THz [Hui15, Hui17b]. Furthermore, optically-induced spin-polarized carriers in semiconductors were shown to experience a spin-dependent deflection at THz frequencies [Pri15]. Finally, Ref. [Kam13a] showed the large potential of THz-emission spectroscopy for studying spintronic phenomena such as the inverse spin Hall effect at THz speeds. However, broadband studies eventually closing the THz spintronic gap and disclosing the fundamental physical processes, have remained challenging.

Generally, merging these two vibrant research fields might foster unforeseen opportunities when exploring terra incognita.

## 1.4. This thesis

This work aims at gaining a deeper understanding of spintronic effects at highest speeds employing terahertz radiation. We not only want to speed-up central spin-to-charge conversion schemes but also hope to discover new high-speed spin-based functionalities possibly even facilitated by the plenty of THz resonances. Eventually, a positive feedback advancing THz spectroscopy and spintronics may be expected.

After first providing the necessary theoretical and experimental background to explore spintronics with THz radiation (Chapters 2 and 3), we present a broadband study of the anomalous Hall effect employing THz ellipsometry in technologically relevant materials in Chapter 4. We find sizable anomalous Hall angles of ~2 %, essentially independent of frequency from DC to 40 THz. This surprising result is explained by the short velocity-relaxation time which strongly broadens any spectral features.

We next exploit such ultrafast charge-to-spin conversion to build a spintronic THz emitter in Chapter 5. It is based on a thin-film stack involving magnetic and heavy metals. After photoexcitation with an ultrashort optical laser pulse (photon energy of 1.6 eV), the concerted action of the ultrafast spin-dependent Seebeck effect and inverse spin Hall effect leads to the emission of a THz transient. The developed THz source features a remarkably broad emission from 1 to 30 THz without gaps, is competitive with standard THz emitters in terms of efficiency and even superior regarding cost, ease of use, flexibility and scalability. In Chapter 6, we upscale the spintronic THz emitter to deliver strong THz pulses even capable of driving nonlinear processes.

On a more fundamental level, we next show that THz-emission spectroscopy of magnetic metal multilayers can complement the workbench of spintronics by providing a convenient, all-optical spintronic material characterization (Chapter 7). To gain further insights into the fundamental steps of the spin-dependent Seebeck effect, we drastically reduce the pump photon energy to 0.1 eV. Our preliminary findings highlight the importance of ultrafast electron heating for spin-current generation. To further test this hypothesis in a less complex structure, we replace the magnetic metal.

Accordingly, THz-emission studies on yttrium-iron-garnet/heavy-metal bilayers are presented in Chapter 8. This experiment is a straightforward extension of the spin Seebeck effect to THz frequencies. Remarkably, the spin current rises on a time scale of ~100 fs, directly monitoring the metal-electron thermalization dynamics. We identify carrier multiplication during the relaxation of photo-excited electrons and subsequent electron-phonon coupling as the pace-setting mechanisms for the ultrafast dynamics of the spin Seebeck effect.

Finally, we turn from using THz pulses as a probe to driving spins with THz stimuli. In Chapter 9, we show promising preliminary results of THz-speed switching of an antiferromagnetic memory device. Our findings suggest that the current-induced Néel spin-orbit torque in metallic antiferromagnets remains equally efficient from seconds down to picoseconds, potentially paving the way toward THz antiferromagnetic data storage.

# 2. Theoretical background

## 2.1. Ultrafast optical excitation of metals

Femtosecond laser pulses allow for the investigation of ultrafast dynamics in solid state systems [Gam11]. Such ultrashort bursts of electromagnetic radiation are the main tool throughout this work which aims at studying spintronic phenomena with THz radiation.

Modern laser systems can routinely provide laser pulses with a femtosecond duration and a typical central photon energy of 1.6 eV. In metallic systems, these laser pulses interact primarily with the metal electrons. The absorption of light creates a nonequilibrium state which subsequently relaxes through various processes [Gam11]. Figure 2.1 summarizes these excitation and equilibration processes within a single-electron framework.

Initially, the laser pulse induces a coherent polarization composed of the superposition of states above and below the Fermi energy $\varepsilon_\mathrm{F}$. Thereafter, interactions lead to dephasing, eventually quenching the induced polarization [All12]. In this state, the nonthermal electron distribution is fully characterized by the occupation numbers. Further thermalization involves simultaneous interactions within the electronic system and with other subsystems of the solid (lattice vibrations, magnetic excitations etc.) which finally equilibrate all subsystems [Gam11].

The fastest processes are determined by electron-electron interactions taking place on a sub-picosecond time scale (see Figs. 2.1b and c). Due to electron-electron scattering, more electron-hole pairs are formed, known as carrier multiplication. Eventually, this results in a thermalized electronic system, which can be described by a Fermi-Dirac-distribution function at an elevated temperature. Electron-phonon and electron-magnon interactions, on the other hand, proceed on a time scale of 0.1-10 ps (see Figs. 2.1d and e), balancing the electronic, magnonic and phononic temperatures [Gam11, Tve15]. Finally, heat diffusion leads to an equilibration with the surrounding on much longer timescales (typically on a nanosecond time scale) [Gam11].

Importantly, in systems with broken inversion symmetry, photoexcitation may also lead to a transport of charge carriers within the sample. This may also imply the transport of spin angular momentum, resulting in spin (-polarized) currents [Kam13a, Tve15, Kal12, Bat10]. The symmetry-breaking can result from the bare crystal structure (bulk inversion asymmetry) or by heterostructures involving several materials (structure inversion asymmetry).

In this thesis, we investigate the generation, interconversion, and relaxation of spin and charge currents in metallic systems with the help of ultrashort laser pulses and THz radiation. In the following, a theoretical background will be established.

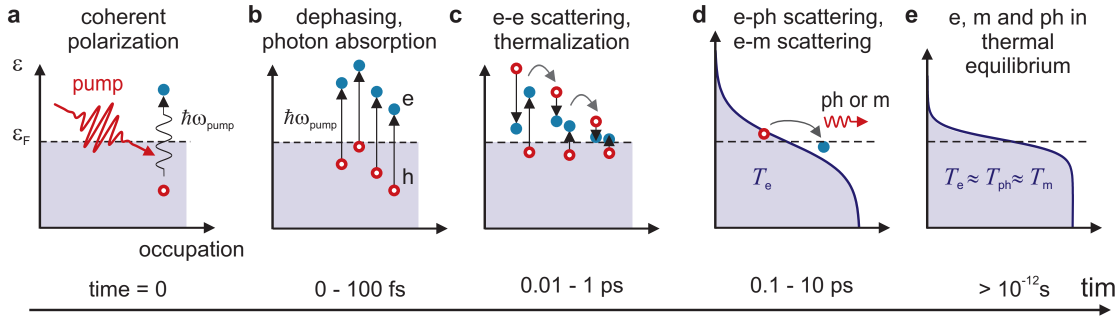

**Figure 2.1.: Ultrafast optical excitation of metals.** **a**, An incident ultrashort laser pulse (pump; central frequency $\omega_{\text{pump}}$) induces a coherent polarization of states above and below the Fermi energy $\varepsilon_{\text{F}}$ in the metal. **b**, Within a few tens of femtoseconds, dephasing quenches this polarization and pairs of electrons (e) and holes (h) are created, above and below $\varepsilon_{\text{F}}$, respectively. **c**, Electron-electron (e-e) interactions thermalize the electronic system on a sub-picosecond time scale, after which the electron occupation is described by a Fermi-Dirac distribution at an elevated temperature. **d**, Meanwhile, energy is exchanged between the electronic, the magnonic and the phononic systems with temperatures $T_{\text{e}}$ and $T_{\text{p}}$, $T_{\text{m}} < T_{\text{e}}$, respectively. Electron-phonon (e-ph) and electron-magnon (e-m) interactions equilibrate the three subsystems on typical time scales of a few picoseconds. **e**, Charge carrier transport and heat diffusion out of the excited volume eventually equilibrate the system with its surrounding. Figure adapted from [Kam06] with the permission of T. Kampfrath.

## 2.2. Electrons in a crystalline solid

**Bloch electrons.** In a solid, atoms are arranged in a periodic manner obeying symmetries which can be classified by crystal classes such as for instance cubic or hexagonal. This regular arrangement and the corresponding discrete translational symmetry have tremendous consequences for the behavior of electrons inside the crystal. In the independent-electron picture, each electron moves in a periodic potential (mean-field) generated by the lattice and the other electrons. The eigenfunctions of the electron are so-called Bloch waves

$$\Psi_{n,\boldsymbol{k}}\left(\boldsymbol{r}\right) = \mathrm{e}^{\mathrm{i}\boldsymbol{k}\cdot\boldsymbol{r}} u_{\boldsymbol{k}}\left(\boldsymbol{r}\right), \tag{2.1}$$

where the plane waves $\mathrm{e}^{\mathrm{i}\boldsymbol{k}\cdot\boldsymbol{r}}$ are modulated by a periodic function $u_{\boldsymbol{k}}\left(\boldsymbol{r}\right)$ following the same periodicity as the crystal lattice, and $\boldsymbol{k}$ is the crystal momentum [Kit05]. These wave functions constitute a complete basis of the Hilbert space and can be classified by the crystal momentum $\boldsymbol{k}$ and the integer index $n$. The latter is referred to as the band index. The corresponding eigenenergies $\varepsilon_{n,\boldsymbol{k}}$ form the band structure of the solid (see Fig. 2.2).

In general, electrons in a solid behave differently than free electrons: their group velocity becomes $\boldsymbol{v} = \hbar^{-1}\mathrm{d}\varepsilon_{n,\boldsymbol{k}}/\mathrm{d}\boldsymbol{k}$, where $\hbar = h/2\pi$ is the reduced Planck constant, and their effective mass is determined by the electron-band's curvature.

**Statistics.** As electrons are Fermions, they obey the Pauli exclusion principle, implying that they are not allowed to occupy the same quantum mechanical state. Consequently, at $T = 0\,\mathrm{K}$ electrons fill the energy bands up to a certain energy, the Fermi energy $\varepsilon_\mathrm{F}$ [Kit05]. Importantly, certain combinations of electron energy and crystal momentum can be forbidden in a solid, resulting in band gaps. For insulators, $\varepsilon_\mathrm{F}$ lies in a band gap, whereas for metals it does not. The latter results in a partially filled upper electronic band, which is called the conduction band, and a filled lower electronic band, which is called the valence band (see Figs. 2.2a and b). For $T > 0\,\mathrm{K}$, thermally activated electrons can occupy higher lying states within an interval of about $k_\mathrm{B}T$. In general, the electron distribution is characterized by the Fermi-Dirac distribution function given by [Kit05]

$$f(\varepsilon, \mu, T) = \frac{1}{1 + \exp\left[\left(\varepsilon - \mu\right)/k_\mathrm{B}T\right]}, \tag{2.2}$$

where $\mu$ is the chemical potential, which accounts for the conservation of the total electron number (see Fig. 2.2c).

**Excitation of electrons.** If electrons are excited to higher-lying states, empty states below $\varepsilon_\mathrm{F}$ remain, which gives rise to states that are called holes (see Figs. 2.1 and 2.2b). They have opposite crystal momentum, mass and energy than the missing electron, but have the same band velocity [Kit05].

If electrons are subject to an external electric field with a frequency $\omega$, they can be excited to energetically higher-lying states, which is called an optical transition (see Fig. 2.1). Within linear response theory, the transition rate between an initial state $|i\rangle$ and a final state $|j\rangle$ can be evaluated by Fermi's golden rule [Kit05]:

$$w_{ij} = \frac{2\pi}{\hbar}\left|M_{ij}\right|^2 \delta\left(\varepsilon_j - \varepsilon_i - \hbar\omega\right). \tag{2.3}$$

Here, $M_{ij}$ is the matrix element of the electric-dipole operator and the term involving the delta distribution ensures energy conservation during the optical transition. Importantly, in Eq. 2.3, the initial and final states can be combined states (possibly involving other degrees of freedom, e. g. phonons or magnons) with their respective total energies $\varepsilon_i$ and $\varepsilon_j$.

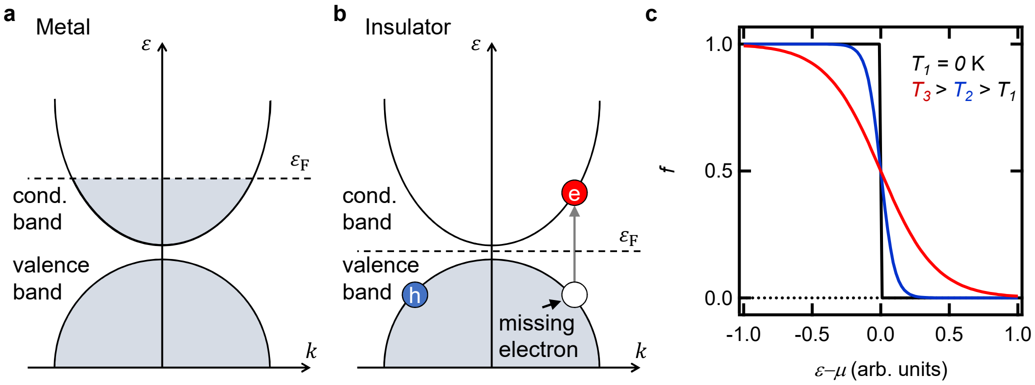

**Figure 2.2.: Schematic band structure of a solid and Fermi-Dirac function. a,** Schematic of a free-electron-like parabolic dispersion relation of a metal at $T = 0\,\mathrm{K}$, which is characterized by a partially filled conduction band. **b,** Same band structure as in **a** but with the Fermi energy $\varepsilon_\mathrm{F}$ inside the band gap between conduction and valence band. This results in an insulating behavior at $T = 0\,\mathrm{K}$. Upon excitation (e. g. by a photon), an electron-hole pair (e and h) is formed. **c,** Fermi-Dirac function $f\,(T)$ for different temperatures, describing the population of electronic states at a given temperature $T$.

## 2.3. Spin interactions

### 2.3.1. Spin angular momentum

In addition to the orbital angular momentum, electrons possess an intrinsic angular momentum which is called the electron spin. An elegant way to derive its properties is provided by the Dirac equation. It is a relativistic version of the Schrödinger equation that is also of first order in the time derivative. However, in contrast to the classical Schrödinger equation, the scalar wave functions become spinors, and the coefficients in the Dirac equation are matrices instead of scalars. These special properties allow for the existence of the electron spin $\boldsymbol{s}$ [Nol09].

Experimentally, the electron spin was first indirectly observed through the study of atomic spectra in the presence of external magnetic fields [Uhl25]. The first direct measurement was achieved through asymmetric spin-dependent scattering of electrons off heavy atoms, known as Mott scattering [Mot29]. Previously, Stern and Gerlach had observed a separation of a beam of silver atoms in an inhomogeneous magnetic field but interpreted their results incorrectly [Stö07].

Similar to the orbital-angular-momentum operator $\hat{\boldsymbol{l}}$, the components of the spin-angular-momentum operator obey the commutation relation

$$[\hat{s}_i, \hat{s}_j] = \mathrm{i}\hbar\epsilon_{ijk}\hat{s}_k, \tag{2.4}$$

where $\epsilon_{ijk}$ is the Levi-Civita permutation symbol [Nol09]. The eigenvalues of any component of the spin operator with respect to an eigenstate of the free electron are $\pm\hbar/2$. Conventionally, a set of eigenstates of the commuting operators $\hat{\boldsymbol{s}}^2$ and $\hat{s}_z$ is chosen as a basis for the spin-subspace. These two operators possess the eigenvalues $\hbar^2\mathfrak{s}\,(\mathfrak{s}+1)$ and $\pm\hbar\mathfrak{s}$ , respectively, where the electron spin quantum number is $\mathfrak{s}=1/2$ . The latter two orientations of the spin with respect to a defined axis are typically referred to as spin-up and spin-down states, respectively.

Importantly, the electron spin is associated with a magnetic moment by

$$\hat{\boldsymbol{\mu}}_{\mathrm{s}} = -\frac{g_{\mathrm{e}}\mu_{\mathrm{B}}}{\hbar}\hat{\boldsymbol{s}}, \tag{2.5}$$

where $g_{\mathrm{e}} \approx 2$ is the electron $g$-factor, $\mu_{\mathrm{B}} = e\hbar/2m_{\mathrm{e}}$ is the Bohr magneton with the electron mass $m_{\mathrm{e}}$ and the elementary charge is $e = |e|$ [Nol09].

With respect to the Bloch wave function $\psi_{n,\mathbf{k}}$ of the electron (see Eq. 2.1), the spin degree of freedom is contained within the band index $n$. If the Hamiltonian of the system is independent of the electron spin, the Bloch functions (Eq. 2.1) factorize into spin and orbital part [Nol09].

In the following, however, we will see that spin-dependent electron interactions have important consequences such as spin-dependent band structures and magnetic ordering.

## 2.3.2. Single-electron relativistic Hamiltonian: Zeeman and spin-orbit interaction

In solids, the band velocity of electrons is typically on the order of 1 nm/fs (see Section 2.2). Although this equals only about one hundredth to the vacuum speed of light $c = 300\,\mathrm{nm/fs}$, relativistic corrections become important in solids [Kit05].

A rigorous derivation of the single-electron relativistic Hamiltonian involves the expansion of the Dirac Hamiltonian up to first order in $1/c$ yielding [Nol09]

$$\hat{H}_{\mathrm{rel}} = \hat{T} + \hat{T}_{\mathrm{rel}} + \hat{H}_{\mathrm{C}} + \hat{H}_{\mathrm{Darwin}} + \hat{H}_{\mathrm{Z}} + \hat{H}_{\mathrm{so}}. \tag{2.6}$$

Here, the first two terms are the kinetic energy and its relativistic correction, respectively. The third term is the Coulomb interaction. The fourth term is called Darwin term, and it is responsible for a relativistic correction known as Zitterbewegung [Whi72]. Typically, it is negligible compared to the other terms in Eq. 2.6.

**Zeeman interaction.** The fifth term in Eq. 2.6 is the Zeeman interaction. It describes the coupling of the magnetic moment of an electron to a classical magnetic field $\hat{\boldsymbol{B}}^{\mathrm{tot}}$. For small magnetic fields (i. e. Zeeman energy is minor compared to other spin-dependent interactions in Eq. 2.6), it takes the simple form [Nol09]

$$\hat{H}_{\mathrm{Z}} = -\hat{\boldsymbol{\mu}}_{\mathrm{e}} \cdot \hat{\boldsymbol{B}}^{\mathrm{tot}}, \tag{2.7}$$

where $\hat{\boldsymbol{B}}^{\mathrm{tot}}$ is the total magnetic field at the position of the electron.

For an electron, two parts contribute to its magnetic moment $\hat{\boldsymbol{\mu}}_{\mathrm{e}}$, namely the orbital magnetic momentum $\hat{\boldsymbol{\mu}}_{\mathrm{orb}} = \mu_{\mathrm{B}}\hbar^{-1}\hat{\boldsymbol{l}}$, and the spin magnetic moment $\hat{\boldsymbol{\mu}}_{\mathrm{s}}$ (see Eq. 2.5):

$$\hat{\boldsymbol{\mu}}_{\mathrm{e}} = \hat{\boldsymbol{\mu}}_{\mathrm{orb}} + \hat{\boldsymbol{\mu}}_{\mathrm{s}}. \tag{2.8}$$

Importantly, since the spin operator does not commute with the Zeeman Hamiltonian (Eq. 2.7), the band structure of the solid can become spin-dependent [Nol09].

**Spin-orbit interaction.** The sixth term in Eq. 2.6 is the spin-orbit interaction (SOI), which reads:

$$\hat{H}_{\mathrm{so}} = \frac{\mu_{\mathrm{B}}}{c\hbar}\hat{\boldsymbol{s}} \cdot \left(\boldsymbol{E}\left(\hat{\boldsymbol{r}}\right) \times \frac{\hat{\boldsymbol{v}}_{\mathrm{e}}}{c} + \frac{\mathrm{i}\hbar}{2cm_{\mathrm{e}}}\left(\boldsymbol{\nabla} \times \boldsymbol{E}\right)\left(\hat{\boldsymbol{r}}\right)\right), \tag{2.9}$$

where $\boldsymbol{E}$ is the total electric field at the position of the electron and $\hat{\boldsymbol{v}}_{\mathrm{e}}$ is the electron band velocity. It results from the interaction of the electron spin with an effective magnetic field generated by other charges in relative motion [Hel12]. In the typical situation of a stationary magnetic field, the second term in Eq. 2.9 vanishes (i. e. $\boldsymbol{\nabla} \times \boldsymbol{E} \propto \partial \boldsymbol{B}/\partial t = 0$ if $\boldsymbol{B}$ is static).

The remaining first term of Eq. 2.9 can be understood as an effective spin-orbit magnetic field $\boldsymbol{B}_{\mathrm{eff}}^{\mathrm{so}} \propto \boldsymbol{E}\left(\hat{\boldsymbol{r}}\right) \times \hat{\boldsymbol{v}}_{\mathrm{e}}/c$ that interacts with the electron spin in close analogy to the Zeeman interaction (see Eq. 2.7).

In a classical view (neglecting quantum-mechanical-operator notation), the SOI can be explained in the following way: In the rest frame of the moving electron, the electric field $\boldsymbol{E}$ close to the nucleus transforms into an effective magnetic field (see Fig. 2.3) given by

$$\boldsymbol{B}_{\mathrm{eff}}^{\mathrm{so}} \propto \boldsymbol{E} \times \frac{\boldsymbol{v}_{\mathrm{e}}}{c}. \tag{2.10}$$

Since the electric field in Eq. 2.10 depends on the distance $\boldsymbol{r}$ between electron and nucleus, one obtains $\boldsymbol{B}_{\mathrm{eff}}^{\mathrm{so}} \propto \boldsymbol{r} \times \boldsymbol{v}_{\mathrm{e}} \propto \boldsymbol{l}$. Consequently, the Zeeman-like interaction $H_{\mathrm{Z}} = g_{\mathrm{e}}\mu_{\mathrm{B}}\hbar^{-1}\boldsymbol{s} \cdot \boldsymbol{B}_{\mathrm{eff}}^{\mathrm{so}}$ couples the electron spin and orbital degrees of freedom [Whi72].

It can be shown that for a spherically symmetric electric potential, the SOI takes the familiar form [Nol09]

$$\hat{H}_{\mathrm{so}} = \lambda\hat{\boldsymbol{l}} \cdot \hat{\boldsymbol{s}}, \tag{2.11}$$

with the spin-orbit parameter $\lambda = \mu_{\mathrm{B}}\hbar^{-1}c^{-2}m_{\mathrm{e}}^{-1}r^{-1}E\left(r\right)$.

**Order-of-magnitude estimate.** In the following, we give some estimates to see the relative importance of certain interactions.

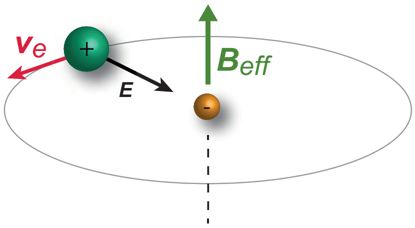

**Figure 2.3.: Classical view of the spin-orbit interaction.** In the rest frame of the moving electron (yellow sphere; velocity $\boldsymbol{v}_\mathrm{e}$), the electric field $\boldsymbol{E}$, caused by the nucleus (green sphere), transforms into an effective magnetic field $\boldsymbol{B}_\mathrm{eff}$. The interaction of the electron spin with this effective field represents the spin-orbit interaction. Figure reproduced from [Mäh16] with the permission of S. F. Mährlein.

We first consider the SOI energy. Starting from Eq. 2.9 and restricting ourselves to the case of a static vector potential, the spin-orbit Hamiltonian is given by the term $\mu_\mathrm{B} c^{-2} m_\mathrm{e}^{-1} \hbar^{-1} \hat{\boldsymbol{s}} \left( \boldsymbol{E}\left(\hat{\boldsymbol{r}}\right) \times \hat{\boldsymbol{p}} \right)$. Thus, for the SOI energy, we obtain approximately

$$\left\langle \hat{H}_\mathrm{so} \right\rangle \approx \frac{\mu_\mathrm{B}}{2c^2 m_\mathrm{e}} \left\langle \boldsymbol{E}\left(\hat{\boldsymbol{r}}\right) \right\rangle \left\langle \hat{\boldsymbol{p}} \right\rangle . \tag{2.12}$$

For a single electron, the Coulomb potential is given by $\left\langle \boldsymbol{E}\left(\hat{\boldsymbol{r}}\right) \right\rangle = Ze/4\pi\epsilon_0 r^2$ with the vacuum permittivity $\epsilon_0$. We can approximate the electron momentum by means of the uncertainty principle, i. e. $\langle \hat{\boldsymbol{p}} \rangle \approx \hbar/2r$. Here, the radius is approximated by the scaled Bohr radius $r \approx a_\mathrm{B}/Z$ where $Z$ is the atomic number [Ash98], yielding:

$$\left\langle \hat{H}_\mathrm{so} \right\rangle \approx \frac{\mu_\mathrm{B}^2}{8\pi\epsilon_0 a_\mathrm{B}^3 c^2} Z^4 \approx 0.1\,\mathrm{meV} \cdot Z^4 . \tag{2.13}$$

Already these basic considerations demonstrate that SOI energies can fall into the THz to infrared energy range ($1\,\mathrm{THz} \mathrel{\hat{=}} 4.1\,\mathrm{meV}$). However, in a more rigorous derivation, the energy in Eq. 2.13 is reduced for electrons further away from the nucleus due to the screening of the nuclear charge by the electrons closer to the nucleus. This often results in an effective $Z^2$-dependence [Lan58].

Following a similar derivation, the effective spin-orbit magnetic field can be estimated to be on the order of

$$\left\langle \boldsymbol{B}_\mathrm{eff}^\mathrm{so} \left(\hat{\boldsymbol{r}}, \hat{\boldsymbol{v}}_\mathrm{e}\right) \right\rangle \approx \frac{\mu_\mathrm{B}}{8\pi\epsilon_0 a_\mathrm{B}^3 c^2} Z \approx 4\,\mathrm{Tesla} \cdot Z . \tag{2.14}$$

Such effective spin-orbit fields are orders of magnitude stronger than typical laboratory external magnetic fields (~1 T).

On the other hand, the Zeeman energy for $|\boldsymbol{B}_\mathrm{tot}| = |\boldsymbol{B}_\mathrm{ext}| = 1\,\mathrm{T}$ is on the order of 0.1 meV (see Eq. 2.7). This is much smaller than the SOI energy in materials with large $Z$ (compare with Eq. 2.13).

Apart from such static magnetic fields, dynamic electric and magnetic fields arise when light is incident. For the magnetic component of the light field, one must distinguish between two regimes: For optical frequencies, i. e. for hundreds of THz, the electron magnetic moment cannot follow the fast oscillations of the light field. On the other hand, it can follow the much slower oscillation frequencies in the THz range.

Nowadays, the highest achievable THz electric field strengths are on the order of $10^3\,\mathrm{MV/m}$ which correspond to a magnetic field component on the order of $1\,\mathrm{T}$ [Kam13b, Sha15]. Thus, the Zeeman interaction of electron spins with the magnetic-field component of light is typically weaker than the SOI. It can be shown [Mon16] that the relativistic interaction of the light field with the electron spin only leads to minor corrections under typical laboratory conditions.

### 2.3.3. Many-electron relativistic Hamiltonian: spin interactions and magnetic order

For a system containing many electrons, a similar treatment can be applied as in the previous Section for a single electron. The crucial difference is that the magnetic and electric fields experienced by one electron (see Eqs. 2.7 and 2.9) also contain the magnetic and electric fields generated by all other electrons $j \neq i$ [Hel12]. In other words, $\boldsymbol{E}_i^{\mathrm{tot}}$ contains the Coulomb field of all other electrons and $\boldsymbol{B}_i^{\mathrm{tot}}$ contains the magnetic field due to the spins and orbital motions of the other electrons.

The many-electron system can be described by the Breit-Pauli Hamiltonian which reads [Hel12]

$$\hat{H}_{\mathrm{BP}} = \sum_i \left( \hat{T}_i + \hat{V}_i + \sum_{j>i} \hat{V}_{ij}^{\mathrm{ee}} \right) + \hat{H}_{\mathrm{rel}}. \tag{2.15}$$

Here, $\hat{V}_{ij}^{\mathrm{ee}}$ is the electron-electron Coulomb interaction, $\hat{T}_i$ is the kinetic energy, and $\hat{V}_i$ is the potential energy of the $i$th electron which includes external fields and internal fields deriving from the atomic nuclei. In the following, we will see how the nonrelativistic part of this Hamiltonian can lead to magnetic ordering via isotropic exchange interaction.

On the other hand, relativistic corrections are contained within $\hat{H}_{\mathrm{rel}}$ such as SOI and spin-spin magnetic dipole interaction. As discussed below, they can give rise to anisotropic interactions such as the Dzyaloshinskii-Moriya interaction, magneto-crystalline anisotropy, and shape anisotropy [Whi72].

**Spin-spin magnetic dipole interaction.** One specific interaction between spins included in the relativistic part of the Breit-Pauli Hamiltonian (see Eq. 2.15) is the spin-spin magnetic dipole interaction [Blu03]. For two spin magnetic moments $\boldsymbol{\mu}_{\mathrm{s}i}$ separated by a distance $\boldsymbol{r}$, it takes the form

$$\hat{H}_{\mathrm{ssmd}} = \frac{\mu_0}{4\pi r^3} \left[ \hat{\boldsymbol{\mu}}_{\mathrm{s1}} \cdot \hat{\boldsymbol{\mu}}_{\mathrm{s2}} - \frac{3}{r^2} \left( \hat{\boldsymbol{\mu}}_{\mathrm{s1}} \cdot \hat{\boldsymbol{r}} \right) \left( \hat{\boldsymbol{\mu}}_{\mathrm{s2}} \cdot \hat{\boldsymbol{r}} \right) \right]. \tag{2.16}$$

This interaction favors a parallel alignment of neighboring spins. However, by taking typical values of $r = 1\,\text{Å}$ and $\mu_\text{s} = \mu_\text{B}$, one obtains $\langle H_\text{ssmd} \rangle \approx 0.1\,\text{meV}$. This value is negligible compared to other spin-ordering interactions as we shall see in the following [Nol09]. Nevertheless, the spin-spin magnetic dipole interaction can lead to important anisotropic contributions to the total energy such as the magnetic shape anisotropy [Cha07b].

**Pauli principle and isotropic exchange interaction.** In 1925, Wolfgang Pauli postulated that two electrons have two differ in at least one of their quantum numbers. In a modern parsing, this postulate reads: The wave function $\Psi$ of a quantum mechanical system is anti-symmetric under exchange of electrons [Nol09].

If we consider a two-particle system with the wave function $\Psi\left(\boldsymbol{r}_1, \boldsymbol{s}_1; \boldsymbol{r}_2, \boldsymbol{s}_2\right)$, Pauli's principle requires $\Psi\left(\boldsymbol{r}_1, \boldsymbol{s}_1; \boldsymbol{r}_2, \boldsymbol{s}_2\right) = -\Psi\left(\boldsymbol{r}_2, \boldsymbol{s}_2; \boldsymbol{r}_1, \boldsymbol{s}_1\right)$. If $\boldsymbol{s}_1 = \boldsymbol{s}_2$, we immediately see that $\Psi = 0$ for $\boldsymbol{r}_1 = \boldsymbol{r}_2$. Thus, electrons circumvent each other, thereby likely lowering their Coulomb-interaction energy compared to the situation of antiparallel spins. This makes parallel spin alignment energetically favored. However, the gain in Coulomb energy may be counteracted by a potentially larger kinetic energy caused by wave functions with a larger curvature in the region $\boldsymbol{r}_1 \sim \boldsymbol{r}_2$.

For a more explicit example of the consequences of the Pauli principle, we neglect SOI for the moment, such that the free-electron-like wave function factorizes, i. e.

$$|\Psi\rangle = |\mathit{\Phi}, \mathit{\Xi}\rangle = |\mathit{\Phi}\rangle \otimes |\mathit{\Xi}\rangle\,, \tag{2.17}$$

into its one-particle orbital part $|\mathit{\Phi}\rangle$ and spin part $|\mathit{\Xi}\rangle$. There are four possible wave functions obeying the Pauli principle: one for a symmetric orbital wave function $\mathit{\Phi}_\text{s} = \mathit{\Phi}\left(\boldsymbol{r}_1\right) \mathit{\Phi}\left(\boldsymbol{r}_2\right) + \mathit{\Phi}\left(\boldsymbol{r}_2\right) \mathit{\Phi}\left(\boldsymbol{r}_1\right)$ and three for an antisymmetric orbital wave function $|\mathit{\Phi}_\text{as}\rangle = \mathit{\Phi}\left(\boldsymbol{r}_1\right) \mathit{\Phi}\left(\boldsymbol{r}_2\right) - \mathit{\Phi}\left(\boldsymbol{r}_2\right) \mathit{\Phi}\left(\boldsymbol{r}_1\right)$:

$$\begin{aligned} |\Psi_\text{singlet}\rangle &= \quad |\mathit{\Phi}_\text{s}\rangle \left(|\uparrow, \downarrow\rangle - |\downarrow, \uparrow\rangle\right)/\sqrt{2} \\ |\Psi_\text{triplet}\rangle &= |\mathit{\Phi}_\text{as}\rangle \begin{cases} |\uparrow, \uparrow\rangle \\ \left(|\uparrow, \downarrow\rangle + |\downarrow, \uparrow\rangle\right)/\sqrt{2} \\ |\downarrow, \downarrow\rangle\,, \end{cases} \end{aligned} \tag{2.18}$$

where the singlet state $\Psi_\text{singlet}$ has the total spin $S = 0$ and the triplet state $\Psi_\text{triplet}$ has $S = 1\hbar$.

Let us now consider the case of two electrons (labeled $a$ and $b$) interacting with a nucleus of positive charge $Ze$, as in the Helium atom. The orbital wave functions $\mathit{\Phi}_{a,b}(\boldsymbol{r})$ of the one-electron Hamiltonian are assumed to be known. The corresponding nonrelativistic Hamiltonian for the two electrons is the sum of the electron kinetic energy $\hat{T}$ and the Coulomb potential energy $\hat{V}\left(\hat{\boldsymbol{r}}\right)$ (compare with Eq. 2.6). The eigenenergies of the one-electron system may be termed $E_a$ and $E_b$. We now add an interaction term $\hat{H}_{a,b}$ resulting in

$$\hat{H} = \hat{H}_a\left(\hat{\boldsymbol{r}}_1\right) + \hat{H}_b\left(\hat{\boldsymbol{r}}_2\right) + \hat{H}_\text{int}\left(\hat{\boldsymbol{r}}_1, \hat{\boldsymbol{r}}_2\right), \tag{2.19}$$

where $\hat{H}_{\text{int}} = e^2/4\pi\epsilon_0 \left|\hat{\boldsymbol{r}}_1 - \hat{\boldsymbol{r}}_2\right|$ represents the electron-electron interaction, whose eigenenergy is assumed to be minor compared to $E_a$ and $E_b$. Under the assumption that there is no coupling between different orbital states, and that the orbital functions are orthogonal, it can be shown [Whi72] that the two states in Eq. 2.18 are eigenfunctions of Eq. 2.19 with the eigenenergies

$$\begin{aligned} E_{\text{singlet}} &= E_a + E_b + K_{ab} + J_{ab} \\ E_{\text{triplet}} &= E_a + E_b + K_{ab} - J_{ab}, \end{aligned} \tag{2.20}$$

with the overlap integral

$$K_{ab} = \int\int \mathrm{d}\boldsymbol{r}_1 \mathrm{d}\boldsymbol{r}_2 \frac{e^2}{4\pi\epsilon_0 r_{12}} \left|\mathit{\Phi}_a\left(\boldsymbol{r}_1\right)\right|^2 \left|\mathit{\Phi}_b\left(\boldsymbol{r}_2\right)\right|^2 \tag{2.21}$$

and the exchange integral

$$J_{ab} = \int\int \mathrm{d}\boldsymbol{r}_1 \mathrm{d}\boldsymbol{r}_2 \mathit{\Phi}_a\left(\boldsymbol{r}_1\right) \mathit{\Phi}_b\left(\boldsymbol{r}_2\right) \frac{e^2}{4\pi\epsilon_0 r_{12}} \mathit{\Phi}_b\left(\boldsymbol{r}_1\right) \mathit{\Phi}_a\left(\boldsymbol{r}_2\right). \tag{2.22}$$

Importantly, $J_{ab}$ in our model system is always positive which has the important consequence that the triplet state is energetically favored over the singlet state (see Eq. 2.20) [Whi72]. Thus, a parallel spin alignment can result. We conclude that the Pauli exclusion principle and the Coulomb interaction can lead to a spontaneous spin ordering. Importantly, this exchange interaction is present even for a spin-independent Hamiltonian.

As noticed first by Dirac, the very same eigenenergies as in Eq. 2.20 result if the wave functions in the above example (see Eq. 2.18) are only taken as products of the spin states, and a spin-dependent term is added to the Hamiltonian [Whi72]. This exchange Hamiltonian reads

$$\hat{H}_{\text{ex}} = \text{const.} - \frac{1}{4} J_{\text{ex}} \hat{\boldsymbol{s}}_1 \cdot \hat{\boldsymbol{s}}_2 / \hbar^2, \tag{2.23}$$

where the exchange constant $J_{\text{ex}} = E_{\text{singlet}} - E_{\text{triplet}}$. In this way, the exchange interaction can effectively be expressed as a spin-spin interaction.

**Magnetically ordered solids.** As we have seen, exchange interactions can result in a spontaneous ordering of the individual magnetic moments of a solid. The magnetization $\boldsymbol{M}$ of a solid is defined as the sum of the quantum mechanical expectation value of the magnetic moments $\langle\hat{\boldsymbol{\mu}}_i\rangle$ per mesoscopic volume $V$:

$$\boldsymbol{M} = \frac{1}{V} \sum_i \langle\hat{\boldsymbol{\mu}}_i\rangle . \tag{2.24}$$

As seen in Eq. 2.8, orbital and spin magnetic moment both contribute to the total electron magnetic moment. However, in a solid, the orbital part is often largely quenched due to the orbital bonding [Stö07]. In the classical ferromagnets Co, Fe, and Ni it accounts for less than 10 % of the entire magnetic moment. Also, nuclear magnetic moments can be neglected since they are typically orders of magnitudes smaller than the electron spin magnetic moments [Stö07].

To describe magnetic ordering, two models have proven especially useful covering two limiting cases: localized and itinerant magnetic moments.

**Localized moments: Heisenberg model.** The simple situation of the above example (exchange interaction in a Helium atom) can be generalized to many electron spins in a solid. A crucial assumption is the localization of the individual electrons at a certain lattice site. In this case, the exchange term in the Hamiltonian prevails its simple form of Eq. 2.23 and can be written as [Whi72]

$$H_{\mathrm{ex}}^{\mathrm{solid}} = \mathrm{const.} - \sum_{\alpha>\alpha',n,n'} J_{\mathrm{ex}}^{nn',\alpha\alpha'} \boldsymbol{S}_{\alpha} \cdot \boldsymbol{S}_{\alpha'}/\hbar^2, \tag{2.25}$$

where $\boldsymbol{S} = \sum_i \boldsymbol{s}_i$ is the total electron spin at each lattice site $\alpha$ with the electron in the orbital state $n$. For simplicity, we have made the transition from the quantum mechanical operators to their expectation values as representing the physical observables because the system contains many particles. Equation 2.25 is known as the Heisenberg exchange Hamiltonian. Although it is only valid under quite restrictive assumptions, it has proven to be very useful as the starting point for studies of magnetic phenomena especially in insulators [Whi72].

In many cases, it is sufficient to restrict Eq. 2.25 to nearest neighbor interaction (since the overlap integral of electronic wave functions decays exponentially) and to the case of the lowest lying orbital states (low temperature limit). By neglecting the spin-independent energy offset, the Heisenberg Hamiltonian then reduces to the simple form

$$H_{\mathrm{ex}}^{\mathrm{eff}} = -J_{\mathrm{ex}} \sum_{\alpha>\alpha'} \boldsymbol{S}_{\alpha} \cdot \boldsymbol{S}_{\alpha'}/\hbar^2, \tag{2.26}$$

where the summation includes nearest neighbors only [Nol09]. In the following, Equation 2.26 will be referred to as the Heisenberg exchange Hamiltonian and $J_{\mathrm{ex}}$ will be called the exchange constant which, in general, can take negative and positive values [Whi72].

Thus, two limiting cases of magnetic ordering can be distinguished: ferromagnetic (parallel orientation of neighboring spins) for $J_{\mathrm{ex}} > 0$ and antiferromagnetic (antiparallel orientation of neighboring spins) for $J_{\mathrm{ex}} < 0$. If the solid consists of more than one magnetic sublattice, a ferrimagnetic ordering can arise in which the two magnetic sublattices have an opposite orientation but do not exactly cancel each other [Nol09].

Experimentally measured direct exchange constants between neighboring spins in, for instance, the ferrimagnetic insulator yttrium-iron garnet are on the order of millielectronvolts [Che93]. Importantly, the Heisenberg model is strictly only valid for localized magnetic moments, i. e. for insulators. However, magnetic interactions in metals can often be mapped onto an effective Heisenberg Hamiltonian. For instance, calculated exchange constants for the ferromagnetic metals Ni, Co, and Fe, are on the order of 10 meV and the sum over all nearest neighbors is on the order of 100 meV [Stö07].

Apart from the direct exchange interaction, exchange coupling may also occur through various indirect mechanisms. These include super exchange, double exchange, sd-exchange, and Ruderman–Kittel–Kasuya–Yosida (RKKY) exchange which can mediate spin interactions in metals and insulators [Nol09].

**Itinerant moments: Stoner model.** The Stoner model is a classical model to predict if a solid with delocalized electrons shows spontaneous ferromagnetic ordering [Stö07] (see Fig. 2.4).

It assumes separate band structures for the d-like spin-up and spin-down states (defined by the direction of an external magnetic field $\boldsymbol{B}_{\text{ext}}$). Depending on the strength of the exchange interaction (see Eq. 2.26) and on the density of states at the Fermi energy, it can be energetically favorable that the two spin channels are split by an energy $\Delta E_{\text{ex}}$. This leads to a population asymmetry (majority and minority spins) and causes a finite spin polarization of the d-like charge carriers near the Fermi energy. If a charge current is passed through the system (typically carried by delocalized sp-electrons), it can become spin-polarized through interactions with the more localized d-electrons [Cha07b].

Typical experimental values of the exchange splitting $\Delta E_{\text{ex}}$ in metals are on the order of 1 eV [Moh06].

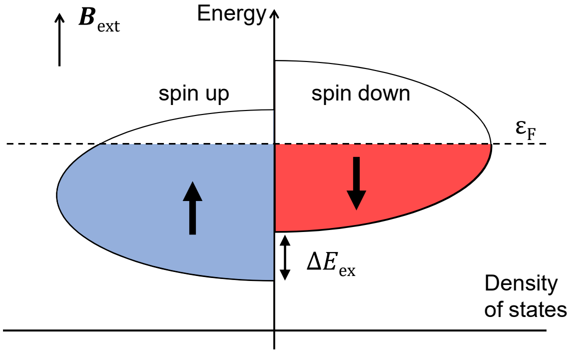

**Figure 2.4.: Stoner model of ferromagnetism.** A model band structure (only d-like bands shown) of a metallic ferromagnet subject to an external magnetic field $\boldsymbol{B}_{\text{ext}}$. The two spin channels (spin up/down) are split by an exchange energy $\Delta E_{\text{ex}}$ and populated up to the Fermi energy $\varepsilon_{\text{F}}$. The population asymmetry leads to majority (blue) and minority (red) spins, resulting in a net spin polarization of the electrons in the d-like bands near $\varepsilon_{\text{F}}$.

**Temperature dependence.** As the exchange interaction (see Eq. 2.26) competes with other energies in a solid, one observes a drastic dependence of the magnetization (see Eq. 2.24) on the temperature. Consequently, there exists a critical temperature $T_{\text{crit}}$ above which the magnetic order vanishes. In ferro-/ferrimagnets, it is called the Curie temperature $T_C$, whereas in antiferromagnets, it is known as the Néel temperature $T_N$. The magnetization is often found to follow a temperature dependence proportional to $(T_{\text{crit}} - T)^{\alpha}$ where $\alpha$ is called critical exponent [Stö07].

**Magnetic anisotropy and hysteresis.** In a real solid, that is, with finite dimensions, a spatially uniform magnetization would cause large stray fields around the solid, which is energetically unfavorable. Therefore, the uniform magnetization breaks up into magnetic domains. These are macroscopic parts of the solid in which the magnetic moments align uniformly. They orient among each other in such a way that the total magnetization and thus the stray field around the solid are minimized. This situation may change in the presence of an external magnetic field, favoring a uniform (single-domain) magnetization [Stö07].

The dependence of the magnetization on an external magnetic field is called a hysteresis curve (see Fig. 2.5). The width of such a curve is called the coercivity and it describes how resistive the magnetization is against an external field. The height of the hysteresis is called the saturation magnetization. The energy it takes to reverse a solid's magnetization is proportional to the area under the hysteresis loop.

The detailed shape of the hysteresis crucially depends on material properties and the sample geometry. As seen above, the exchange interaction is isotropic. However, due to SOI and spin-spin magnetic dipole interaction, also anisotropic spin-dependent energy terms may appear (see Eq. 2.15). This can cause energetically favored directions of the magnetization [Stö07].

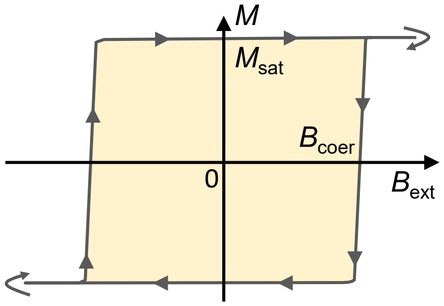

**Figure 2.5.: Magnetic hysteresis curve.** Typical dependence of the magnetization $M$ on the external magnetic field $B_{\text{ext}}$. The width is called coercivity ($B_{\text{coer}}$) and the height is called saturation magnetization ($M_{\text{sat}}$).

## 2.4. Spin dynamics

So far, we have considered equilibrium states of the spin system only. However, to eventually manipulate and control electron spins, their dynamics are essential.

### 2.4.1. Spin precession

In quantum mechanics, the Ehrenfest theorem states that the time evolution of the expectation value of an operator is given by the expectation value of its commutator with the Hamiltonian [Nol09]. For a single electron spin, it reads

$$\frac{\mathrm{d}}{\mathrm{d}t}\left\langle \hat{\boldsymbol{s}} \right\rangle = \frac{\mathrm{i}}{\hbar}\left\langle \left[\hat{H}, \hat{\boldsymbol{s}}\right] \right\rangle, \tag{2.27}$$

where $\langle ... \rangle$ denotes the quantum mechanical expectation value.

We concentrate for the moment on the special case of an externally applied time-dependent classical magnetic field $\boldsymbol{B}_{\mathrm{ext}}(t)$. By considering the Zeeman term, i. e. $\hat{H} = \hat{H}_{\mathrm{Z}} = g_{\mathrm{e}}\mu_{\mathrm{B}}\hbar^{-1}\hat{\boldsymbol{s}} \cdot \boldsymbol{B}_{\mathrm{ext}}(t)$ (see Eq. 2.7), it can be shown [Lak11] that using the spin commutation relations (Eq. 2.4), the spin dynamics are given by

$$\frac{\mathrm{d}}{\mathrm{d}t}\left\langle \hat{\boldsymbol{s}} \right\rangle = -\frac{g_{\mathrm{e}}\mu_{\mathrm{B}}}{\hbar}\left\langle \hat{\boldsymbol{s}} \right\rangle \times \boldsymbol{B}_{\mathrm{ext}}(t). \tag{2.28}$$

Equation 2.28 describes an undamped precession of the spin around an external magnetic field at a characteristic frequency $\omega_{\mathrm{L}} = \mu_{\mathrm{B}}B_{\mathrm{ext}}/\hbar$ which is called the Lamor frequency [Mon16].

In the following, we omit the quantum-mechanical operators and only consider their expectation values as the representation of the classical physical variables, e. g.

$$\left\langle \hat{\boldsymbol{s}} \right\rangle \to \boldsymbol{s}. \tag{2.29}$$

In the many-electron system, the Hamiltonian (Eq. 2.15) contains additional spin-dependent terms. Phenomenologically, they can lead to isotropic and anisotropic exchange terms (see Section 2.3.3), as well the magneto-elastic and the demagnetization contributions [Whi72]. The net effect of all these additional energy terms in the Hamiltonian $H$ is that the spin precesses around an effective field given by

$$\boldsymbol{B}_{\mathrm{eff}} = \frac{\hbar}{g_{\mathrm{e}}\mu_{\mathrm{B}}}\frac{\partial H(\boldsymbol{s})}{\partial \boldsymbol{s}}. \tag{2.30}$$

Here, $H(\boldsymbol{s})$ is the spin-dependent energy of the system [Mae17b]. As a result, various torques can act on the spin via $\boldsymbol{B}_{\mathrm{eff}}$ such as spin-orbit or exchange torques [Man09].

Note that $\boldsymbol{s}$ is just one spin at site $i$ and its motion depends on all other spins at sites $j \neq i$.

**Precessional damping.** It is an empirical fact that the disturbed (i. e. precessing) system will eventually return to equilibrium meaning that a damping term needs to be added to Eq. 2.28. It can be understood by considering the interaction of the spin system with other degrees of freedom (also called baths) such as the crystal lattice or orbital degrees of freedom [Eva14]. Accordingly, it results from a coupling of the spin system to the bath and the corresponding back action. The interaction of the spin to the bath alters the effective field given by

$$\boldsymbol{B}_{\text{eff}} \to \boldsymbol{B}_{\text{eff}} + \Delta \boldsymbol{B}_{\text{eff}}. \tag{2.31}$$

In linear response theory, $\Delta \boldsymbol{B}_{\text{eff}}$ can be related to $\boldsymbol{s}$ by a convolution (see App. A.2) with a linear response function $\chi_{\text{bath}}$:

$$\Delta \boldsymbol{B}_{\text{eff}} = \chi_{\text{bath}} * \boldsymbol{s} = \int_{-\infty}^{\infty} \mathrm{d}t' \, \chi_{\text{bath}} \left(t'\right) \mathbf{s} \left(t - t'\right). \tag{2.32}$$

Here, the symbol $*$ denotes the convolution. Thus, $\Delta \boldsymbol{B}_{\text{eff}}$ depends on past events at times $(t - t')$ weighted by $\chi_{\text{bath}}$. By expanding $\boldsymbol{s}\left(t - t'\right)$ in Eq. 2.32 up to first order, i. e. $\boldsymbol{s}\left(t - t'\right) \approx \boldsymbol{s}\left(t\right) + \dot{\boldsymbol{s}}\left(t\right)\left(t - t'\right)$, we can rewrite the effective-field correction as

$$\Delta \boldsymbol{B}_{\text{eff}} = a_1 \boldsymbol{s}\left(t\right) + a_2 \dot{\boldsymbol{s}}\left(t\right), \tag{2.33}$$

where $a_i$ are constants given by $\chi_{\text{bath}}$.

By inserting this result into Eq. 2.28, we obtain

$$\dot{\boldsymbol{s}} = \frac{g_{\text{e}} \mu_{\text{B}}}{\hbar} \left(\boldsymbol{s} \times \boldsymbol{B}_{\text{eff}} + a_2 \boldsymbol{s} \times \dot{\boldsymbol{s}}\right). \tag{2.34}$$

In this equation, the first term induces the precessional motion and is referred to as the field-like torque. The second term in Eq. 2.34 causes damping of the precession and is called the damping-like torque.

To see the effect of the damping term in Eq. 2.34 in more detail, we note that the energy dissipation is given by

$$\frac{\mathrm{d}H}{\mathrm{d}t} = \frac{\mathrm{d}H}{\mathrm{d}\boldsymbol{s}} \cdot \dot{\boldsymbol{s}} \propto \boldsymbol{B}_{\text{eff}} \cdot \dot{\boldsymbol{s}}. \tag{2.35}$$

Thus, only the damping term in Eq. 2.34, which contains the memory of the past $(t' < t)$, can relax the spin precession through the interactions of the spin system and the bath degrees of freedom.

### 2.4.2. Landau-Lifshitz-Gilbert equation

In systems involving many spins, one is typically interested in the dynamics of the normalized average magnetization, the so-called macrospin, given by $\boldsymbol{m} = \sum_{i=1}^{N} \boldsymbol{\mu}_i / N \mu_{\text{s}}$, where $\boldsymbol{\mu}_i$ is the local magnetic moment and $\mu_{\text{s}}$ is the electron spin magnetic moment (compare with Eq. 2.5) [Atx16]. It can be shown [Gil04] that the dynamic equation of $\boldsymbol{m}$ for $T \ll T_{\text{C}}$ has an analogous form as for a single spin (Eq. 2.34). The resulting Landau-Lifshitz-Gilbert (LLG) equation reads

$$\frac{\partial \boldsymbol{m}}{\partial t} = -\gamma_{\text{G}} \boldsymbol{m} \times \boldsymbol{B}_{\text{eff}} + \alpha \left|\gamma_{\text{G}}\right| \boldsymbol{m} \times \frac{\partial \boldsymbol{m}}{\partial t}, \tag{2.36}$$

where $\gamma_\mathrm{G} = \gamma/(1+\alpha^2)$ with the gyromagnetic ratio $\gamma$ and the Gilbert damping parameter $\alpha$. Conceptually, the damping term (i. e. the second term in Eq. 2.36) describes the dissipation of energy and angular momentum of macroscopic motion to microscopic thermal motion (coupling to the baths of conduction electrons, phonons, and magnons) [Atx16]. In real systems, however, details of the damping are typically very complex [Gil04].

A qualitative picture of the magnetization dynamics resulting from Eq. 2.36 is given in Fig. 2.6. Importantly, the LLG equation (Eq. 2.36) preserves the length of $\boldsymbol{m}$ [Mon16].

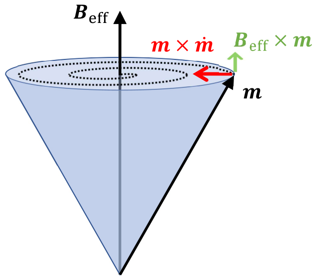

**Figure 2.6.: Magnetization dynamics.** Schematic of the dynamics of the macrospin $\boldsymbol{m}$ according to the Landau-Lifshitz-Gilbert equation (see Eq. 2.36). The effective magnetic $\boldsymbol{B}_\mathrm{eff}$ exerts a torque $\propto \boldsymbol{B}_\mathrm{eff} \times \boldsymbol{m}$ on $\boldsymbol{m}$, resulting in a precessional motion. Meanwhile, dissipation causes an additional damping torque $\propto \boldsymbol{m} \times \dot{\boldsymbol{m}}$, eventually leading to a parallel alignment of the magnetization and the effective field.

### 2.4.3. Magnons

The Heisenberg exchange Hamiltonian (Eq. 2.26) favors a collinear spin orientation at $T = 0\,\mathrm{K}$. However, for $T > 0\,\mathrm{K}$, thermal excitations will diminish the spin ordering. Consequently, small transverse components appear, which can be treated as a superposition of harmonic modes called spin waves or magnons.

To understand their origin, we note that in a solid, the spins do not only follow the damped precessional motion described by Eq. 2.34 but are also coupled to neighbor spins by for instance the exchange interaction (see Section 2.3.3) [Whi72]. Thus, the perturbation of a single spin will lead to a collective response of the spin system.

A systematic derivation follows a harmonic approximation of the spin Hamiltonian (see Eq. 2.26) [Kit05]. We consider a spin at site $\alpha$ interacting only with nearest-neighbor spins at sites $\alpha \pm 1$ described by the Hamiltonian

$$\hat{H}_\mathrm{ex}^\mathrm{nn} = -J_\mathrm{ex} \hat{\boldsymbol{s}}_\alpha \cdot \left(\hat{\boldsymbol{s}}_{\alpha-1} + \hat{\boldsymbol{s}}_{\alpha+1}\right)/\hbar^2 =: \hat{\boldsymbol{s}}_\alpha \cdot \hat{\boldsymbol{B}}_\alpha^\mathrm{ex} , \tag{2.37}$$

where we have defined the effective exchange field as $\hat{\boldsymbol{B}}_\alpha^\mathrm{ex} = -J_\mathrm{ex}\left(\hat{\boldsymbol{s}}_{\alpha-1} + \hat{\boldsymbol{s}}_{\alpha+1}\right)/\hbar^2$. The corresponding spin dynamics can be obtained by an Ehrenfest equation of motion. A similar problem has been considered in Section 2.4.1 and the solution is a precession of the spin around $\hat{\boldsymbol{B}}_\alpha^\mathrm{ex}$:

$$\frac{\mathrm{d}\left\langle \hat{\boldsymbol{s}}_\alpha \right\rangle}{\mathrm{d}t} = \frac{\mathrm{i}}{\hbar} \left\langle \left[ \hat{H}_\mathrm{ex}^\mathrm{nn}, \hat{\boldsymbol{s}}_\alpha \right] \right\rangle = \frac{g_\mathrm{e}\mu_\mathrm{B}}{\hbar} \left\langle \hat{\boldsymbol{s}}_\alpha \times \hat{\boldsymbol{B}}_\alpha^\mathrm{ex} \right\rangle . \tag{2.38}$$

By evaluating Eq. 2.38 for the different components of $\langle \hat{\boldsymbol{s}}_\alpha \rangle$ under the assumptions that $s_\alpha^{x,y} \ll s_\alpha$, neglecting terms in the $z$-component containing products of $s^x$ and $s^y$, and replacing the operators by their expectation values, we obtain the three coupled equations [Kit05]:

$$\begin{aligned}
\frac{\mathrm{d}}{\mathrm{d}t} s_\alpha^x &= -\frac{J_\mathrm{ex} g_\mathrm{e} \mu_\mathrm{B}}{\hbar} \left(2 s_\alpha^y - s_{\alpha-1}^y - s_{\alpha+1}^y\right) \\
\frac{\mathrm{d}}{\mathrm{d}t} s_\alpha^y &= -\frac{J_\mathrm{ex} g_\mathrm{e} \mu_\mathrm{B}}{\hbar} \left(2 s_\alpha^x - s_{\alpha-1}^x - s_{\alpha+1}^x\right) \\
\frac{\mathrm{d}}{\mathrm{d}t} s_\alpha^z &= 0.
\end{aligned} \tag{2.39}$$

We are interested in solutions that describe traveling waves proportional to $\exp\left[\mathrm{i}\left(\alpha k a - \omega t\right)\right]$, where $a$ is the lattice constant and $k$ is the length of the wave vector [Kit05]. It can be shown that the system of coupled Equations 2.39 has nontrivial solutions if

$$\omega = -2 J_\mathrm{ex} g_\mathrm{e} \mu_\mathrm{B} \left[1 - \cos\left(ka\right)\right] \overset{ka \ll 1}{\approx} -J_\mathrm{ex} g_\mathrm{e} \mu_\mathrm{B} a^2 k^2, \tag{2.40}$$

where the latter approximation is the long wavelength limit [Kit05]. Thus, the single spins follow a circular motion with frequency $\omega \propto k^2$ in the $x$-$y$-plane diminishing effectively the $z$-component (although this has been explicitly neglected in our derivation). Such collective excitations of the spin system are called magnons. In a ferromagnet, the lowest spin angular momentum carried by a magnon is the equivalent of flipping a single spin, i. e. $\pm\hbar$. Thus, magnons carry an integer spin and obey Bose statistics [Kit05]. Their energy is quantized and given by

$$\varepsilon_\mathrm{mag} = \left(n_\mathrm{mag} + \frac{1}{2}\right) \hbar\omega, \tag{2.41}$$

where $n_\mathrm{mag}$ is the occupation number of a certain magnon [Kit05].

The above considerations are only valid for perfectly ferromagnetic systems. The situation becomes more involved for systems with more than one magnetic sublattice, e. g. ferri- and antiferromagnets [Cot86].

### 2.4.4. Spin currents and torques

So far, we were mainly concerned with the directional dynamics of spins (i. e. no translational motion). However, in spintronics the spatial dynamics, that is, the flow of spin angular momentum through space, is also of crucial importance.

As seen in Section 2.3.3, an electrical current in a magnetically-ordered solid may become spin-polarized. On the other hand, pure spin currents may result from a counter-flow of spin up and spin down electrons that exactly cancels the charge current (see Fig. 2.7a). In addition to such conduction electron spin currents, there is an additional channel for the transport of spin angular momentum, that is, magnon spin currents (see Fig. 2.7b and Section 2.4.3).

In the following, we want to formulate an equation for spins similar to the continuity equation known for charges [Mae17b]. In contrast to the charge current (a vector), the spin current is a tensor of 2nd rank. It contains the direction of flow and the spin polarization (see Fig. 2.7). However, the spin is not a conserved quantity, only its length remains constant (i. e. $\hbar/2$) [Sun05].

Thus, the spin magnetic moment $\boldsymbol{\mu}_\mathrm{s}$ has two possible kinds of motion: a translational and a rotational. To describe the vector flow, essentially three quantities are required: the local magnetization $\boldsymbol{M}$ (see Eq. 2.24), the linear velocity $\boldsymbol{v}$, and the angular velocity $\boldsymbol{\omega}$ [Sun05]. It can be shown that the continuity equation for the local spin density then reads [Sun05]:

$$\frac{\mathrm{d}\boldsymbol{M}}{\mathrm{d}t} = -\boldsymbol{\nabla} \cdot \boldsymbol{v} \otimes \boldsymbol{M} + \boldsymbol{\omega} \times \boldsymbol{M}, \tag{2.42}$$

where $(\boldsymbol{v} \otimes \boldsymbol{M})_{ij} = v_i M_j$ are the tensor elements of $\boldsymbol{v} \otimes \boldsymbol{M}$. The first term of Eq. 2.42 describes the translational motion and the second term the rotational motion (i. e. spin torques). By defining the linear current density as $\underline{\boldsymbol{j}_\mathrm{s}} := \boldsymbol{v} \otimes \boldsymbol{M}$ and the angular current density (i. e the torque due to field $\boldsymbol{\omega}$) as $\boldsymbol{j}_\omega := \boldsymbol{\omega} \times \boldsymbol{M}$, Eq. 2.42 turns into

$$\frac{\mathrm{d}\boldsymbol{M}}{\mathrm{d}t} = -\boldsymbol{\nabla} \cdot \underline{\boldsymbol{j}_\mathrm{s}} + \boldsymbol{j}_\omega. \tag{2.43}$$

This equation for the spin density very much resembles the charge continuity equation. However, an important difference is that the linear current density is not conserved. Instead, we find in the steady state: $\boldsymbol{\nabla} \cdot \underline{\boldsymbol{j}_\mathrm{s}} = \boldsymbol{j}_\omega$. This means that torques acting on the local magnetic moments (represented by $\boldsymbol{j}_\omega$) can be sinks or sources of the linear current density even in the steady state [Sun05].

However, it should be noted that the above considerations are only valid in the nonrelativistic limit [An12, Rüc17]. In the relativistic treatment, Eq. 2.43 is reformulated in terms of the total angular momentum current density. Details can be found in [An12].

In summary, we see that the spin can be changed by two distinct mechanisms: spin torques ($\boldsymbol{j}_\omega = \boldsymbol{\omega} \times \boldsymbol{M}$) and spin transport ($\boldsymbol{\nabla} \cdot \underline{\boldsymbol{j}_\mathrm{s}}$). It should finally be noted that transport of spin angular momentum in insulators is mediated by magnons (see Section 2.4.3 and Fig. 2.7b), whereas in metals, it is dominated by conduction-electron spin currents (see Fig. 2.7a).

## 2.5. Spintronic transport effects

Spintronic devices rely on an efficient generation, transport, and detection of spin currents [Sin15]. These functionalities can be implemented by different spintronic effects that will be discussed in the following.

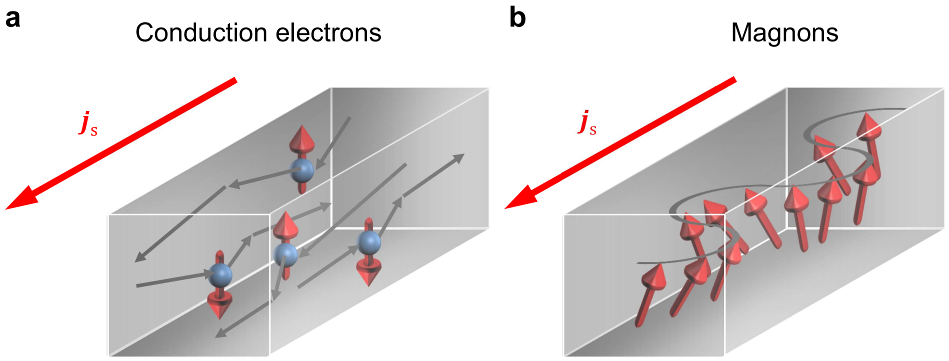

**Figure 2.7.: Conduction-electron and spin-wave spin currents.** **a,** Spin current $\boldsymbol{j}_{\mathrm{s}}$ in a metal carried by conduction electrons through diffusive motion. Electrons having opposite spin polarization flow in opposite directions, thereby leading to a pure spin current. **b,** Magnon spin current carried by a collective magnetic moment precession which is also known as a spin wave. Figure redrawn from [Kaj10].

As seen above, SOI has two important consequences: On one hand, it can lead to torques and induce a precession of the electron spin. On the other hand, it can influence the orbital motion of electrons resulting in the transport of spin angular momentum. The latter includes the spin-dependent Hall effects and the spin (-dependent) Seebeck effect that will be discussed below.

Generally, spin-dependent forces can modify spin transport. The corresponding Newton's law reads

$$m\ddot{\boldsymbol{r}} = \boldsymbol{F}\left(\boldsymbol{s}, \boldsymbol{r}, t\right). \tag{2.44}$$

As shown by a classical treatment [Chu07], SOI can result in a spin-dependent Lorentz-like force

$$\boldsymbol{F} \propto \frac{e}{c}\boldsymbol{v} \times \boldsymbol{B}_{\mathrm{eff}}^{\mathrm{so,\ orb}} \tag{2.45}$$

on the orbital motion with the effective spin-orbit field $\boldsymbol{B}_{\mathrm{eff}}^{\mathrm{so,\ orb}} \propto \boldsymbol{\nabla} \times (\boldsymbol{s} \times \boldsymbol{E})$. It causes a spin-dependent deflection of moving electrons enabling important spintronic phenomena such as the anomalous Hall and the spin Hall effect (see Fig. 2.8).

The spin-orbit field $\boldsymbol{B}_{\mathrm{eff}}^{\mathrm{so,\ orb}}$ that acts on the orbital motion of the electron must be differentiated from the one acting on the directional dynamics of the electron spin, that is, $\boldsymbol{B}_{\mathrm{eff}}^{\mathrm{so,\ s}}$.

The SOI-Hamiltonian $H = \boldsymbol{s} \cdot \boldsymbol{B}_{\mathrm{eff}}^{\mathrm{so}}$ (see Section 2.3.2 and Eq. 2.10) leads to a torque on the spins of the form (see Section 2.4.1)

$$\boldsymbol{j}_{\omega} \propto \boldsymbol{s} \times \boldsymbol{B}_{\mathrm{eff}}^{\mathrm{so,\ s}} \propto \boldsymbol{s} \times \left(\boldsymbol{E} \times \frac{\boldsymbol{v}}{c}\right), \tag{2.46}$$

which is known as the spin-orbit torque [Man09].

In the following, we classify important spintronic effects by the mediator of the spin current (i. e. electronic or magnonic spin currents) and by the stimulus (e. g. heat-driven or electric-field-driven).

**Field-driven effects.** The most prominent field-driven spintronic phenomena are the spin-dependent Hall effects [Sin15], i. e. the anomalous Hall, the spin Hall effect and its inverse. Importantly, their realization is not limited to DC driving currents. As we shall see later, free-space THz electromagnetic pulses may drive ultrafast charge currents in the studied material. This allows for the realization of the anomalous Hall effect and the current induced Néel spin-orbit torque [Jun16] at THz speeds.

Another important class of field-driven spintronic transport phenomena occur in heterostructures involving magnetic materials. An example are magneto-resistance effects such as the giant, tunneling, and spin-Hall magneto-resistance [Nak13, Bai88, Bin89, Jul75]. They manifest themselves as a dependence of the electrical resistance on the magnetization state of the individual constituents.

Another example is spin pumping and its inverse, the spin transfer torque effect. In spin-pumping experiments, a coherent precession of the magnetization in one of the layers is driven by an external microwave field. The damping-like torque acting on the precessing magnetization (see Eq. 2.36 and Fig. 2.6) results in the emission of a spin current, polarized perpendicular to the magnetization, into an adjacent layer [Mos10].

**Thermal effects.** So far, only electric fields, that is, gradients of electrostatic potentials, have been considered as the driver of spintronic effects. However, temperature gradients can also give rise to interesting phenomena, as explored in the field of spincaloritronics. Such heat-driven effects allow for the transport of spin and are even found in insulators.

Depending on the mediator of the spin current, two prominent spincaloritronic effects can be distinguished: The conduction-electron-mediated spin-dependent Seebeck effect (SDSE) and the magnon-mediated spin Seebeck effect (SSE; see Fig. 2.7). In heterostructures, these thermal effects can be enhanced due to the breaking of inversion symmetry.

For the experimental realization of the ultrafast SSE and SDSE, we use ultrashort optical laser pulses which induce a nonequilibrium state in a magnetic heterostructure on a femtosecond time scale. As will be shown later, the photo-induced SSE and SDSE currents can be monitored by THz-emission spectroscopy.

### 2.5.1. Spin-dependent Hall effects

In the ordinary Hall effect, the Lorentz force deflects moving charges transversely to their velocity and to an external magnetic field. In close analogy, the effective spin-orbit field results in a spin-dependent electron deflection (see Eq. 2.45). In magnetic materials this results in the anomalous Hall effect (AHE) whereas in nonmagnetic materials it is known as the spin Hall effect (SHE; see Fig. 2.8). In spintronics,

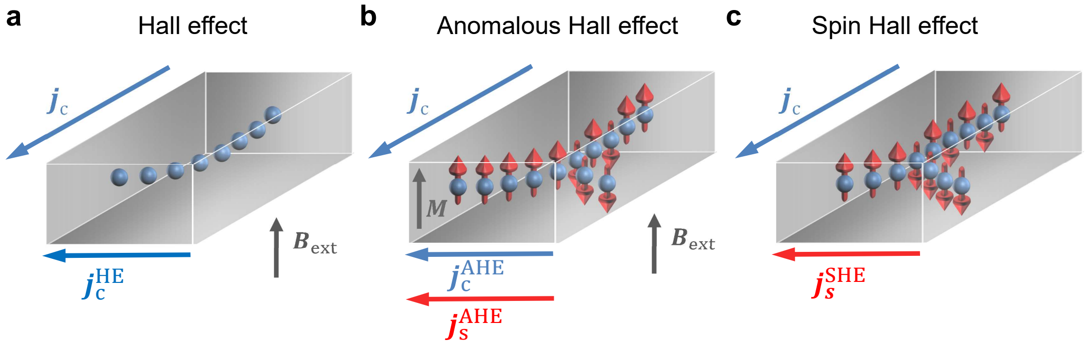

**Figure 2.8.: Hall effects.** **a**, In the ordinary Hall effect, the Lorentz force deflects charges transversely to the direction of the driving charge current $\boldsymbol{j}_{\mathrm{c}}$ and to the direction of the external magnetic field $\boldsymbol{B}_{\mathrm{ext}}$, giving rise to a Hall charge current $\boldsymbol{j}_{\mathrm{c}}^{\mathrm{HE}}$. **b**, In a magnetic material (magnetization $\boldsymbol{M} \neq 0$), the anomalous Hall effect induces a transverse spin-polarized charge current (i. e. a transverse charge and spin current $\boldsymbol{j}_{\mathrm{c,s}}^{\mathrm{AHE}}$). **c**, In a nonmagnetic material, the spin Hall effect induces a transverse spin current $\boldsymbol{j}_{\mathrm{s}}^{\mathrm{SHE}}$. In **b** and **c**, an effective spin-orbit field causes the spin-dependent deflection in analogy to the external magnetic field $\boldsymbol{B}_{\mathrm{ext}}$ in the Hall effect (**a**). Figure redrawn from [Cha16].

both effects and the inverse SHE (ISHE) are employed for the mutual conversion of charge and spin currents.

Importantly, the AHE describes a charge-to-charge conversion, whereas the SHE describes a charge-to-spin conversion. In contrast to the charge, the spin is not a conserved quantity in a closed system, making the theoretical understanding of the SHE more involved [Sin15].

In modern theories [Sin15], the different contributions to the spin-dependent Hall effects (AHE, SHE and ISHE) are classified with respect to their dependence on the electron momentum scattering time $\tau$. For this purpose, the disorder in a solid is treated perturbatively with respect to $\tau$.

In general, the spin-Hall-conductivity tensor $\underline{\sigma}^{\mathrm{SH}}$ can be defined by

$$j_{\mathrm{s},ij} = \sum_k \sigma_{ijk}^{\mathrm{SH}} E_k, \tag{2.47}$$

with the electric field $\boldsymbol{E}$.

The spin Hall conductivity consists of three parts:

$$\underline{\sigma}^{\mathrm{SH}} = \underline{\sigma}^{\mathrm{INT}} + \underline{\sigma}^{\mathrm{SS}} + \underline{\sigma}^{\mathrm{SJ}}. \tag{2.48}$$

The intrinsic contribution $\underline{\sigma}^{\mathrm{INT}}$ is already present without any disorder and thus independent of $\tau$. There are two disorder-induced contributions to the spin Hall conductivity: The skew scattering contribution $\underline{\sigma}^{\mathrm{SS}}$ is defined as the term that scales linearly with $\tau$, whereas the side-jump contribution $\underline{\sigma}^{\mathrm{SJ}}$ is defined as the term independent of $\tau$. A pictorial representation of the different (historically-derived) contributions is given in Fig. 2.9. However, it should be noted that the mechanisms shown in Fig. 2.9 differ in the detailed $\tau$-dependence from the above definition (Eq. 2.48) within the modern theoretical framework [Sin15].

Importantly, the spin-dependent Hall effects cannot be entirely explained by semi-classical approaches such as Boltzmann theory. As we will see, they are instead a consequence of coherent band mixing effects. This makes their treatment more involved than classical diagonal single-band transport [Sin15].

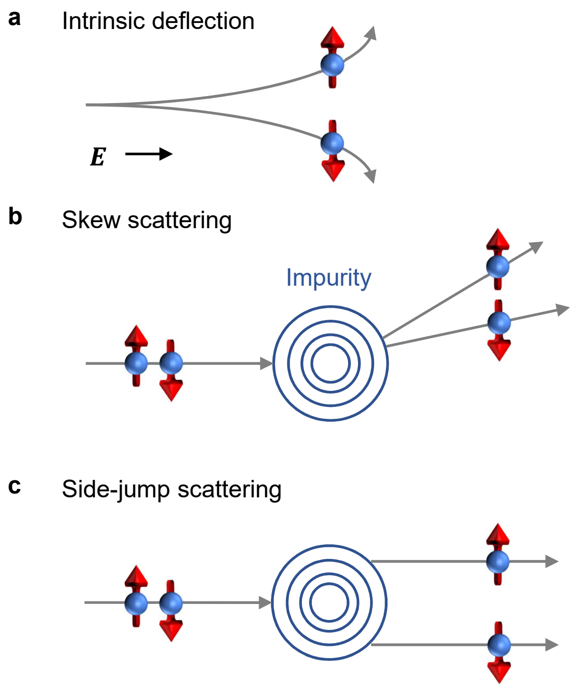

**Figure 2.9.: Schematic of the spin-Hall-effect mechanisms.** Three distinct spin-deflection mechanisms historically evolved: **a**, The intrinsic contribution to the SHE is a direct consequence of the perfect crystal lattice and induces an additional spin-dependent velocity component transverse to the drift velocity along the driving electric field $\boldsymbol{E}$. **b**, The skew scattering describes the spin-dependent inelastic scattering off impurities. Two main contributions can be distinguished: The first is in close analogy to the Mott scattering [Mot29], where the SOI is solely included in the impurity potential. The second arises due to the scattering of charge carriers moving in a spin-orbit-coupled band structure off an impurity without SOI. **c**, The side-jump scattering also describes the electron scattering off an impurity but it conserves the electron momentum. Electrons get displaced in the direction transverse to their velocity and dependent on their spin. Figure redrawn from [Nag10].

### Intrinsic mechanisms

SOI-induced spin-dependent scattering in a solid is much richer than the Mott scattering of atoms in vacuum, as it entails a contribution that originates from the perfect crystal lattice only and does not require any scattering [Sin15]. As observed in early works on the intrinsic AHE [Kar54], electrons traveling through a solid can be subject to an internal spin-orbit force (in addition to an external magnetic field). This force is similar to the classical Lorentz force in which the external magnetic field is replaced by a SOI-induced effective field resulting in an additional, transverse electron velocity (see Fig. 2.9a and Eq. 2.45).

The emergence of this anomalous velocity might be understood by considering an electron in a periodic lattice where its state is represented by a Bloch wave function (see Section 2.2). The time evolution of the position $\langle \hat{\boldsymbol{r}}_\mathrm{e} \rangle$ of an electron wave packet centered at wave vector $\boldsymbol{k}$ can be found from the Ehrenfest theorem [Ong06]:

$$\boldsymbol{v}_\mathrm{e} := \frac{\mathrm{d}}{\mathrm{d}t} \langle \hat{\boldsymbol{r}}_\mathrm{e} \rangle = \frac{\mathrm{i}}{\hbar} \left\langle \left[ \hat{H}, \hat{\boldsymbol{r}}_\mathrm{e} \right] \right\rangle = \boldsymbol{\nabla}_{\hbar \boldsymbol{k}} \varepsilon_{n,\boldsymbol{k}} + \left( \frac{1}{\hbar} \boldsymbol{E} \times \boldsymbol{\Omega} \right) (\boldsymbol{k}) \,. \tag{2.49}$$

In Eq. 2.49, the first term is the ordinary band velocity whereas the second term is called the anomalous velocity. It includes the Berry curvature $\boldsymbol{\Omega}(\boldsymbol{k})$, which is a gauge-invariant representation of the geometrical properties of the Bloch electrons in the band structure and it is strongly enhanced near avoided electron-band crossings [Sak95, Mae17b, Fre10]. The resulting anomalous velocity is oriented perpendicular to both, the applied electric field $\boldsymbol{E}$ and the electron band velocity $\nabla_{\hbar \boldsymbol{k}} \varepsilon_{\mathrm{n},\boldsymbol{k}}$. This extra term takes the form of the classical Lorentz force, where $\boldsymbol{\Omega}(\boldsymbol{k})$ acts as a magnetic field in momentum space [Ong06].

The intrinsic spin Hall contribution can be calculated accurately by *ab initio* methods within the framework of linear response theory by the Kubo formula [Kub57].

It can be shown [Wei11, Yao04] that the (anomalous-Hall) charge-current response to an electric field is directly proportional to the Berry curvature and given by

$$\begin{aligned} \sigma_{xy}^{\mathrm{int}} &= -\frac{e^2}{2\hbar} \int \frac{d^3k}{(2\pi)^3} \sum_{n \neq m} (f_n - f_m) \Omega_{nm,z}(\boldsymbol{k}) \\ &= \frac{e^2}{\hbar} \int \frac{d^3k}{(2\pi)^3} \mathrm{Im} \sum_{n \neq m} (f_n - f_m) \frac{v_{nm,x}(\boldsymbol{k})\, v_{mn,y}(\boldsymbol{k})}{(\omega_n - \omega_m)^2} , \end{aligned} \tag{2.50}$$

where the indices $n$ and $m$ run over all electronic bands, whose occupation is described the Fermi function $f$ (see Eq. 2.2). The summation further includes the matrix elements $v_{nm,i} = \langle \hat{v}_{nm,i} \rangle$ of the velocity operator $\hat{v}_i = \partial_{\hbar k_i} \hat{H}$ and the eigenfrequencies are $\omega_n = \varepsilon_{n,\boldsymbol{k}} / \hbar$.

Note that Eq. 2.50 is only valid for a DC driving field. However, for $\omega > 0$ a similar expression can be derived [Opp91]. Moreover, the effect of finite temperatures might be considered by including a phenomenological band broadening in the energy denominator of Eq. 2.50 [Opp91].

As is evident from Eq. 2.50, the intrinsic deflection mechanism arises from all occupied states. This contrasts with the diagonal transport which only depends on the occupied states near the Fermi energy (see Section 2.1). Remarkably, it can even be shown that the intraband contributions in Eq. 2.50 exactly cancel [Opp91]. The intrinsic mechanism tends to dominate in systems with large SOI [Sin15].

### Extrinsic mechanisms

**Skew scattering.** As the diagonal conductivity, the skew scattering mechanism is proportional to $\tau$. Therefore, it tends to dominate for small disorder. As seen in Fig. 2.9b, it involves a momentum change of the electron depending on its spin.

Two main contributions to $\underline{\sigma}^{\mathrm{SS}}$ can be distinguished: electrons scattering off an impurity with strong SOI or electrons moving in a spin-orbit-coupled band structure scattering off an impurity without SOI. The former is closely related to Mott-scattering (see Section 2.3.1). Thus, it also appears in Boltzmann theory without taking interband-coherence effects into account. However, theoretical predictions crucially rely on treating the disorder correctly [Sin15].

**Side-jump scattering.** In the modern parsing, the side-jump contribution is independent of $\tau$ and given through the above definitions by the relation

$$\underline{\sigma}^{\mathrm{SJ}} = \underline{\sigma}^{\mathrm{SH}} - \underline{\sigma}^{\mathrm{INT}} - \underline{\sigma}^{\mathrm{SS}}. \tag{2.51}$$

The mechanism that is historically-connected with side-jump scattering is depicted in Fig. 2.9c and can be understood as a lateral spin-dependent displacement of a Gaussian wave packet upon scattering off a spherical impurity with SOI. However as pointed out in Ref. [Sin15], in systems with strong SOI, also the spin-orbit-coupled part of the wave packet itself contributes to $\underline{\sigma}^{\mathrm{SJ}}$.

The side-jump mechanism is an elastic scattering process. The electron keeps its energy and momentum but is displaced in the transverse direction. The displacement is the same but opposite in sign for opposite spins (so the total momentum is conserved, contrary to skew scattering) [Sin15].

The fact that this contribution derives from impurities but does not depend on their density, probably makes it the most intriguing mechanism [Wei11].

### Relative strengths of the spin Hall mechanisms

A way to estimate the relative strengths of the spin-Hall-effect mechanisms is to distinguish between the regimes of strong and weak disorder (small and large $\tau$, respectively). Experimentally, a strong dependence of the off-diagonal conductivity on the diagonal conductivity could be observed as the sample temperature (and thereby $\tau$) was varied [Miy07]. In the weak disorder regime (large $\tau$), the spin Hall conductivity will be dominated by the mechanism proportional to the electron lifetime, i. e. the extrinsic skew scattering mechanism. In the limit of strong disorder, on the other hand, side-jump and intrinsic contributions will dominate the spin Hall response as they are independent of the electron lifetime. Their relative sizes depend on specific material parameters [Sin15]. However, it has been shown experimentally [Dhe67] and theoretically [Wei11] that in transition metals, the intrinsic contribution tends to be much larger than the side-jump mechanism.

## 2.5.2. Spincaloritronic effects

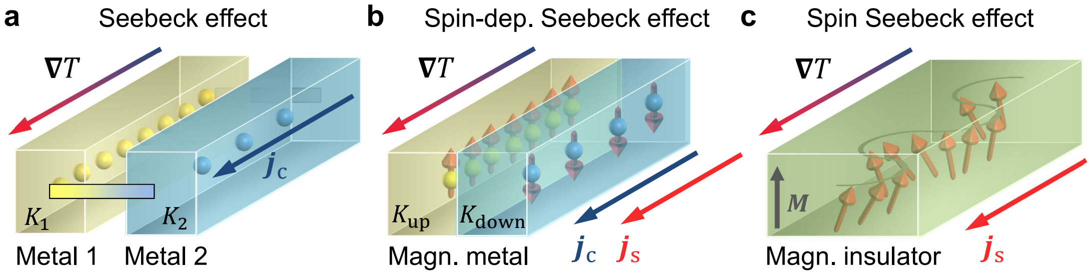

**Figure 2.10.: Seebeck effects.** **a**, In the Seebeck effect, a temperature gradient $\nabla T$ in a solid leads to charge redistribution along the gradient. If two metals with different Seebeck coefficients $K_{1,2}$ are electrically connected, a charge current flows proportional to $\nabla T \cdot (K_1 - K_2)$. **b**, The spin-dependent Seebeck effect can be observed in metals with a net magnetization. In analogy to the two materials in the classical Seebeck effect, the two spin species, called up and down, possess different Seebeck coefficients $K_{\text{up,down}}$. This causes a spin-polarized charge current along and proportional to $\nabla T \cdot (K_{\text{up}} - K_{\text{down}})$. For clarity, the two spin channels are laterally displaced **c**, The spin Seebeck effect describes the appearance of a pure spin current carried by magnons along and proportional to $\nabla T$. This effect is also present in metallic magnets, but is typically overwhelmed by the spin-dependent Seebeck effect. Consequently, it is typically observed in magnetic insulators. Figure partially redrawn from [Uch08].

The SHE and its inverse (ISHE) are nowadays a standard tool for the measurement of spin currents, having led to the discovery of the spin Seebeck effect [Uch08] opening the vibrant field of spincaloritronics [Bau12].

In the Seebeck effect, two metals with different transport properties are brought into electrical contact. Eventually, a thermal gradient $\nabla T$ drives a charge current in the bulk (see Fig. 2.10a). This effect thus enables the conversion of a temperature difference into an electrical voltage, which is the basis for thermocouples [Uch08].

### Spin-dependent Seebeck effect

In the spin-dependent Seebeck effect (SDSE), a temperature gradient along a magnetic metal, induces a spin-polarized conduction-electron current (see Fig. 2.10b) [Joh85].

The SDSE can be understood as the unification of the two metals from the Seebeck effect within a single magnetic material [Uch08]: Minority- and majority-spin electrons possess different transport properties (see Section 2.3.3) giving rise to a spin-polarized current along the temperature gradient (see Fig. 2.10b).

### Spin Seebeck effect

The spin Seebeck effect (SSE) has been first observed in magnetic insulators [Uch08]. A temperature gradient induces a pure spin current $\boldsymbol{j}_\mathrm{s}$ in the bulk which is carried by collective spin waves, so-called magnons (see Section 2.4.3 and Fig. 2.10c). Since pure spin currents are difficult to detect, the SSE is typically measured with the help of an additional heavy-metal layer which converts the spin current into a charge current through the ISHE (see Section 2.5.1).

In such a bilayer system, the SSE spin current inside the metal is thought to arise from the temperature difference between the metal electrons and the magnetic insulator magnons ($T_\mathrm{N} - T_\mathrm{F}$) [Ada13].

In the static SSE, the spin current $j_\mathrm{s}$ is given by

$$j_\mathrm{s} = \mathcal{K} \cdot (T_\mathrm{N} - T_\mathrm{F}) \,, \tag{2.52}$$

where $\mathcal{K}$ is the spin Seebeck coefficient. According to theory [Ada13], the SSE is thought to result from an effective exchange coupling (see Eq. 2.26) across the F/N interface. Qualitatively, this mechanism is described in Fig. 2.11. However, it is an open question, how Eq. 2.52 should be modified for time-dependent temperature variations. We will answer this question in this thesis (see Chapter 8 and App. A.3).

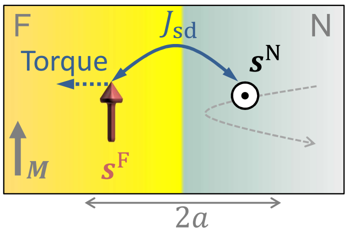

**Figure 2.11.: Model schematic of the sd-like exchange coupling at the F/N interface in the spin Seebeck effect.** To illustrate the action of the exchange torque between the spins in the metal (N) and in the magnetic insulator (F), we consider the case of an N-cell spin perpendicular to the magnetization $\boldsymbol{M}$ of the F layer. An N-electron entering the interaction region of width $2a$ induces a fluctuation $\boldsymbol{s}^\mathrm{N}$ of the total N-cell spin, thereby exerting the effective exchange torque $J_\mathrm{sd}\boldsymbol{s}^\mathrm{N}/\hbar$ on the adjacent F-cell spin $\boldsymbol{s}^\mathrm{F}$.

## 2.6. Light-matter interaction

In this Section, we want to describe the basic interaction of light and matter on a phenomenological level. This is of crucial importance because ultrashort optical laser pulses and THz pulses are the experimental tool of choice to study spintronic effects (see last Section). We will mainly focus on photo-induced currents.

Apart from its amplitude, a wave (e. g. electromagnetic radiation) is characterized by two further quantities: the angular frequency $\omega$ at which it oscillates in time and the wave vector $\boldsymbol{k}$ which describes its spatial periodicity. For light, these two quantities are related by $\omega = ck$, where $c$ is the speed of light in the medium. The wavelength is related to the wave vector by $\lambda = 2\pi/k$ and the energy carried by a single photon of the light wave is given by $\hbar\omega$. Note that the light field is treated classically throughout this work because we are always dealing with large photon numbers.

In the following, we will always assume that the spatial component of the electromagnetic wave can be described by a plane wave:

$$\boldsymbol{E}\left(\omega, \boldsymbol{k}\right) \propto \boldsymbol{E}\left(\omega\right) \exp\left(\mathrm{i}\boldsymbol{k} \cdot \boldsymbol{r}\right)). \tag{2.53}$$

This assumption is justified since for all cases in this thesis, the light-beam width is much smaller than the typical lateral dimensions of the studied samples, and the studied films are much thinner than the involved wavelengths. Therefore, we can restrict ourselves to the case of propagation along a certain axis, defined as the $z$-direction, i. e. $\boldsymbol{k} = k\hat{e}_z$. We further only consider the case of normal incidence, i. e. surface normal along $z$. The case of oblique incidence can be conveniently treated with a transfer-matrix approach (see below).

A laser pulse results from a superposition of electromagnetic waves spanning a certain spectral bandwidth and can be written in the frequency domain as

$$\boldsymbol{E}\left(\omega\right) = \sum_j \boldsymbol{A}_j\left(\omega_j\right) \mathrm{e}^{-\mathrm{i}\omega_j t} + \boldsymbol{A}_j\left(\omega_j\right)^* \mathrm{e}^{\mathrm{i}\omega_j t}, \tag{2.54}$$

where the coefficients $\boldsymbol{A}_j$ describe the amplitude spectrum of the contributing electromagnetic waves with angular frequencies $\omega_j$. The electric field in the time domain can be obtained by Fourier-transforming Eq. 2.54 (see App. A.1). The bandwidth and the duration of a laser pulse are closely connected via the uncertainty principle, stating that the product of pulse duration and bandwidth has a lower bound. Consequently, shorter laser pulses have a larger bandwidth [Boy03].

In the following, we will first consider local light matter interaction before we turn to the propagation of electromagnetic waves.

## 2.6.1. Local light-matter interaction

The response of a medium to an electric field can be treated perturbatively if the external electric field is much smaller than the atomic electric fields (typically on the order of $10^9\,\mathrm{V\,cm^{-1}}$) [Boy03]. The macroscopic response of the medium to an electric field can be described by the polarization it induces. It is defined as the total electric dipole moment per unit volume. Phenomenologically, it can be expanded in powers of the driving field and may be symbolically expressed in the frequency domain by:

$$\boldsymbol{P} = \epsilon_0 \sum_{i=1}^{\infty} \underline{\chi^{(i)}} \boldsymbol{E}^i. \tag{2.55}$$

The $(i+1)$-ranked susceptibilities tensors $\underline{\chi^{(i)}}$ depend on the material [Boy03].

The response of the medium to the magnetic component of the light wave is typically neglected because the magnetic dipoles cannot follow the fast light field oscillations [Pas13].

The induced current density is given by

$$\boldsymbol{j}_{\mathrm{ind}}(\omega) = -\mathrm{i}\omega \boldsymbol{P}(\omega). \tag{2.56}$$

These photo-induced currents provide the essential link to study spintronic transport phenomena as introduced in Section 2.3.3 using ultrashort laser pulses.

The induced polarization $\boldsymbol{P}$ (or photocurrent $\boldsymbol{j}_{\mathrm{ind}}$) re-emits electromagnetic waves. This radiated wave may have an altered spectrum and may even contain additional frequency components due to higher-order terms in Eq. 2.55. They become increasingly important if the driving fields have large amplitudes as easily achieved with state-of-the-art lasers [Boy03]. Throughout this work, it will be sufficient to consider effects up to third order in the expansion of $\boldsymbol{P}$ (see Eq. 2.55). In the following, these different orders will be discussed separately.

#### Linear response

The linear term in Eq. 2.55 reads

$$\boldsymbol{P}^{(1)}(\omega) = \epsilon_0 \underline{\chi}(\omega) \boldsymbol{E}(\omega). \tag{2.57}$$

The response function $\underline{\chi(\omega)}$ is a $3 \times 3$-matrix. In an isotropic medium, it reduces to a scalar [Jen37].

Apart from the susceptibility, often other quantities are used to describe the linear electric response. These include the dielectric function $\underline{\epsilon}$, the refractive index $\underline{n}$, and the electrical conductivity $\underline{\sigma}$. They are related to the susceptibility in the frequency domain by [Jen37]:

$$\underline{\epsilon} = 1 + \underline{\chi}, \ \underline{\epsilon} = \underline{n}^2, \ \text{and} \ \underline{\sigma} = -\mathrm{i}\epsilon_0\omega(\underline{\epsilon} - 1). \tag{2.58}$$

In this way, the induced current density is related to the electric field by

$$\boldsymbol{j}_{\mathrm{ind}}(\omega) = \underline{\sigma}(\omega) \boldsymbol{E}(\omega). \tag{2.59}$$

The diagonal components of the conductivity tensor are typically referred to as the longitudinal electrical conductivity in the sense that it relates to the current component parallel to the driving field.

The off-diagonal components, on the other hand, give rise to Hall-like contributions to the current which are transverse to the driving electrical filed. It can include contributions from the spin and the anomalous Hall effect as introduced in Section 2.5.1.

**The Drude model.** A simple model relating the macroscopic response function to microscopic quantities is the Drude model [Ash98]. Here, electrons are treated as free independent particles in an isotropic medium. This often resembles conduction electrons in real metals, where the Drude model has been applied with remarkable success. When subject to an external electric field $E\left(t\right)$, the conduction electrons get accelerated. Collisions, e. g. with impurities, phonons or other electrons, appearing at an average rate $\mathit{\Gamma}$, randomize the electron velocity $v$. This friction term causes a diffusive electron motion characterized by a drift velocity $v_{\mathrm{D}}$ [Ash98].

The corresponding equation of motion reads

$$m_{\mathrm{e}}\dot{v}\left(t\right)+m_{\mathrm{e}}\Gamma v\left(t\right)=-eE\left(t\right), \tag{2.60}$$

where $m_{\mathrm{e}}$ is the effective electron mass.

For a driving field oscillating at a frequency $\omega\neq 0$, Eq. 2.60 yields

$$v_{\mathrm{D}}\left(\omega\right)=-\frac{e/(m_{\mathrm{e}}\mathit{\Gamma})}{1-\mathrm{i}\omega/\mathit{\Gamma}}E\left(\omega\right). \tag{2.61}$$

By relating the drift velocity to the current through $j=-en_{\mathrm{e}}v_{\mathrm{D}}$ [Ash98], where $n_{\mathrm{e}}$ is the electron density, we arrive at the Drude formula for finite frequencies:

$$\sigma_{\mathrm{Drude}}\left(\omega\right)=\frac{\sigma_{\mathrm{DC}}}{1-\mathrm{i}\omega/\mathit{\Gamma}}, \tag{2.62}$$

where the conductivity at $\omega=0$ is given by

$$\sigma_{\mathrm{DC}}=\frac{e^2n_{\mathrm{e}}}{m_{\mathrm{e}}\Gamma}. \tag{2.63}$$

**Off-diagonal linear transport.** Spin-dependent Hall effects can convert charge currents into transverse spin (-polarized) currents and vice versa (see Section 2.5.1). In magnetic materials and at optical frequencies, these spin-dependent Hall effects are better known as the magneto-optical Kerr effect (MOKE) or the Faraday effect [Stö07]. Macroscopically, they are captured by the off-diagonal components of the conductivity tensor. In an isotropic magnetically-ordered solid, this tensor reads

$$\underline{\sigma}=\begin{pmatrix}\sigma & \sigma_{xy} & \sigma_{xz}\\ -\sigma_{xy} & \sigma & \sigma_{yz}\\ -\sigma_{xz} & -\sigma_{yz} & \sigma\end{pmatrix}, \tag{2.64}$$

with the diagonal conductivity $\sigma$ and the Hall conductivities $\sigma_{ij}$. Note that the Onsager relations impose $\sigma_{ij}(\boldsymbol{M}) = -\sigma_{ij}(-\boldsymbol{M})$ [Kit05].

A schematic of the anomalous Hall effect at THz frequencies is depicted in Fig. 2.12. Here, a THz transient drives an in-plane charge current in an out-of-plane-magnetized ferromagnetic metal. Consequently, a transverse anomalous Hall current is induced, and a new electric field component is radiated into the optical far-field. As a result, the initially linearly-polarized THz field acquires an elliptical polarization upon traversing the sample.

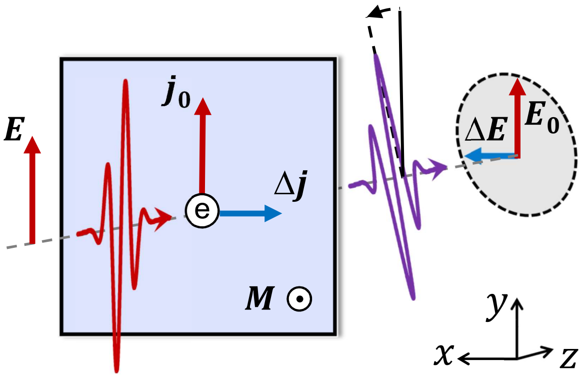

**Figure 2.12.: Anomalous Hall effect at terahertz frequencies.** The electric field $\boldsymbol{E}$ of a linearly-polarized THz pulse drives a $y$-directed charge current $\boldsymbol{j}_0$ in the plane a ferromagnetic sample with out-of-plane magnetization $\boldsymbol{M}$. Due to the anomalous Hall effect, a transverse, $x$-directed spin-polarized current $\Delta\boldsymbol{j}$ is induced. Consequently, the transmitted field acquires an elliptical polarization with the two orthogonal electric field components $\boldsymbol{E}_0$ and $\Delta\boldsymbol{E}$.

### Second-order nonlinear response

According to Eq. 2.54, the second-order nonlinear polarization is given by

$$P_i^{(2)}(\omega) = \epsilon_0 \sum_{j,k=1}^{3} \int \mathrm{d}\omega_1 \int \mathrm{d}\omega_2 \chi_{ijk}^{(2)}(\omega, \omega_1, \omega_2) E_j(\omega_1) E_k(\omega_2). \tag{2.65}$$

Importantly, to have a finite second-order nonlinear susceptibility $\chi^{(2)}$, the medium needs to have a broken inversion symmetry. This can be accomplished by the bare crystal symmetry or by the presence of additional structures such as interfaces [Boy03].

From Eq. 2.54, it is clear that mixing terms of the form $\mathrm{e}^{\mathrm{i}(\omega_1 \pm \omega_2)t}$ appear in the above expression for $\boldsymbol{P}^{(2)}$. These terms are responsible for the generation of difference and sum frequencies of the driving light field [Boy03].

Of special importance for the field of THz photonics is the difference-frequency generation. It allows for the conversion of optical laser pulses into THz laser pulses.

If the mixed frequency components originate from the same driving laser pulse, this process is called optical rectification [Boy03].

Another effect of interest here is the linear electro-optic effect, in which the refractive index of a medium is linearly proportional to an applied electric field. In the field of THz spectroscopy, it allows for the detection of the THz electric field with a second ultrashort optical laser pulse. The corresponding electro-optic sampling can be described as a sum-frequency generation between the THz and the probing pulse [Kam06].

Lastly, also photocurrents are found to depend on the square of the driving electric field (i. e. light power) and thus obey the symmetries of a second-order nonlinear response.

### Higher-order nonlinear response

Out of the manifold of third-order nonlinear effects, the optical Kerr effect is of importance within this thesis. It causes a change in refractive index proportional to the square of the electric field [Boy03].

It is also found in inversion-symmetric media. For isotropic media, the change in refractive index between the two axes along and perpendicular to the linearly-polarized driving field $E\left(\omega\right)$ is given by

$$\Delta n\left(\omega\right) = n_2\left(\omega\right) c\epsilon_0 E^2\left(\omega\right), \tag{2.66}$$

where $n_2$ describes the strength of the nonlinear response [Boy03].

This effect is important for the operation of femtosecond lasers as transient Kerr lenses represent one way to achieve mode-locking [Fer02b].

## 2.6.2. Wave propagation

So far, we have only considered the local response of matter to electric fields. Now we will turn to the propagation of light inside a medium.

For a plane wave propagating in the $z$-direction, the wave equation in the time domain as derived from the Maxwell equations reads [Boy03]:

$$\left(\partial_z^2 - \frac{1}{c^2}\frac{\partial^2}{\partial t^2}\right)\boldsymbol{E}\left(z,t\right) = \frac{1}{\epsilon_0 c^2}\frac{\partial^2}{\partial t^2}\boldsymbol{P}\left(z,t\right). \tag{2.67}$$

It describes the propagation of an electromagnetic wave in time and space inside a medium.

Accordingly, we find in the frequency domain:

$$\left(\partial_z^2 + \frac{\omega^2}{c^2}\right)\boldsymbol{E}\left(z,\omega\right) = -\frac{\omega^2}{\epsilon_0 c^2}\boldsymbol{P}\left(z,\omega\right). \tag{2.68}$$

### Linear electric polarization

In linear optics, we are concerned with finding a solution of Eq. 2.68 for $\boldsymbol{P}$ containing only terms linear in $\boldsymbol{E}$.

In the following, we may restrict ourselves to the case of linearly-polarized $\boldsymbol{E}$ and $\boldsymbol{P}(\boldsymbol{E})$, such that $\boldsymbol{E} \| \boldsymbol{P}(\boldsymbol{E})$, as well as to an isotropic, homogeneous, and nonmagnetic medium (i. e. the dielectric function is given by a complex scalar). Thus, combining Eq. 2.68 with Eq. 2.57, and neglecting vectorial notation, we find

$$\left(\partial_z^2 + \frac{\omega^2}{c^2}\epsilon\right) E(z,\omega) = 0. \tag{2.69}$$

The solution of Eq. 2.69 is a plane wave traveling along $z$:

$$E(z,t) = E_0 \exp\left[\mathrm{i}\left(k_z z - \omega t\right)\right], \tag{2.70}$$

where $E_0$ is the amplitude and $k_z$ is the $z$-component of the complex-valued wave vector. The latter is defined by

$$\boldsymbol{k}^2 = \frac{\omega^2}{c^2}\epsilon. \tag{2.71}$$

In the more general case of an anisotropic nonmagnetic medium, the wave vector will depend on the propagation direction (through $\underline{\epsilon}$).

In the case of an isotropic magnetic medium, on the other hand, the MOKE (see Section 2.6.1) may lead to a change of the spatial components of the electric field with $z$. Thus, a linearly-polarized wave may become elliptically polarized.

These more complex cases can be treated by a transfer-matrix formalism, which will be introduced below.

### Nonlinear electric polarization

We now allow for a nonlinear polarization but restrict ourselves to the case of an isotropic nonmagnetic medium, to linearly-polarized $\boldsymbol{E}$ and $\boldsymbol{P}(\boldsymbol{E})$, such that $\boldsymbol{E} \| \boldsymbol{P}(\boldsymbol{E})$ and vectorial notation can be neglected.

For a nonlinear electric polarization $P^{\mathrm{NL}} := P - P^{(1)}$, Eq. 2.68 turns into:

$$\left(\partial_z^2 + \frac{\omega^2}{c^2}\right) E(z,\omega) = -\frac{\omega^2}{\epsilon_0 c^2} P^{\mathrm{NL}}(z,\omega) =: S(z,\omega), \tag{2.72}$$

where we have defined the source term $S(z,\omega)$.

### Analytical solution of the wave equation: a Green's function approach

An elegant way to solve Eq. 2.72 employs Green's functions. It can be shown [Mil12] that if the function $G_{z'}(z,\omega)$ is a solution of Eq. 2.72 for a delta-like source term $\delta_{z'}$ at $z'$, then the general solution to Eq. 2.72 is given by

$$E(z,\omega) = \int \mathrm{d}z' G_{z'}(z,\omega)\, S(z',\omega)\,. \tag{2.73}$$

The function $G_{z'}(z,\omega)$ is called Green's function, which can be seen as the propagator of the field of a delta-like source at position $z'$ to the point of observation $z$. The most interesting case for this thesis is the Green's function of two infinite half spaces with their interface at $z = 0$ (see Fig. 2.13). In medium 2, the outgoing Green's function reads [Kam06]

$$G_{z'}(z,\omega) = \frac{\exp\left(\mathrm{i}k_2\left|z-z'\right|\right)}{2\mathrm{i}k_2}\left[1 + r_{21}\exp\left(2\mathrm{i}k_2 z\right)\right]. \tag{2.74}$$

With these tools at hand, we are ready to calculate the wave propagation for some important examples.

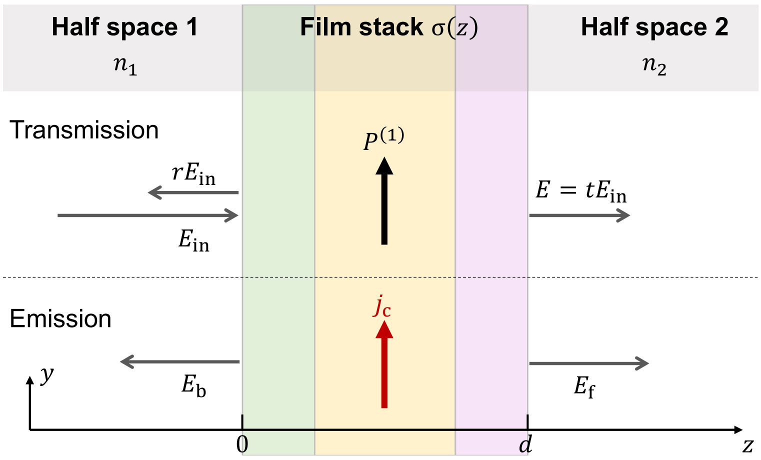

**Figure 2.13.: Film stack between two half spaces.** A film stack of thickness $d$ with the conductivity distribution $\sigma(z)$ is located in between two half-spaces 1 and 2 with refractive indices $n_{1,2}$. In the transmission problem (upper part), an electric field $E_{\text{in}}$ is propagating in $z$-direction and incident onto the film stack. As a result, it induces the linear polarization $P^{(1)}$. This re-emits a wave in the forward and backward direction characterized by the reflection and transmission coefficients $r$ and $t$, respectively. Consequently, the incoming wave gets partially reflected ($rE_{\text{in}}$) and transmitted ($tE_{\text{in}}$). In the emission problem (lower part), a $y$-directed charge current density inside the film stack acts as a source of electromagnetic waves. Two waves get emitted traveling in the negative ($E_{\text{f}}$) and positive ($E_{\text{b}}$) $z$-direction.

**Transmission through a thin-film stack.** A typical problem in THz spectroscopy is the transmission of an incoming electric field $E_{\text{in}}$ through a thin-film stack in between two half spaces (see Fig. 2.13).

We first consider two infinite half spaces without any film stack, where the wave equation reads

$$\left[\partial_z^2 + k_0^2\left(z,\omega\right)\right] E\left(z,\omega\right) = 0, \tag{2.75}$$

and the solution is given by Eq. 2.70.

However, when a film of thickness $d$ is brought into the medium, an additional term appears in the wave-vector distribution $k_0^2\left(z,\omega\right)$ that is given by $\Delta(k^2) = iZ_0\sigma\omega/c$. Here, we have assumed that the thin film stack, with conductivity $\sigma\left(z,\omega\right)$, replaces the second half space with refractive index $n_2 \approx 1$ (as for air). Consequently, we find for the wave equation

$$\left[\partial_z^2 + \left(k_0^2\left(z,\omega\right) + \Delta(k^2)\left(z,\omega\right)\right)\right] E\left(z,\omega\right) = 0. \tag{2.76}$$

We can bring Eq. 2.76 into the form:

$$\left[\partial_z^2 + k_0^2\left(z,\omega\right)\right] E\left(z,\omega\right) = S\left(z,\omega\right), \tag{2.77}$$

where $S\left(z,\omega\right) = -\Delta(k^2)\left(z,\omega\right) E\left(z,\omega\right)$. With the help of the Green's function formalism (Eqs. 2.73 and 2.74), we can find the solution to Eq. 2.77 in medium two (see Fig. 2.13). It is given by the superposition of the incoming wave and an additional wave due to the thin film stack. We thus find

$$E\left(z,\omega\right) = t_{12}E_{\mathrm{in}} + \int_0^d \mathrm{d}z' G_{z'}\left(z,\omega\right) S\left(z',\omega\right), \tag{2.78}$$

where the Fresnel transmission coefficient is $t_{12} = 2n_1/(n_1+n_2)$ [Jen37] and the Green's function of the reference system without metal film is given by Eq. 2.74.

At this point, we make two important assumptions: Firstly, we consider a film stack much thinner than the wavelength and the attenuation length of the light. This allows us to approximate all phase factors by 1, resulting in $G_{z'}\left(z,\omega\right) \approx c/[\mathrm{i}\omega\left(n_1+n_2\right)]$. Secondly, we assume that the electric field $E$ is constant throughout the thin-film stack.

Consequently, $G_{z'}$ and $E$ may be pulled out of the integral on the right-hand side of Eq. 2.78 to yield:

$$E\left(\omega\right) = t_{12}E_{\mathrm{in}}\left(\omega\right) - \frac{c}{\mathrm{i}\omega\left(n_1+n_2\right)} E\left(\omega\right) \int_0^d \mathrm{d}z' \frac{\mathrm{i}Z_0\sigma\left(z',\omega\right)\omega}{c}, \tag{2.79}$$

where $Z_0 = 377\,\Omega$ is the vacuum impedance. This finally yields for the transmission function through the thin film stack

$$t\left(\omega\right) := \frac{E\left(\omega\right)}{E_{\mathrm{in}}\left(\omega\right)} = \frac{2n_1}{n_1 + n_2 + Z_0\int_0^d \mathrm{d}z'\sigma\left(z',\omega\right)}. \tag{2.80}$$

Equation 2.80 may be understood as a generalization of the famous Tinkham formula [GI57] to a stack of thin films. Notably, in Eq. 2.80, the film stack conductivities add up to an overall conductance analogous to an electrical parallel connection. In a sense, the thin film stack forms an effective medium with $\sigma = \langle\sigma_i\rangle$ [Lal03].

**Emission from a thin-film stack.** A further typical problem in THz spectroscopy is the emission of an electric field by a charge current density $-ej_\mathrm{c}$ inside a thin-film stack in between two half spaces (see Fig. 2.13).

We are interested in the radiated field in medium 2 (forward propagating wave). In this case, the wave equation reads:

$$\left[\partial_z^2 + k^2\left(z,\omega\right)\right] E\left(z,\omega\right) = -eZ_0\omega j_\mathrm{c}\left(z,\omega\right)/\mathrm{i}c =: Q\left(z,\omega\right). \tag{2.81}$$

Following the same perturbational approach as before, we find that the thin-film stack changes the wave vector landscape to $k^2\left(z,\omega\right) = k_0^2\left(z,\omega\right) + \Delta(k^2)\left(z,\omega\right)$. By again taking the part containing $\Delta(k^2)$ to the right-hand side of Eq. 2.81, we find:

$$E\left(z,\omega\right) = \int_0^d \mathrm{d}z' G_{z'}\left(z,\omega\right) S\left(z',\omega\right), \tag{2.82}$$

where $G_{z'}\left(z,\omega\right)$ is again the Green's function for the reference system without any film stack (see Eq. 2.74). The source term now contains two terms:

$$S\left(z,\omega\right) = Q\left(z,\omega\right) - \Delta(k^2)\left(z,\omega\right) E\left(z,\omega\right), \tag{2.83}$$

where again $\Delta(k^2) = iZ_0\sigma\omega/c$, which assumes that the thin film stack, with conductivity $\sigma\left(z,\omega\right)$, replaces the second half space with refractive index $n_2 \approx 1$ (as for air). Restricting to the case that all involved wavelengths of the electromagnetic waves and their attenuation lengths are much larger than the film thickness, and considering the quasi-static limit, i. e. the electric field $E$ is constant within the heterostructure, Eq. 2.82 turns into:

$$E\left(\omega\right) = \int_0^d \mathrm{d}z' \frac{c}{\mathrm{i}\omega\left(n_1+n_2\right)}\left[-\frac{eZ_0\omega j_\mathrm{c}\left(z',\omega\right)}{\mathrm{i}c} - \frac{\mathrm{i}Z_0\sigma\left(z',\omega\right)\omega}{c}E\left(\omega\right)\right], \tag{2.84}$$

which is equivalent to

$$E\left(\omega\right) = \frac{eZ_0\int_0^d \mathrm{d}z' j_\mathrm{c}\left(z',\omega\right)}{n_1+n_2+Z_0\int_0^d \mathrm{d}z'\sigma\left(z',\omega\right)}. \tag{2.85}$$

### General transmission problem: transfer-matrix approach

If the thin-film limit does not apply and if more than one layer is involved in the transmission process, the problem becomes more involved.

For the simple case of a single film in between two half spaces 1 and 2 (see Fig. 2.13), the solution can be written as

$$t^\mathrm{film}\left(\omega\right) = t_{13}t_{32}F\exp\left(\mathrm{i}kd\right), \tag{2.86}$$

where $t_{ij} = 2n_i/(n_i+n_j)$ is the Fresnel transmission coefficient for a wave traveling from medium $i$ to medium $j$ [Jen37], $k = n_3\omega/c$ is the wave vector of the film with its refractive index $n_3$ and thickness $d$. The Fabry-Pérot term $F$ accounts for the multiple reflections of the wave within the film and is given by

$$F = \left(1 - r_{32} r_{31} \exp\left(\mathrm{i} 2 k d\right)\right)^{-1}, \tag{2.87}$$

where $r_{ij} = \left(n_j - n_i\right) / \left(n_i + n_j\right)$ is the Fresnel reflection coefficient [Jen37].

For more than one film, an elegant way to solve the problem analytically is a transfer-matrix approach, which is even applicable to anisotropic magnetic materials [Zak90].

In general, the Maxwell equations impose certain boundary conditions at the interfaces between two media for the electromagnetic fields: The continuity of the electric field $\boldsymbol{E}$ itself and of its derivative $\partial_z \boldsymbol{E}$ along the surface normal of the film [Boy03]. Based on these conditions, the transmission problem can be cast into a multiplication of matrices which involve two steps: the transmission from one medium into another, and the propagation inside a medium. The detailed expressions for these matrices may be found in [Zak90].

Accordingly, with the help of the transmission matrix $\underline{D}$ and the propagation matrix $\underline{P}$ of the single layers, the complete transfer matrix $\underline{T}$ of the film stack composed of $i-1$ layers might be constructed as

$$\underline{T} = \underline{D}_1^{-1} \underline{D}_2 \underline{T}_2 \underline{D}_2^{-1} ... \underline{D}_{i-1} \underline{T}_{i-1} \underline{D}_{i-1}^{-1} \underline{D}_i, \tag{2.88}$$

where $\underline{D}_1$ and $\underline{D}_i$ are the transmission matrices of the two outer half spaces. By writing the $(4 \times 4)$ $\underline{T}$-matrix in terms of four $(2 \times 2)$-matrices $\underline{G}$, $\underline{H}$, $\underline{I}$ and $\underline{J}$ as

$$\underline{T} = \begin{pmatrix} \underline{G} & \underline{H} \\ \underline{I} & \underline{J} \end{pmatrix}, \tag{2.89}$$

it can be shown [Zak90] that the transmission and reflection coefficients can be obtained from

$$\begin{pmatrix} t_{\mathrm{ss}} & t_{\mathrm{sp}} \\ t_{\mathrm{ps}} & t_{\mathrm{pp}} \end{pmatrix} = \underline{G}^{-1} \tag{2.90}$$

and

$$\begin{pmatrix} r_{\mathrm{ss}} & r_{\mathrm{sp}} \\ r_{\mathrm{ps}} & r_{\mathrm{pp}} \end{pmatrix} = \underline{I} \underline{G}^{-1}, \tag{2.91}$$

where the subscripts s and p refer to the polarization directions of the electric field perpendicular and parallel to the plane of incidence, respectively.

# 3. Experimental methods

*To access spin and charge dynamics on the femtosecond time scale, an all-optical approach involving optical and THz pulses is chosen. Two basic operational modes of a THz spectrometer can be distinguished: First, the THz-emission mode, in which a femtosecond optical pump pulse triggers the emission of a THz transient, which is directly measured and contains information on the charge and spin dynamics in the emitter. Second, the THz transmission mode, in which optical properties of a material in the THz range can be characterized by sending a THz pulse through the studied sample. In all cases, the detection is implemented via the linear electro-optic effect (see Section 2.6.1) enabling electro-optic sampling.*

## 3.1. Laser systems

A laser consists of an active medium, a device creating a population inversion inside that medium (pump), and an optical cavity. Under these circumstances, the process of stimulated emission can result in the amplification of coherent radiation [Fer02b]. If the active medium has a large gain bandwidth and the different laser modes are mutually phase locked (mode locking), femtosecond-pulsed operation can be achieved. Within this thesis, the laser medium capable of sustaining femtosecond-pulsed operation is titanium-doped sapphire (Ti:Sapphire), which has a gain from 670 to 850 nm [Fer02b].

Two complementary laser systems are operated: A high-repetition-rate, low-pulse-energy system, and a low-repetition-rate, high-pulse-energy system. The latter is used to create strong THz fields which allow not only for probing but also for driving elementary excitations in solids [Kam13b]. However, if low THz peak fields are sufficient, as for most experiments within this thesis, the oscillator-based setup (high repetition rate, low pulse energy) has the big advantage of being substantially easier to operate while delivering a similar or even better signal-to-noise ratio compared to the amplified laser system. Importantly, the oscillator-derived laser pulses offer a large bandwidth, thereby allowing for short pulses and a time resolution as fine as 10 fs [Bra16a].

**High repetition rate laser oscillator.** The high-repetition-rate laser oscillator (Femtosource M1, Spectra-Physics) is shown in Figure 3.1. It is pumped by a continuous-wave Nd:$YVO_4$ laser at a wavelength of 532 nm. Mode locking is achieved by a passive scheme relying on Kerr lensing (see Section 2.6.1), in which a transiently induced lens favors amplification of the most intense modes. To control the laser-pulse duration, chirped mirrors are used for dispersion compensation. This laser system can generate ultrashort laser pulses with a central wavelength of 800 nm, a duration of 10 fs, a pulse energy of 11 nJ, and a repetition rate of 75 MHz. The output is split at a ratio of 80:20 to seed the THz generation and detection path, respectively. More details on this laser system are provided in [Bra16a].

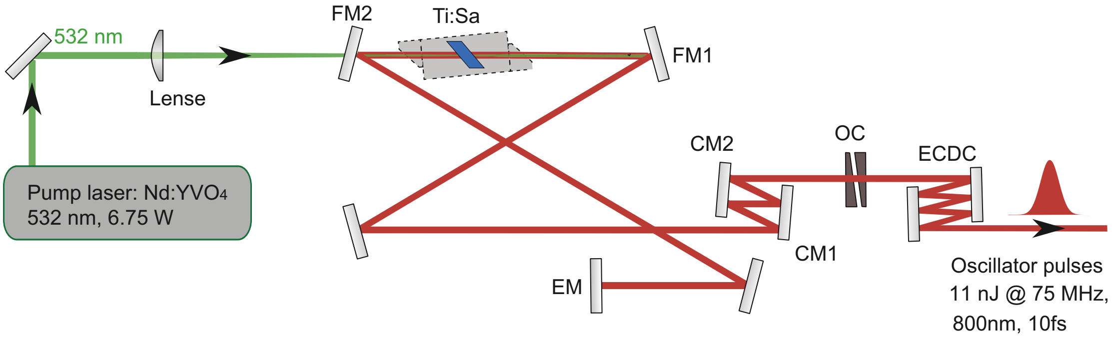

**Figure 3.1.: Megahertz laser oscillator.** The active medium, a titanium-doped sapphire crystal (Ti:Sa), is optically pumped with a continuous-wave Nd:YVO$_4$ laser at a wavelength of 532 nm. The optical cavity consists of an end mirror (EM) and a partially transmissive output coupler (OC). Focusing mirrors (FM1/2) lead to high intensities inside the active medium. The laser-pulse dispersion is controlled by a pair of chirped mirrors (CM1/2) inside the laser cavity as well as a pair of wedges (part of the OC). The external cavity-dispersion control (ECDC) allows for fine tuning of the pulse duration. Figure reproduced from [Bra16a] with the permissions of L. Z. Braun and S. F. Mährlein.

**Low repetition rate laser amplifier.** The low-repetition-rate laser system relies on the input from a femtosecond laser oscillator similar to the one in Section 3.1 but with slightly different specifications. In detail, it is a Venteon Pulse One PE system operating at a repetition rate of 80 MHz, a pulse duration of 8 fs, a central wavelength of 750 nm, and a pulse energy of 24 nJ (details can be found in [Mäh16]). The output of this laser oscillator is split at a ratio of 25:75 to seed the detection path as well as the subsequent laser amplifier, respectively.

An amplification of the low-energy oscillator-derived laser pulses by a factor of about $10^6$ is achieved by a combination of a regenerative amplifier (Coherent Legend Elite Duo USP) and a subsequent single-pass amplifier (see Fig. 3.2).

In order not to destroy the optical components and to avoid undesired nonlinear effects, the pulse peak intensity is lowered by lengthening the pulse duration with a grating stretcher from femtoseconds to hundreds of picoseconds. In addition, the average heat load on the optical components is minimized by reducing the repetition rate to 1 kHz with two Pockels cell.

The two successive amplification stages result in laser pulses with a repetition rate of 1 kHz, a pulse energy of 10 mJ, and a central wavelength of 800 nm. A subsequent temporal shortening in a grating compressor gives a pulse duration of 35 fs. Details can be found in [Mäh16].

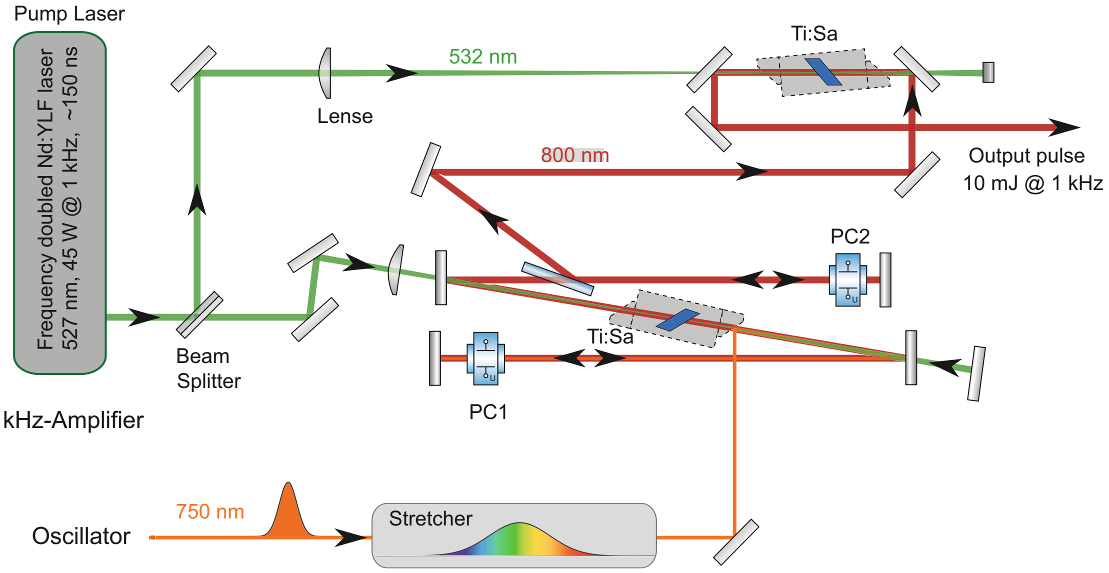

**Figure 3.2.: Kilohertz laser amplifier.** The femtosecond seed pulses of a megahertz laser oscillator with a central wavelength of 750 nm are temporally lengthened by a grating stretcher. The active media, two titanium-doped sapphire crystals (Ti:Sa), are optically pumped with a nanosecond Nd:YLF laser at a wavelength 527 nm. Two Pockels cells (PC1/2) reduce the repetition rate from 80 MHz down to 1 kHz. The first amplification stage is passed several times by the laser pulses (regenerative amplifier), whereas the second stage is a single-pass amplifier. The output pulses have an energy of 10 mJ, a repetition rate of 1 kHz, and are compressed to a duration of 35 fs with a grating compressor (not shown). Figure reproduced from [Mäh16] with the permission of S. F. Mährlein.

## 3.2. Terahertz generation: optical rectification

When light is incident onto a nonlinear optical medium (see Section 2.6.2), the induced second-order nonlinear polarization $P^{(2)}$ contains frequency components at the difference of the fundamental frequencies, i. e. at $\Omega = \omega_1 - \omega_2$. The femtosecond laser pulses described in Sections 3.1 and 3.1 span a broad range of frequencies. Consequently, the generated difference frequencies $\Omega_i$, situated in the far- and mid-infrared, also span a large bandwidth (see Fig. 3.3). In a modern parsing, the far-infrared and a part of the mid-infrared spectral range are typically called the THz window. It spans the frequency range from 0.1 to 30 THz [Ton07] which corresponds to photon energies between 0.4 and 120 meV.

Importantly, the process of optical rectification can only take place in media with broken inversion symmetry (see Section 2.6.2). The second-order nonlinear susceptibility $\chi^{(2)}(\Omega, \omega_1, \omega_2)$ determines the efficiency of the frequency conversion. It contains material specific parameters, which strongly influence the spectral dependence of $\chi^{(2)}$ [Boy03].

Apart from the conversion efficiency, a crucial factor is the so-called phase-matching condition. To maximize the emitted THz radiation, the THz waves generated throughout the thickness of the generation medium must be in phase with one another. In this way, they can add up constructively along the propagation direction of the optical driving pulse. This is achieved by matching the group velocity of the driving pulse to the phase velocity of the generated THz wave. Through a proper choice of material and its thickness, phase matching can be achieved over a broad THz-frequency range [Boy03]. The phase-matching condition may however be relaxed in a thin (thickness is below half the THz wavelength inside the medium) generation medium. Consequently, the generated THz waves cannot interfere destructively, regardless of the velocity mismatch between driving and THz field.

The resulting THz transients have a locked carrier-envelope phase which enables a coherent detection scheme as introduced below.

Throughout this thesis, different THz emitters are used. They can be classified into resonant and nonresonant sources with respect to the pump frequency [Zha17b]. The former includes the crystals zinc telluride (ZnTe), gallium phosphide (GaP), and gallium selenide (GaSe). The latter comprise photoconductive switches (PCS) and metallic heterostructures.

Depending on the requirements, different emitters are chosen as they vary in covered THz bandwidth and conversion efficiency. For frequencies from 1 to 3 THz, a PCS is the best choice [Win12]. It is based on a biased semiconductor. If a visible laser pulse excites charge carriers above the band gap, they are accelerated in the biasing field. The resulting current burst emits a THz pulse into the optical far-field [Win12]. The transparent nonlinear crystals, on the other hand, cover the frequency ranges from 1 to 5 THz (ZnTe), 1 to 8 THz (GaP), and 10 to 40 THz (GaSe) [Lei99a]. The latter is the best choice for THz frequencies above 10 THz [Sel08]. For the crystal-based emitters, a further tuning of the spectral weight is possible by changing the crystal thickness, which effectively alters the phase-matching condition [Boy03].

A new class of sources, the spintronic THz emitter (STE), is presented within this thesis (see Chapter 5 and Ref. [Sei16]). It consists of a nanometer-thin heterostructure involving magnetic and heavy metals. When pumped with an optical femtosecond pulse, the ultrafast spin-dependent Seebeck effect (see Section 2.5.2) injects a spin current into the heavy metal. There, it is converted into a transverse charge current by the inverse spin Hall effect (see Section 2.5.1; further details can be found in Chapter 5). As these photocurrents exhibit sub-picosecond dynamics, they give rise to the emission of a THz pulse, covering a remarkably large bandwidth from 1 to 30 THz without spectral gaps. Meanwhile, its conversion efficiency is compatible or even better than for the standard oscillator-driven THz sources introduced above.

Typical spectra of these THz emitters are shown in Fig. 3.4.

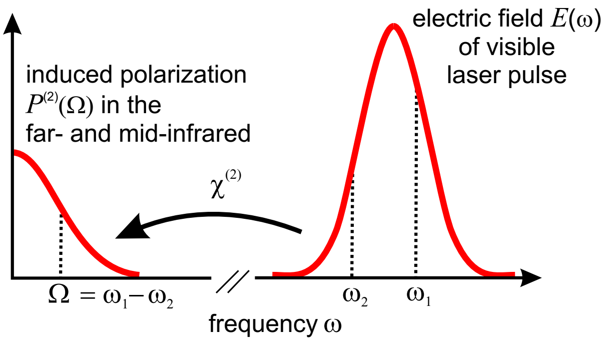

**Figure 3.3.: Terahertz generation by optical rectification.** In a second-order nonlinear process, pairs of frequencies of a broadband visible laser pulse $E(\omega)$ are mixed. The resulting nonlinear polarization $P^{(2)}(\Omega)$ contains frequency components at $\Omega = \omega_1 - \omega_2$. These difference frequencies are typically located in the far- and mid-infrared spectral region, i. e. in the THz range. The efficiency of the optical-rectification process depends on the second-order nonlinear susceptibility $\chi^{(2)}$. Figure reproduced from [Kam06] with the permission of T. Kampfrath.

## 3.3. Terahertz detection: electro-optic sampling

A major advantage of THz time-domain spectroscopy is the simultaneous detection of phase and amplitude of the THz transient. This allows for a complete characterization of for instance the complex dielectric function of a material without the need of demanding retrieval schemes, as for instance the Kramers-Kronig relations [Boy03]. They relate real and imaginary part of the dielectric function through causality. However, idealized conditions are assumed that are never met in reality (such as an infinitely fine time resolution).

**Linear electro-optic effect.** The linear electro-optic effect, also called the Pockels effect, describes a change in the refractive index of a medium in response and linear to an applied electric field (such as a THz electromagnetic pulse) [Boy03]. It is a $\chi^{(2)}$-effect and therefore only present in media with broken inversion symmetry (see Section 2.6.1).

Effectively, the medium becomes transiently birefringent if the THz electric field is present. This induced birefringence is proportional to the THz electric field, i. e. $\Delta n \propto E_{\mathrm{THz}}$ [Zha10] and is probed by co-propagating visible short probe pulse from the same oscillator [Wu97]. It experiences the transient birefringence and changes its polarization state from linear to elliptical. Typical detection media used in this work are ZnTe and GaP crystals [Lei99a].

**Balanced detection.** The induced probe ellipticity is measured using a balanced detection scheme [Zha10]. It consists of a $\lambda/4$-waveplate, a polarizing beam splitter, and two photodiodes (see Fig. 3.5). In absence of the THz electric field, the

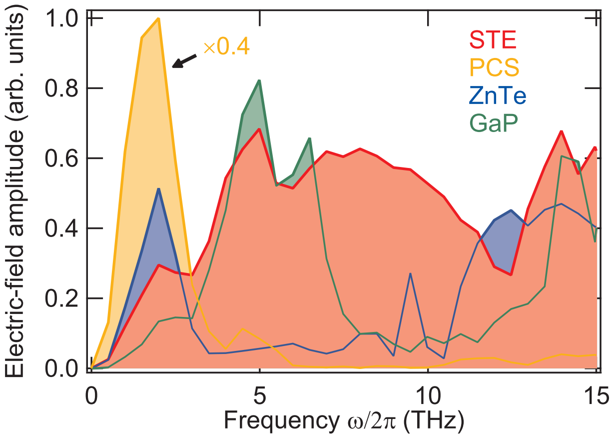

**Figure 3.4.: Comparison of terahertz emitters.** Spectral amplitudes of the electric field at the detector position (see text below) for a 5.8-nm-thick spintronic THz emitter (STE), a photoconductive switch (PCS, TeraSED© from Laser Quantum), a 1-mm-thick zinc-telluride crystal (ZnTe), and a 0.25-mm-thick gallium-phosphide crystal (GaP). Curves are all normalized by the same value.

$\lambda/4$-waveplate transforms the initial linear probe polarization into circular. A subsequent polarizing beam splitter separates two orthogonal linear polarization components which gives rise to equally-sized signals on the two photodiodes. However, in the presence of the THz electric field, a probe ellipticity is induced leading to an unbalance on the photodiodes proportional to twice the probe ellipticity. Typically, only slight changes in probe ellipticity are expected. Accordingly, by subtracting the signals from the two photodiodes, of the large background can be eliminated thereby significantly improving the signal-to-noise ratio.

In the limit of perfect phase matching, for small probe ellipticities, neglecting dispersion, and assuming a delta-like probe pulse, i. e. $I(t) = I_0 \delta(t)$, the light intensities $I_{1,2}$ (where $I_1 + I_2 = I_0$) measured with these photodiodes relate to the THz electric field at the detector position $E_{\mathrm{det}}$ by

$$S(\Delta t) := \frac{I_1 - I_2}{I_1 + I_2} = \frac{2\pi d n_0^3 r_{\mathrm{eff}}}{\lambda_{\mathrm{pr}}} E_{\mathrm{det}}(\Delta t) \,. \tag{3.1}$$

Here, $\Delta t$ is the relative time delay between probe and THz pulse, $d$ is the crystal thickness, $n_0$ is its unperturbed refractive index, $\lambda_{\mathrm{pr}}$ is the central probe-pulse wavelength inside the crystal, and $r_{\mathrm{eff}}$ is the effective electro-optic coefficient that also considers the polarization states of the THz and the probing light [Zha10].

The complete THz electric field can thus be temporally mapped out by delaying the probe with respect to the THz pulse (see Fig. 3.5).

However, Eq. 3.1 is only valid under strict assumptions (no velocity mismatch, no dispersion, infinite probe bandwidth). All these effects can be considered by the detector response function, defined by $S = h_{\mathrm{det}} * E_{\mathrm{det}}$ and introduced below.

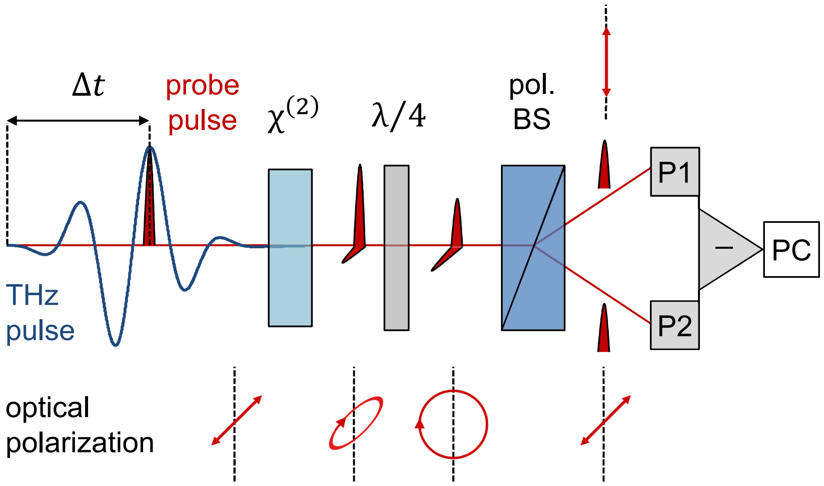

**Figure 3.5.: Electro-optic sampling and balanced detection.** In the electro-optic-sampling scheme, a THz and a femtosecond optical probe pulse co-propagate through a detection crystal with a finite second-order nonlinear susceptibility $\chi^{(2)}$. The THz electric field induces a transient birefringence in the crystal through the linear electro-optic effect, which changes the probe polarization from linear to elliptical. This change in probe ellipticity is measured with a balanced detection setup. It consists of a $\lambda/4$-waveplate, a polarizing beam splitter (pol. BS), and two photodiodes (P1/2). The normalized intensity difference between the two photodiodes' signals is proportional to the THz electric field at a given THz-probe delay $\Delta t$. By varying this delay, the complete THz waveform can be mapped out and visualized on a personal computer (PC). Figure redrawn from [Zou13].

## 3.4. Terahertz transmission and emission setups

Parts of this Section have been published in [Sei16].

Two THz spectrometers are employed in this work. The first is driven by pump pulses generated from the MHz laser oscillator (see Section 3.1) and the second by pump pulses generated from the kHz laser amplifier (see Section 3.1). The near-infrared femtosecond optical probe pulses used for electro-optic sampling (see Section 3.3) are derived from the corresponding laser oscillator. The general principle of both setups is shown in Fig. 3.6.

Further details on the THz spectrometer driven by amplified laser pulses, which has been constructed during the work of this thesis to upscale the spintronic THz emitter, can be found in Chapter 6.

In the case of the MHz-oscillator-based setup, we increase the signal-to-noise ratio by combining lock-in detection of the signal $S$ and rapid scanning of $S$ vs $t$ [Bra16a]. For this purpose, we modulate the amplitude of the THz beam with a mechanical chopper (frequency of 30 kHz) and vary the delay $t$ at a frequency of 25 Hz with a so-called shaker (APE GmbH). The result is a shot-noise limited detection of the electro-optic signal $S$.

Further details on the data acquisition for MHz- and kHz-spectrometer setups can be found in the works of L. Z. Braun [Bra16a] and S. F. Mährlein [Mäh16], respectively.

**Terahertz emission mode.** In this mode, a THz emitter is placed in the first or second focus of the spectrometer (see Fig. 3.6) and the resulting THz emission is directly measured via electro-optic sampling.

**Terahertz transmission mode.** In addition to the THz emitter (placed in the first focus), the sample under is placed in the second focus (see Fig. 3.6). Measuring the THz waveform with ($S_{\text{sample}}$) and without ($S_{\text{no sample}}$) sample, by shifting the sample mechanically back and forth, allows us to extract the sample transmission function (see Section 2.6.2; assuming normal incidence) given by

$$t\left(\omega\right)=\frac{S_{\text{sample}}\left(\omega\right)}{S_{\text{no sample}}\left(\omega\right)}\cdot \mathrm{e}^{\mathrm{i}k_2(\omega)d}=\frac{n_1+n_2}{n_1+n_2+Z_0\int_0^d \mathrm{d}z'\sigma\left(z',\omega\right)}\cdot \mathrm{e}^{\mathrm{i}k_2(\omega)d}, \tag{3.2}$$

where $n_1$ is the substrate refractive index, $k_2 = n_2\omega/c$ is the wave vector of the medium replacing the sample (typically air, i. e. refractive index $n_2 = 1$), $\sigma$ is the sample conductivity, and $d$ is the sample thickness.

## 3.4.1. From electro-optic signals to electric fields at the detector position

To extract the THz electric field $E_{\text{det}}$ incident onto the detector from the THz signal $S$ measured by electro-optic sampling (see Section 3.3), we note that these waveforms are connected by the convolution (see App. A.2) [Kam07]

$$S\left(t\right)=\left(h_{\text{det}}*E_{\text{det}}\right)\left(t\right). \tag{3.3}$$

Here, the detector response function $h_{\text{det}}$ depends on the parameters of the electro-optic crystal and on the sampling pulse [Gal99, Kam07]. Figure 3.7 shows the spectral amplitude and phase of the calculated $h_{\text{det}}\left(\omega\right)$ for detectors used in this work. The optical constants are taken from Refs. [Lei99a] and [Zhe06]. By equidistant sampling of the measured $S\left(t\right)$ and the calculated $h_{\text{det}}\left(t\right)$, we rewrite Eq. 3.3 as an overdetermined matrix equation and numerically solve for $E_{\text{det}}$. The resulting fields in the frequency domain are obtained by calculating the Fourier transformation (see App. A.1).

## 3.4.2. From electro-optic signals to electric fields at the sample position

To extract the emitted THz electric field $E_{\text{em}}$ at the sample position from the THz signal $S$ measured by electro-optic sampling at the detector position, we note that

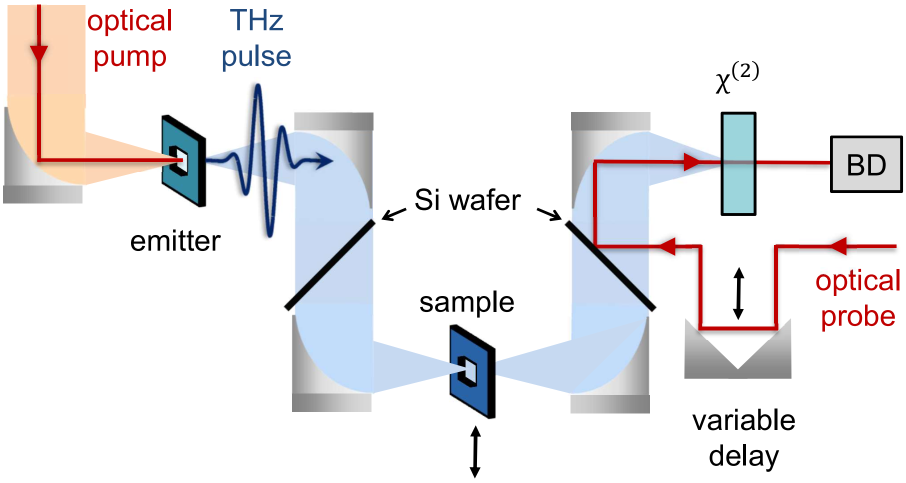

**Figure 3.6.: Terahertz emission and transmission setup.** A near-infrared femtosecond laser pulse (optical pump) is focused by a 90°-off-axis parabolic mirror into a THz emitter. The generated THz pulse is collimated and again focused onto the sample position. The residual pump light is blocked by a silicon wafer inserted at Brewster angle to maximize THz transmission. Depending on the operational mode, a sample is present (THz-transmission spectrometer) or absent (THz-emission spectrometer) at the second focal spot. With an additional pair of 90°-off-axis parabolic mirrors, the THz beam is collimated and eventually focused into the detection crystal ($\chi^{(2)}$). A co-propagating near-infrared laser pulse (optical probe) is coupled into the THz beam path by an additional silicon wafer. The probe pulse samples the THz transient via the linear electro-optic effect in the detection crystal (see Fig. 3.5). The resulting probe-pulse ellipticity is measured by a balanced-detection (BD) unit. The relative THz-to-probe-pulse delay is adjusted by a variable delay line.

these waveforms are connected by the convolution (see App. A.2)

$$S(t) = (h * E_{\mathrm{em}})(t)\,. \tag{3.4}$$

Here, the setup response function $h$ includes the propagation from the sample to the detector as well as for the detector response function (see Section 3.4.1) [Gal99, Kam07].

In principle, the propagation function can be calculated [Bra16b, Kam13a]. However, this approach assumes a perfect alignment of the optical setup which is hard to achieve. Therefore, we use an approach in which the propagation together with the detector response function is directly measured.

To this end, we make use of a well-understood THz reference emitter for which the emitted THz pulse can be calculated [Kam07]. To disturb the beam propagation as little as possible, the reference emitter is chosen to be as similar as possible to the THz emitter under study (i. e. similar thickness and substrate).

The actual extraction procedure consists of two steps:

First, the emission from the reference is measured and with the help of the calculated THz emission $E_{\mathrm{ref}}$, the complete setup response function is found by deconvolving

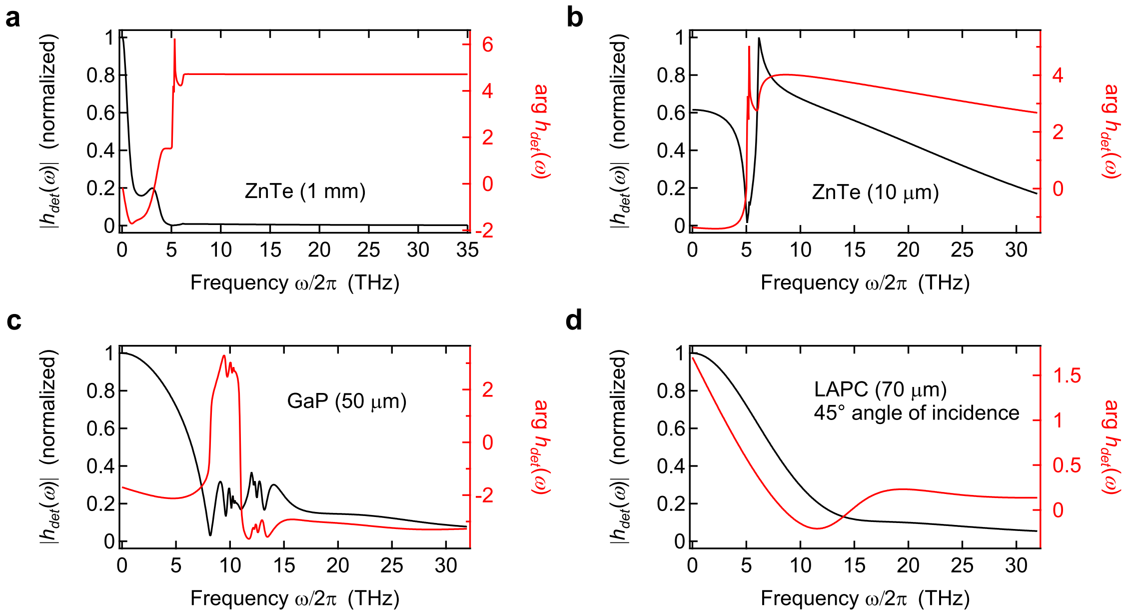

**Figure 3.7.: Detector response function.** Spectral amplitude and phase of the calculated response functions $h_{\mathrm{det}}(\omega)$ of some electro-optic detectors used in this work. **a**, 10-µm-thick (110)-oriented ZnTe on an inactive ZnTe(001) substrate. **b**, 1-mm-thick ZnTe(110). **c**, 50-µm-thick GaP(110). **d**, 70-µm-thick Lemke/amorphous polycarbonate (LAPC) under 45° angle of incidence. All curves are normalized to 1.

the relationship

$$S_{\mathrm{ref}}(t) = (h * E_{\mathrm{ref}})(t) \,. \tag{3.5}$$

In a second step, the reference emitter is replaced by the actual sample and its THz-emission signal $S(t)$ is recorded. Subsequently, the electric field right behind the sample is again obtained via deconvolving of Eq. 3.4 using the setup response function $h$ determined in the first step (Eq. 3.5).

All deconvolutions are done by equidistant sampling of the measured signals and the calculated $E_{\mathrm{ref}}(t)$, and by rewriting Eqs. 3.4 and 3.5 each as an overdetermined matrix equation which are numerically solved for the sought-after quantity. The resulting fields in the frequency domain are obtained by calculating the Fourier transformation (see App. A.1).

# 4. The anomalous Hall conductivity of magnetic metals is flat from DC up to 40 THz

*In this study, we measure the anomalous Hall effect of common and relevant magnetic metals in the elusive THz-frequency window, broadband and contact-free from 0 to 40 THz. The extrapolated DC anomalous Hall conductivities of* $0.8\cdot 10^4$ *S/m for dysprosium-cobalt (*$DyCo_5$*),* $4.4\cdot 10^4$ *S/m for cobalt-iron (*$Co_{32}Fe_{68}$*), and* $2.3\cdot 10^4$ *S/m for gadolinium-iron (*$Gd_{24}Fe_{76}$*) are explicitly confirmed for* $DyCo_5$ *by DC transport experiments. In general, we find a very weak frequency dependence. Strikingly, the anomalous Hall angle* $\gamma\left(\omega\right) = \sigma_{xy}\left(\omega\right)/\sigma_{xx}\left(\omega\right)$ *is virtually constant from DC up to 40 THz. We obtain* $\gamma = 0.026$ *for* $DyCo_5$ *and* $\gamma = 0.029$ *for GdFe. Thus, the AHE is operative up to the highest THz frequencies. The flat frequency response is explained by the large electron scattering rate which strongly broadens the spectral response. We argue that in this strongly diffusive regime, the intrinsic spin Hall mechanism is dominant. Our results are highly relevant for future high-speed, ultrabroadband spintronic applications as will be exploited in the Chapters hereafter.*

## 4.1. Motivation

Incorporating the electron spin into future electronic devices is the key concept of spintronics [San17]. This growing field aims at generating, controlling, and detecting spin currents at the highest speeds possible, eventually approaching the THz regime [Wal16]. For implementing such spin operations, SOI, despite being weak, plays a key role because it couples the motion of an electron to its spin state [Man15]. From a classical viewpoint [Chu07], SOI can be understood as a spin-dependent effective magnetic field that deflects copropagating spin-up and spin-down conduction electrons in opposite directions (see Fig. 4.1a). Important consequences of SOI are the spin Hall effect (SHE) and its ferromagnetic counterpart, the anomalous Hall effect (AHE). For details see Section 2.5.1.

Such SOI-induced effects have found broad application in spintronic devices for spin-current generation and detection as well as for switching operations [Sin15]. Up to now, however, most spintronics work has been limited to frequencies below 10 GHz, significantly lagging behind other information carriers such as electrons in field-effect transistors where cut-off frequencies of ~1 THz have been demonstrated [DA11]. Therefore, the question arises how SOI-related effects evolve at THz frequencies. Previous ultrafast works have shown that the SOI-induced spin deflection is still operative on a picosecond time scale [Wer11, Pri15], but its actual strength, in comparison to low frequencies down to DC, is a relevant open question. Such transfer of spintronic functionalities to the THz frequency range can provide access to magnetic excitations at their natural frequency [Wie12], including exchange modes in ferrimagnets or collective spin excitations in antiferromagnets [Kam11].

Besides this applied motivation, studying the THz SHE and AHE is also expected to allow for fundamental insights into the energetic structure of SOI because the THz photon energy (4 meV at 1 THz) is comparable to typical SOI energy scales in solids (~10 to 100 meV band splitting in 3*d* transition metals, see Section 2.3.2). So far, neither SHE nor AHE data have been acquired over the entire range from 0 to 100 meV for magnetic metals relevant to spintronics. Rare exceptions are measurements below 3 THz on $SrRuO_3$ [Shi11], magnetic semiconductors [Hui15], and metals [Hui17b]. At the high-frequency end, there are a few works at infrared frequencies >25 THz on $SrRuO_3$ [Kim07, Kim10] and related compounds [Kim13]. Since pure spin currents are much more difficult to measure than charge currents, it is reasonable to start with addressing the THz AHE.

Here, we present an experimental study of the AHE from 0 to 40 THz of magnetic metals with high relevance for spintronics, thereby closing the gap between DC and optical frequencies. We employ broadband THz time-domain ellipsometry to extract the complete in-plane conductivity tensor of magnetic metals (see Fig. 4.1b). The large electron scattering rate suggests that the intrinsic contribution to the AHE dominates.

Cobalt-iron-boron (CoFeB) has been proven to be a versatile magnetic layer system for magnetic tunnel junction of up to 500 % tunnel magneto resistance ratio [Lee07], exceptional out-of-plane anisotropy [Ike10, Bau15], large spin-Hall angles in metallic double layer systems [Liu12a], generation of a skyrmion bubble [Jia15], and low damping metallic film for magnonics [Len11]. It is therefore one of the leading materials for spintronic applications such as the spin-transfer torque magnetic random-access memory, read heads and sensors [Ken15].

Metallic ferrimagnetic alloys containing rare-earth (RM) and transition (TM) metals, such as $DyCo_5$ and $Gd_{24}Fe_{76}$, have been successfully used in high-density magneto-optical recording devices [Gre89]. Applications have been facilitated by their strong perpendicular magnetic anisotropy, large magneto-optical effects, tunable magnetic properties, and enlarged magneto-optical signals (caused by their amorphous state). In more recent studies, the all-optical magnetization switching has been demonstrated on these materials [Sta07, Rad11, Man14]. Thus, RM-TM alloys are a material class of high interest in current research [Kir10].

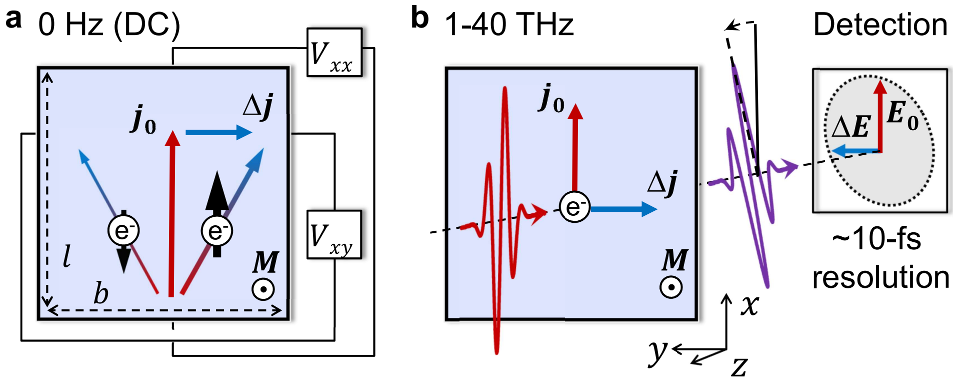

**Figure 4.1.: Schematic of DC and terahertz anomalous Hall effect measurements. a**, In the static AHE measurement, an applied external voltage $V_{xx}$ drives a DC charge current $\boldsymbol{j}_0$ ($x$-directed) through the out-of-plane magnetized sample of length $l$ and width $b$. SOI deflects spin-up and spin-down electrons (black arrows) into opposite directions perpendicular to their velocity and to the sample magnetization $\boldsymbol{M} \| z$. The different number of majority (spin-up) and minority (spin-down) electrons in the magnet causes a perpendicular charge current $\Delta\boldsymbol{j}$ ($y$-directed) measured by a volt meter. **b**, In the all-optical AHE measurement, a THz electromagnetic pulse drives an AC charge current $\boldsymbol{j}_0$ with frequencies from 1 to 40 THz in the plane of the magnetic metal. SOI induces a transverse current component $\Delta\boldsymbol{j}$ which subsequently radiates into the optical far-field and leads to an elliptically-polarized THz transient behind the sample. With the electric-field-sensitive detector, both polarization components $\boldsymbol{E}_0$ and $\Delta\boldsymbol{E}$ are separately measured with a femtosecond time resolution.

## 4.2. Experimental details

**General idea.** In the all-electrical measurement of the AHE (see Fig. 4.1a and Ref. [Wei14]), a DC voltage drives a spin-polarized current through a magnetic sample whose out-of-plane magnetization is saturated by an external magnetic field. Due to SOI, spin-up and spin-down conduction electrons are deflected in opposite directions perpendicular to the sample magnetization and the primary current. The resulting transverse spin-polarized anomalous Hall current is measured electrically, typically limited to gigahertz frequencies.

To cover much higher frequencies, we make use of an all-optical and contact-free scheme as depicted in Fig. 4.1b. A linearly-polarized THz electromagnetic pulse drives a spin-polarized current in the plane of the sample. The SOI-induced perpendicular anomalous Hall current consequently radiates into the far-field such that the transmitted THz pulse acquires an elliptical polarization (see Section 2.5.1). Employing broadband THz time-domain ellipsometry allows us to simultaneously extract the driving and induced THz field from 1 to 40 THz (see Section 3.4). In contrast to mid-infrared experiments, no use of Kramers-Kronig relations [Kit05] or subsequent reflection and transmission measurements is necessary to reconstruct amplitude and phase information. These features make our scheme less involved and more accurate.

We note our quasi-optical scheme is analogous to the familiar Faraday effect at optical frequencies (see Section 2.6.1). Following this analogy, an out-of-plane sample magnetization maximizes the THz-AHE signal. In contrast, a very small signal is expected for in-plane sample magnetization because the anomalous Hall current would flow normal to the sample surface, and emission into the far field would be hampered by the large THz refractive index of metals. Unlike with optical frequencies, our scheme allows us to study directly the Drude-response (see Section 2.6.1) of conduction electrons (governed by intraband transitions) relevant for spintronics (see Eq. 2.13). For photon energies in the MIR region (above ~0.1 eV), however, the free-carrier-like dynamics would be masked by interband transitions.

**Samples.** We investigate various magnetic metals representative of a whole class of materials with large SOI that become increasingly important in spintronic devices. All samples have an out-of-plane magnetic anisotropy, perfectly suited to achieve large THz-AHE signals. We study two crystalline ($Co_{32}Fe_{68}$ and $DyCo_5$) and one amorphous ($Gd_{27}Fe_{73}$) material.

The $Co_{32}Fe_{68}$ samples were prepared and characterized by U. Martens and M. Münzenberg (Institute of Physics, Ernst Moritz Arndt University, 17489 Greifswald, Germany). The ferromagnetic $Co_{20}Fe_{60}B_{20}$ (CoFe) film with the layer stacking MgO(2 nm)/$Co_{20}Fe_{60}B_{20}$(1 nm)/Ta(8 nm)/$Si_3N_4$(150 nm) is prepared by magnetron sputtering and by electron-beam evaporation, respectively. As prepared, $Co_{20}Fe_{60}B_{20}$ grows extremely smooth because of its amorphous nature. Post growth annealing at 300 °C for 1 hour allows a diffusion of the boron into the tantalum layer which is known to exhibit strong out-of-plane magnetic anisotropy originating from the MgO/CoFe interface after crystallization. A Co:Fe-ratio of 1:2.1 is obtained by a detailed composition analysis. An atomically-smooth $Co_{20}Fe_{60}B_{20}$ film surface is revealed by transmission electron microscopy [Leu15].

The $DyCo_5$ and $Gd_{27}Fe_{73}$ samples were prepared and characterized by F. Radu and I. Radu (Institute for Optics and Atomic Physics, Technical University Berlin and Helmholtz-Zentrum Berlin für Materialien und Energie, Berlin, Germany). Ferrimagnetic amorphous $Gd_{27}Fe_{73}$ (GdFe) and polycrystalline $DyCo_5$ alloys with out-of-plane magnetic anisotropy having the layer stacking Ta(3 nm)/X(20 nm)/Ta(5 nm) /$Si_3N_4$(150 nm) (where X is $Gd_{27}Fe_{73}$ or $DyCo_5$) are grown by magnetron sputtering at room temperature in a $1.5 \cdot 10^{-3}$ mbar ultra-clean Ar atmosphere. The ferrimagnets' stoichiometry is controlled by varying the deposition rate of the separate elemental targets during the co-sputtering process [Rad12].

**Sample characterization.** We characterize our samples by Faraday rotation measurements (see Section 2.6.1) using a continuous-wave laser diode (wavelength of 628 nm). A typical square-like hysteresis curve for $DyCo_5$ is shown in Fig. 4.3b.

The microstructuring and the electrical measurements were conducted by G. Woltersdorf [Institute of Physics, Martin-Luther Universität Halle-Wittenberg, 06120 Halle

(Saale), Germany]. Static conductivity and AHE measurements are done by pattering the metallic layer in Hall bar structures. Subsequent magneto-transport measurements reveal the longitudinal and transverse conductivities [Wei14]. In more detail, the Ta/$DyCo_5$/$Si_3N_4$ and Ta/$Si_3N_4$ samples are patterned into Hall bar structures by electron beam lithography and dry etching steps. A DC current of $j_0 = 200\,\mu\mathrm{A}$ is passed along the Hall bar structure while the voltages $V_{xx}$ and $V_{xy}$ are recorded (see Fig. 4.1a). A typical measurement of $V_{xy}$ is shown in Fig. 4.2. The longitudinal and transverse resistance values, defined by $\rho_{xy} = V_{xy}d/j_0$ and$\rho_{xx} = V_{xx}db/lj_0$, respectively, are converted into corresponding conductivities using $\sigma_{xx} = \rho_{xx}/\left(\rho_{xx}^2 + \rho_{xy}^2\right)$ and $\sigma_{xy} = \rho_{xy}/\left(\rho_{xx}^2 + \rho_{xy}^2\right)$. The conductivity contribution of the Ta layer is separated using a Ta(8 nm)/$Si_3N_4$(150 nm) reference sample. Importantly, because of the requirements for microstructuring, these DC measurements are performed on a part of the sample with a 500-µm-thick $Si_3N_4$.

For a complete sample characterization, we also measure THz transmission of our metallic films. As a reference, we use samples without metal films as well as just air (see Section 3.4).

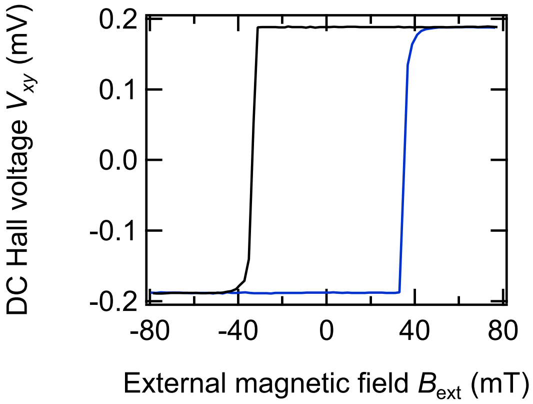

**Figure 4.2.: Electrical anomalous Hall measurement of dysprosium cobalt.** DC anomalous Hall voltage $V_{xy}$ vs the out-of-plane-oriented external magnetic field $B_{\mathrm{ext}}$ measured electrically on a microstructured $DyCo_5$ sample.

**Technical details of the terahertz spectrometer.** We use 80 % of the output of a Ti:sapphire laser oscillator to generate THz pulses by optical rectification in a nonlinear optical material [a GaSe crystal (thickness of 50 µm) or a spintronic THz emitter ($Co_{40}Fe_{40}B_{20}$(3 nm)/Pt(2 nm))] (see Sections 3.2, 3.4 and Chapter 5).

First, the THz pulse traverses a wire-grid polarizer (WGP), making it p-polarized (residual ellipticity in field $< 10^{-2}$). Then, a parabolic mirror focuses the THz beam onto the sample under an angle of incidence of 45°. Behind the sample, the beam is collimated by a second parabolic mirror. Afterwards, a second WGP set to an angle of 45° with respect to the table plane makes the detector equally sensitive to s- and p-polarization. We emphasize that we employ a 45°-analyzer configuration, which does not require rotation of the polarizer, in contrast to often-used (nearly-crossed) crossed polarizer-analyzer configurations. In this way, we minimize systematic errors arising from the inhomogeneity of the moving polarizer which are pronounced at higher THz frequencies.

**Measurement procedure.** The sample magnetization $\boldsymbol{M}$ is saturated by an external magnetic field (max. ±180 mT). Since the AHE is relatively small, the sample magnetization is typically switched every 10 s (measurements are performed in remanence, except for the GdFe sample, where an external field of about ±50 mT is applied owing to the non-square-like hysteresis) and we average over about 1000 cycles. By using various emitter and detector combinations, we can cover the entire range from 1 to 40 THz (see Sections 3.2 and 3.3). All measurements are conducted at room temperature in a dry $N_2$ atmosphere.

## 4.3. Results

**Raw data.** Figure 4.3a displays the electro-optic signal of THz pulses obtained from a $DyCo_5$ sample for opposite orientations of the sample magnetization. We see that the magnetization-induced modulation of the signal is small. To evaluate these data, we assume the measurement signal $S$ as a sum of a term independent of $\boldsymbol{M}$ and a small term linear in $\boldsymbol{M}$ (see discussion below). Effects of higher order in $\boldsymbol{M}$ are neglected. In this approximation, $S_0 = S(+\boldsymbol{M}) + S(-\boldsymbol{M})$ is independent of $\boldsymbol{M}$ whereas $\Delta S = S(+\boldsymbol{M}) - S(-\boldsymbol{M})$ scales with the sample magnetization. Applying this procedure to the waveforms of Fig. 4.3a, we find the magnetization-dependent signal is on the order of $\Delta S/S_0 \approx 2\,\%$. In addition, $S(+\boldsymbol{M})$ and $S(-\boldsymbol{M})$ are almost in phase (see Inset of Fig. 4.3a), indicating that the transmitted THz pulse is still linearly polarized.

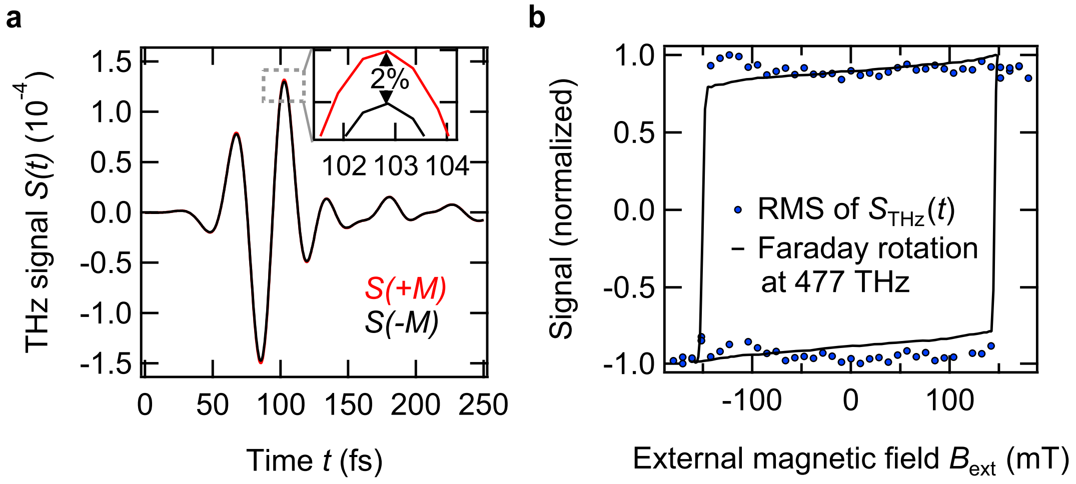

**Figure 4.3.: Terahertz ellipsometry raw data of dysprosium cobalt from 10 to 40 THz.** **a**, Signal of an initially linearly-polarized THz pulse after having passed an out-of-plane magnetized dysprosium cobalt layer ($DyCo_5$). The anomalous Hall effect induces a new perpendicular polarization component, depending on the orientation of the sample magnetization (red and black curve). **Inset**: A magnification shows that the effect is on the order of 2 %, suggesting an anomalous Hall angle of similar magnitude. **b**, Faraday-rotation hysteresis curve at optical (628 nm≙477 THz, black solid line) and terahertz (10 to 40 THz, blue circles) frequencies (root mean square, RMS).

As a check, we also perform a reference measurement of the bare substrate (150-nm-thick $Si_3N_4$ membrane) which does not result in any detectable signal odd in sample magnetization (see Fig. 4.4). To further verify the magnetic origin of the signal, we measure the complete THz waveform for varying external magnetic field. Figure 4.3b shows the root-mean-square (RMS) of these THz waveforms vs the external magnetic field $\boldsymbol{B}_{\mathrm{ext}}$. We find that the THz hysteresis curve agrees well with the optical Faraday-rotation hysteresis curve. Therefore, $\Delta S$ indeed scales with the sample magnetization. Discrepancies in the coercivity field between DC and optical hysteresis curves (compare Figs. 4.2 and 4.3b) may originate from the different substrate thickness used in these two measurements (150 nm and 500 µm). This scenario appears reasonable since the magnetic anisotropy and thus the coercivity highly depend on the strain state of the material [Stö07].

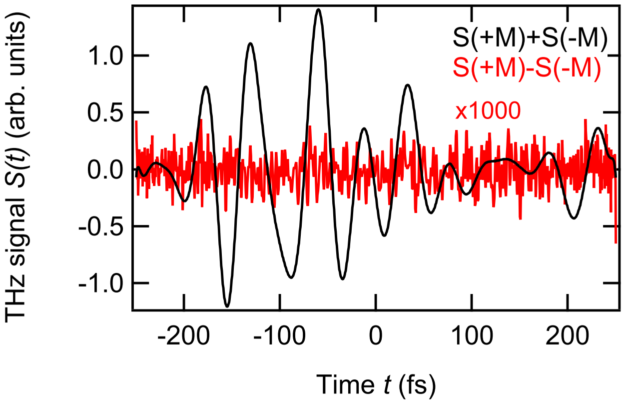

**Figure 4.4.: Reference measurement using a $Si_3N_4$ membrane without metallic layers.** THz signal odd (red curve) and even (black curve) in the external magnetic field for a bare 150-nm-thick $Si_3N_4$ membrane. The signal odd in magnetization is multiplied by a factor of 1000.

**Conductivity-tensor extraction.** The data presented so far still depend on extrinsic factors such as the spectrum of the driving THz pulse and the impact of the substrate of the magnetic thin film. Significantly more material-specific information is provided by extracting the conductivity tensor from our data. For the analysis, it is sufficient to restrict ourselves to the $x$-$y$-plane (see Fig. 4.1) because all currents flow in the sample plane. In an isotropic magnetically-ordered solid (sample magnetization $\boldsymbol{M}\|\boldsymbol{z}$), a current $\boldsymbol{j}$ is related to a driving electric $\boldsymbol{E}$ field in the frequency domain by (see Section 2.6.1)

$$\boldsymbol{j} = \underline{\sigma}\boldsymbol{E} = \begin{pmatrix} \sigma_{xx} & \sigma_{xy} \\ -\sigma_{xy} & \sigma_{xx} \end{pmatrix} \boldsymbol{E}, \tag{4.1}$$

with the diagonal conductivity $\sigma_{xx}$ and the off-diagonal conductivity $\sigma_{xy}$. Note that the Onsager relations impose $\sigma_{xy}(\boldsymbol{M}) = -\sigma_{xy}(-\boldsymbol{M})$ [Kit05].

The connection to the experiment is provided by a transmission matrix $\underline{t} = \left( t_{\mathrm{pp}} \quad t_{\mathrm{ps}}, \quad t_{\mathrm{sp}} \quad t_{\mathrm{ss}} \right)$ which relates the incoming and transmitted electric fields by $\boldsymbol{E}_{\mathrm{trans}} = \underline{t}\boldsymbol{E}_{\mathrm{in}}$ (see Section 2.6.2). Using two independent measurements allows us to determine first $t_{\mathrm{pp}}$ from a THz transmission measurement (see Section 3.4) and then $t_{\mathrm{sp}} = t_{\mathrm{pp}} \cdot \Delta S/S_0$ from a THz AHE measurement.

In more detail, in our time-domain experiment, we measure a signal $S\,(t)$, which is related to $E\,(t)$ by a convolution with a setup transfer function $h\,(t)$ (see Section 3.4.2). This convolution turns into a simple multiplication upon Fourier transforming the signals $S\,(t, \boldsymbol{M})$ (see App. A.1). Thus, the measured signal behind the wire-grid polarizer oriented at 45° with respect to the table plane reads

$$S\,(\omega, \boldsymbol{M}) \propto [1 + \sigma_{xy}\,(\omega, \boldsymbol{M})]\, h\,(\omega)\, E_0\,(\omega)\,. \tag{4.2}$$

Then, by taking the ratio $\Delta S/S_0 = t_{\mathrm{sp}}/t_{\mathrm{pp}}$, all setup specific parameters cancel out.

With the help of a $4x4$-tranfer-matrix formalism [Zak90], we establish a relation between $\underline{t}$ and the in-plane conductivity tensor $\underline{\sigma}$, which is solved for $\underline{\sigma}$ numerically (see Section 2.6.2). We note this procedure provides a unique physically meaningful solution because our samples are optically much thinner than the involved THz wavelengths.

In the data extraction procedure, we assume that the conductivities of the multilayer sample add up as in a parallel connection, which may lead to systematic errors as interface resistances are neglected [Fuc38]. As a result, we obtain the complex-valued conductivity tensor $\underline{\sigma}$ of all studied materials over more than 5 octaves from 1 to 40 THz (see Fig. 4.6).

**Details on the conductivity-tensor extraction.** For the polycrystalline $\mathrm{DyCo_5}$ sample, the conductivity is the average of the ordinary and the extraordinary contribution because of the random orientation of crystallites in the sample plane ($\mathrm{DyCo_5}$ has a hexagonal crystal structure with the c-axis oriented in the sample plane [Rad12]). This is confirmed by rotating the $\mathrm{DyCo_5}$ sample around the sample normal which has no impact on the measured conductivity (not shown).

For the CoFe sample, we only determine the average diagonal conductivity of the $\mathrm{Co_{32}Fe_{68}}$(1 nm)/Ta(8 nm)/$\mathrm{Si_3N_4}$(150 nm) stack because a referencing with a Ta(8 nm)/$\mathrm{S}i_3\mathrm{N}_4$(150 nm) sample is impossible. The reason is that the sample preparation includes annealing at 300 °C, which causes the boron to diffuse from the $\mathrm{Co_{40}Fe_{40}B_{20}}$ layer into the Ta layer. Thereby the tantalum layer changes its chemical composition and most likely also its optical properties. However, for the off-diagonal conductivity of CoFe no such complications arise because a referencing is unnecessary in this case (see Eq. 4.2).

The conductivity of the tantalum seed and capping layer (relevant for all samples not involving CoFe) are measured on individual samples containing only the substrate and the substrate with an 8-nm-thick tantalum layer on top, respectively (see Fig. 4.5).

The optical properties of $Si_3N_4$ are taken from Ref. [Cat12] according to which they can be described with a superposition of five Lorentzians.

By using the literature values for the $Si_3N_4$ substrate [Cat12], all extracted metal conductivities show spectral features around 24 THz in the diagonal conductivity. It is known that $Si_3N_4$ has three pronounced phonon resonances in this frequency range [Cat12]. A possible explanation is that during the growth of the metal films on top of the only 150-nm-thick $Si_3N_4$ membrane, a significant amount of strain is induced in the membrane. This can cause changes in its optical constants. To correct for this, the central frequency $\omega_{\mathrm{T}j}$ and the broadening $\Gamma_j$ of the three Lorentzians in this spectral range and the dielectric constant for large frequencies $\varepsilon_\infty$ of the $Si_3N_4$ substrate are slightly adapted (see Table 4.1). In this way, the most-likely strain-induced spectral feature around 24 THz in the metal conductivities is minimized. We note that for samples fabricated in different laboratories (Berlin and Greifswald), the $Si_3N_4$ optical parameters are adapted separately.

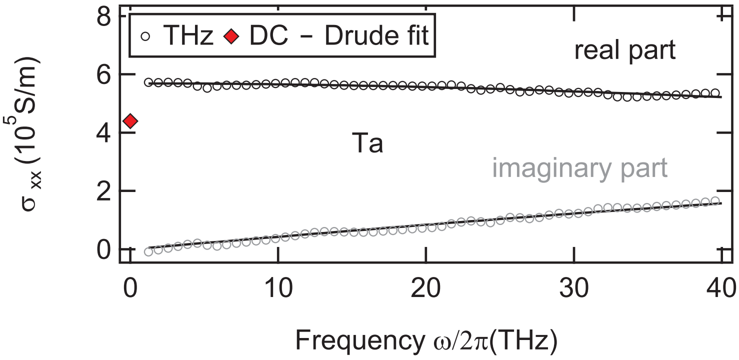

**Figure 4.5.: Measured complex-valued diagonal conductivity of tantalum from DC to THz.** Diagonal conductivity $\sigma_{xx}$ of Ta measured in the THz frequency range (real part: dark circles, imaginary part: light circles) and at DC (diamond symbol). The fit (solid lines) is obtained using the Drude model (see Eq. 4.3 and Table 4.2).

## 4.4. Discussion

**Diagonal conductivity $\sigma_{\mathrm{xx}}$.** Figure 4.6a shows the diagonal conductivity extracted from THz transmission experiments from 1 to 40 THz for all studied materials. We find a good match between the DC and THz conductivity for $DyCo_5$. In metals, the conductivity is typically governed by the itinerant electrons close to the Fermi energy (see Section 2.2). Its frequency dependence can often be well described by the Drude model which treats the conduction electrons as classical particles which scatter from immobile impurities at a characteristic rate $\Gamma$ (see Section 2.6.1). For

| Parameter | Literature value [Cat12] | Constants for Ta, $DyCo_5$, and GdFe | Constants for CoFe(1 nm)/ Ta(8 nm) |
|---|---|---|---|
| $\omega_{T3}/2\pi$ (THz) | 24.52 | 23.98 | 23.82 |
| $\omega_{T4}/2\pi$ (THz) | 26.44 | 26.06 | 26.11 |
| $\omega_{T5}/2\pi$ (THz) | 31.72 | 29.73 | 30.38 |
| $\Gamma_3/2\pi$ (THz) | 2.75 | 4.43 | 2.96 |
| $\Gamma_4/2\pi$ (THz) | 3.48 | 4.11 | 3.55 |
| $\Gamma_5/2\pi$ (THz) | 5.95 | 2.97 | 5.53 |
| $\varepsilon_\infty$ | $4.56 + 0.01\mathrm{i}$ | $4.36 + 2.53\mathrm{i}$ | $5.62 + 1.43\mathrm{i}$ |

**Table 4.1.: Used optical constants of $\mathbf{Si_3N_4}$.** Constants used for the refractive index calculation $Si_3N_4$ [Cat12]. Slight adaptions are necessary due to possibly strain-induced modifications during sample growth (see text for details). For the samples prepared at the Helmholtz-Zentrum Berlin (Ta, $DyCo_5$, and GdFe) different constants are used than for the sample prepared at the University of Greifswald [CoFe(1 nm)/Ta(8 nm)].

all materials, we observe a typical Drude-like behavior, that is, a monotonously decreasing $\mathrm{Re}\left(\sigma_{xx}\right)$ with increasing frequency. By fitting the Drude formula

$$\sigma_{\mathrm{Drude}}\left(\omega\right) = \frac{\sigma_{\mathrm{DC}}}{1 - \mathrm{i}\omega/\Gamma} \tag{4.3}$$

to our data, we obtain the DC conductivity $\sigma_{\mathrm{DC}}$ and the velocity relaxation rate $\Gamma$ given in Table 4.2. The large Drude scattering rate $\Gamma$ implies strong disorder for all samples (e. g. impurities, diffuse scattering at interface).

For CoFeB, we find good agreement with the reported value in Ref. [Wu13] ($5 \cdot 10^5$ S/m). For $DyCo_5$, the only literature value was measured for a much thicker film and the conductivity is 2 orders of magnitudes larger than our result ($285 \cdot 10^5$ S/m in Ref. [Boc73]). However, we find good agreement between our conductivity and the one reported for $DyCo_3$ ($3.3 \cdot 10^5$ S/m in Ref. [DP92]). In the case of GdFe, our extracted conductivity matches the values reported in the literature ($5 \cdot 10^5$ S/m) [Hon85, Hau09].

| Material | $\sigma_{\mathrm{DC}}$ ($10^5$ S/m) | $\Gamma/2\pi$ (1/ps) |
|---|---|---|
| $DyCo_5$ | 3.1 | >200 |
| CoFe(1 nm)/Ta(8 nm) | 5.8 | 132 |
| GdFe | 9.0 | 99 |
| Ta | 5.7 | 133 |

**Table 4.2.:** Drude-model fit parameters for the experimental diagonal-conductivity data in Fig. 4.6a.

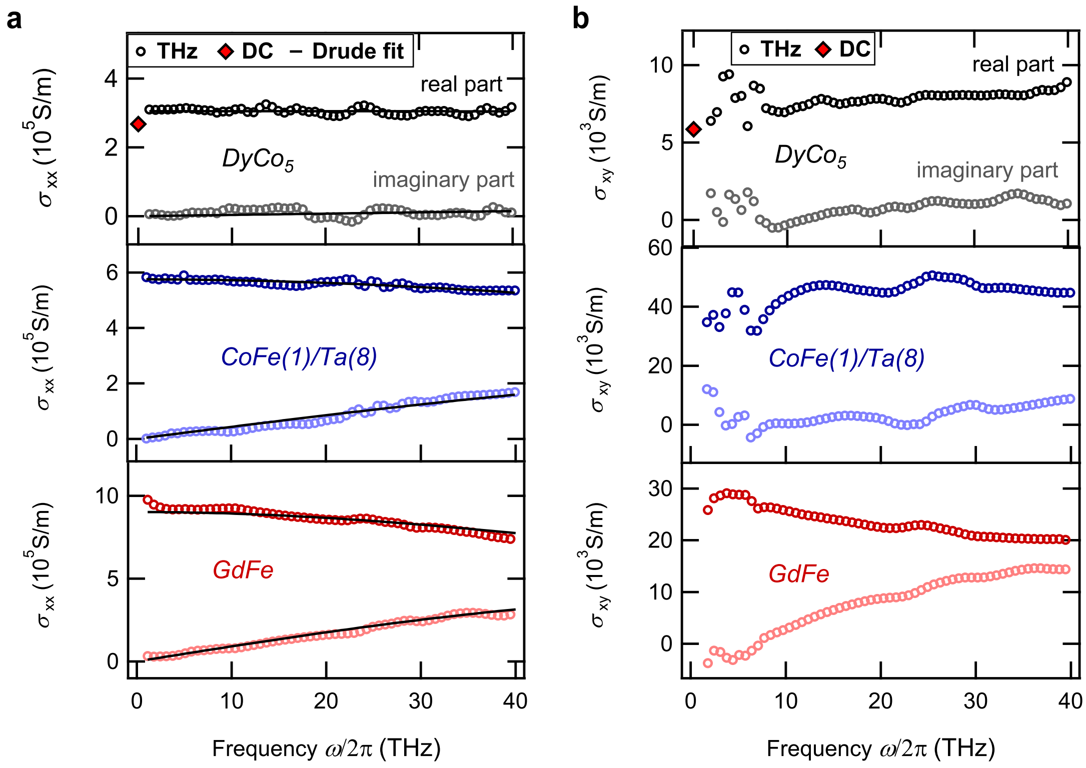

**Figure 4.6.: Measured complex-valued in-plane conductivity tensor of DyCo$_5$, CoFe, and GdFe from DC to 40 THz.** **a**, Diagonal conductivities $\sigma_{xx}$ measured in the THz frequency range (real part: dark circles, imaginary part: light circles) and at DC (red diamond symbol). For the CoFe sample, only the average conductivity of the CoFe(1 nm)/Ta(8 nm) stack is extracted (for details see main text). Fits (solid lines) are obtained using the Drude model (see Eq. 4.3 and Table 4.2). **b**, Off-diagonal conductivities $\sigma_{xy}$ measured in the THz frequency range (real part: dark circles, imaginary part: light circles) and at DC (red diamond symbol).

**Off-diagonal conductivity $\sigma_{\mathrm{xy}}$.** Figure 4.6b shows the off-diagonal conductivity extracted from DC and THz anomalous Hall measurements in the range from 0 to 40 THz. Again, we find a good agreement between DC and THz measurements. Discrepancies may originate from different substrate thicknesses (0.15 vs 500 µm).

Surprisingly, we find a largely frequency independent $\sigma_{xx}$. A possible explanation for this are the huge Drude scattering rates (see Table 4.2). They lead to a significant homogeneous broadening of optical electronic transitions underlying the AHE (see Section 2.5.1), thereby smearing out any spectral feature in the off-diagonal conductivity [Opp91].

In comparison to reported values, we find a good agreement for GdFe ($2.5 \cdot 10^4$ S/m in Ref. [Hau09]). For DyCo$_5$, the values reported in Ref. [Boc73] for much thicker films are 3 times larger ($3.3 \cdot 10^4$ S/m). For CoFeB, our measured spin Hall conductivity agrees well with *ab initio* calculation of the intrinsic spin Hall mechanism ($3.3 \cdot 10^4$ S/m in Ref. [See11]).

We argue that the intrinsic AHE mechanism is the dominant one in our samples for two reasons. First, this contribution is inversely proportional to the conductivity which is lower in samples with high disorder [Sin15]. This holds also true for the extrinsic side-jump contribution (but not for skew scattering) which however is typically an order of magnitude smaller than the intrinsic contribution [Wei11]. Second, the intrinsic contribution is favored by higher orbital momentum of electrons (as by d-electrons around the Fermi energy in our samples), because it leads via SOI to a larger spin current (see Sections 2.5.1 and 2.3.2).

In this sense, the large quasi-particle scattering rate has two important consequences. First, it reinforces the intrinsic AHE contribution. Second, it smears out any spectral feature in the off-diagonal conductivity [Opp91].

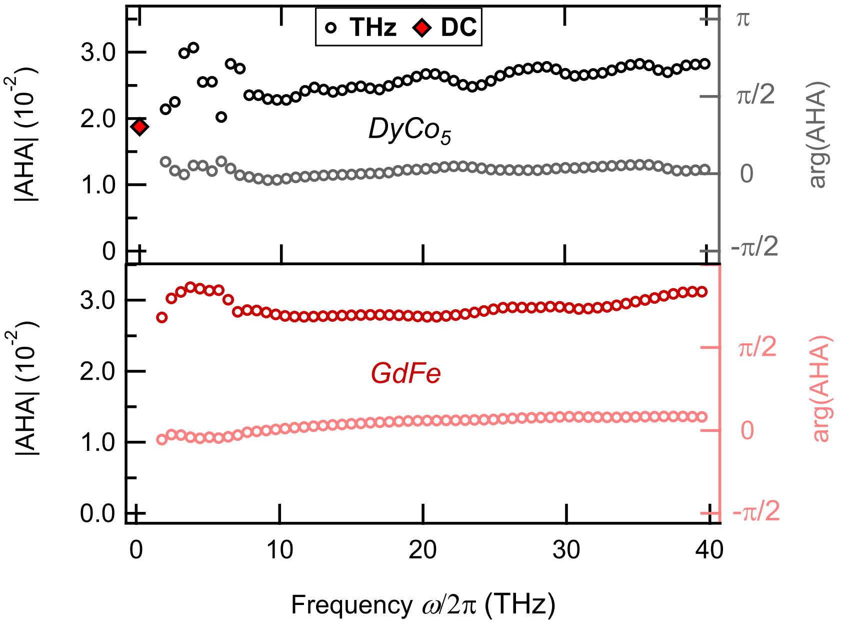

**Figure 4.7.: Measured terahertz anomalous Hall angle of DyCo$_5$ and GdFe from DC to 40 THz.** Anomalous Hall angle in the THz frequency range [absolute value (left scale): dark circles, phase (right scale): light circles] and at DC (diamond symbol).

**Anomalous Hall angle.** We find a largely frequency-independent anomalous Hall angle (AHA) from DC to 40 THz with frequency-averaged values of $2.6 \cdot 10^{-2}$ for DyCo$_5$ and $2.9 \cdot 10^{-2}$ for GdFe (see Fig. 4.7). The THz AHA of DyCo$_5$ approximately agrees with its DC value of $1.9 \cdot 10^{-2}$.

We note that these results are consistent with the raw data of Fig. 4.3a, where $\Delta E/E_0 \approx 0.02$. Note that $E_0$ and $\Delta E$ are in-phase, thereby indicating a real-valued AHA. In the electrostatic limit (see Section 2.5.1), this ratio corresponds to $-\Delta j/j_0$ (see Fig. 4.1) implying that $\mathrm{Re}\,\mathrm{AHA} \approx 0.02$.

Remarkably, in the division $\sigma_{xy}/\sigma_{xx}$, the phase of the complex-valued quantities $\sigma_{xx}$ and $\sigma_{xy}$ seems to cancel exactly and results in a real-valued Hall angle. Thus, the

AHA (as a real number) appears to be a meaningful physical concept here. In a classical picture, the real-valued AHA implies that the longitudinal and transverse electron oscillations are in phase.

We find a good agreement of our measured spin Hall angles with reported values for GdFe (2.5 % in Ref. [Sto85] and 4 % in Ref. [Har83]). We are not aware of any reported AHA for $DyCo_5$.

## 4.5. Conclusion and outlook

In summary, we have developed a new technique which allows us to study the AHE in metals from DC to 40 THz, which is a highly relevant spectral window with respect to SOI energy scales. We find that the AHE is operative even at highest THz frequencies. In $DyCo_5$, our high-frequency AHE measurements match the results of a DC-AHE measurement very well. We argue that the intrinsic contribution to the AHE is dominant in the studied materials and that the spectrally-flat responses of the off-diagonal conductivities are due to the huge quasi-particle scattering rates.

Future studies based on the methodology developed here will allow us to gain even more insight into SOI at THz frequencies. Theoretically, we expect more pronounced spectral features in the anomalous Hall conductivity for samples with small broadening on the order of 10 meV. Experimentally, such reduced level broadening can be achieved by either measuring at low temperatures or by using samples with fewer impurities. As Kim *et. al* [Kim10] could already show, a distinction between extrinsic and intrinsic contributions to the AHE conductivity becomes possible if $\mathit{\Gamma}/2\pi$ lies in the THz measurement window. This case may be especially interesting for systems with roughly equally sized in-/extrinsic effects at low frequencies such as $L1_0$ FePt [Wei11]. Finally, an extension of this measurement scheme to nonmagnetic materials with the help of spin injection will permit the direct observation of the dynamics of the SHE all-optically [Wer11, Pri15].

# 5. Efficient metallic spintronic emitters of ultrabroadband terahertz radiation

*Terahertz electromagnetic radiation is extremely useful for numerous applications such as imaging and spectroscopy. Therefore, it is highly desirable to have an efficient table-top emitter covering the* 1*-to-*30*-THz window whilst being driven by a low-cost, low-power femtosecond laser oscillator. So far, all solid-state emitters solely exploit physics related to the electron charge and deliver emission spectra with substantial gaps.*

*Based on the spectrally-flat THz functionality of the anomalous Hall effect (see Chapter 4), we take advantage of the electron spin to develop a conceptually new THz source. It relies on tailored fundamental spintronic and photonic phenomena in magnetic metal multilayers: ultrafast photo-induced spin currents, the inverse spin Hall effect and a broadband Fabry-Pérot resonance. Guided by an analytical model, such spintronic route offers unique possibilities for systematic optimization. We find that a 5.8-nm-thick* $W/Co_{20}Fe_{60}B_{20}/Pt$ *trilayer generates ultrashort THz pulses fully covering the* 1*-to-*30*-THz range. Our novel source outperforms standard emitters such as ZnTe(*110*) crystals in terms of bandwidth, THz-field amplitude, flexibility, scalability, and cost.*

Parts of this Chapter have been published in [Sei16].

## 5.1. Motivation

As the THz spectral window coincides with many fundamental resonances of materials [Fer02a, Ton07], THz radiation enables highly selective spectroscopic insights into all phases of matter with high temporal [Ulb11, Kam13b] and spatial [Cha07a, Coc13, San14, Zei07] resolution. Consequently, numerous applications in basic research [Ulb11, Kam13b], imaging [Cha07a], and quality control [Zei07] have emerged.

To fully exploit the potential of THz radiation, energy-efficient and low-cost sources of ultrashort THz pulses are required. Most broadband table-top emitters are driven by femtosecond laser pulses that generate the required THz charge current by appropriately mixing the various optical frequencies [Rei07, Bla11]. Sources made from solids typically consist of semiconducting or insulating structures with naturally or artificially broken inversion symmetry (see Section 3.2). When the incident photon energy is below the semiconductor band gap, optical rectification causes a charge displacement that follows the intensity envelope of the incident pump pulse [Rei07, Bla11, Ric94, Kai99, Hub00, Zhe05, Zhe07, Bru08, Kat10]. For above-band-gap excitation, the response is dominated by a photocurrent [Sha04, Apo14, Kla10, She03, Win12, Hal14, Ber13] with a temporally step-like onset and, thus, generally smaller bandwidth than optical rectification [Rei07]. Apart from rare exceptions [Zhe05], most semiconductors used are polar (such as ZnTe, GaP [Fer02a, Ton07], GaSe [Kai99, Hub00], GaAs [Kla10, She03], or organic materials [Zhe07, Bru08, Kat10]) and strongly attenuate THz radiation around optical phonon resonances, thereby preventing emission in the so-called Reststrahlen band located between ~1 and 15 THz. Consequently, nonpolar materials should be used to achieve broadband, gap-free THz emission.

The so far most promising sources covering the full range from 1 to 20 THz and above are photocurrents in transient gas plasmas [Rei07, Bla11, Kim12, Tho07, Lu14, Bar05, Buc15]. The downside of this appealing approach is that the underlying ionization process typically requires amplified laser pulses with high threshold energies on the order of 0.1 mJ. Measurable THz waveforms can be obtained with pump-pulse energies down to ~1 µJ, which is, however, still 2 to 3 orders of magnitude larger than what low-cost femtosecond laser oscillators can provide.

Another promising material class for realizing THz sources are metals[Ram14] because they exhibit a pump absorptivity largely independent of wavelength [Zha15], short electron lifetimes of ~10 to 50 fs [Zhu06] (implying broadband photocurrents), a featureless THz refractive index [Lam08] (favoring gap-free emission), and a large heat conductivity (for efficient removal of excess heat). In addition, metal thin-film stacks (heterostructures) are well established, simple, and cheap to fabricate, and they can be scaled easily. Recent works have indeed demonstrated THz emitters based on metal structures [Ram11, Pol11, Kad05, Wel07]. However, the bandwidth did not exceed 3 THz and THz field amplitudes competitive with those of ZnTe emitters were obtained only in conjunction with amplified laser pulses [Kad05, Wel07]. Consequently, the full potential of metal-based THz emitters is far from being achieved and the key issue remains: to develop efficient sources covering the range from 1 to 30 THz without gaps, whilst being driven by laser pulses with an energy of ~1 nJ from a typical, high-repetition-rate femtosecond laser oscillator.

At this point, it is important to acknowledge that all previously demonstrated THz emitters have taken advantage exclusively of the charge but not the spin of the electron. On the other hand, very recent tremendous progress in the fields of spintronics [Sai06, Hof13, Sin15, Wei14] and femtomagnetism [Bat10] has shown that the electron spin offers entirely new possibilities to generate, tailor, and optimize transient currents in metals. In fact, spin-to-charge conversion has been revealed lately as a new mechanism for the generation of ultrafast photocurrents [Kam13a, Hér06]. Unfortunately, even though fed by a millijoule-class laser, the resulting THz fields were much too weak for practical applications[Kam13a]. It remains to be shown whether the spintronic route can lead to a competitive THz emitter.

In this work, we exploit the unique spintronic and photonic properties of ultrathin metal films to develop a laser-oscillator-driven THz emitter that combines the benefits of existing emitters in one device: large bandwidth, large THz-field amplitude at low pump power, straightforward operation, scalability, and low cost. This achievement results because our widely tunable approach provides access to a large set of spintronic metals and geometrical parameters for optimization.

## 5.2. Experimental details

Figure 5.1a illustrates the basic principle of our spintronic THz emitter by means of a bilayer structure consisting of a ferromagnetic (FM) and nonferromagnetic (NM) metal thin film [Kam13a]. The FM layer is magnetized in-plane (antiparallel to the $y$-axis). An incident femtosecond laser pulse excites electrons in the metals to states above the Fermi energy, thereby disturbing thermal equilibrium. Since FM and NM layers have different transport properties, a $y$-polarized primary current is launched along the z-axis during thermalization (see Section 2.1). In addition, because the product of density, band velocity and lifetime of spin-up (majority) electrons in FM metals (such as Fe, Co, and Ni) is significantly higher than that of the spin-down (minority) electrons [Zhu06, Jin15], the $z$-current is strongly spin-polarized [Bat10]. We note that the pump photon energy (~1.6 eV) leads to an electron distribution function that has strong nonequilibrium character directly after sample excitation [Ale17]. Since relaxation toward a Fermi-Dirac distribution proceeds on a time scale of 100 fs [Hoh00], both nonequilibrium and equilibrium electrons are expected to contribute to spin transport and THz emission [Nen16]. This mechanism can be considered an ultrafast version of the spin-dependent Seebeck effect which arises from the different transport properties of the photo-induced charge carriers [Ale17].

Once the spin current enters the NM layer, SOI deflects spin-up and spin-down electrons in opposite directions [Sai06, Hof13, Sin15, Wei14, Wer11] (Fig. 5.1a). This inverse spin Hall effect (ISHE) converts the longitudinal ($z$-directed) spin current density $j_\mathrm{s}$ into an ultrafast transverse ($x$-directed) charge current density $j_\mathrm{c} = \gamma j_\mathrm{s}$ acting as a source of THz radiation. Here, $j_\mathrm{s}$ and $j_\mathrm{c}$ are measured in units of electrons per area and time, and $\gamma$ is the spin Hall angle which can be understood as the mean deflection angle of a moving electron. Importantly, $\gamma$ can have opposite sign in different metals such that engineering of spin Hall currents becomes possible.

**Sample fabrication.** The samples from the Mainz group were prepared and characterized by S. Jaiswal, J. Henrizi, G. Jakob, M. Jourdan and M. Kläui (Institute of Physics, Johannes Gutenberg University, 55128 Mainz, Germany). They are deposited by Ar sputter deposition using a Singulus Rotaris deposition tool with

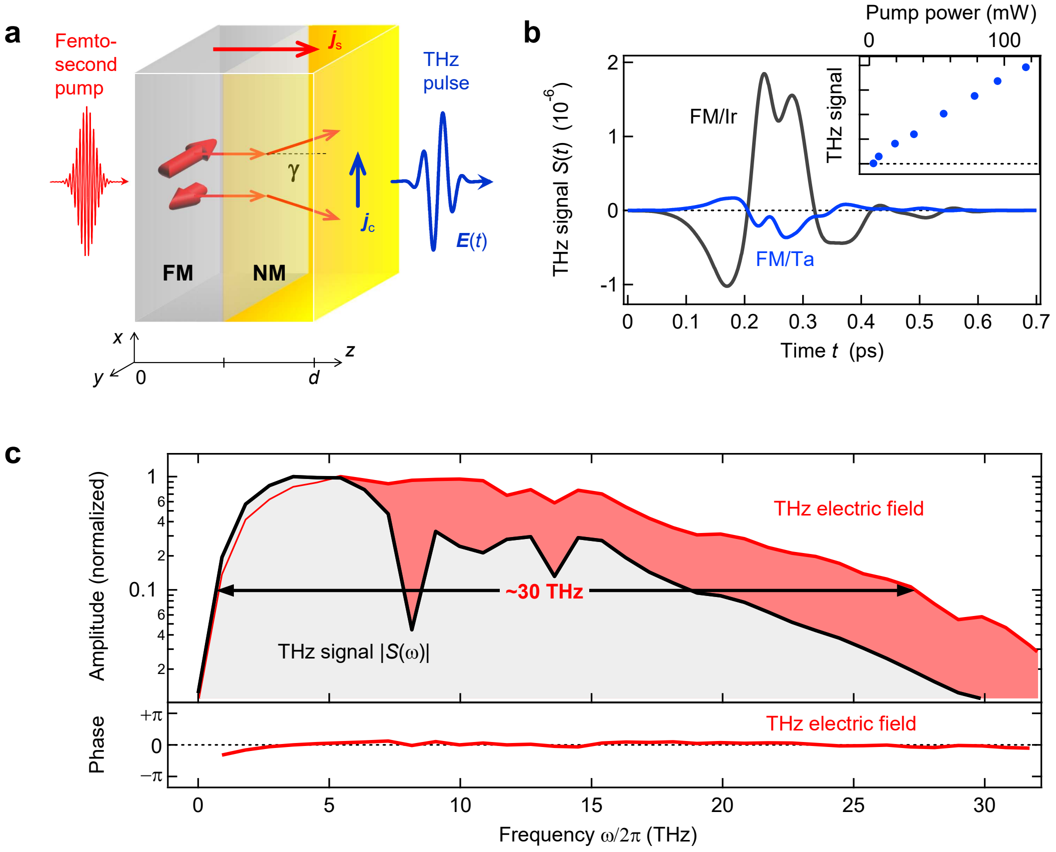

**Figure 5.1.: Metallic spintronic terahertz emitter.** **a**, Principle of operation. A femtosecond laser pulse excites electrons in the metal stack having an in-plane sample magnetization. Since the transport properties (mobility, lifetime, density) of excited spin-up (majority) electrons differ significantly from that of spin-down (minority) electrons, a $y$-polarized primary spin current is launched during thermalization into the normal metal (NM) layer. There, SOI deflects spin-up and spin-down electrons in opposite directions and transforms the spin current $j_\mathrm{s}$ into an ultrafast transverse charge current $j_\mathrm{c}$, leading to the emission of a THz electromagnetic transient. **b**, Electro-optic signal $S(t)$ of THz pulses obtained from photo-excited Ta- and Ir-capped $\mathrm{Co_{20}Fe_{60}B_{20}}$ thin films and detected by a 50-µm-thick GaP crystal. **Inset**: THz-signal amplitude as a function of the incident pump power. **c**, Fourier spectra of the THz signal $S(t)$ and the transient THz electric field directly before the sensor as obtained by deconvolving the detector response function from typical raw data such as those of **b**. Both spectra are normalized to peak amplitude 1. The double-arrow illustrates the about 30-THz-large bandwidth of the emitter. The flat spectral phase attests the THz pulse is Fourier-limited.

targets of 100-mm diameter. The typical Ar pressure range is 2 to $4 \cdot 10^{-3}$ mbar and the power setting is 800 W. Typical deposition rates are 1.2 Ås$^{-1}$ for the FM layer and 2.1 Ås$^{-1}$ for the NM layer. Prior to deposition, a short plasma etch is performed to clean the substrate surface from organic contaminants. The epitaxial Fe(100) thin film (thickness of 3 nm) is prepared by RF-sputtering on a MgO(100) substrate at room temperature. After confirmation of the epitaxial growth by reflection high-energy electron diffraction, an epitaxial Pt(100) layer (3 nm) is DC-sputtered on top.

The $Co_{20}Fe_{60}B_{20}$ films from the Greifswald group were prepared and characterized by U. Martens and M. Münzenberg (Institute of Physics, Ernst Moritz Arndt University, 17489 Greifswald, Germany). They are deposited by magnetron sputtering while NM metal films are grown by electron-beam evaporation under ultrahigh-vacuum conditions (base pressure $5 \cdot 10^{-10}$ mbar) using *in situ* transfer. Composition analysis of the films yields a Co/Fe ratio of 1/2.1. Characterization by transmission-electron microscopy reveals smooth $Co_{20}Fe_{60}B_{20}$ film surfaces below the atomic-monolayer limit. The magnetic materials exhibit typical thin-film properties [Bou11], in-plane magnetic anisotropy, and a nearly rectangular hysteresis curve with a coercive field well below 10 mT. Substrate materials used are glass, sapphire, and MgO.

**Experimental setup.** In the optical experiment (Fig. 5.1a), the sample is kept in an external magnetic field of 10 mT. It is excited by linearly-polarized laser pulses (duration of 10 fs, central wavelength of 800 nm, energy of 2.5 nJ) from a Ti:sapphire laser oscillator (repetition rate of 80 MHz) under normal incidence from the substrate side (beam diameter at sample 50 µm full width at half maximum of the intensity). For details on the setup see Section 3.4. Depending on signal strength, duration, and bandwidth required, we use various electro-optic materials: ZnTe(110) (thickness of 10 µm and 1 mm) [Lei99a], GaP(110) (50 and 250 µm) [Lei99a], and the poled-polymer guest-host system Lemke/amorphous polycarbonate (LAPC)[Zhe05] (70 µm) (see Sections 3.3 and 3.2). The LAPC sensor was fabricated by J. Hannegan and L. M. Hayden (Department of Physics, University of Maryland Baltimore County, Baltimore, Maryland 21250, USA). In the performance evaluation, the spintronic trilayer and the reference emitters (Figs. 5.6 and 5.7) are operated with the same pump-beam specifications. The THz amplitude obtained from the photoconductive switch (TeraSED3, based on interdigitated electrodes on a semi-insulating GaAs substrate [Win12]) is maximized by setting the DC bias voltage to 12 V (20 % above the maximum value recommended by the technical specifications). All measurements are performed at room temperature in a $N_2$ atmosphere.

**Theoretical model and calculations of spin Hall angles.** The calculations were done by F. Freimuth and Y. Mokrousov (Peter Grünberg Institute and Institute for Advanced Simulation, Forschungszentrum Jülich and JARA, 52425 Jülich, Ger-

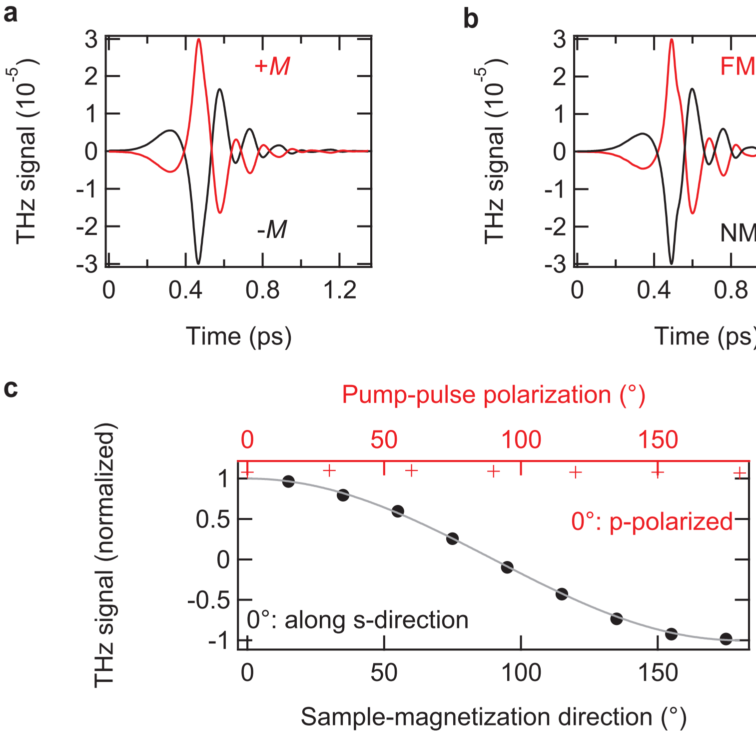

**Figure 5.2.: Symmetry properties of the terahertz signal.** **a**, THz signal from a $Co_{20}Fe_{60}B_{20}$(3 nm)/Pt(3 nm) bilayer as a function of the sample-magnetization direction. **b**, THz signal obtained for an FM/NM [$Co_{20}Fe_{60}B_{20}$(3 nm)/Pt(3 nm)] and NM/FM [Pt(3 nm)/$Co_{20}Fe_{60}B_{20}$(3 nm)] bilayer. **c**, THz-signal amplitude as a function of the orientation of the linear pump polarization (red crosses) and as a function of the direction of the sample magnetization (black circles). For the latter measurement, a THz wire-grid polarizer (blocking the s-polarized THz-field component) is placed before the detection. The gray solid line is the cosine of the angle between the polarizer wires and the sample magnetization.

many). The spin Hall conductivity (Fig. 5.3) is obtained by the Kubo formula (see Eq. 2.50) within density-functional theory. The full-potential linearized augmented plane-wave (FLAPW) program FLEUR (see http://www.flapw.de) is employed. In detail, the generalized gradient approximation of the exchange correlation potential, a plane-wave cutoff at a wave vector of $85\,\mathrm{nm}^{-1}$ and the experimental lattice constants (2.91, 3.892, 3.302, 3.166, 3.8402, and 3.926 Å for Cr, Pd, Ta, W, Ir, and Pt, respectively) are used. Further details on the computation are given in [Fre10].

## 5.3. Results and discussion

We start with bilayers consisting of FM $Co_{20}Fe_{60}B_{20}$ (thickness of 3 nm) capped by either NM Ta or Ir (3 nm). Typical THz electro-optic signals $S(t)$ obtained from these samples for the same orientation of the external magnetic field are displayed in Fig. 5.1b. Consistent with the generation mechanism outlined above [Kam13a], the emitted radiation has the following properties: The spin current and, thus, THz field are reversed entirely, either when the external saturating magnetic field of 10 mT is reversed or when the two metallic films are grown in reverse order on the substrate (see Fig. 5.2a and b). It is linearly polarized with the electric-field direction perpendicular to the sample magnetization, but it is independent of the pump polarization (see Fig. 5.2c). Finally, the THz-signal amplitude grows linearly with the pump power (Inset of Fig. 5.1b), in contrast to plasma sources, which require a threshold pump intensity for THz emission [Tho07, Kim12, Lu14]. The linear power scaling also shows that signal saturation due to pump-induced sample demagnetization is negligible here, consistent with the estimate that ultrafast magnetization quenching is less than 1 % at the maximum pump fluence used [Kam13a].

Fourier-transforming the time-domain signals $S(t)$ yields the spectral amplitude $|S(\omega)|$ versus frequency $\omega/2\pi$. A typical example is shown in Fig. 5.1c. Note this spectrum covers the large bandwidth from about 1 to 18 THz. We emphasize that spectral features such as the dip at 8 THz arise from the 50-µm-thick GaP electro-optic sensor and not from the emitter [Lei99a]. By deconvolving the detector response function from the signal $S(t)$, we obtain the THz electric field directly in front of the sensor (see Section 3.4.1). Strikingly, the field amplitude spectrum (Fig. 5.1c) is remarkably smooth and extends from 1 to nearly 30 THz full width at 10 % amplitude maximum, without any gaps. In addition, the spectral phase of the transient field is flat (Fig. 5.1c), thereby demonstrating that the THz pulse is Fourier-limited. As discussed above, these features derive from the unique properties of metals: short-lived photocurrents and a featureless frequency dependence of the optical constants, in stark contrast to semiconductor THz emitters [Rei07].

While its bandwidth is already remarkably large, the $Co_{20}Fe_{60}B_{20}$/Ta bilayer (Fig. 5.1b) generates a THz peak signal about 2 orders of magnitude smaller than what is obtained from a standard emitter in linear THz spectroscopy [Rei07], i. e. a 1-mm-thick ZnTe(110) crystal (see Fig. 5.6). To massively boost the emitted THz field, we need to understand the key factors that determine it.

To derive a relationship between the emitted THz electric field and its source current, we note that within our sample the beam diameter is much larger than the sample thickness ($d \sim 10\,\mathrm{nm}$). Therefore, plane-wave propagation along the $z$-axis (see Fig. 5.1) is assumed. The charge current density $-ej_\mathrm{c} = -e\gamma j_\mathrm{s}$ (resulting from the laser-driven spin current density $j_\mathrm{s}$ and the inverse spin Hall effect) generates an electromagnetic wave with an electric field $E(z,t)$ polarized along the $x$-axis (see Fig. 5.1a).

As seen in Section 2.6.2 and Eq. 2.85, we obtain for the THz electric field $E$ (Fig. 5.1a) directly behind the multilayer

$$E(\omega) = Z(\omega)\, e \int_0^d \mathrm{d}z\, \gamma(z)\, j_\mathrm{s}(z,\omega)\,. \tag{5.1}$$

This equation can be interpreted as a generalized Ohm's law because the emitted field equals the total charge current $-e\int \mathrm{d}z\,\gamma j_\mathrm{s}$ times an impedance $Z(\omega)$ which

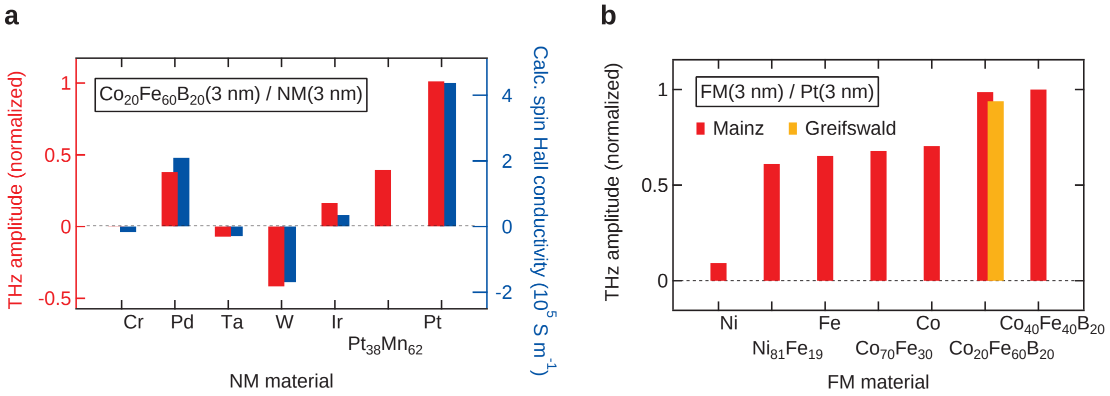

**Figure 5.3.: Impact of material choice on emitter performance.** **a**, THz-signal amplitude (RMS) as a function of the NM material used for the $Co_{20}Fe_{60}B_{20}(3\,nm)/NM(3\,nm)$ stack (red bars). For comparison, *ab initio*-calculated values of the intrinsic spin Hall conductivity are also shown (blue bars), except for $Pt_{38}Mn_{62}$. A Cr cap layer leads to nearly vanishing THz signal. **b**, THz-signal amplitude (RMS) of a FM(3 nm)/Pt(3 nm) heterostructure as a function of the FM material chosen. Distinct colors indicate different labs for sample fabrication.

quantifies how efficiently a current is converted into electromagnetic radiation. Here, $e$ is the electron charge and $Z$ is determined by

$$\frac{1}{Z(\omega)} = \frac{n_1(\omega) + n_2(\omega)}{Z_0} + \int_0^d \mathrm{d}z\,\sigma(z,\omega)\,, \tag{5.2}$$

where $\omega/2\pi$ is the THz frequency, $Z_0 = 377\,\Omega$ is the vacuum impedance, $n_1$ and $n_2$ denote, respectively, the refractive indices of the film substrate and the air, $d$ is the film thickness, and $\sigma$ is the conductivity of the metals. Equation 5.2 accounts for the propagation of the THz radiation inside the sample (including all reflection echoes) and the irradiation into free space. From a quasistatic viewpoint, $1/Z$ can be interpreted as the effective conductance of a parallel connection of all metal layers ($\int \mathrm{d}z\,\sigma$) shunted by the two adjacent half-spaces $[(n_1 + n_2)/Z_0]$. When the sheet conductance $\int \mathrm{d}z\,\sigma$ of the metal stack is much larger than the shunt conductance $(n_1 + n_2)/Z_0$ of the two half-spaces, Eq. 5.1 turns into the familiar Ohm's law [Kam07]. We again emphasize this equation is only valid in the thin-film limit, that is, for films much thinner than the wavelength and attenuation length of the THz wave inside the metal.

Equations 5.1 and 5.2 readily show that maximizing $Z$, and $j_s$ will lead to maximum THz output of the emitter for a given pump power. The numerous sample parameters that can be tuned in such an optimization are the FM/NM materials and the geometry of the heterostructure.

### Maximizing the terahertz output

**Nonmagnetic layer.** We start with varying the NM material which primarily affects the emitted THz field through the magnitude and sign of the spin Hall angle $\gamma$

(see Eq. 5.1). Consequently, we consider such metals for which large $\gamma$ values have been reported [Hof13]. Importantly, for all samples studied here, we find emitted THz waveforms and spectra whose shape is very similar to those shown in Figs. 5.1b and c. Therefore, it is sufficient to quantify the strength of the emitted THz field by the root mean square (RMS) of the THz signal $S\,(t)$. This quantity is displayed in Fig. 5.3a as a function of the NM metal in $\mathrm{Co_{20}Fe_{60}B_{20}}(3\,\mathrm{nm})/\mathrm{NM}(3\,\mathrm{nm})$ heterostructures.

Figure 5.3a clearly shows that the THz field amplitude and polarity depend drastically on the NM material chosen: for instance, Pt delivers a one order of magnitude larger amplitude than Ta and Ir. Interestingly, choosing W for the NM layer leads to a comparable magnitude as with Pd or Pt, but with opposite sign. This observation is consistent with previous works [Hof13]. The sign change arises because $\gamma$ is roughly proportional to the spin-orbital polarization of the electronic states around the Fermi energy [Kon09], which is opposite for the half-filled *d*-shell in W and the almost full *d*-shell in Pt. More generally, we find that the entire trend of THz amplitude versus NM material (Fig. 5.3a) is in good semiquantitative agreement with spin Hall conductivities measured previously [Hof13] and calculated by us (see Fig. 5.3a and Section 5.2). The remarkable agreement with *ab initio*-calculated values of the intrinsic spin-Hall conductivity appears plausible since it is believed to dominate in transition metal film with thicknesses of only a few nanometers implying large disorder (see Section 2.5.1). This observation provides further evidence for the transport scenario outlined in Fig. 5.1a and in Ref. [Kam13a]. However, the major conclusion drawn from Fig. 5.3a is that Pt is the most promising NM material for our THz FM/NM-bilayer emitter.

**Ferromagnetic layer.** In the second optimization step, we use Pt for the NM layer and study the THz emission as a function of the FM material. We consider $\mathrm{FM}(3\,\mathrm{nm})/\mathrm{Pt}(3\,\mathrm{nm})$ heterostructures with the FM metals Fe, Co, Ni, and their binary alloys. Fig. 5.3b shows that all materials provide similar output, except Ni, which yields less than 20 % of the maximum THz amplitude. The reason for this behavior is not yet understood but may be related to the fact that the Curie temperature of Ni (627 K) is considerably lower than that of all other FM materials ($> 1000\,\mathrm{K}$). Additional temperature-dependent measurements (not shown) could support this notion. Note that adding B to Co-Fe alloys leads to an increase of the THz amplitude by about 30 %. We attribute this behavior to the reduction of the FM conductivity by B impurities (see Eqs. 5.1 and 5.2). The essential conclusion is that $\mathrm{Co_{40}Fe_{40}B_{20}}/\mathrm{Pt}$ heterostructures provide best THz-emission performance.

**Optical properties of the samples.** To characterize our FM/NM metallic heterostructures, optical reflectance and transmittance are measured using the same pump beam as in the THz-emission setup. Our experimental data (Fig. 5.4) show that the multilayers absorb about 50 % of the incident laser power, largely inde-

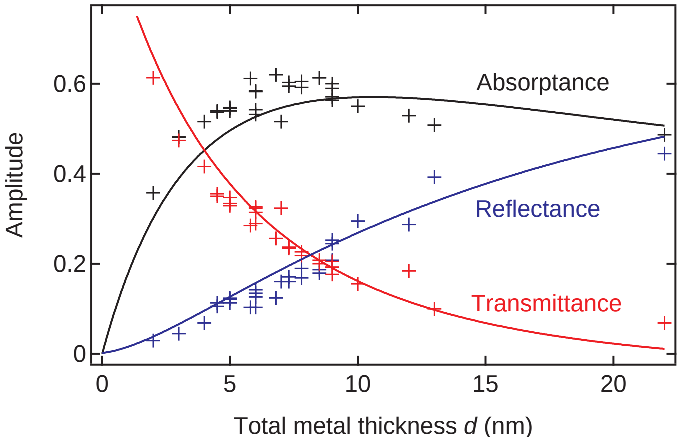

**Figure 5.4.: Optical properties of the metal heterostructures.** Reflectance, transmittance, and resulting absorptance $A$ of metal stacks as a function of metal thickness $d$ measured with the pump beam of the THz-emission setup. The solid lines show calculations (see text).

pendent of the total metal thickness $d$. The measured values of reflectance and transmittance agree excellently with calculations based on a transfer-matrix formalism (see Section 2.6.2 and Ref. [Yeh05]) and literature data of the optical constants of the materials involved [Lia15, Ord88] (solid lines in Fig. 5.4). Such good agreement is indicative of an optically homogeneous and flat metal film as expected from the optimized film deposition. The THz conductivities of the Pt and FM films are measured by THz transmission experiments (see Sect. 3.4). We find values of $\sigma = (2.9 + 0.1\mathrm{i}) \cdot 10^6 \mathrm{S\,m}^{-1}$ for Pt and $\sigma = (6.5 + 0.1\mathrm{i}) \cdot 10^5 \mathrm{S\,m}^{-1}$ for $\mathrm{Co}_{40}\mathrm{Fe}_{40}\mathrm{B}_{20}$ (assumed to be the same for $\mathrm{Co}_{20}\mathrm{Fe}_{60}\mathrm{B}_{20}$), approximately independent of frequency below 10 THz due to the high Drude scattering rate, which is on the order of 50 THz (see Section 4.4).

**Sample thickness.** In the third optimization step, we vary the stack geometry and first measure the THz emission as a function of the total sample thickness $d$ while keeping the FM and NM layer approximately equally thick. Our experimental data reveal a surprising behavior (Fig. 5.5a): the THz amplitude increases with decreasing emitter thickness $d$. Maximum amplitude is reached at $d = 4\,\mathrm{nm}$, below which the THz signal falls off rapidly.

Such behavior is highly counterintuitive and in sharp contrast to most phase-matched frequency conversion schemes such as optical rectification and second-harmonic generation [Rei07]. Indeed, Eq. 5.1 suggests that the THz amplitude scales with metal thickness $d$. Note, however, this trend is overcompensated by a remarkable photonic effect: our metal thin film acts as a Fabry-Pérot cavity that resonantly enhances both pump and THz waves. Because the cavity length $d$ is much smaller than all wavelengths involved, all reflection echoes inside the film interfere constructively (Fig. 5.5b). The shorter the cavity, the more echoes occur before the wave has decayed, resulting in even more enhancement. Effectively, a thinner film increases the pump-pulse excitation density, and improves the impedance matching between the metal and the surrounding substrate and air, facilitating the THz-pulse outcoupling to free-space. Below a critical thickness $d_\mathrm{c}$, however, reflection losses at the cavity faces exceed attenuation in the metal bulk. Then, the enhancement of pump and THz field saturates at $d < d_\mathrm{c}$ and no longer compensates for the shrinking emitter volume. Therefore, the emitted THz amplitude should first grow with decreasing $d$ and, after reaching a maximum, decrease, in agreement with our experimental bilayer data (Fig. 5.5a).

We now make use of Eq. 5.1 to model the THz-emission amplitude, as a function of the thickness of the FM/NM bilayer (with FM being Fe, $\mathrm{Co_{40}Fe_{40}B_{20}}$ or $\mathrm{Co_{20}Fe_{60}B_{20}}$ and NM=Pt). The impedance (see 5.2) is determined by the measured THz conductivities of the materials involved (see Sect. 5.2). The rest of Eq. 5.1 requires knowledge of the charge current density $j_\mathrm{c}(z) = \gamma(z)\, j_\mathrm{s}(z)$. To model its spatial structure, we neglect $\gamma$ in the FM layer and determine the spin current density $j_\mathrm{s}$ in the NM layer by considering the following simplified scenario: after excitation by the pump pulse, spin-polarized electrons from the FM layer enter the NM layer in which they first propagate ballistically away from the FM/NM interface (see Fig. 5.1a). However, once an electron undergoes scattering, its velocity is randomized such that its contribution to the ultrafast photocurrent and, thus, to the THz signal is assumed to become negligible. To account for such velocity randomization, we assume the density of ballistic electrons behind the FM/NM interface decreases according to $e^{-(z-d_\mathrm{FM})/\lambda_\mathrm{rel}}$ where $\lambda_\mathrm{rel}$ can be considered as an electron velocity relaxation length [Hof13]. We furthermore assume that the electrons undergo perfect reflection at the NM/air and the NM/FM interface. As shown by Mosendz et al. [Mos10], these assumptions imply a spatial dependence of the ballistic spin current density inside the NM layer ($d_\mathrm{FM} < z < d = d_\mathrm{FM} + d_\mathrm{NM}$) according to

$$j_\mathrm{s}(z) = j_\mathrm{s}(d_\mathrm{FM}) \frac{\sinh\left[(z-d)/\lambda_\mathrm{rel}\right]}{\sinh\left(d_\mathrm{NM}/\lambda_\mathrm{rel}\right)}, \tag{5.3}$$

where $j_\mathrm{s}(d_\mathrm{FM})$ is the spin current density directly after the FM layer. Finally, the linear fluence dependence of the emitted THz field (Fig. 5.1b) indicates the spin current is proportional to the energy density deposited by the pump pulse. Therefore, one has $j_\mathrm{s}(d_\mathrm{FM}) \propto A/d$ where $A$ is the absorbed fraction of the incident pump power (see Fig. 5.4). Plugging Eq. 5.3 and all other assumptions into Eq. 5.1, we obtain

$$E(d) \propto \gamma_\mathrm{NM} \lambda_\mathrm{rel} \frac{A}{d} \frac{\tanh\left(d_\mathrm{NM}/2\lambda_\mathrm{rel}\right)}{n_1 + n_2 + Z_0 \int_0^d \mathrm{d}z\, \sigma(z)}. \tag{5.4}$$

The film impedance $Z$ is obtained from Eq. 5.2 with the metal conductivities measured by THz transmission spectroscopy (see Section 3.4). The spin current density $j_\mathrm{s}$ is assumed to scale with the mean excitation density $A/d$. The measured sample absorptance amounts to as much as ~60 %, nearly constant for $d$ between 5 and 20 nm (see Fig. 5.4). We note that the thickness dependence of both $Z$ and $A/d$ exhibits the expected $1/(d + d_\mathrm{c})$-like behavior. We fit our model (Eq. 5.4) to the

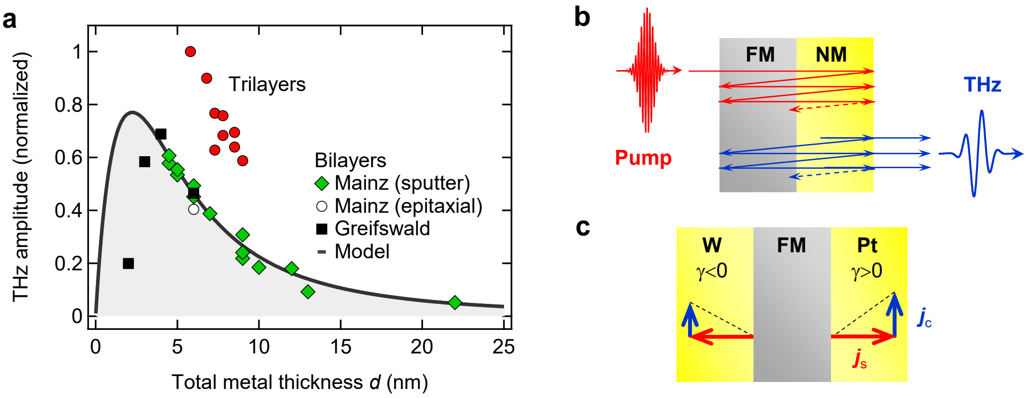

**Figure 5.5.: Impact of stack geometry on emitter performance.** **a**, THz-signal amplitude (RMS) as a function of the thickness $d$ of the metal stack. Different symbols represent different sample-fabrication schemes. The solid line is a fit using a transport model (see Eq. 5.4). **b**, Schematic of the thin-film Fabry-Pérot cavity that enhances both incident pump and emitted THz radiation. **c**, Schematic of the trilayer emitter that converts the backward- and forward-propagating spin current $j_s$ into a unidirectional charge current $j_c$ with approximately equal efficiency.

THz amplitude data of Fig. 5.5a with $\lambda_{rel}$ and a global amplitude factor being the only free parameters. The best fit (solid curve in Fig. 5.5a) is obtained for $\lambda_{rel} = 1\,\mathrm{nm}$ and describes the thickness dependence of the emitted THz amplitude very well, including the existence of a maximum. The discrepancy for $d < 4\,\mathrm{nm}$ is most likely due to shortcomings of our simplified transport model and due to changes in the magnetic properties (such as the Curie temperature) of the sample when approaching small thicknesses. Thus, Fig. 5.5a shows that the largest THz signal is provided by the 4-nm-thick $Co_{20}Fe_{60}B_{20}$/Pt emitter. This performance is very close to the absolute maximum predicted by the model. We do not expect higher-order Fabry-Pérot resonances for the pump because the decay length of the pump intensity (~15 nm) is much shorter than the wavelength (~300 nm) of the pump radiation inside the metal film.

**Trilayer.** Having identified the best bilayer emitter, we finally engineer the sequence of the spintronic metal layers. Figure 5.1a suggests that only the forward-propagating half of the photo-induced spin current travels into the NM layer where it is converted into a charge current. To also take advantage of the backward-flowing electrons, we introduce another NM layer on the left-hand side of the FM film (Fig. 5.5c). We choose W/$Co_{40}Fe_{40}B_{20}$/Pt because W and Pt exhibit the largest spin Hall angles $\gamma$ yet with opposite sign (Fig. 5.3a). Owing to this unique possibility of spintronic engineering, the spin Hall currents $j_c$ in the W and Pt layer flow in the same direction, radiate in phase and, thus again, boost the THz amplitude (Fig. 5.5c). Indeed, as seen in Fig. 5.5a, the THz amplitude from each W/$Co_{40}Fe_{40}B_{20}$/Pt trilayer is approximately twice as high as that from a bilayer counterpart with the same total thickness. The W(2 nm)/$Co_{40}Fe_{40}B_{20}$(1.8 nm)/Pt(2 nm) trilayer delivers a 40% higher THz amplitude than the best bilayer $Co_{20}Fe_{60}B_{20}$(2 nm)/Pt(2 nm), even though the trilayer is about 50% thicker. This result indicates that the conversion of both forward and backward spin currents into THz radiation overcompensates the larger metal thickness (see Eq. 5.1). Figure 5.5a concludes our model-guided optimization strategy and identifies the 5.8-nm-thick W/$Co_{40}Fe_{40}B_{20}$/Pt trilayer as the best THz emitter out of the comprehensive set of more than 70 heterostructures studied here. With this extensive procedure, we have gone beyond all previous approaches for emitter design and fully exploited the spintronic nature of our THz source. The evolution of our efforts is illustrated by Fig. 5.6a: the trilayer delivers a more than two orders of magnitude larger THz amplitude than $Co_{20}Fe_{60}B_{20}$(10 nm)/Ta(2 nm), which is one of the bilayers we started with.

### Performance test

To evaluate our STE, we compare its performance to that of three state-of-the-art THz sources routinely used to cover the range from about 0.3 to 8 THz: the nonlinear optical crystals ZnTe(110) and GaP(110) [Fer02a, Rei07], and a high-performance photoconductive switch with interdigitated electrodes [Win12]. For all emitters, the THz emission is measured under identical conditions and the THz-signal amplitude is found to scale linearly with the pump power (see Inset of Fig. 5.1b for the STE). Consequently, comparison of THz spectral amplitudes provides a direct measure of how well each emitter covers a given frequency window. To directly identify spectral emission gaps, we choose a 70-µm-thick Lemke/amorphous polycarbonate (LAPC) electro-optic sensor [Zhe05] that permits gap-free detection from about 0.3 to 15 THz. Figures 5.6a and b display THz waveforms $S(t)$ from the four sources and the respective amplitude spectra. Deconvolving the detector response function (see Sect. 3.4.1) yields the transient THz electric fields which are shown in Fig. 5.7. For ZnTe and GaP, the electro-optic signal $S(t)$ consists of a slow and fast oscillating part which is, respectively, related to frequencies below and above the Reststrahlen band of these crystals. Strong wave attenuation in the Reststrahlen region [Lei99a] leads to considerable gaps from 3 to 10 THz, and from 7 to 13 THz in the ZnTe and GaP amplitude spectra $|S(\omega)|$, respectively (Fig. 5.6b). In contrast, the time-domain signal from the spintronic trilayer features a higher peak amplitude, is much shorter (Fig. 5.6a) and even Fourier-limited (Fig. 5.1c). Remarkably, the spectrum is gap-free and exceeds the spectral amplitude of the ZnTe and GaP crystals from 2.5 to 11.5 THz. While the photoconductive switch and the STE exhibit comparable THz-signal amplitudes in the time domain (Fig. 5.6a), their performance is complementary in frequency space (Fig. 5.6b). In case that exceptionally high amplitudes are required below3 THz, the photoconductive switch is the source of choice. In contrast, the STE provides more amplitude above 3 THz and exhibits a much wider bandwidth from 1 to 30 THz without gap (see Fig. 5.7). Finally, the corresponding electric fields at the detector position (Fig. 5.7) are

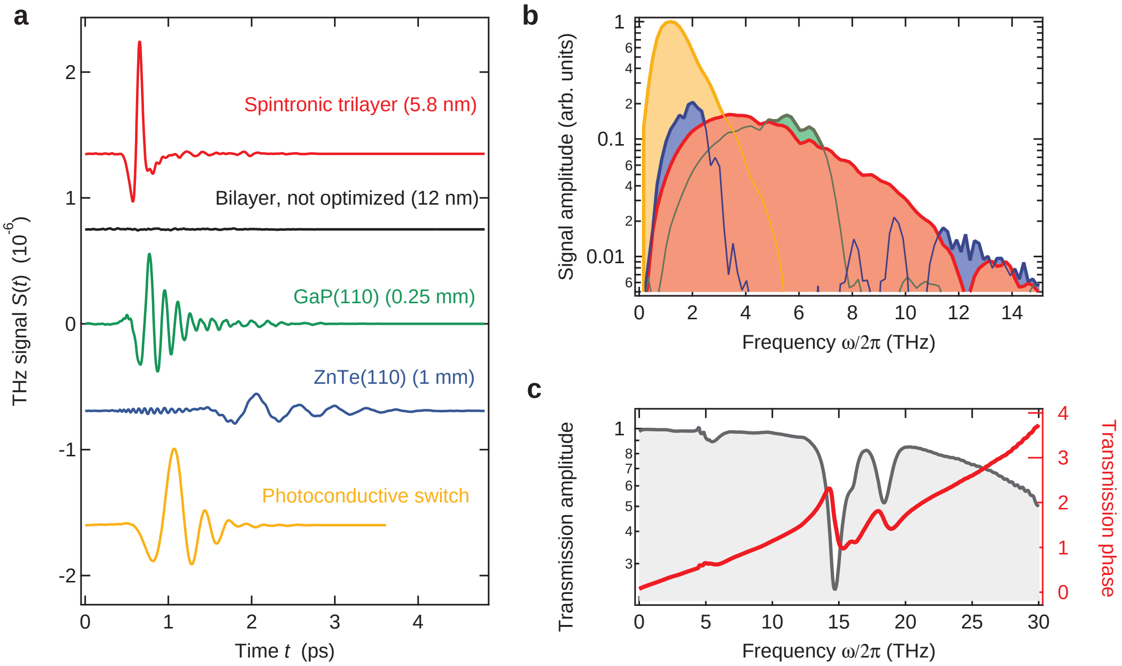

**Figure 5.6.: Spintronic emitter performance and spectroscopic application.** **a**, THz-signal waveforms and **b**, resulting amplitude spectra of the spintronic trilayer emitter in comparison to standard THz emitters as measured with a 70-µm-thick LAPC electro-optic sensor. Measurements are performed under identical conditions, such that the output of the three emitters can directly be compared. **c**, Spectral amplitude and phase of the THz transmission of a 7.5-µm-thick PTFE thread-seal tape measured with our spintronic emitter using a 10-µm-thick ZnTe sensor. Curves in **a** are offset for clarity.

obtained by a deconvolution procedure as described in Section 3.4.1.

**Estimate of the quadratic nonlinear susceptibility.** The amplitude of the THz pulses emitted from the STE grows linearly with the pump fluence (Inset of Fig. 5.1b). Therefore, optically-induced THz emission from the STE can be described phenomenologically as a $\chi^{(2)}$-type nonlinear-optical process in which the pump field $E_\mathrm{p}$ induces an electric dipole density (polarization) (see [Mil12] and Section 2.6.1)

$$P^{(2)}(\omega) = \frac{\chi^{(2)}(\omega)}{Z_0 c} \int_{\omega_\mathrm{p}>\omega>0} \mathrm{d}\omega_\mathrm{p}\, E_\mathrm{p}(\omega_\mathrm{p})\, E_\mathrm{p}^{*}(\omega_\mathrm{p}-\omega) =: \frac{\chi^{(2)}(\omega)}{Z_0 c} F(\omega) \tag{5.5}$$

at the difference $\omega$ of all pump-frequency pairs $\omega_\mathrm{p}$ and $\omega_\mathrm{p}-\omega$. In writing Eq. 5.5, we have assumed that the second-order response function $\chi^{(2)}$ is independent of the pump frequency and abbreviated the integral by $F(\omega)$. In general, the dependence of $\chi^{(2)}$ on THz frequency $\omega$ makes the response delayed, that is, longer than the driving optical pump pulse. Since $-\mathrm{i}\omega P^{(2)}(\omega)$ equals the charge-current density $-ej_\mathrm{c}(\omega)$, we use Eq. 5.1 to rewrite the THz electric field directly after the STE as

$$E(\omega) = \frac{Z(\omega)}{Z_0} \frac{\mathrm{i}\omega F(\omega)}{c} \int_0^d \mathrm{d}z\, \chi^{(2)}(z,\omega)\,. \tag{5.6}$$

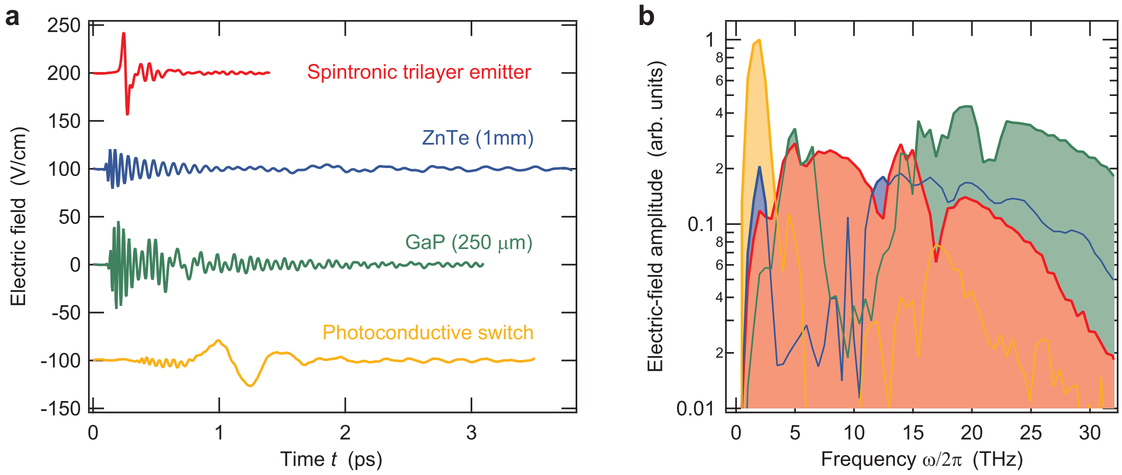

**Figure 5.7.: Electric field emitted by the spintronic and other standard terahertz emitters.** **a**, Transient THz electric field $E_{\mathrm{det}}$ incident on the electro-optic detection crystal [1-mm-thick ZnTe(110)] following emission by the STE, the (110)-oriented nonlinear optical crystals ZnTe and GaP, and a photoconductive switch. **b**, Corresponding field amplitudes obtained by Fourier transformation of the data of panel **a**. Curves in **a** are offset for clarity.

To estimate the $\chi^{(2)}$-magnitude of our STE, we compare the THz amplitude generated by the STE to that of a suitable reference emitter. We choose a 50-µm-thick GaP(110) crystal because the magnitude ($5.4 \cdot 10^{-11}\,\mathrm{mV}^{-1}$) of its only nonvanishing $\chi^{(2)}$ tensor element is well known [Lei99a]. In addition, THz-wave generation is still phase-matched at this thickness. According to Ref. [Kai99], the THz amplitude directly after the GaP is given by a formula analogous to Eq. 5.6,

$$E_{\mathrm{GaP}}(\omega) = \frac{\exp\left[i n_{\mathrm{GaP}}(\omega)\,\omega d/c\right]}{n_2(\omega) + n_{\mathrm{GaP}}(\omega)} \cdot \frac{i\omega F_{\mathrm{GaP}}(\omega)}{c} d_{\mathrm{GaP}} \chi^{(2)}_{\mathrm{GaP}}(\omega)\,. \tag{5.7}$$

Here, $d_{\mathrm{GaP}}$ is the GaP thickness, and $n_{\mathrm{GaP}}$ is the refractive index of GaP. As with Eq. 5.6, $n_2$ is the refractive index of air. In our experiment, we find that the peak electro-optic signal (Fig. 5.6a) and the THz field amplitude (Fig. 5.7a) of the STE are comparable to those of GaP. Consequently, we have$|E| \approx |E_{\mathrm{GaP}}|$. Similarly, the first and second term of Eq. 5.6 have the same order of magnitude as their GaP counterparts in Eq. 5.7. Therefore, the ratio of the nonlinear optical coefficients is roughly given by

$$\left|\chi^{(2)}/\chi^{(2)}_{\mathrm{GaP}}\right| \sim d_{\mathrm{GaP}}/d_{\mathrm{eff}}, \tag{5.8}$$

that is, by the ratio of the GaP thickness ($d_{\mathrm{GaP}} = 50\,\mu\mathrm{m}$) and the effective thickness $d_{\mathrm{eff}}$ of the STE region in which the THz charge current is generated. Since $d_{\mathrm{eff}} \sim \lambda_{\mathrm{rel}} \sim 1\,\mathrm{nm}$ (see Fig. 5.5), the $\chi^{(2)}$-coefficient of the STE is nearly 5 orders of magnitude larger than that of GaP, yet located in a sheet of only about 1-nm thickness at the FM/NM interface.

### Application in linear terahertz spectroscopy

We routinely use our STE to measure ultrabroadband linear transmission spectra (see Section 3.4 and Chapter 4). As an example, Fig. 5.6c displays amplitude and phase of the complex transmission of a 7.5-µm-thick polytetrafluoroethylene (PTFE, Teflon®) sample, obtained by using the trilayer emitter and a 10-µm-thick ZnTe(110) sensor [Lei99a]. Resonant features around 6, 15, and 18 THz are found, and they arise, respectively, from $CF_2$ twisting, rocking/wagging, and rocking in the molecular chain [Cha74]. Our observation agrees excellently with previous PTFE studies using gas-plasma THz emitters [D'A14], which, however, require 5 orders of magnitude higher pump-pulse energies. We finally note that such broadband and gapless THz spectroscopy would not be possible at all with standard solid-state emitters.

## 5.4. Conclusion and outlook

We have developed a conceptually new, efficient, and versatile THz source for broadband linear THz spectroscopy based on optically driven spin currents in ultrathin magnetic metal heterostructures. Our approach unifies the benefits of different emitter types in one device: it approaches the bandwidth of much more expensive gas-plasma spectroscopy systems and delivers short, Fourier-limited pulses covering the full range from 1 to 30 THz without gap. As with often-used optical-rectification crystals, our heterostructure is robust, passive, easy-to-use (in transmission mode under normal incidence), and driven by a low-cost, compact femtosecond laser oscillator. At the same time, the THz field amplitude emitted exceeds that of standard emitters such as ZnTe, GaP, and a biased photoconductive switch. As for such switches, direction and amplitude of the emitted THz field can easily be modulated by applying an oscillating magnetic field with a small amplitude below 10 mT. In addition to these benefits, the broadband optical absorption of metals implies that the spintronic THz source can be driven by any oscillator, virtually independent of its output wavelength, for instance a Ti:sapphire (800 nm), $Yb^{3+}$ fiber (1030 nm) or $Er^{3+}$ fiber (1550 nm) laser. We emphasize that fabrication of our emitter is inexpensive, straightforward, and scalable, without involving any lithography steps. Fabrication costs are dominated by the substrate price and we can deposit homogeneous layers on substrates with diameters as large as 20 cm. As will be demonstrated in the following, STEs exhibit a high potential for enabling nonlinear-optical studies [Liu12b, Vic13] in the difficult-to-access region between 5 and 10 THz.

Our results highlight metallic magnetic multilayers as a new and very promising class of high-performance and broadband THz emitters. Finally, this work is an example for a rapid translation of recently discovered fundamental physical effects into useful technology that can straightforwardly be employed by the broad femtosecond-laser community.

**Acknowledgments.** We would like to thank I. Radu (Helmholtz-Zentrum Berlin für Materialien und Energie, Berlin, Germany), E. Beaurepaire (Institut de Physique et Chimie des Matériaux de Strasbourg, 67200 Strasbourg, France), P. M. Oppeneer (Department of Physics and Astronomy, Uppsala University, SE-75120 Uppsala, Sweden) and D. Turchinovich (Fakultät für Physik, Universität Duisburg-Essen, 47057 Duisburg, Germany) for valuable comments on this work.

# 6. Upscaling of a metallic spintronic terahertz emitter

*Based on the promising results of the last Chapter, we explore the capabilities of metallic spintronic thin-film stacks as a source of intense and broadband THz electromagnetic fields. For this purpose, we excite a W/CoFeB/Pt trilayer (thickness of 5.8 nm) on a large-area glass substrate (diameter of 7.5 cm) by a femtosecond laser pulse (energy of 5.5 mJ, duration of 35 fs, wavelength of 800 nm). After focusing, the emitted THz pulse is measured to have a duration of 230 fs, a peak field of 300 kV/cm and an energy of 5 nJ. In particular, the waveform exhibits a gapless spectrum extending from 1 to 10 THz at 10 % of its amplitude maximum, thereby facilitating nonlinear control over matter in this difficult-to-reach frequency range on the sub-picosecond time scale.*

Parts of this Chapter have been published in [Sei17b], which has been selected for the cover article of that issue (see Fig. 6.1).

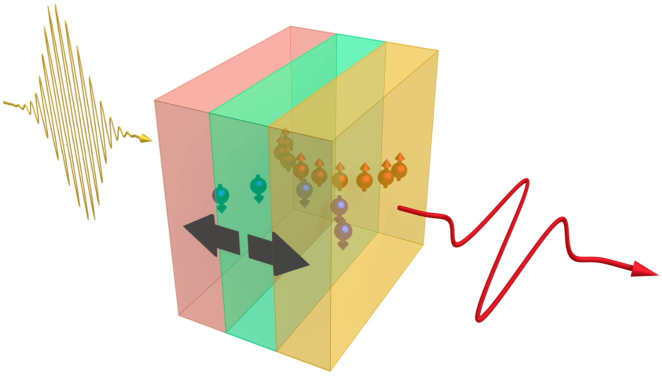

**Figure 6.1.: Cover artwork.** Applied Physics Letters (Volume 110, Issue 25) cover page related to the article “Ultrabroadband single-cycle terahertz pulses with peak fields of 300 kV/cm from a metallic spintronic emitter” [Sei17b]. Figure created with the help of J. Heitz.

## 6.1. Motivation

Terahertz pulses covering the range from 1 to 20 THz are resonant probes of numerous low-energy excitations in all phases of matter (see Chapter 1). Completely unexplored research avenues open when THz pulses are used to drive rather than probe material resonances [Hof12, Kam13b, Hwa15, Els15, Nic16]. In solids, examples are the ultrafast coherent control over the motion of lattice ions and ordered electron spins, and the transport of charge carriers, even across the atomic-scale junction of scanning tunneling microscopes [Coc16]. To implement such material control, elevated field strengths >100 kV/cm over a wide frequency range are required. Furthermore, to access more resonances with better time resolution, higher bandwidth is highly desirable.

User facilities based on electron accelerators can provide both broadband and narrowband THz pulses with tunable central frequency, peak fields approaching 1 MV/cm, and repetition rates as high as 1 MHz [Gre16]. Table-top sources [Zha17b], on the other hand, operate at a rate of typically ~1 kHz. At the low-frequency side, they are based on optical rectification in photoconductive switches [Ber13], or in inorganic [Fül16] and organic [Hir11, Hau11, Vic15] crystals. For frequencies above 5 THz, difference frequency mixing of the two outputs of a dual optical parametric amplifier [Sel08, Liu17], was shown to yield field strengths >10 MV/cm. Regardless of the high conversion efficiencies reached with these schemes, they are affected by spectral gaps between 1 and 10 THz (see Section 3.2). Emission from a dual-color-laser-excited air plasma [Kim12] can even cover frequencies from below 1 to above 10 THz with field strengths of up to 8 MV/cm [Oh14]. However, the experimental realization is not as straightforward as with emitters relying on optical rectification. Thus, the frequency range from about 5 to 15 THz is still challenging in terms of high fields and table-top setups [Dhi17].

Recently, metallic [Ram14, Pol11] and metallic spintronic heterostructures were shown to be promising THz emitters (see Chapter 5 and Refs. [Kam13a, Hui16a, Wu17, Yan16, Awa16]). When a W/CoFeB/Pt trilayer of 5.8-nm thickness was excited with optical pulses (duration of 10 fs, energy of ~1 nJ) from an 80-MHz laser oscillator, THz pulses with a gapless spectrum from 1 to 30 THz and a conversion efficiency even better than standard oscillator-based THz sources were achieved (see Figs. 5.1 and 5.6). However, the capability of spintronic THz emitters as high-field sources driven by millijoule-class laser pulses remains to be shown.

Here, we demonstrate upscaling of metallic spintronic THz emitters, resulting in a practical and ultrabroadband source delivering THz pulses as short as 230 fs, a spectrum from 1 to 10 THz (full width at 10 % of amplitude maximum) and peak fields of 300 kV/cm.

## 6.2. Experimental details

**Sample fabrication.** The samples were prepared and characterized by S. Jaiswal, J. Henrizi, G. Jakob, M. Jourdan and M. Kläui (Institute of Physics, Johannes Gutenberg University, 55128 Mainz, Germany). Our metallic spintronic THz emitter (STE, see Fig. 6.2a) is a nanometer-thick trilayer structure NM1/FM/NM2, made

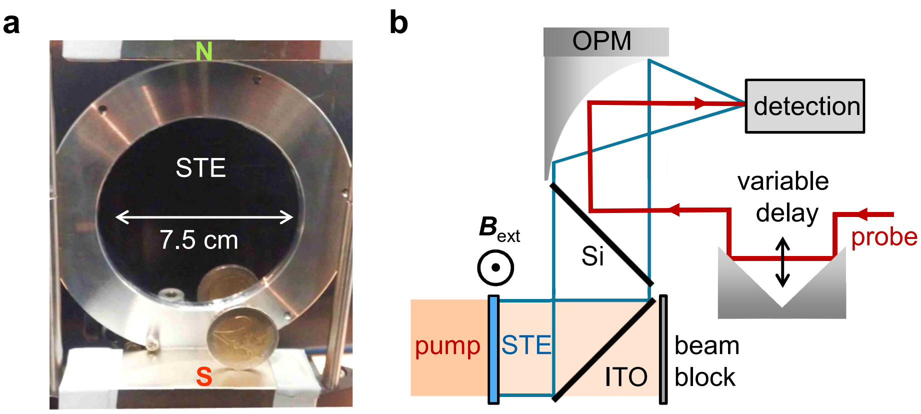

**Figure 6.2.: High-field spintronic terahertz emitter.** **a**, Photograph of the spintronic THz emitter (STE). Two bar magnets labeled N and S provide a magnetic field of ≥10 mT across the entire emitter area. A 2-€ coin serves as a scale reference. **b**, Experiment schematic. For details, see the main text. Abbreviations: $\boldsymbol{B}_{\mathrm{ext}}$: external magnetic field, ITO: indium-tin-oxide-covered glass, Si: silicon wafer, OPM: 90°-off-axis parabolic mirror.

of a ferromagnetic (FM) layer FM= $Co_{20}Fe_{60}B_{20}$ between two nonmagnetic (NM) layers, NM1=Pt and NM2=W, on a fused-silica substrate (see Chapter 5), which also acts as a heat sink. The detailed stack structure is fused silica (thickness of 500 µm)/W(2 nm)/$Co_{20}Fe_{60}B_{20}$(1.8 nm)/Pt (2 nm). The magnetic heterostructures are grown in a Singulus Rotaris© sputter tool equipped with targets of 100 mm diameter. Typical deposition conditions are a sputter power of 800 W at an Argon pressure of 2 to $4 \cdot 10^{-3}$ mbar. The resulting deposition rates are 1.2 Å/s for the FM layer and 2.1 Å/s for the NM layers. A short plasma etch with a 500 eV Ar-ion beam is applied to the substrate to clean the surface from organic contaminants. The cost of the emitter is mainly determined by the substrate price of ~$ 20 for 7.5 cm diameter.

**Experimental setup.** Details on the spintronic THz emitter working principle can be found in Chapter 5.

In our experiment (see Fig. 6.2b for a schematic), we use laser pulses (energy of 5.5 mJ, central wavelength of 800 nm, duration of 35 fs, repetition rate of 1 kHz) from an amplified Ti:sapphire laser system (see Section 3.1). The collimated beam [diameter of 4.8 cm full width at half maximum (FWHM) of intensity] is incident onto the STE, whose in-plane magnetization is saturated by permanent magnets delivering a field of about 10 mT. To spectrally separate the pump from the THz radiation, the emitted THz beam is reflected by a float glass with indium-tin-oxide coating (thickness of 100 nm, sheet resistance <7 Ω/sq, covered with a $SiO_2$ passivation layer) under an angle of 45°. After transmission through a silicon wafer (angle of incidence of 45° ± 2°), blocking the residual pump radiation, the THz beam is eventually focused on two different detectors to characterize the THz power and the

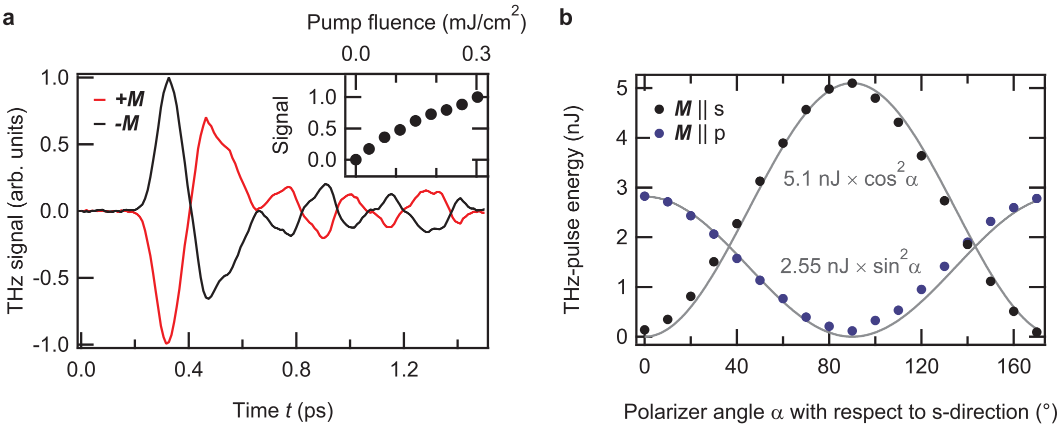

**Figure 6.3.: Raw data. a**, Typical THz electro-optic signals measured with a 50-µm-thick Quartz detector for opposite sample magnetizations $\pm\boldsymbol{M}$. **Inset**: Pump-fluence dependence of the THz signal (root mean square). **b**, THz-pulse energy as a function of the rotation angle $\alpha$ of a THz polarizer inserted before the THz power meter for two orthogonal sample magnetizations (black and blue dots). Gray lines are $\cos^2\alpha$- and $\sin^2\alpha$-fits. THz-pulse energies are corrected for polarizer transmission losses.

transient THz electric field. The THz power is measured with a power meter (Gentec THz-B), which requires chopping of the near-infrared pump beam at 25 Hz. To determine the THz polarization state, we employ a rotatable free-standing wire-grid polarizer (InfraSpecs model P02) placed directly behind the silicon wafer.

We characterize the transient THz electric field by standard electro-optic (EO) sampling (see Section 3.3) in crystals of either (110)-oriented GaP (thickness of 50 µm), (110)-oriented ZnTe (10 and 50 µm) or (001)-oriented Quartz (50 µm). The detection crystals are sufficiently thin to ensure a linear scaling of the EO signal with the THz electric field. If not mentioned otherwise, measurements are conducted at room temperature in air. Details on EO detection with a Quartz crystal will be published elsewhere.

## 6.3. Results and discussion

### Raw terahertz signals

Figure 6.3a shows a typical EO signal as recorded with a 50-µm-thick Quartz crystal. We observe an almost complete reversal of the THz signal when the sample magnetization is reversed. This behavior is consistent with our understanding of the THz-emission process (see Chapter 5). The pump-fluence dependence (Inset of Fig. 6.3a) demonstrates that the THz emission is still well below saturation. We note that the temporal shape of the THz pulse is independent of the pump fluence (not shown). The observed ringing after the main pulse (Fig. 6.3a) may arise from the THz absorption of water vapor in air. This notion is corroborated by the fact that additional purging with $N_2$ leads to a 10 % increase in THz amplitude and a slight reduction of the ringing. Another possible origin is the absorption by phonon resonances of the EO Quartz detector at around 4, 8, and 12 THz [Rus67, Spi61].

Figure 6.3b displays the measured THz power behind a wire-grid polarizer as a function of its azimuthal rotation angle $\alpha$ for the sample magnetization set perpendicular ($\boldsymbol{M}||$s) and parallel ($\boldsymbol{M}||$p) to the optical table. The measured data are well described by an $\alpha$-dependence proportional to $\cos^2\alpha$ and $\sin^2\alpha$, respectively. Therefore, the THz radiation measured by the power detector is polarized linearly and oriented perpendicularly to the sample magnetization. These polarization properties agree with the SDSE/ISHE-THz-emission scenario of Chapter 5. The different maximum power amplitudes obtained for the $\boldsymbol{M}||$s- and $\boldsymbol{M}||$p-configurations can easily be explained by the polarization-dependent transmittance of the silicon window (see Fig. 6.2b): a calculation of the Fresnel transmission coefficients yields a transmittance ratio of p- and s-polarized THz radiation of $2.0 \pm 0.1$ [Dai04]. This value is in good agreement with the experimental observation (see Fig. 6.3b). By accounting for the transmittance of the polarizer (86 %, averaged over the THz intensity spectrum [Inf17]), we obtain an energy of about 5.1 nJ for a p-polarized THz pulse.

We note that both coherent THz pulses and incoherent black-body radiation of the pump-heated STE can contribute to the measured THz power. In addition, THz radiation can also be generated by the residual pump light absorbed in the silicon beam combiner (Fig. 6.2b). However, the coherent part of the THz emission from the silicon slab is expected to be independent of the STE's magnetization direction, in contrast to the measurements of Fig. 6.3a. Similarly, the black-body radiation from both STE and silicon slab is largely unaffected by the external magnetic field. Therefore, the power behind the polarizer should be identical for the $\boldsymbol{M}||$s- and $\boldsymbol{M}||$p-configurations, in stark contrast to our observations (see Fig. 6.3b). Thus, the black-body radiation arriving at the power detector makes a minor or even negligible contribution to the detector signal. This observation can be explained by the following two scenarios. First, the black-body radiation arriving at the detector has a much smaller power than the coherent THz radiation. Second, the instantaneous temperature of STE and silicon wafer and the resulting black-body radiation are not able to follow the pump-power modulation frequency of 25 Hz, thereby being suppressed by our phase-locked power detector. Therefore, each coherent THz pulse stems from the STE, has an energy of 5.1 nJ, and a linear polarization perpendicular to the sample magnetization.

### Extraction of terahertz electric fields

To extract the actual THz electric field at the detector position, the measured EO signal is deconvolved with respect to the transfer function of the EO detection process (see Section 3.4.1). The deconvolution is performed in the time domain for three different detector crystals [10-µm-thick ZnTe on a (100)-oriented ZnTe substrate [Lei99a], and 50-µm-thick free-standing ZnTe or GaP]. The resulting field waveforms are low-pass filtered with a Gaussian function centered at 0 THz and having a FWHM of 40 THz.

Figure 6.4a shows typical EO signals recorded in a dry nitrogen atmosphere with the three different detectors. The extracted THz electric fields $E_{\mathrm{THz}}(t)$ are displayed in Fig. 6.4b.

We find single-cycle waveforms whose temporal shape and amplitude are in excellent agreement for all detectors used. This observation demonstrates the robustness of our deconvolution scheme. The extracted transient THz electric field reaches a peak value of 300 kV/cm and has a duration of 230 fs (FWHM of the field envelope, see Fig. 6.4b). Fourier-transformation (see App. A.1) of the field waveforms $E_{\mathrm{THz}}(t)$ yields the complex-valued field amplitude spectrum $|E_{\mathrm{THz}}(\omega)|$ vs frequency $\omega/2\pi$ that is shown in Fig. 6.4c along with the respective THz-signal spectrum. Note that the THz field spectrum is gapless and spans the entire range from 0.1 to 10 THz with respect to 10 % of the peak spectral amplitude. The spectral phase is flat and varies by less than $2\pi/10$ (standard deviation).

**Pulse energy of a Gaussian beam.** As a cross-check, we compare the extracted transient THz electric field $E_{\mathrm{THz}}(t)$ in the focus (Fig. 6.4b) to the measured THz-pulse energy $W$ (Fig. 6.3b). To this end, we derive in the following a relationship between the electric field in the focus and the beam energy.

In the frequency domain, the energy of an electromagnetic pulse with cylindrically symmetric beam profile is given by

$$W = 2\pi Z_0^{-1} \int\int \mathrm{d}\omega \mathrm{d}r\, r\, |E'(\omega, r)|^2 . \tag{6.1}$$

Here, $E'(\omega, r)$ is the amplitude spectrum at distance $r$ from the optical axis (propagation direction), and $Z_0 \approx 377\,\Omega$ is the free-space impedance. As the pump beam incident on the emitter is a collimated Gaussian beam with diameter $2b$ (full width at half intensity maximum), the THz beam, collimated directly behind the emitter, is also Gaussian. Therefore, we assume a radial field profile of the form

$$E'(\omega, r) = E'(\omega) \exp\left(-r^2 \ln 2/b^2\right), \tag{6.2}$$

where $E'(\omega)$ is the complex-valued Fourier amplitude measured on the optical axis. After integrating Eq. 6.1, we find

$$W = \pi b^2 (2Z_0 \ln 2)^{-1} \int_{-\infty}^{\infty} \mathrm{d}\omega\, |E'(\omega)|^2 . \tag{6.3}$$

Note that in our experiment, we sample the THz electric field $E(\omega)$ which results from focusing of the collimated beam with on-axis field $E'(\omega)$ (see Fig. 6.2b). The two fields are related by

$$E(\omega) = E'(\omega)\, b^2 \omega \ln 2/2\mathrm{i}cf, \tag{6.4}$$

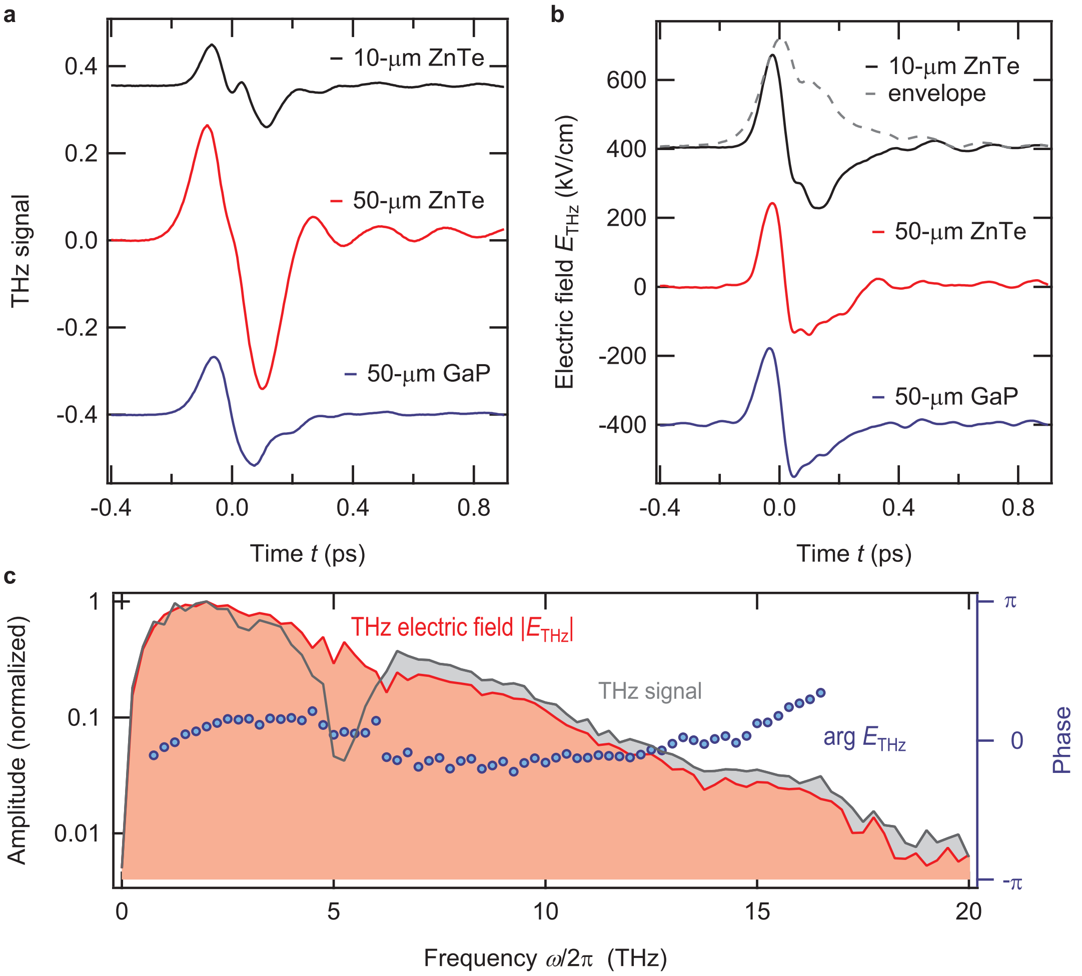

**Figure 6.4.: Terahertz-electric-field extraction.** **a**, Electro-optic signals of the spintronic THz emitter as recorded with three different detection crystals (10-µm ZnTe, 50-µm ZnTe, and 50-µm GaP) in a dry nitrogen atmosphere. **b**, Resulting THz electric fields at the detector position obtained by deconvolving the detector response function. The gray dashed line is the field envelope. Curves in panels **a** and **b** are offset for clarity. **c** Spectra of signal amplitude, electric-field amplitude, and field phase as obtained with the 10-µm-thick ZnTe detector.

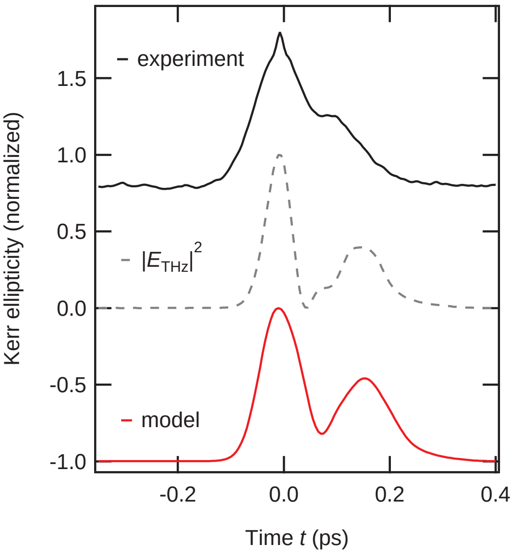

**Figure 6.5.: Terahertz Kerr effect of diamond.** Transient ellipticity (solid black) of a near-infrared probe pulse induced by a THz pump pulse generated with our STE. The squared THz electric field (dashed gray) and the simulated Kerr ellipticity (solid red) are also shown. For details of the model, see the main text. All curves are normalized to 1 and offset for clarity.

where $c$ is the vacuum speed of light and $f$ is the focal length of the parabolic mirror. Substituting Eq. 6.4 into Eq. 6.3 finally yields

$$W = 2\pi \ln 2 Z_0^{-1} c^2 f^2 b^{-2} \int_{-\infty}^{\infty} \mathrm{d}\omega \, \left| E'(\omega) \right|^2 / \omega^2. \tag{6.5}$$

Using $f = 5.1\,\mathrm{cm}$, $b = 2.4\,\mathrm{cm}$, and the measured field at the focus (see Fig. 6.4b), we find a pulse energy of 4.1 nJ, which agrees very well with the power measurements of 5.1 nJ (see Fig. 6.3b).

### Terahertz Kerr effect of diamond

To demonstrate the capability of these pulses for THz nonlinear optics, we measure the THz Kerr effect [Hof09, Cor14, Saj15] of diamond. To study this $\chi^{(3)}$-type nonlinear-optical effect (see Section 2.6.1), the p-polarized THz transient is focused into a 320-µm-thick polycrystalline diamond sample in a dry nitrogen atmosphere. We measure the transient birefringence using a co-propagating probe beam with the same pulse specifications as in EO sampling, but linearly polarized with an angle of 45° with respect to the THz-electric-field direction.

Figure 6.5 shows the induced ellipticity acquired with a moderate measurement time of 5 min. Its striking similarity to the squared THz electric field suggests the sample response to be quadratic in the THz field, that is, of $\chi^{(3)}$-type. To support this understanding, we model the Kerr-type pump-probe signal by taking the velocity mismatch between pump and probe beam into account [Saj15]. In detail, the phase difference between the two probe polarization components along and perpendicular to the THz electric field polarization is given by

$$\Delta\varphi(t) = \frac{2\pi}{\lambda_{\mathrm{pr}}} \int_0^d \mathrm{d}z \, \Delta n(t + \beta z). \tag{6.6}$$

Here, $\lambda_{\mathrm{pr}}$ is the central probe wavelength, $d$ is the sample thickness, and the change in refractive index $\Delta n$ is given by the Fourier-transform of Eq. 2.66. "The inverse velocity mismatch $\beta = \nu_{\mathrm{pr}}^{-1} + \nu_{\mathrm{THz}}^{-1}$ quantifies the temporal walk-off of pump and probe pulses per propagation length" [Saj15]. Importantly, Eq. 6.6 can be understood as a convolution with a box-like function of duration $\beta d$ and thus leads to a distortion of the measured THz transient. As seen in Fig. 6.5, we find good agreement with the measured data. Small discrepancies may originate from neglecting lensing effects due to the sharply focused THz field [Sch09], and the dispersion of diamond's THz refractive index. The THz Kerr effect observed here demonstrates the capability of the STE as a high-field THz source.

## 6.4. Conclusion and outlook

In conclusion, a large-area spintronic emitter of only 5.8-nm thickness is implemented as a high-field THz source. Excitation by 5.5-mJ optical pump pulses results in single-cycle THz pulses with a duration of only 230 fs (FWHM of the field envelope) and peak electric fields of 300 kV/cm. The capability of these THz pulses in terms of driving nonlinear effects is demonstrated by inducing a transient $\chi^{(3)}$-type response in diamond. We note that the THz-generation mechanism relies on ultrafast electron heating and should, therefore, be virtually independent of the pump wavelength. The combination of ease-of-use, versatility, and scalability makes this high-field emitter concept very interesting for THz nonlinear optics. It holds the promise for an even improved emitter performance in the near future.

We emphasize that this work is only a first step toward spintronic strong-field THz sources. Numerous improvements are anticipated, for example by optimization of the fluence and duration of the pump pulse. Finally, in terms of the emitter itself, many degrees of freedom can be tuned, including the emitter temperature, the choice of materials with large spin Hall angle [Dem16], the layer sequence, and the arrangement of cascaded emitters [Saj14].

# 7. Terahertz emission from thin-film heterostructures containing complex magnetic compounds

*The last two Chapters showed that THz-emission spectroscopy of ultrathin multilayers of magnetic and heavy metals provides fundamental insights into photo-induced spin transport and SOI at highest frequencies. Notably, it has also paved the way toward applications such as efficient and ultrabroadband emitters of THz electromagnetic radiation.*

*So far, predominantly standard ferromagnetic materials have been exploited in THz-emission spectroscopy from metallic heterostructures (see Fig. 5.3b). Here, by introducing a suitable figure of merit, we systematically compare the strength of THz emission from X/Pt bilayers with X being a complex ferro-, ferri-, and antiferromagnetic metal, that is, dysprosium cobalt (*$DyCo_5$*), gadolinium iron (*$Gd_{24}Fe_{76}$*), magnetite (*$Fe_3O_4$*), and iron rhodium (FeRh). Employing optical pump pulses centered at a photon energy of 1.6 eV, we find that the performance in terms of spin-current generation not only depends on the spin polarization of the magnet's conduction electrons but might also be influenced by the specific interface conditions, thereby suggesting THz-emission spectroscopy to be a highly interface-sensitive technique. Eventually, we present preliminary results employing pump pulses centered at 30 THz (0.12 eV), which indicate that excited electrons near the Fermi energy are important for the THz-emission process. In general, our results are relevant for all applications that rely on the optical generation of ultrafast spin currents in spintronic metallic multilayers.*

Parts of this Chapter have been published in [Sei17c].

## 7.1. Motivation

Exploiting the electron's spin degree of freedom is envisioned to be of crucial importance for future information technology [Wol01]. In spintronic devices, the building blocks are related to the efficient generation, conduction, and detection of spin currents. New fundamental effects are currently in the focus of spintronics research, for instance the spin-dependent Seebeck effect (SDSE) [Uch08], the spin Seebeck effect (SSE) [Uch10], and the inverse spin Hall effect (ISHE) [Wun05]. On one hand, the

SDSE/SSE describes, respectively, the generation of a spin current carried by conduction electrons/magnons along a temperature gradient in a magnetically-ordered solid (see Section 2.5.2). On the other hand, spin-current detection can be accomplished by the ISHE which transforms a spin current into a transverse charge current in materials with strong SOI (see Section 2.5.1).

A promising approach for characterizing materials relevant for spintronic applications is THz spectroscopy [Gan06] and, in particular, THz-emission spectroscopy (TES). As shown in Chapter 5 and in Ref. [Kam13a], upon illumination of ferromagnetic (FM)/ nonmagnetic (NM) heterostructures with femtosecond near-infrared laser pulses, a combination of the SDSE and the subsequent ISHE gives rise to the emission of electromagnetic radiation with frequencies extending into the THz range (see Chapter 5).

Besides such material-science-driven interest, spintronic heterostructures also show a large potential as efficient and broadband THz emitters. So far, standard FM materials have predominantly been explored with TES of FM/NM heterostructures, that is, Ni, Co, Fe, and binary alloys thereof (see Chapter 5 and Refs. [Yan16, Hui16b, Hui17a, Wu17]). However, a relatively straightforward access to a much larger variety of magnetic materials is provided by TES.

Here, we explore several complex metallic compounds in terms of their THz-emission response following femtosecond laser excitation of FM/Pt bilayers. Guided by a simple model of THz emission, our comparative study is performed under conditions that allow for fair comparison of the FM materials. We provide a theory that highlights the key parameters for THz emission from FM/NM bilayers (e. g. impact of thickness, conductivity, spin Hall angle). The studied magnetic compounds exhibit distinct types of magnetic ordering: ferrimagnetic magnetite ($Fe_3O_4$), (anti-) ferromagnetic iron rhodium (FeRh), and the ferrimagnetic alloys dysprosium cobalt ($DyCo_5$) and gadolinium iron ($Gd_{24}Fe_{76}$). Finally, preliminary results are presented focusing on the driving mechanism of the ultrafast SDSE spin current. To this end, we trigger the THz emission with drastically reduced photon energies, providing evidence for a scenario based on ultrafast heating.

## 7.2. Experimental details

**Principle.** A schematic of TES of magnetic heterostructures and the details on the experimental setup are provided in Chapter 5 and Section 3.4.

The emitted THz electric field directly behind the sample can straightforwardly be calculated in the limit of thin metal films (total metal thickness $d$ negligible compared to the attenuation length and wavelength of the THz field inside the metal). In the frequency domain, we obtain for the THz electric field per incident fluence (see Chapter 5 and Section 2.6.2)

$$E^0_{\mathrm{THz}}(\omega) = C(\omega) \cdot e j^0_{\mathrm{s}}(\omega) \gamma \lambda_{\mathrm{rel}}, \tag{7.1}$$

where $e$ is the elementary charge, $j_{\mathrm{s}}^{0}$ is the spin current density injected into the NM layer (measured directly behind the FM/NM interface and normalized to the incident pump excitation density, i. e. having the unit A m/J), and $\gamma$ and $\lambda_{\mathrm{rel}}$ are the spin Hall angle and relaxation length of the THz spin current within the NM layer, respectively. The function

$$C(\omega)=\frac{A/d}{\left(n_1+n_2\right)/Z_0+\int_0^d \mathrm{d}z\,\sigma(\omega,z)} \tag{7.2}$$

quantifies how efficiently pump and THz radiation are, respectively, coupled into and out of the metal stack. $C$ summarizes all sample parameters unrelated to spintronic properties. In Eq. 7.2, $A$ is the (unit-free) fraction of the pump-pulse energy absorbed by the stack having thickness $d$, $n_1$ and $n_2$ are the refractive indices of air and the substrate, respectively, $Z_0 = 377\,\Omega$ is the vacuum impedance, and $\sigma$ is the metal conductivity at THz frequencies. As shown below, $C(\omega)$ depends on frequency only weakly and can approximately be considered as a constant.

It is important to note that $j_{\mathrm{s}}^{0}$ includes spin currents generated by the SDSE as well as a spin-dependent FM/NM-interface transmission amplitude, which may depend on sample preparation details. In the derivation of Eq. 7.1, multiple reflections of the spin current inside the NM layer are neglected since all Pt-layer thicknesses throughout this work are well above the relaxation length $\lambda_{\mathrm{rel}}$ of Pt (~1 nm) (see Chapter 5). The linear scaling of the THz electric field with the absorbed pump power in connection with Eq. 7.1 reflects the second-order nonlinearity of the spin-current-generation process.

Maximizing the performance of the THz emitter thus requires the optimization of the material parameters. As seen in Chapter 5, Pt with a thickness of about 3 nm is the best choice for the NM material. Here, we focus on the variation of the FM material which has a direct impact on the magnitude of $j_{\mathrm{s}}^{0}$ and $C$ (through $A$ and $\sigma$). To quantify the efficiency of a magnetic material X in injecting a spin current into the adjacent Pt layer in a X/Pt bilayer, we introduce a figure of merit (FOM) that compares the spin current $j_{\mathrm{s,X}}^{0}$ flowing across a X/Pt bilayer to that of a CoFeB/Pt reference sample. The FOM is calculated according to

$$\mathrm{FOM}_{\mathrm{X}}=\frac{\left\|j_{\mathrm{s,X}}^{0}\right\|}{\left\|j_{\mathrm{s,ref}}^{0}\right\|}=\frac{\left\|S_{\mathrm{X}}\right\|/C_{\mathrm{X}}}{\left\|S_{\mathrm{ref}}\right\|/C_{\mathrm{ref}}}, \tag{7.3}$$

where $\|S\|$ denotes the maximum magnitude of the measured THz-signal waveform $S(t)$. We choose CoFeB as the reference ferromagnet because it features the highest THz-emission performance among Ni, Co, Fe, and their binary alloys (see Chapter 5).

To summarize, our macroscopic model of the THz-emission amplitude (Eqs. 7.1, 7.2 and 7.3) allows us to perform a systematic comparison of different magnetic materials X and to disentangle the crucial material parameters to obtain maximum THz emission.

**Experimental setup.** The THz-emission spectrometer driven by a MHz laser oscillator is outlined in Section 3.1. Note that some samples (see Table 7.1) have an unpolished substrate backside and are, therefore, studied in reflection geometry under a pump-beam angle of incidence of 45°.

The sample magnetization is saturated in the film plane by means of two permanent magnets. For measurements in transmission and reflection geometry, we apply a magnetic field of $\pm 70\,\mathrm{mT}$ and $\pm 100\,\mathrm{mT}$, respectively. By switching between opposite magnetization directions, the contribution odd in the sample magnetization can be extracted. For the samples studied here, the contribution even in the magnetization is typically one order of magnitude smaller and is neglected throughout this article. The temperature of the sample is varied by thermal contact with a massive metal block that is either cooled by a liquid nitrogen reservoir or heated by a resistive coil attached to it. To avoid water condensation, we apply a steady flow of gaseous nitrogen directed onto the sample surface. During temperature-dependent measurements, a magnetic field of $40\,\mathrm{mT}$ is applied.

The absorptance of the near-infrared pump pulse is determined by measuring the power reflected by and transmitted through the sample. To determine the THz conductivity of the thin film, we perform THz transmission measurements (see Sections 2.6.2 and 3.4, and Ref. [Duv96]), referenced to a part of the substrate free of any sample material. All THz measurements are conducted in a dry nitrogen atmosphere.

**Samples details.** The studied samples consist of two or three metal layers. The bilayer structure is X/Pt with X being the magnetic compound, while Pt is chosen as the nonmagnetic layer because of its large spin Hall angle. The trilayer structure is Pt/X/Pt which allows for a consistency check of our theoretical model (see Chapter 5). An overview of all samples used for THz-emission measurements is given in Table 7.1. Details on sample fabrication are described in the following.

**Beijing: FeRh.** The FeRh samples were prepared and characterized by M. A. W. Schoen[1], X. Z. Chen[2], H. S. Körner[1], C. Back[1] and C. Song[2] ([1]Institute for Experimental and Applied Physics, University of Regensburg, 93053 Regensburg, Germany; [2]Key Laboratory of Advanced Materials, School of Materials Science and Engineering, Tsinghua University, 100084 Beijing, China). The FeRh film is grown on a (001)-oriented single crystal MgO substrate using DC magnetron sputtering. The base pressure of the chamber is $2 \cdot 10^{-5}\,\mathrm{Pa}$. The substrate is kept at $573\,\mathrm{K}$ for $30\,\mathrm{min}$. Then, FeRh (thickness of $10\,\mathrm{nm}$) is deposited at an Ar pressure of $0.7\,\mathrm{Pa}$, corresponding to a stoichiometric $Fe_{51}Rh_{49}$ film. The sputtering power is $30\,\mathrm{W}$ for 3-inch-diameter $Fe_{50}Rh_{50}$ targets. Afterwards, the film is heated to $1023\,\mathrm{K}$ and annealed for $100\,\mathrm{min}$. When the film has cooled down to room temperature, it is capped with $5\,\mathrm{nm}$ Pt in situ [Jia16a].

**Helmholtz-Zentrum Berlin: $DyCo_5$ and $Gd_{24}Fe_{76}$.** The $Gd_{24}Fe_{76}$ and $DyCo_5$ samples were prepared and characterized by F. Radu and I. Radu (Institute for Optics and Atomic Physics, Technical University Berlin and Helmholtz-Zentrum Berlin für Materialien und Energie, Berlin, Germany). Thin films (thickness of 3 nm) of ferrimagnetic amorphous $Gd_{24}Fe_{76}$ and polycrystalline $DyCo_5$ alloys are grown by magnetron sputtering on $(11\bar{2}0)$-oriented single-crystal $Al_2O_3$ substrates at room temperature in an ultra-clean Ar atmosphere of $1.5 \cdot 10^{-3}$ mbar pressure. Pt films (thickness of 3 nm) are used as a capping layer. Alternatively, samples with both Pt capping and buffer layers (thickness of 3 nm) are grown. The stoichiometry of the ferrimagnetic alloy is controlled by varying the deposition rate of the separate elemental targets during the co-sputtering process [Rad12]. These samples were prepared and characterized by F. Radu and I. Radu (Institute for Optics and Atomic Physics, Technical University Berlin and Helmholtz-Zentrum Berlin für Materialien und Energie, Berlin, Germany).

**Zaragoza: $Fe_3O_4$.** The $Fe_3O_4$ samples were prepared and characterized by I. Lucas[1], R. Ramos[2], M. H. Aguirre[3], P. A. Algarabel[4], A. Anadón[3], M. R. Ibarra[1], L. Morellón[1], E. Saitoh[2] and K. Uchida[5] ([1]Instituto de Nanociencia de Aragón, Universidad de Zaragoza, E-50018 Zaragoza, Spain; [2]WPI Advanced Institute for Materials Research, Tohoku University, 980-8577 Sendai, Japan; [3]Departamento de Física de la Materia Condensada, Universidad de Zaragoza, 50009 Zaragoza, Spain; [4]Instituto de Ciencia de Materiales de Aragón, Universidad de Zaragoza and Consejo, Superior de Investigaciones Científicas, E-50009 Zaragoza, Spain; [5]National Institute for Materials Science, 305-0047 Tsukuba, Japan). The $Fe_3O_4$ film (thickness of 24 nm) is grown on a (001)-oriented MgO substrate by pulsed-laser deposition using a KrF excimer laser (wavelength of 248 nm, repetition rate of 10 Hz, irradiance of $3 \cdot 10^9\,\mathrm{W/cm^2}$) in an ultrahigh-vacuum (UHV) chamber. The Pt film (thickness of 8 nm) is deposited in the same UHV chamber by DC magnetron sputtering without breaking the vacuum. Further details on the growth can be found in Ref. [Orn10]. The film thickness is measured by x-ray reflectivity. The structural quality is confirmed by x-ray diffraction and transmission electron microscopy. The film cross sections are prepared by a focused ion beam and measured by high-angle annular dark-field scanning transmission electron microscopy. The measurements are carried out in a probe-aberration corrected FEI Titan 60-300 operated at 300 kV.

**Greifswald: CoFeB.** The $Co_{20}Fe_{60}B_{20}$ samples were prepared and characterized by U. Martens, J. Walowski and M. Münzenberg (Institute of Physics, Ernst Moritz Arndt University, 17489 Greifswald, Germany). The samples are deposited on substrates of glass with a surface roughness $< 1$ nm and on (100)-oriented MgO, both with the dimensions $10 \times 10 \times 0.5\,\mathrm{mm}^3$. The amorphous CoFeB layers are fabricated by magnetron sputtering from a nominal target composition of $Co_{20}Fe_{60}B_{20}$. A detailed analysis yields a cobalt-iron ratio of 32:68. The Pt films on top are deposited using electron-beam evaporation under UHV conditions with a base pressure of $5 \cdot 10^{-10}$ mbar after the sputtering procedure without breaking the vacuum. All substrates are kept at room temperature during the deposition.

| # | Sample structure | Prepared in | AOI (°) | $A$ | $C$ ($10^9$ Ω/m) | FOM |
|---|---|---|---|---|---|---|
| 1 | Sapphire//$DyCo_5$(3)/Pt(3) | Berlin | 0 | 0.56 | 3.5 | 0.85 |
| 2 | Sapphire//$Gd_{24}Fe_{76}$(3)/Pt(3) | Berlin | 0 | 0.52 | 3.0 | 0.79 |
| 3 | Sapphire//Pt(3)/$DyCo_5$(3)/Pt(3) | Berlin | 0 | 0.56 | 1.5 | - |
| 4 | Sapphire//Pt(3)/$Gd_{24}Fe_{76}$(3)/Pt(3) | Berlin | 0 | 0.53 | 1.3 | - |
| 5 | Glass//CoFeB(3)/Pt(3) | Greifswald | 0 | 0.57 | 3.5 | 1.00 |
| 6 | MgO//$Fe_3O_4$(24)/Pt(8) | Zaragoza | 45 | 0.44 | 2.7 | 0.09 |
| 7 | MgO//CoFeB(25)/Pt(5) | Greifswald | 45 | 0.52 | 2.5 | 1.00 |
| 8 | MgO//$Fe_{51}Rh_{49}$(10)/Pt(5) | Beijing | 45 | 0.60 | 1.0 | 0.28 |
| 9 | Glass//CoFeB(10)/Pt(2) | Greifswald | 45 | 0.47 | 1.2 | 1.00 |
| 10 | Glass//CoFeB(20)/Pt(2) | Greifswald | 45 | 0.46 | 0.5 | 1.00 |

**Table 7.1.: Overview of samples used for terahertz emission measurements.** Sample structure including location of preparation. Also given are the pump-beam angle of incidence (AOI), absorptance $A$ of the near-infrared pump light, the coupling function $C$ (calculated at a frequency of 1 THz; see Eq. 7.2) and the figure of merit (FOM; see Eq. 7.3). In the column "Sample structure", the numbers in brackets indicate the film thickness in nm. The substrate thickness of MgO, sapphire, and glass is 500 µm.

To evaluate each FM material's capability to emit a spin current into an adjacent NM layer according to Eq. 7.3, for each of the three sample groups (see Table 7.1) a suitable CoFeB/Pt reference sample of similar structure is fabricated. These reference samples have coupling functions $C$ (see Eq. 7.2 and Table 7.1) comparable to those of their counterparts containing complex magnetic compounds.

## 7.3. Results and discussion

### $DyCo_5$ and $Gd_{24}Fe_{76}$

Metallic ferrimagnetic alloys consisting of rare-earth (RM) and transition metal (TM) elements, such as $DyCo_5$ and $Gd_{24}Fe_{76}$, have been among the first magnetic media used for high-density magneto-optical recording [Gre89]. Because of their strong perpendicular magnetic anisotropy, tunable magnetic properties, large magneto-optical effects, and enlarged signal-to-noise ratios in magneto-optical detection (due to their amorphous state), they found applications as the first magnetic re-writable memories. More recently, the all-optical magnetization switching phenomenon (i. e. purely laser-driven spin switching in the absence of an external magnetic field) has been discovered on these ferrimagnets [Sta07, Rad11, Man14],

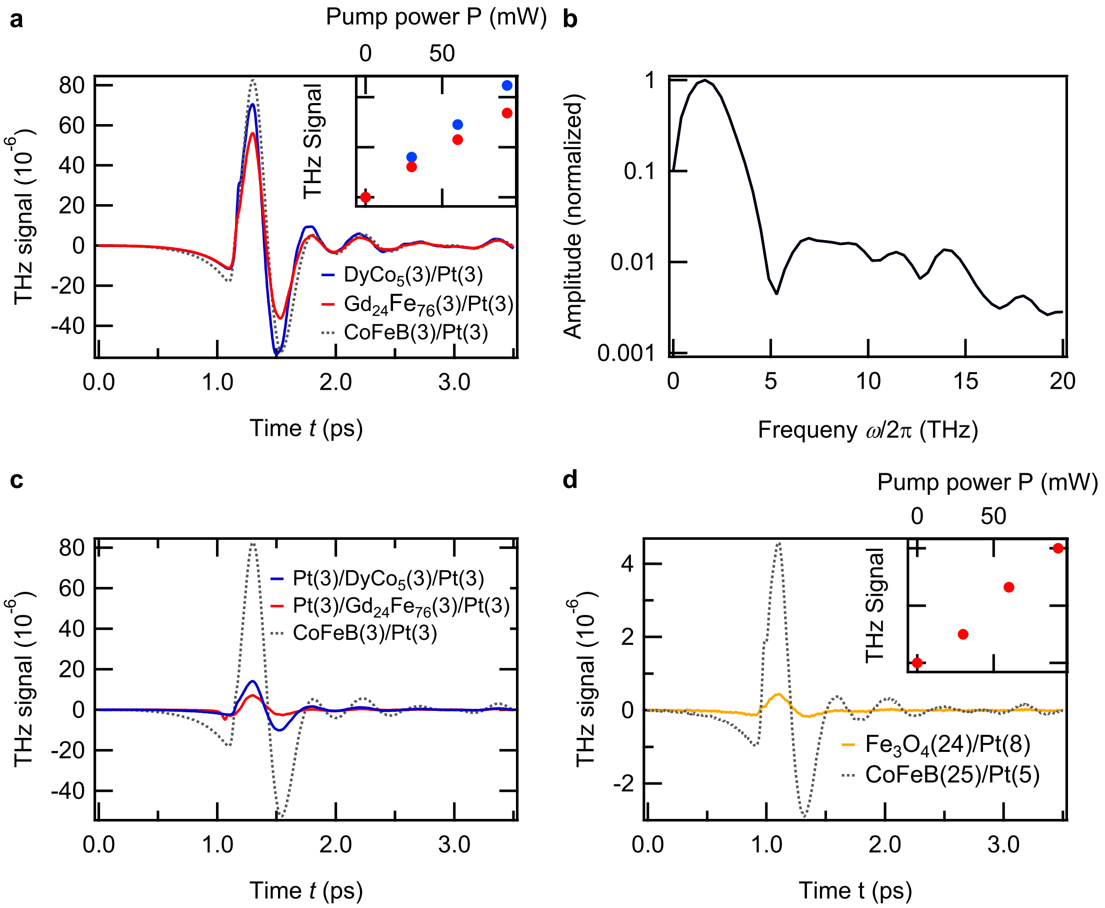

**Figure 7.1.: THz emission from complex magnetic compounds**. Raw data comparing the THz emission (odd in sample magnetization) from magnetic heterostructures containing **a**, **b**, $DyCo_5$ and $Gd_{24}Fe_{76}$, **c**, symmetric trilayer structures and **d**, $Fe_3O_4$. The dashed line of each panel shows emission from a CoFeB/Pt reference bilayer with similar structure. **Insets**: Pump-power dependence of the respective THz signal (root mean square, RMS). The amplitude spectrum of the waveform emitted by the bilayer containing $DyCo_5$ is shown in panel **b**.

which has brought this class of RM-TM alloys into the focus of ultrafast magnetic studies over the last years [Kir10].

Figure 7.1 shows typical THz waveforms emitted from magnetic heterostructures containing $DyCo_5$ and $Gd_{24}Fe_{76}$ (Panels a, b, and c). For comparison, we also show the THz waveform from the CoFeB/Pt reference sample that has a similar thickness (dashed lines in Figs. 7.1a and c, for sample details see Table 7.1). For all these samples, we observe similar temporal dynamics of the THz-signal waveform and a linear pump-power dependence (see Inset of Fig. 7.1a), as expected for a second-order nonlinear process. Fourier-transformation of the emitted waveform from the bilayer containing $DyCo_5$ yields the complex-valued spectrum whose amplitude is shown in Fig. 7.1b. We note that the bandwidth of about 3 THz is limited by the 1-mm-thick ZnTe detection crystal used for electro-optic sampling (see Fig. 3.7).

The DC conductivities $\sigma_{\mathrm{DC}}$ (see Eq. 2.62) as determined by THz transmission spectroscopy (see Sections 3.4, 2.6.2, and Ref. [Gri90]) are $3.1 \cdot 10^5\,\mathrm{S/m}$ for $\mathrm{DyCo_5}$, $9 \cdot 10^5\,\mathrm{S/m}$ for $\mathrm{Gd_{24}Fe_{76}}$, $13.5 \cdot 10^5\,\mathrm{S/m}$ for CoFeB, and $50.5 \cdot 10^5\,\mathrm{S/m}$ for Pt. These values are approximately constant up to 10 THz. Thus, we find an almost frequency-independent and similar coupling function $C$ for samples containing $\mathrm{DyCo_5}$, $\mathrm{Gd_{24}Fe_{76}}$, and the respective reference (compare with Table 7.1). This fact enables direct comparison of the raw data in Figs. 7.1a and c.

We observe that the heterostructure containing $\mathrm{DyCo_5}$ shows similar THz emission and, thus, magnitude of $j_{\mathrm{s}}^0$ as the reference ferromagnetic CoFeB/Pt sample. This result is remarkable given the reduced net magnetization due to the ferrimagnetic order of $\mathrm{DyCo_5}$. In contrast, $\mathrm{Gd_{24}Fe_{76}}$-capped heterostructure shows reduced performance as spin ejector compared to CoFeB/Pt layers. In terms of the FOMs, we find 0.85 for $\mathrm{DyCo_5}$ and 0.79 for $\mathrm{Gd_{24}Fe_{76}}$ (compare with Eq. 7.3 and Table 7.1).

Such lowered performance could arise from a reduced spin polarization of conduction electrons which are believed to play a key role in the spin-current generation. Although no published data on the spin polarization for $\mathrm{DyCo_5}$ and $\mathrm{Gd_{24}Fe_{76}}$ are available, we estimate it to be about 40 % and 36 %, respectively, based on Eq. (S1) in the supplementary information of Ref. [Pal09]. Note that this estimation neglects any contribution from 5d electrons. These spin-polarization values are lower than the reported values for CoFeB (~65 %) and could thus explain the observed differences in terms of spin-current emission [Man12].

This reasoning is further supported by the relatively low Curie temperature of 550 K for $\mathrm{Gd_{24}Fe_{76}}$ as compared to 925 K for $\mathrm{DyCo_5}$ (Ref. [Tsu83]). At room temperature, the lower critical temperature might lead to a reduction of the relative spin polarization of the conduction electrons and, in turn, to a reduced spin current. This effect can be enhanced by accumulative heating of the sample region at the laser focus by the train of pump pulses (repetition rate is 80 MHz).

**Symmetric trilayers.** As a check of the sample quality, we also conducted measurements on samples having the symmetric structure Pt/X/Pt, in which the FM layer X=$\mathrm{DyCo_5}$ or $\mathrm{Gd_{24}Fe_{76}}$ is embedded between two Pt layers of nominally identical thickness (see Table 7.1). As seen in Fig. 7.1c, the THz-emission measurements on the symmetric trilayers yield a THz-signal amplitude about one order of magnitude lower than for the respective bilayers. This behavior can be understood based on our picture of the microscopic mechanism underlying the THz emission from magnetic heterostructures (see Chapter 5). Since the pump field is homogeneous throughout the thickness of the thin-film sample, the backward- and forward-directed spin currents injected into the back and front Pt layer generate transverse charge currents that cancel each other. Consequently, the resulting THz emission is quenched, consistent with our experimental observation and indicating a high sample quality. The small residual emission may originate from a slight sample asymmetry, for example due to slightly different Pt film thicknesses or higher strain closer to the substrate.

### $Fe_3O_4$

Magnetite ($Fe_3O_4$) is one of the strongest naturally occurring ferrimagnets and shows a Verwey transition at a temperature of typically 120 K [Ver41]. The spin polarization at the Fermi energy is predicted to be close to unity [Yan84], which makes this material promising for spintronic applications.

The $Fe_3O_4$ sample shows a THz emission that is about 10 times smaller than from the CoFeB/Pt reference (Fig. 7.1d). The THz-signal amplitude again depends linearly on the pump power as seen from the Inset of Fig. 7.1d and the THz waveform shows similar temporal dynamics as the reference. Magnetite's DC conductivity of about $0.1 \cdot 10^5$ S/m [Pim05] is about two orders of magnitude lower than that of CoFeB. However, due to a different NM/FM-layer-thickness ratio of the magnetite sample, the coupling function $C$ has a magnitude similar to that of the reference sample (see Table 7.1). Note that any inhomogeneity in the excitation density across the metal stack is expected to be balanced out within a few tens of femtoseconds due to electron transport [Hoh00]. We extract a FOM for $Fe_3O_4$ of 0.09 with respect to CoFeB (see Eq. 7.3 and Table 7.1).

The low efficiency of spin current emission of $Fe_3O_4$ into Pt cannot straightforwardly be understood in terms of its spin polarization since $Fe_3O_4$ is believed to be a half-metal with reported experimental spin polarization values [Wan13] of about 72 %, which is larger than that of CoFeB (~65 %) [Man14]. In particular, the spin polarization is a function of the electron energy and depends on the gap size of the minority spin channel. Nonetheless, it is well known that magnetite's room-temperature conductivity is governed by electron hopping [Zie00, Ram08] and much lower than for CoFeB. On one hand, this conduction mechanism could diminish the SDSE contribution to the spin current and so could affect the efficiency of spin current emission into an adjacent Pt layer, in agreement with previous spin pumping experiments [Cze11]. On the other hand, the SSE contribution to the spin current is believed to be much weaker than the SDSE in general, as indicated by measurements in bilayers containing an FM insulator (see Chapter 8).

### FeRh

Iron rhodium is a remarkable material as it exhibits a transition from an antiferromagnetic (AFM) to a FM phase at a temperature that is strongly depending on the exact composition and sample preparation [Swa84, Jia16b]. This feature makes FeRh a promising candidate for heat-assisted magnetic recording, which benefits from the inherent magnetic stability of the AFM ordering [Sai16].

Figure 7.2 shows temperature-dependent THz-emission data from an FeRh sample (15 nm total metal-film thickness) in comparison to two CoFeB/Pt reference samples (12 and 22 nm total metal-film thicknesses). For all these samples, we again observe similar temporal dynamics of the emitted THz waveform. We find that the

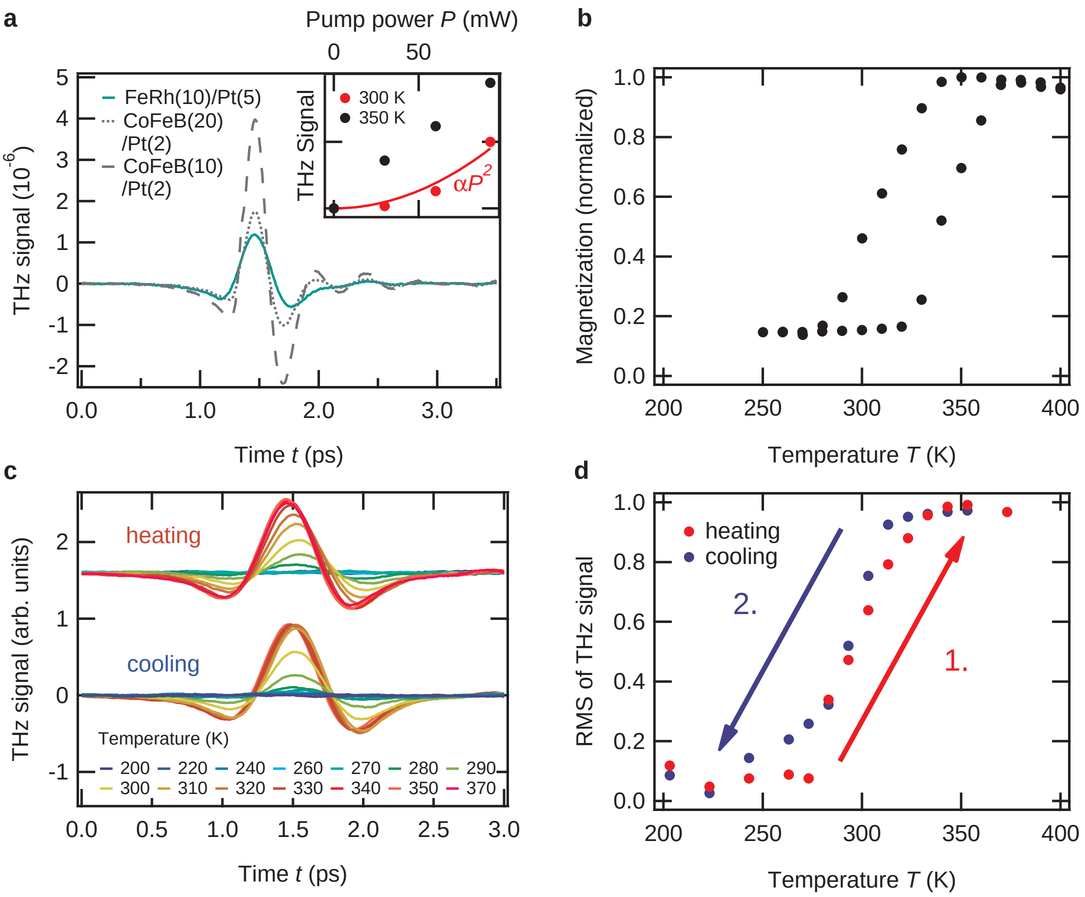

**Figure 7.2.: Temperature-dependent terahertz emission from FeRh/Pt.** **a**, Raw data comparing the THz emission (odd in sample magnetization) at room temperature from a magnetic heterostructure containing FeRh with two CoFeB/Pt bilayers having similar thicknesses (dashed lines). **Inset**: Pump-power dependence of the THz signal (RMS) at room temperature (red dots) together with a quadratic fit (solid red line) and at 350 K (black dots). **b**, Temperature dependence of the sample bulk magnetization measured by a superconducting quantum interference device. **c**, Dependence of the THz emission on sample temperature below and above the antiferromagnet-to-ferromagnet transition temperature. **d**, Temperature dependence of the root mean square (RMS) of the THz signal.

FeRh sample has a lower THz-emission performance than both CoFeB/Pt reference samples at room temperature (Fig. 7.2a).

Remarkably, the emitted THz signal scales quadratically with the pump power at 300 K (see Inset of Fig. 7.2a), whereas it scales linearly at an elevated temperature of 350 K. From measurements employing a superconducting quantum interference device (SQUID), we find that the studied FeRh sample undergoes a transition from an antiferromagnetically to a ferromagnetically-ordered state at ~320 K (see Fig. 7.2b). Therefore, the distinct pump-power dependencies might be due to the mixed AFM/FM state of the FeRh sample just above room temperature. In this regime, the magnetization and, thus, spin polarization scales roughly linearly with temperature. Therefore, the pump pulse plays a two-fold role: it not only heats the electrons transiently (linear absorption) but it also increases the sample temperature statically via accumulative heating by many pump pulses. This double action explains the observed quadratic pump-power scaling at room temperature. Note that any significant contribution of a single laser pulse to driving the phase transition is unlikely because the pump-pulse fluence (about $0.1\,\mathrm{mJ/cm^2}$) is ten times smaller than the critical fluence found in previous pump-probe works on comparable samples [Qui12].

From the DC conductivity of FeRh ($3.3 \cdot 10^5\,\mathrm{S/m}$, Ref. [Kou62]), we deduce a coupling function $C$ comparable to that of the 12-nm-thick CoFeB/Pt reference sample, whereas $C$ is twice as large as for the 22-nm-thick reference sample (see Eq. 7.2 and Table 7.1). Since even the 22- nm-thick CoFeB/Pt sample shows higher THz-emission efficiency than the FeRh film (despite its lower coupling function $C$), we conclude that FeRh is a less efficient spin-current emitter than CoFeB at room temperature and for the applied pump fluence. This notion is bolstered by the calculated FOM of 0.28 for FeRh relative to the reference samples (see Eq. 7.3 and Table 7.1). However, the pump-power dependence of the THz-signal amplitude at elevated temperatures (see Inset of Fig. 7.2a) suggests a two-fold enhancement of the THz-signal amplitude, potentially approaching the performance of CoFeB, at significantly higher pump powers than utilized in this study. It is noteworthy that the two reference samples exhibit identical FOMs despite their different thickness, thereby demonstrating the robustness of our evaluation method.

We also perform temperature-dependent THz-emission measurements on FeRh (see Figs. 7.2c and d). As shown in Fig. 7.2c, we observe a complete quenching of the THz-emission signal upon cooling the sample below 250 K. When the sample is subsequently heated back to room temperature and above, the THz signal completely recovers. The temperature dependence of the root mean square of the THz signal is displayed in Fig. 7.2d, demonstrating the reversibility of the AFM/FM phase transition. Note that the temperature range in our experiment should suffice to fully set the FeRh into the AFM and FM state, respectively [see SQUID measurements in Fig. 7.2b; conducted and evaluated by H. S. Körner (Institute for Experimental and Applied Physics, University of Regensburg, 93053 Regensburg, Germany)].

Interestingly and in contrast to the SQUID measurements, we do not observe a clear hysteretic behavior in our THz data. A similar phenomenon has been observed in previous experiments [Ino08, Suz15]. Instead, the THz-signal amplitude rather seems to follow the cooling branch of the SQUID hysteresis with indications of a small hysteretic behavior at the kink regions (around 270 and 310 K).

We note that the nominal temperatures in Figs. 7.2a, c, and d refer to the substrate temperature and not to the actual sample temperature at the focus of the laser beam which is increased due to accumulative pump heating. Based on the pump-power dependence and the SQUID data, we estimate this temperature discrepancy to be below 20 K. However, such accumulative heating of the sample would just lead to a rigid shift of the equilibrium hysteresis loop (Fig. 7.2b) along the temperature axis, in contrast to the temperature dependence of the THz-signal amplitude observed here (Fig. 7.2d).

On the other hand, a single pump pulse transiently increases the electronic temperature by several 100 K. Thus, a second potential explanation for the distinct temperature hysteresis is that the pump pulses transiently lower the magnetic domain-nucleation energy barrier, thereby shrinking the THz temperature hysteresis close to the critical temperature. This notion is bolstered by the experimentally observed small hysteretic behavior in the kink regions further away from the critical temperature, where the nucleation energy barrier could not yet be sufficiently lowered by the pump pulses [Bea98].

A third possible scenario may be related to the fact that the magnetic structure of the FeRh sheet close to the Pt interface is modified as observed in earlier studies [Jia16b, Fan10, Pre16]. Along these lines, it has been shown in Chapter 5 that the laser-induced ultrafast spin current decays within a length $\lambda_{\mathrm{rel}}$ of about 1 nm in Pt (see Eq. 7.1). We anticipate similar length scales inside the FM layer. This fact suggests that TES of magnetic heterostructures is in general more sensitive to the interfacial region between FM and NM layers than to their bulk. This interpretation is plausible because at least at 350 K, the THz signal depends quadratically on the pump field (i. e. the laser power) and must, therefore, to a significant extent arise from photo-induced THz currents flowing in regions with broken inversion symmetry (see Section 2.6.1), thus, close to the interface of the thin film studied here. Consequently, the above-mentioned differences between temperature-dependent SQUID and THz-emission measurements might be also understood in terms of an altered surface magnetism in FeRh. This notion is bolstered by the remarkable agreement with the results obtained in Ref. [Jia16b].

## 7.4. Conclusion

In conclusion, we demonstrate the feasibility of THz-emission spectroscopy in conjecture with complex magnetic metallic compounds. We introduce a figure of merit that permits direct comparison of the spin injection efficiency of different magnetic materials into an adjacent layer. This efficiency is not only relevant for the development of better spintronic THz emitters, but for all research involving ultrafast spin current injection, including spin control by the spin transfer torque [Hui16b].

We find that X=CoFeB is still the most efficient spin current emitter in X/Pt-type bilayers. The observed differences in THz-emission performance between the various magnetic materials may be understood in terms of the spin polarization at the Fermi energy for samples containing $DyCo_5$ and $Gd_{24}Fe_{76}$. However, our data on $Fe_3O_4$ indicate a crucial role of the specific conduction mechanism and the spin-dependent FM/NM interface transmission. Our results on FeRh further suggest that THz-emission spectroscopy provides additional insights into the magnetic structure of a broad range of materials compared to well-established techniques such as SQUID. Further experiments involving half-metallic or spin-gapless semiconductors may help clarify the role of (non-)thermal electrons during the THz-emission process.

Furthermore, the few-nanometer length scale over which the THz currents flow across the interface might ultimately lead to a sensitive probe of surfaces and buried interfaces. To fully explore this opportunity, future studies with a profound control of interface parameters are required.

## 7.5. Outlook

Finally, we would like to focus on the driving mechanism of the ultrafast spin-dependent Seebeck effect. So far, THz emission from all-metallic magnetic heterostructures has been believed to originate from superdiffusive spin currents induced by the distinct transport properties of highly excited majority and minority electrons [Kam13a]. This mechanism relies on the photoexcitation of the majority spins from d-like to sp-like electronic bands, split in energy by more than 1 eV [Bat10]. It is still unclear to which extent electrons at lower excitation energies, i. e. closer to the Fermi energy, contribute to the ultrafast SDSE.

Therefore, we conduct preliminary THz-emission experiments on FM/NM bilayers, in which the pump-pulse photon energy is dramatically reduced. We employ pump pulses centered at a photon energy of 120 meV (30 THz), thus 13 times less energetic than before (this Chapter, and Chapters 5 and 6). This energy is significantly below the transition energy of ~1 eV suggested by the above scenario. The 30-THz pump pulses (see Fig. 7.3a) are generated by difference frequency mixing of two infrared pulses in the nonlinear crystal gallium selenide [Mäh16] and have a pulse energy of 5 mJ [Sel08]. The sample is a $\mathrm{Co_{20}Fe_{60}B_{60}}$(3 nm)/W(3 nm) bilayer on a glass substrate (see Section 5.2 for sample preparation details), magnetized along the pump-pulse polarization direction (i. e. sample magnetization $\boldsymbol{M}||\mathrm{s}$). We discriminate the emitted p-polarized THz signal from the THz pump pulse with a wire-grid polarizer.

Figure 7.3b shows the measured THz emission which flips sign by reversing $\boldsymbol{M}$, indicating a magnetic origin. The pump-power dependence (Fig. 7.3c) is linear with indications of a saturating behavior for high powers. Preliminary comparative measurements at the same setup, using pump pulses centered at a photon energy of 1.6 eV (i. e. 375 THz) and 0.12 eV (i. e. 30 THz), reveal similar THz-generation efficiencies and similar pump-power dependencies (not shown). This suggests that the THz-emission mechanism only weakly depends on the pump photon energy.

To further support this observation, we vary the NM-layer thickness and compare the THz-emission strength for these two very distinct driving photon energies (Fig. 7.3d). Note that the measurements using optical pump pulses (centered at a photon energy of 1.6 eV) are performed at the oscillator-based THz spectrometer (see Section

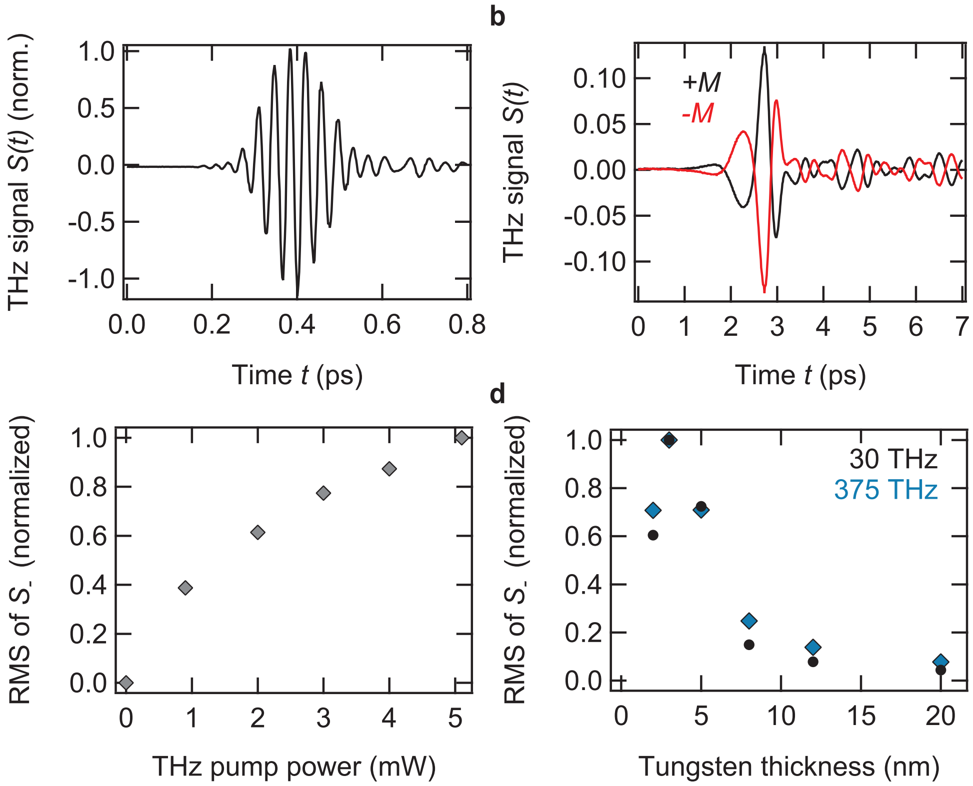

**Figure 7.3.: Spintronic terahertz emitter driven by 30-THz and 375-THz pump pulses.** **a**, THz pump pulse with a central frequency of 30 THz and a pulse energy of 5 mJ derived from difference-frequency generation in gallium selenide. **b**, Emitted THz waveform from a magnetic metallic bilayer [fused silica (500 µm)/CoFeB(3 nm)/W(3 nm)] excited from the metal side with 30-THz pulses (see **a**). The signal inverts by flipping the sample magnetization $\boldsymbol{M}$. Separation of the perpendicularly-polarized THz emission and THz pump pulses is accomplished with a wire-grid polarizer. **c**, THz-pump-power dependence of the emitted THz signal odd in magnetization (root mean square, RMS). **d**, Comparison of emitted THz signal (RMS) for a varying tungsten thickness for the THz pump pulses (see **a)** and 10-fs optical pump pulses with a central wavelength of 800 nm (corresponding to 375 THz), derived from a separate oscillator-based setup (see Section 3.1).

3.1). Remarkably, we find a qualitatively identical thickness dependence for the pump pulses centered at 30 THz and 375 THz. Since the spin-current-relaxation length is believed to strongly depend on the electron energy [Aes97], our results might indicate that electrons of similar energies contribute to the ultrafast spin current in the NM layer.

The above presented results suggest that the dominant contribution to the ultrafast spin current might not predominantly arise from highly excited electrons. They rather suggest a scenario in which electrons closer to the Fermi energy contribute significantly.

To improve the spintronic THz emitter, further insights are indispensable. At the same this will provide a better understanding of the elementary steps of the ultrafast spin-dependent Seebeck effect. Since identifying these processes is challenging, we next consider a potentially easier situation: In the following Chapter, we replace the magnetic material with an insulator and monitor the THz emission from such archetypal spin-Seebeck-effect structure.

# 8. Launching magnons at terahertz speed with the spin Seebeck effect

*Since identifying the elementary steps in the ultrafast spin-current generation in all-metallic magnetic heterostructures is challenging, we first turn to a potentially simpler situation. Therefore, we replace one of the materials in the FM/NM multilayer with an insulator. Accordingly, we will investigate the THz emission of yttrium-iron-garnet/platinum bilayers in this Chapter.*

*Transport of spin angular momentum is an essential operation in spintronic devices. In magnetic insulators, spin currents are carried by magnons and can be launched simply by heating an adjacent metal film. Here, we reveal the initial elementary steps of this spin Seebeck effect with 10-fs time resolution in prototypical bilayers of the ferrimagnet yttrium-iron garnet and platinum. Exciting the metal with an ultrashort laser pulse, the spin Seebeck current is measured all-optically using the inverse spin Hall effect and THz electro-optic sampling. It rises within ~200 fs, a hallmark of the photo-excited electrons in the metal approaching a Fermi-Dirac distribution. Model-supported analysis shows the spin Seebeck current follows the dynamics of the metal electrons quasi-instantaneously because they impinge on the interface with a correlation time of only ~4 fs and deflect the ferrimagnetic spins without inertia. Promising applications for material characterization, interface probing, spin-noise detection, and THz spin pumping emerge.*

This Chapter is based on the article “Launching magnons at terahertz speed with the spin Seebeck effect” in preparation by Seifert et al. (2017) [Sei17a].

## 8.1. Motivation

The electron spin holds an enormous potential to extend charge-based electronics into spintronics, thereby sparking novel functionalities (see Chapter 1). An important example is the transport of information carried by spin angular momentum. In contrast to charge currents, such spin currents can also flow in magnetic insulators in the form of spin waves (magnons; see Section 2.4.3). They can be launched, for instance, by simply applying temperature gradients [Bau12, Ada13, Cho13, Boo14, Chu15]. As illustrated by Fig. 8.1a, this spin Seebeck effect [Uch10] (SSE) is typically observed at the interface [Ada13, Agr14, Sch16], of a magnetic insulator (F) and a nonmagnetic metal (N) where a temperature difference $T^{\mathrm{N}} - T^{\mathrm{F}}$ induces a spin current with density [Bau12, Xia10]

$$j_{\mathrm{s}} = \mathcal{K} \cdot \left( T^{\mathrm{N}} - T^{\mathrm{F}} \right). \tag{8.1}$$

It is readily measured in the N layer through the inverse spin Hall effect (ISHE) which converts the longitudinal $\boldsymbol{j}_{\mathrm{s}}$ into a detectable transverse charge current $\boldsymbol{j}_{c}$ (Fig. 8.1a and Section 2.5.1). In the case of temperature gradients in the YIG bulk, magnon accumulation at the F/N interface can make an additional contribution not included in Eq. 8.1 [Ada13, Rez14].

Note that Eq. 8.1 presumes a static temperature difference and a frequency independent spin Seebeck coefficient $\mathcal{K}$. It is still an open question how the SSE current $j_{\mathrm{s}}$ evolves for fast temporal variations of temperature and in the presence of non-thermal states. Insights into these points are crucial to reveal the role of elementary processes such as magnon creation in F [Bar16] and spin relaxation in N [Fre17] in the formation of the SSE current. The high-frequency behavior of the SSE is also highly relevant for applications such as magnetization control by THz spin currents [Sch14, Ale17, Raz17] and spintronic THz-radiation sources (see Chapter 5 and Refs. [Wu17, Yan16]).

In previous time-resolved SSE works, a transient $T^{\mathrm{N}} - T^{\mathrm{F}}$ was induced by heating the N layer with an optical or microwave pulse [Agr14, Sch16, Bar17, Kim17]. It was shown that Eq. 8.1 remains valid on the time resolution of these experiment, from microseconds [Agr14], through to ~0.1 ns [Sch16], and even down to 1.2 ps [Kim17]. To search for the SSE speed limit, even finer time resolution is required, ultimately reaching the 10-fs scale which resolves the fastest spin dynamics in magnetic materials [Kir10].

## 8.2. Experimental details

In this work, we make a straightforward extension of the archetypal longitudinal SSE scheme to the THz regime (see Fig. 8.1). We excite the metal of yttrium iron garnet (YIG)/Pt bilayers with ultrashort laser pulses (duration of 10 fs, central photon energy of 1.6 eV, pulse energy of 3.2 nJ) from a Ti:sapphire laser oscillator (see Section 3.1). Any spin current $\boldsymbol{j}_{\mathrm{s}}(t)$ arising in the metal is expected to be converted into a charge current $\boldsymbol{j}_{\mathrm{c}}(t)$ by the ISHE (see Section 2.5.1) with a bandwidth extending into the THz range (see Chapters 5, 6 and 7). These extremely high frequencies are, however, inaccessible to electrical measurement schemes. We therefore sample the transient electric field of the concomitantly emitted electromagnetic pulse by contact-free electro-optic detection over a bandwidth of 45 THz (see Section 3.3). This technique allows us to determine the spin current $\boldsymbol{j}_{\mathrm{s}}(t)$ with a time resolution of 10 fs (see Section 3.4.2 and Ref. [Bra16b]).

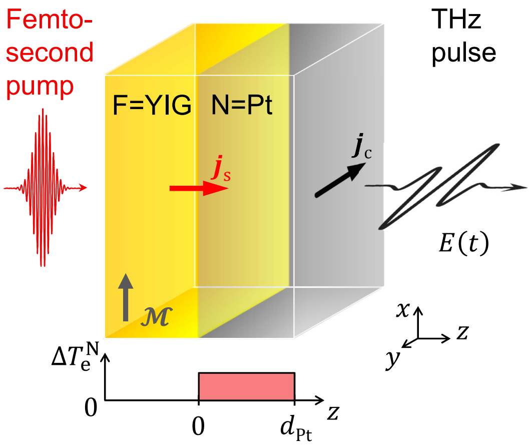

**Figure 8.1.: Experiment schematic.** To probe the ultimate speed of the spin Seebeck effect, a femtosecond laser pulse (duration of 10 fs, central photon energy of 1.6 eV) is incident on a F/N bilayer made of platinum (N=Pt, thickness of $d_\mathrm{Pt} = 5\,\mathrm{nm}$) on top of yttrium iron garnet (F=YIG, thickness of 5 µm, in-plane magnetization $\boldsymbol{M}$, and electronic band gap of 2.6 eV). While the YIG film is transparent to the pump pulse, the Pt film is excited homogeneously, resulting in a transient increase of its electronic temperature $\Delta T_\mathrm{e}^\mathrm{N}$ after thermalization. Any ultrafast spin-current density $\boldsymbol{j}_\mathrm{s}(t)$ arising in Pt is converted into a transverse charge-current density $\boldsymbol{j}_\mathrm{c}(t)$ by the inverse spin Hall effect, thereby acting as a source of a THz electromagnetic pulse whose transient electric field $E(t)$ is detected by electro-optic sampling with 10 fs time resolution.

**Sample preparation and characterization.** The YIG samples were prepared and characterized by S. Jaiswal[1], J. Cramer[1], S. Watanabe[2], C. Ciccarelli[3], J. Henrizi[1], G. Jakob[1], M. Jourdan[1] and M. Kläui[1] ([1]Institute of Physics, Johannes Gutenberg University, 55128 Mainz, Germany; [2]Department of Advanced Materials Science, School of Frontier Sciences, University of Tokyo, Chiba 277-8561, Japan; [3]Cavendish Laboratory, University of Cambridge, CB3 0HE Cambridge, United Kingdom). The YIG films (thickness of 2, 3, and 5 µm) are grown by liquid-phase epitaxy on GGG substrates (Innovent e. V., Jena, Germany). Subsequently, films of Pt, W, and MgO are grown on YIG using the Singulus Rotaris sputter deposition system. The MgO serves as a protection against oxidation for the W film. Pt and W are grown using DC magnetron sputtering whereas radio-frequency sputtering is used for MgO growth from a composite target. The deposition rates for Pt, W, and MgO are 3.1, 1.5, and 0.08 Å/s, respectively, and at pressures of 5.7, 3.5, and 1.8 µbar, respectively. Pt and Cu bilayers are grown using a home-built deposition system with DC magnetron sputtering at rates of 0.7 and 0.63 Å/s, respectively, and at pressures of 0.01 and 0.025 mbar, respectively.

We further characterize the samples characterized magneto-optically by the Faraday effect using a 512-nm laser diode under an angle of incidence of 45° (see Section 2.6.1). In this way, hysteresis loops are measured by slowly varying the external magnetic field.

**Terahertz emission setup.** In the optical experiment, the in-plane sample magnetization is saturated by an external magnetic field of 10 mT. For setting the sample temperature $T_0$ between 300 and 600 K, a resistive heating coil is attached to the sample holder onto which the sample is glued with a heat-conducting silver paste. The temperature is measured with a *type-K* thermocouple. As schematically shown in Fig. 8.1, the sample is excited by linearly- or circularly-polarized laser pulses (for details see Section 3.4) under normal incidence from the GGG/YIG side (beam diameter at sample 22 µm full width at half maximum of the intensity). If not mentioned otherwise, all measurements are performed at room temperature in a dry $N_2$ atmosphere.

**Transient reflectance.** The transient-reflectance measurements were conducted by I. Razdolski and A. Melnikov (Department of Physical Chemistry, Fritz Haber Institute of the Max Planck Society, 14195 Berlin, Germany). To conduct optical-pump reflectance-probe measurements, the beam of p-polarized laser pulses (duration of 14 fs, central wavelength of 800 nm) from a cavity-dumped Ti:sapphire oscillator (repetition rate of 1 MHz) is split into pump and probe pulses at a power ratio of 4:1. The pump fluence is on the order of $0.5\,\mathrm{mJ/cm^2}$. The pump and probe beams are incident onto the sample at angles of 45° and 50°, respectively. The pump-induced modulation of the reflected probe power is measured using a photodiode and lock-in detection.

## 8.3. Results

**Signal symmetries.** Typical THz electro-optic signals $S$ versus time $t$ for a YIG(3 µm)/Pt(5.5 nm) bilayer are displayed in Fig. 8.2a. The signal inverts when the in-plane sample magnetization $\boldsymbol{M}$ is reversed. Since the SSE current is odd in $\boldsymbol{M}$, we focus on the THz-signal difference $S_- = S(+\boldsymbol{M}) - S(-\boldsymbol{M})$ in the following.

As seen in Fig. 8.2b, the root mean square (RMS) of $S_-(t)$ grows approximately linearly with the absorbed pump fluence. Figure 8.2c shows the amplitude of $S_-$ as a function of the external magnetic field, along with the sample magnetization $\boldsymbol{M}$ measured by the magneto-optic Faraday effect. Both curves coincide. When reversing the layer sequence from F/N to N/F, $S_-(t)$ changed polarity (see Fig. 8.3a). Furthermore, the THz electric field associated with $S_-(t)$ is found to be linearly polarized and oriented perpendicular to $\boldsymbol{M}$ (see Fig. 8.3b). Also, $S_-(t)$ is independent of the pump-pulse polarization (linear and circular; not shown). These observations are in line with the scenario suggested by Fig. 8.1.

To test the relevance of the ISHE, we replaced the Pt with a W layer. The resulting $S_-(t)$ exhibits a reduced amplitude and reversed sign (Fig. 8.2d), consistent with previous ISHE works (see Ref. [Sin15] and Fig. 5.3). On bare YIG (see Fig. 8.3a) and bare Pt films, no signal $S_-(t)$ could be detected above the noise floor. These

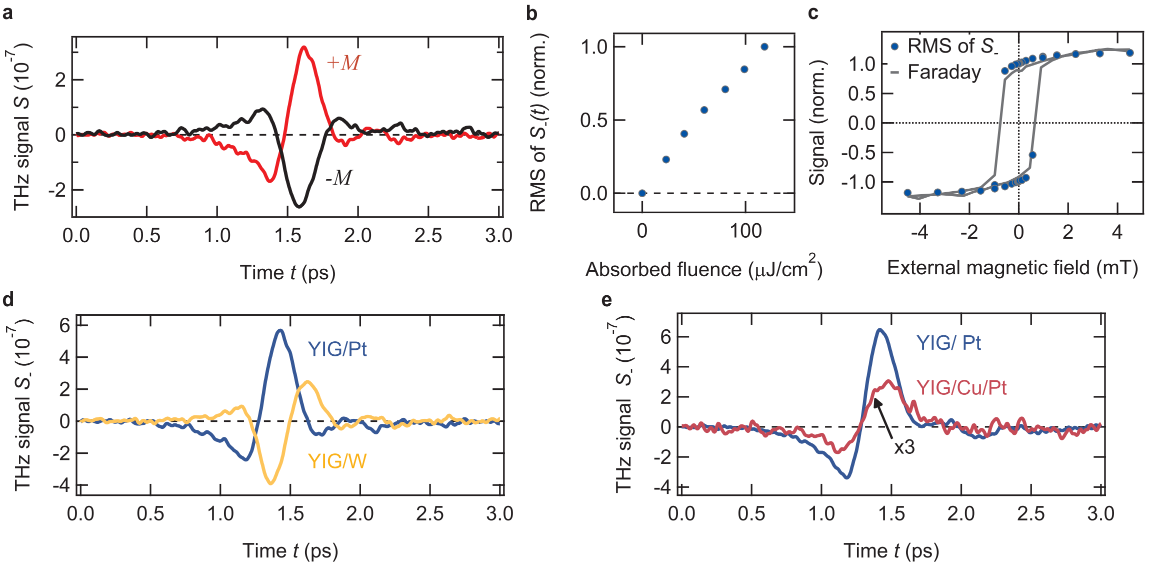

**Figure 8.2.: Terahertz emission of photo-excited F/N bilayers.** **a**, THz-emission signals $S(\pm\boldsymbol{M})$ from a YIG(3 µm)/Pt(5.5 nm) sample for opposite directions of the in-plane YIG magnetization $\boldsymbol{M}$ as a function of time $t$. We focus on the difference $S_- = S(+\boldsymbol{M}) - S(-\boldsymbol{M})$ odd in $\boldsymbol{M}$. **b**, Amplitude of $S_-$ (root-mean-square, RMS) as a function of the absorbed pump fluence. **c**, Amplitude of the THz signal $S_-$ and Faraday rotation of a continuous-wave laser beam (wavelength of 532 nm) as a function of the external magnetic field. Both hysteresis loops are measured under identical pump conditions at room temperature. **d**, THz-emission signal from a 3-µm-thick YIG film capped with platinum (Pt) and tungsten (W), both 5.5-nm thick. **e**, THz-emission signal from a 5 µm YIG film capped with 5.6 nm Pt, and with a bilayer of 1.9 nm Cu and 5.4 nm Pt.

measurements provide supporting evidence that the femtosecond pump pulse injects an ultrafast, $\boldsymbol{M}$-polarized spin current out of the plane and into the N layer where the ISHE is operative (see Fig. 8.1a).

Figure 8.2e shows that even when introducing a 1.9 nm Cu spacer layer between YIG and Pt a measurable THz signal still exists. Any (Nernst-like) contribution due to YIG-proximity-induced magnetic moments in Pt is therefore negligibly small, in agreement with previous results [Gep12, Kik13]. Likewise, a photo-spin-voltaic effect [Ell16] does not make a noticeable contribution to the THz signal. Our result is fully consistent with the picture of a heat-induced spin current flowing from cold YIG into hot Pt, traversing the Cu layer. The presence of the Cu film decreases the current amplitude due to loss [Wu17, Du14] and due to the reduced optical excitation density [Wu17]. In summary, the THz-emission signal $S_-(t)$ exhibits all characteristics expected for the SSE. We, therefore, regard the THz data of Figs. 8.2 and 8.3 as a manifestation of the SSE at THz frequencies.

**Temperature Dependence.** As the SSE current depends on the ferrimagnet's magnetization $\boldsymbol{M}$ (see Fig. 8.2c), a marked temperature dependence of the THz-emission signal is expected. Figure 8.4a displays the bulk magnetization of the YIG(3 µm)/Pt(5.5 nm) sample versus the ambient temperature $T_0$ as determined

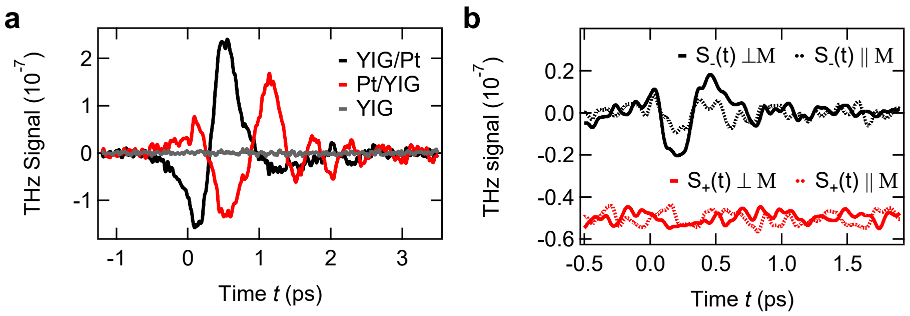

**Figure 8.3.: Terahertz-signal symmetries of photo-excited F/N bilayers.** **a**, Effect of reversing the YIG/Pt bilayer and THz emission from pure YIG. Reversing a GGG (substrate)/YIG(3 µm)/Pt(5.5 nm) sample leads to reversal of the signal $S_-(t)$ odd in the sample magnetization (red and black curves). For the reversed sample, the propagation of the THz pulse through the GGG substrate leads to significant distortion of the THz signal. To correct for the different dispersion of the GGG substrate for THz and optical radiation, waveforms from Pt/YIG are shifted to earlier time delays by 1 ps. Gray curve shows the THz-signal component $S_-(t)$ from YIG (thickness of 10 µm) without metal coating on a diamond substrate. **b**, Polarization state of the emitted THz pulses. THz-signal components with polarization perpendicular and parallel to the in-plane sample magnetization $\boldsymbol{M}$. For the polarization discrimination, two wire-grid polarizers are place behind the YIG(3 µm)/Pt(5.5 nm) sample. The THz field related to $S_-(t)$ is oriented perpendicular to the sample magnetization. $S_+(t)$ is below the noise level. Data are low-pass-filtered with a Gaussian function of 15-THz FWHM centered at 0 THz.

by the Faraday effect. The Faraday signal disappears at the Curie temperature $T_\mathrm{C} = 550\,\mathrm{K}$ of bulk YIG. Figure 8.4b reveals that the RMS of $S_-(t)$ and, thus, the THz spin current also decreases with rising $T_0$, but more rapidly than the YIG bulk magnetization. A similar monotonous decrease was seen in static experiments on YIG/Pt bilayers where a temperature gradient in the YIG bulk drives the spin current [Wan15, Uch14]. Fitting the model function $\propto (T_\mathrm{C} - T_0)^x$ to our data yields an exponent of $x = 2 \pm 0.5$, close to the exponents 1.5 and 3 found in Refs. [Wan15] and [Uch14], respectively. This agreement provides further evidence that the THz signal $S_-(t)$ arises from the ultrafast SSE.

**Ultrafast spin Seebeck current.** To determine the temporal evolution and speed of the SSE, we extract the spin current $\boldsymbol{j}_\mathrm{s}(t)$ by applying an inversion procedure to our THz-electro-optic signals (see Section 3.4.2). The polarization of the spin current is calibrated based on a metallic reference emitter (see Chapter 5). Figure 8.5a shows the central experimental result of this study: the ultrafast dynamics of the SSE current induced by a 10-fs laser pulse. Strikingly, $\boldsymbol{j}_\mathrm{s}$ rises on an ultrafast time scale of 100 fs, more than one order of magnitude faster than any SSE response time reported so far [Agr14, Sch16, Bar17, Kim17].

**Dynamic spin-Seebeck-effect model.** It should be noted that, apart from the numerical implementation, the following model has been derived to the largest extent

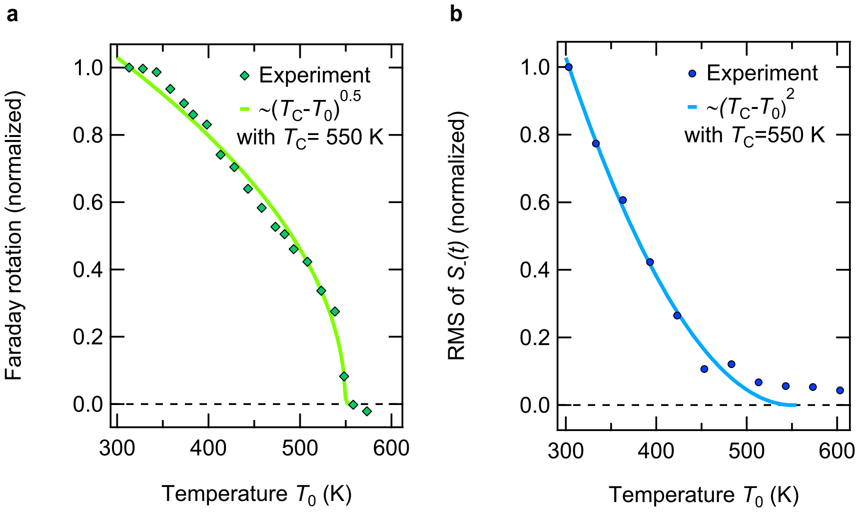

**Figure 8.4.: Effect of sample temperature.** **a**, Faraday rotation of a continuous-wave laser beam (wavelength of 532 nm) as a function of the sample temperature. A fit $\propto (T_C - T_0)^x$ (Ref. [Uch14]) gives a critical exponent of $x = 0.5$ and a Curie temperature of $T_C = 550\,\mathrm{K}$. **b**, Temperature dependence of the magnetic THz-emission signal, which differs from that of the sample magnetization in **a**, similar to previous works on the DC SSE [Uch14, Wan15]. The solid line is a fit $\propto (T_C - T_0)^x$, here yielding $x = 2 \pm 0.5$.

by T. Kampfrath (Department of Physical Chemistry, Fritz Haber Institute of the Max Planck Society, 14195 Berlin, Germany) with valuable help of P. W. Brouwer (Department of Physics, Freie Universität Berlin, 14195 Berlin, Germany).

To understand the ultrafast SSE dynamics, we adapt the static SSE theory of Ref. [Ada13] to the dynamic case and employ a linear-response approach to spin pumping [Šim03, Tse05]. Our treatment (see App. A.3) is based on the microscopic mechanism that is schematically shown in Figs. 8.5b-e and detailed in the following. According to *ab initio* calculations [Jia11], the spins of the interfacial F and N layers are coupled by an sd-exchange-like Hamiltonian [Ada13, Uch10, Sil79, Kaj10] $J_{\mathrm{sd}}\boldsymbol{S}^{\mathrm{F}} \cdot \boldsymbol{S}^{\mathrm{N}}/\hbar^2$ over a thickness of about one YIG lattice constant $a = 1.24\,\mathrm{nm}$, where $\hbar$ is the reduced Planck constant. Here, $J_{\mathrm{sd}}$ quantifies the coupling strength, and $\boldsymbol{S}^{\mathrm{F}}$ and $\boldsymbol{S}^{\mathrm{N}}$ are the total electron spin angular momentum contained in an interfacial cell of dimension $a^3$ on the F and N side, respectively. Thermal spin fluctuations $\boldsymbol{s}^{\mathrm{F}}(t)$ in F and $\boldsymbol{s}^{\mathrm{N}}(t)$ in N cause stochastic effective magnetic fields and, therefore, torques on each other, which cancel in thermal equilibrium.

However, this balance is broken in our experiment by the pump pulse exciting exclusively the N-cell electrons. Consequently, we focus on elementary interactions caused by spin fluctuations in N. After the arrival of the pump pulse, at time $t'$, the conduction-electron spins within an N cell give rise to a random field $J_{\mathrm{sd}}\boldsymbol{s}^{\mathrm{N}}(t')/\hbar$ on the F-cell spins [Ada13] (Fig. 8.5a). Subsequently, at time $t > t'$, the F-cell spin has changed dynamically by $\Delta s_i^{\mathrm{F}} = \sum_j \chi_{ij}^{\mathrm{F}}(t-t')\,J_{\mathrm{sd}}s_j^{\mathrm{N}}(t')$ where $\chi_{ij}^{\mathrm{F}}$ is the spin susceptibility tensor of the F cell [Ada13, Šim03] (Fig. 8.5b). However, $\Delta\boldsymbol{s}^{\mathrm{F}}$ is can-

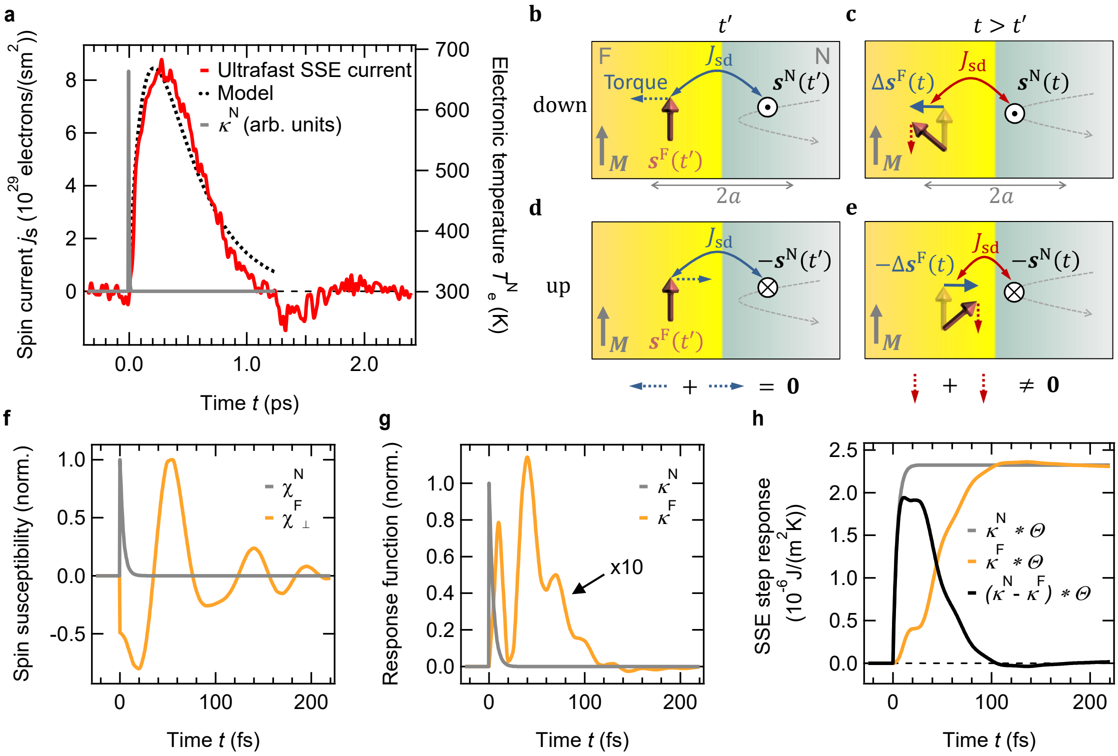

**Figure 8.5.: Ultimate speed of the spin Seebeck effect.** **a**, Extracted spin current density $j_s(t)$ entering the Pt layer together with a phenomenological model function $[1 - \exp(-t/\tau_1)] \cdot \exp(-t/\tau_2)$. The time constants of electron thermalization ($\tau_1$) and cooling ($\tau_2$) are taken from literature [Lei02, Caf05]. **b-e**, Model schematic of the F/N interface. To illustrate the action of the exchange torque between the excited spins in the metal (N) and the magnetization of the magnetic insulator (F), it is sufficient to consider the “up” (**a**, **b**) and “down” (**c**, **d**) case of an N-cell spin perpendicular to the magnetization $\boldsymbol{M}$ of the F layer. **a**, At time $t'$, an N electron entering the interaction region induces a fluctuation $\boldsymbol{s}^N(t')$ of the total N-cell spin, thereby exerting the effective magnetic field $J_{sd}\boldsymbol{s}^N(t')/\hbar$ on the adjacent F-cell spin. **b**, Consequently, at a slightly later time $t$, the F-cell spin has changed by $\Delta\boldsymbol{s}^F(t)$ proportional to $J_{sd}\boldsymbol{s}^N(t')$. **c**, The opposite fluctuation $-\boldsymbol{s}^N(t')$ at time $t'$ induces **d**, the change $-\Delta\boldsymbol{s}^F(t)$, resulting in zero change in the F-cell spin, $\langle\Delta\boldsymbol{s}^F(t')\rangle = 0$. However, as seen in panels **b** and **d**, a second interaction at $t > t'$ with the N-cell field leads to the same rectified torque $J_{sd}\boldsymbol{s}^N(t) \times \Delta\boldsymbol{s}^F(t)/\hbar^2$ for both “up” and “down” spin. Thus, a net spin current flows between F and N. **f**, Calculated time-domain spin susceptibility of the F=YIG cell (transverse $\chi_\perp^F(t)$) and the N=Pt cell (isotropic $\chi^N(t)$). **g**, Calculated dynamics of the SSE response functions $\kappa^N(t)$ and $\kappa^F(t)$ which quantify, respectively, the spin current induced by a $\delta(t)$-like temperature increase of the N (Pt) and F (YIG) layer (see text). For comparison, $\kappa^N$ is also shown in panel **a**. **h**, Resulting SSE step responses $\int_0^t \mathrm{d}t'\,\kappa^N(t')$ and $\int_0^t \mathrm{d}t'\,\kappa^F(t')$ (gray and yellow curve, respectively) induced by the same temporally step-like temperature increase $\Theta(t)$ at $t = 0$ in both layers. Their difference, which equals the total response, is also shown (black curve). To obtain an absolute ordinate scaling, in agreement with the experiment, an interfacial exchange constant of $J_{sd} = 4\,\text{meV}$ is used.

celed by an oppositely oriented field $-J_{sd}\boldsymbol{s}^N(t')/\hbar$ occurring with equal probability (see Figs. 8.5c and d). In other words, the average induced moment $\Delta\boldsymbol{s}^F$ cancels because $\left\langle \boldsymbol{s}^{\mathrm{N}} \right\rangle = 0$.

Nevertheless, a net effect results from a second interaction of F with $J_{\mathrm{sd}}\boldsymbol{s}^{\mathrm{N}}/\hbar$ at time $t > t'$ (Figs. 8.5b and d). The corresponding torque $J_{\mathrm{sd}}\boldsymbol{s}^{\mathrm{N}}(t) \times \Delta\boldsymbol{s}^{\mathrm{F}}(t)/\hbar^2$scales with $J_{\mathrm{sd}}^2$ and, therefore, rectifies the random field $J_{\mathrm{sd}}\boldsymbol{s}^{\mathrm{N}}/\hbar$. Its expectation value is parallel to the F magnetization $\boldsymbol{M}$ (Figs. 8.5b and d). By integration over all first-interaction times $t'$ (see App. A.3), we find the spin current due to N-cell fluctuations equals

$$j_{\mathrm{s}}^{\mathrm{N}}(t) = \frac{J_{\mathrm{sd}}^2}{a^2\hbar^2} \int \mathrm{d}t'\, \chi_{\perp}^{\mathrm{F}}(t-t') \left\langle s_z^{\mathrm{N}}(t)\, s_z^{\mathrm{N}}(t') \right\rangle . \tag{8.2}$$

Equation 8.2 provides the key to understanding the ultrafast dynamics of the SSE. The spin correlation function $\left\langle s_z^{\mathrm{N}}(t)\, s_z^{\mathrm{N}}(t') \right\rangle$ implies that a net spin current only arises if the two interactions with $J_{\mathrm{sd}}\boldsymbol{s}^{\mathrm{N}}/\hbar$ occur within the correlation time $\tau^{\mathrm{N}}$ of the N-cell spin, that is, $|t-t'| < \tau^{\mathrm{N}}$. The $\tau^{\mathrm{N}}$ can be estimated by the time it takes an electron to traverse the N cell (Figs. 8.5b-e), yielding $\tau^{\mathrm{N}} \sim 3.5\,\mathrm{fs}$ for Pt [Ket68]. As this time constant is shorter than the 10-fs-pump-pulse duration, the N-cell spin correlation function mirrors the instantaneous state of the optically-excited electrons in the metal. Interestingly, the F-cell spins react instantaneously too, because they have no inertia [Kim09]. This fact is illustrated by the step-like onset of the transverse F-cell susceptibility $\chi_{\perp}^{\mathrm{F}}(t) = \chi_{yz}^{\mathrm{F}}(t) - \chi_{zy}^{\mathrm{F}}(t)$ at $t = 0$ (Fig. 8.5f). Consequently, the spin current follows the dynamics of the electron distribution in the metal without delay.

To put this conclusion on a more quantitative basis, we note that the strength of the N-cell spin fluctuations is proportional to the frequency at which Pt conduction electrons scatter off the F/N interface (Figs. 8.5b-e). Assuming elastic and diffuse scattering (see App. A.3), this rate scales with the number of occupied incident and unoccupied outgoing Bloch states, that is, with the quantity

$$k_{\mathrm{B}}\widetilde{T}_{\mathrm{e}}^{\mathrm{N}} = \int \mathrm{d}\epsilon\, n(\varepsilon, t) \cdot [1 - n(\varepsilon, t)] . \tag{8.3}$$

Here, $k_{\mathrm{B}}$ is the Boltzmann constant, and $n(\varepsilon, t)$ is the occupation number of a Bloch state at electron energy $\varepsilon$ (see Section 2.2). Interestingly, when $n(\varepsilon, t)$ equals a Fermi-Dirac function at temperature $T_{\mathrm{e}}^{\mathrm{N}}(t)$, we obtain $\widetilde{T}_{\mathrm{e}}^{\mathrm{N}}(t) = T_{\mathrm{e}}^{\mathrm{N}}(t)$, thereby identifying $\widetilde{T}_{\mathrm{e}}^{\mathrm{N}}(t)$ as a generalized (nonequilibrium) electronic temperature. Using linear-response theory (see App. A.3), we can, thus, express the correlation function $\left\langle s_z^{\mathrm{N}}(t)\, s_z^{\mathrm{N}}(t') \right\rangle$ by means of $\widetilde{T}_{\mathrm{e}}^{\mathrm{N}}(t)$ and the isotropic spin susceptibility $\chi^{\mathrm{N}}$ of the N cell. As the F layer remains cold at temperature $T_0$, we obtain

$$j_{\mathrm{s}}(t) = \int \mathrm{d}t'\, \kappa^{\mathrm{N}}(t-t') \cdot \left[\widetilde{T}_{\mathrm{e}}^{\mathrm{N}}(t') - T_0\right] , \tag{8.4}$$

which is the desired generalization of Eq. 8.1 for time-dependent temperatures and nonthermal electron distributions of the N layer.

The response function $\kappa^{\mathrm{N}}(t) \propto J_{\mathrm{sd}}^{2}\chi^{\mathrm{N}}(t)\int \mathrm{d}t'\,\chi_{\perp}^{\mathrm{F}}(t-t')\,\chi^{\mathrm{N}}(t')$ can be understood as the spin current induced by a $\delta(t)$-like change in $\widetilde{T}_{\mathrm{e}}^{\mathrm{N}}$. It is determined by the susceptibilities of the F- and N-cell spins. For N=Pt, we assume an isotropic spin susceptibility [Clo64, Fra75], $\chi^{\mathrm{N}}(t)$ that rises step-like and decays with time constant $\tau^{\mathrm{N}}$ (see Fig. 8.5f). In contrast, $\chi_{\perp}^{\mathrm{F}}(t)$ is obtained by atomistic spin-dynamics simulations [[Bar16, Ell15], implemented by J. Barker (Institute for Materials Research, Tohoku University, Sendai 980-8577, Japan)], and exhibits a strongly damped oscillation reflecting the superposition of many magnon modes (see App. A.3 and Fig. 8.5f). The resulting SSE response function $\kappa^{\mathrm{N}}(t)$ is shown in Fig. 8.5g.

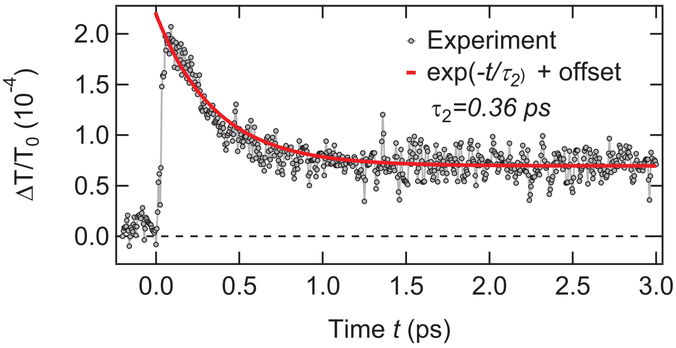

**Figure 8.6.: Transient reflectance of a YIG/Pt film.** Transient reflectance measurement employing degenerate optical pump and probe pulses (central wavelengths of 800 nm) of a YIG(3 µm)/Pt(5.5 nm) sample together with a mono-exponential fit including an offset. Best agreement is obtained for a time constant of $\tau_2$ =0.36 ps.

## 8.4. Discussion

Consistent with our qualitative discussion following Eq. 8.2, $\kappa^{\mathrm{N}}(t)$ has an ultrashort duration on the order of $\tau^{\mathrm{N}}$, much faster than the onset of the measured spin current (Fig. 8.5a). Accordingly, the evolution of $j_{\mathrm{s}}(t)$ directly reflects the dynamics of the laser-excited Pt electrons. Indeed, $j_{\mathrm{s}}(t)$ is captured remarkably well by the phenomenological model function $[1-\exp(-t/\tau_1)]\cdot\exp(-t/\tau_2)$. Here, the time constants $\tau_1 = 0.26\,\mathrm{ps}$ and $\tau_2 = 0.36\,\mathrm{ps}$ quantify the speed at which the photo-excited electrons in Pt are known to approach a Fermi-Dirac distribution [Lei02] and to transfer their excess energy to the lattice [Caf05], respectively (see Section 2.1). Moreover, there is an excellent agreement between the relaxation dynamics of $j_{\mathrm{s}}(t)$ and the transient optical reflectance, which is known to approximately mirror the decay of the electron temperature [Caf05] (see Fig. 8.6). We ascribe the ultrafast rise and decay of the SSE current therefore to the thermalization and cooling of the optically-excited Pt electrons.

This notion is consistent with Eqs. 8.3 and 8.4: maximum spin current is achieved when the photo-excited N-cell electrons have an occupation number $n(\varepsilon, t)$ of 0.5

over an electron-energy interval as wide as possible. Therefore, as many electron-hole pairs as possible should be generated for a given deposited pump-pulse energy. Initially, photoexcitation induces electrons and holes at approximately half the pump photon energy of $\hbar\omega_\mathrm{p} = 1.6\,\mathrm{eV}$ away from the Fermi level (see Section 2.1). However, subsequent scattering cascades increase their number on the time scale $\tau_1$ by a factor on the order of $\hbar\omega_\mathrm{p}/k_\mathrm{B}T_\mathrm{e}^\mathrm{N} \sim 30$. This carrier multiplication, in turn, strongly increases the generalized temperature $\widetilde{T}_\mathrm{e}^\mathrm{N}(t)$ and the spin current. The rise of the measured $j_\mathrm{s}(t)$ can, therefore, be considered as an experimental confirmation of the notion that the SSE current is due to electrons impinging on the YIG/Pt interface [Tse05, Žut11, Ber96, Sti02]. Accordingly, we have added a temperature scale on the right ordinate of Fig. 8.5a.

In our experiment, the SSE efficiency is given by the THz peak field per peak increase $T_\mathrm{e}^\mathrm{N} - T_0$ of the Pt electron temperature and estimated to be $1\,\mathrm{V\,m^{-1}\,K^{-1}}$ (Fig. 8.5a). This value is comparable to results from SSE experiments on samples with Pt layers of similar thickness, that is, for static heating ($0.1\,\mathrm{Vm^{-1}K^{-1}}$) [Keh15], and for laser heating at MHz ($0.7\,\mathrm{V\,m^{-1}\,K^{-1}}$) [Agr14] and at GHz frequencies ($37\,\mathrm{V\,m^{-1}\,K^{-1}}$) [Sch16]. Our modeling (see App. A.3) also allows us to extract the YIG/Pt interfacial exchange coupling constant, yielding $J_\mathrm{sd} = 4\,\mathrm{meV}$ or $\mathrm{Re}\,g^{\uparrow\downarrow}{=}2.4{\cdot}10^{18}\,\mathrm{m^{-2}}$ in terms of the spin-mixing conductance $g^{\uparrow\downarrow}$, in good agreement with calculated [Jia11] and measured values [Bur13, Wei13].

We note that the positive sign of the measured spin current $j_\mathrm{s}(t)$ (Fig. 8.5a) implies that the magnetization of YIG decreases. The peak electronic temperature induced by the pump pulse is determined using the absorbed pump-pulse energy density and the Pt electronic specific heat [Gra82, Lin08]. The integrated $j_\mathrm{s}(t)$ is equivalent to increasing the temperature of the thin YIG interfacial layer by about 50 K (see Fig. 8.4a). As this value is one order of magnitude smaller than the increase of the Pt electron temperature $T_\mathrm{e}^\mathrm{N}$, we can neglect the back-action of the heated YIG layer on the spin current.

So far, our experiments have been restricted to excitation of the metal part of YIG/Pt. Our modeling, however, allows us to also calculate the SSE response function $\kappa^\mathrm{F}(t)$ related to heating of the F=YIG layer (see Eq. A.16 in App. A.3). If YIG and Pt layers were uniformly and simultaneously heated by a sudden temperature jump, Eq. 8.1 would imply a vanishing current. In surprising contrast, our theory predicts a 100-fs-short current burst (Fig. 8.5h) which reflects the inherent asymmetry of the F/N structure. At times $t > 100\,\mathrm{fs}$, the total spin current vanishes, consistent with the familiar static result of Eq. 8.1.

## 8.5. Conclusion

We measured an ultrafast spin current in the prototypical SSE system YIG/Pt triggered by femtosecond optical excitation of the metal layer. The current exhibits all the hallmarks expected from the THz SSE. A dynamic model, based on sd-exchange-coupled YIG/Pt layers, can reproduce both the magnitude and the dynamics of the measured ultrafast spin current. It allows us to identify the elementary steps leading to the formation of the initial SSE current: optically-excited metal electrons impinge on the interface with the magnetic insulator. They apply random torque which is rectified by two subsequent interactions, thereby resulting in a net spin current from YIG into the metal. This response is quasi-instantaneous because the YIG spins react without inertia to the impinging metal spins which have a correlation time of less than 5 fs. Consequently, the SSE current directly monitors the thermalization and cooling of the photo-excited electrons which proceed on a time scale of 100 fs.

In terms of applications, the observed ultrafast SSE current can be understood as a first demonstration of incoherent THz spin pumping. Therefore, an instantaneously heated metal layer is a promising transducer for launching ultrashort THz magnon pulses into magnetic insulators. They may prove useful for magnon-based transport of information, for exerting ultrafast torques on remote magnetic layers, and for spectroscopy of spin waves with nanometer wavelengths [Bos16].

From a fundamental viewpoint, our experimental approach permits the characterization of the interfacial SSE and the ISHE of metals in standard bilayer thin-film stacks with a large sample throughput and without extensive microstructuring. As an example, we have already characterized YIG/$\mathrm{Cu}_x\mathrm{Ir}_{1-x}$ stacks with varying Cu:Ir-ratio and found qualitatively the same concentration dependence for THz and DC SSE signals [Cra17]. Furthermore, our approach allows for all-optically probing of the magnetic texture and the exchange coupling at interfaces. Since our setup is driven by a femtosecond laser oscillator rather than a significantly more demanding amplified laser system, our methodology is accessible to a broad community.

As indicated by Eq. 8.2, the THz SSE current is also sensitive to the local electron spin noise at the highest frequencies, even under conditions far from equilibrium. Such type of spin-noise spectroscopy is difficult to accomplish with other methods. Finally, our theoretical approach can be extended to a large variety of magnetic systems in which lasers drive spin transfer between two constituents [Tve15] such as spin sublattices [Kir13], or spins and phonons [Koo10].

## 8.6. Outlook

With the advanced understanding of photo-induced spin currents in magnetic-insulator/metal bilayers obtained here, we may turn again to the driving force of the ultrafast spin-dependent Seebeck effect (SDSE) in all-metallic magnetic heterostructures (see Section 7.5).

To this end, we present preliminary results directly comparing the two THz-emission signals (under identical experimental conditions) of YIG/Pt and $\mathrm{Co}_{20}\mathrm{Fe}_{60}\mathrm{B}_{20}$/Pt thin films deposited on the very same substrate. Remarkably, already the raw data (see Fig. 8.7a) indicate that the SDSE-related THz signal (all-metallic structure) follows faster dynamics. This becomes even more evident by comparing the two extracted spin current densities (see Fig. 8.7b). First, the all-metallic structure shows an almost three orders of magnitude larger spin current, highlighting the dominant role of conduction-electron spin currents (see Section 2.4.4). Second, the SDSE-related spin current follows distinctly faster dynamics than the ultrafast SSE current. The rise time of less than 50 fs approaches the experimental temporal resolution.

Surprisingly, the signal from the all-metallic sample resembles the time-derivative of the SSE-driven transient. This observation suggests a close relation of the ultrafast SDSE to the time derivative of the generalized electron temperature (see Eq. 8.3) in the metals. This observation supports the notion of an ultrafast-electron-heating scenario as outlined in Section 7.5.

To gain further insights, we are currently developing a model based on the spin drift-diffusion model [Kal12, Nen16] and a temperature-dependent chemical potential [Mue15, Fog17]. Once these insights are gained, we hope to boost ultrafast spin currents which is of crucial importance for the spintronic-THz-emitter performance and for ultrafast switching operations [Jun16, Liu12a].

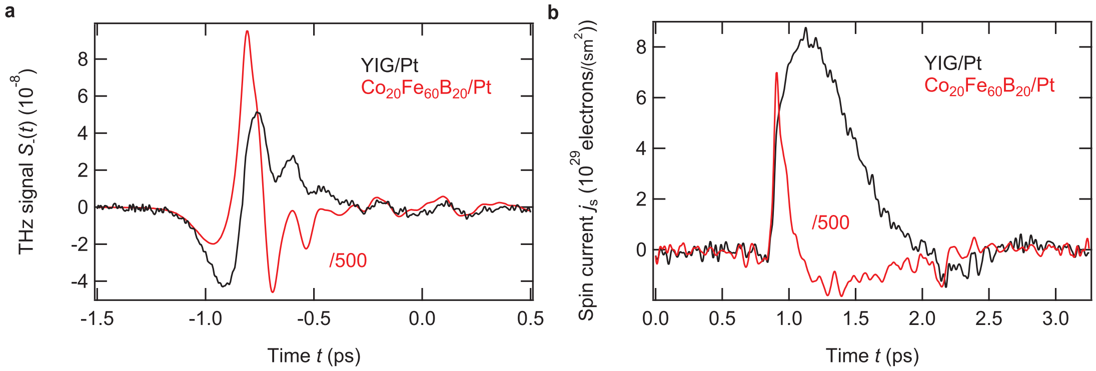

**Figure 8.7.: Direct comparison of the ultrafast transients related to the spin Seebeck effect and the spin-dependent Seebeck effect. a**, Raw THz-emission signal from photo-excited YIG(3 µm)/Pt(5 nm) (black curve) and YIG(3 µm)/Pt(5 nm)/$Co_{20}Fe_{60}B_{20}$(3 nm)/MgO(5 nm) (red curve) heterostructures deposited on the very same substrate. Note that the signal from CoFeB/Pt has been inverted and divided by 500 for better comparison. **b**, Extracted spin current densities from the raw data in **a** using a 50-µm-thick GaP reference emitter (see Section 3.4.2).

**Acknowledgments.** We would like to thank S. T. B. Gönnenwein (Institute of Structural Physics, Technische Universität Dresden, 01062 Dresden, Germany), M. Münzenberg (Institut für Physik, Ernst-Moritz-Arndt-Universität Greifswald, 17489 Greifswald, Germany), G. Woltersdorf (Institute of Physics, Martin-Luther-Universität Halle, 06120 Halle, Germany) and P. W. Brouwer (Department of Physics, Freie Universität Berlin, 14195 Berlin, Germany) for valuable comments on this work.

# 9. Terahertz writing speed of an antiferromagnetic memory device

*So far, we employed THz pulses to monitor spin dynamics. In the following, we would like to turn to using THz pulses as a stimulus to control the dynamics of magnetic order. A material class showing enormous potential for future high-speed spintronic devices are antiferromagnets as they exhibit long-wavelength THz magnons presumably favoring picosecond dynamics. In the following, we present first results of the switching of an antiferromagnetic memory device triggered by THz pulses.*

These preliminary results are a shortened version of the article “THz electrical writing speed in an antiferromagnetic memory” in preparation by K. Olejnik, T. Seifert et al. (2017) [Ole17b] and were obtained in close collaboration with the research groups of R. P. Campion, P. Gambardella, P. Nemec, J. Wunderlich, J. Sinova and T. Jungwirth.

## 9.1. Motivation

In antiferromagnets (AFMs), the Néel vector provides a means to encode information. Regarding information-technology applications, valuable properties are unified by this class of materials, such as inherent stability to external fields, lack of stray fields, and its abundance in nature. Therefore, possible AFM-based devices promise higher integration density and long-term stability. On the other hand, the insensitivity of AFMs to external fields made applications challenging until recently.

However, in 2006, the electrical switching of the magnetic order of AFMs using Néel spin-orbit torques (NSOT) was demonstrated for the first time [Wad16]. These prototype devices are based on the metallic AFM CuMnAs, whose tetragonal unit cell is shown in Fig. 9.1a. The two compensating magnetic manganese sublattices (red and purple spheres in Fig. 9.1a) are inversion partners. This symmetry together with the SOI causes a staggered spin polarization once a current parallel to the $x$-$y$-plane is passed through the system (compare Fig. 9.1a). Importantly, the nonequilibrium spin polarization is of opposite sign on the two magnetic sublattices, oriented in the $x$-$y$-plane, and perpendicular to the current direction [Žel14]. Consequently, an identical torque is exerted on the two magnetic sublattices, favoring a Néel vector orientation perpendicular to the current direction within the $x$-$y$-plane. Remarkably, the described current-induced NSOT mechanism circumvents any canting of the magnetic moments. This dramatically reduces the energy needed for switching the Néel vector compared to schemes employing external magnetic fields [Jun16].

Importantly, spin dynamics in AFMs are expected to be much faster than in ferromagnets, whose switching rates are limited to the GHz range. In contrast, in AFMs, the frequencies of long-wavelength magnons are strongly enhanced by the exchange interaction opening the potential for THz switching speeds [Kam11]. Previous studies showed the feasibility of the NSOT-driven electrical writing of AMFs with pulse lengths from milliseconds to hundreds of picoseconds [Ole17a].

Here, we test the ultrafast writing speed of AFM memory cells fabricated from epitaxial CuMnAs films. Employing an all-optical writing scheme based on free-space THz electromagnetic pulses, we further reduce the current duration down to the picosecond time scale. With these picosecond laser pulses, we observe the analogous switching phenomenology as with millisecond and nanosecond current pulses. Our preliminary results suggest that the current-induced NSOT switching mechanism for AFMs is operative in the THz range.

## 9.2. Experimental details

Sample growth, device fabrication and electrical measurements were carried out by K. Olejnik, Z. Kaspar and V. Novack (Institute of Physics, Czech Academy of Sciences, 162 00 Prague, Czech Republic).

**Antiferromagnetic memory device.** Figure 9.1b shows a microscopy image of an antiferromagnetic device based on epitaxial CuMnAs grown on a GaAs substrate (thickness of 0.5 mm). Electrical contact is provided by four gold contacts (thickness of 100 nm) that narrow down towards the central device region. The antiferromagnetic CuMnAs (thickness of 50 nm) is in the middle of the device (see electron microscope image in Fig. 9.1c) and consist of a cross-like region with a 2-µm-wide central region of highest current density.

The reading of the antiferromagnetic state is implemented by the anisotropic magnetoresistance (AMR) which is measured via the transverse resistance $R_{xy}$. In brief, the AMR is an SOI-induced effect in which the resistance of a material depends on the orientation of its magnetization (see Section 2.3.3). Importantly, the AMR is even in the magnetization and therefore equally present in ferromagnets and AFMs. More details on the AMR read-out can be found in [Wad16].

The writing of the AFM is accomplished by sending trains of MHz current pulses (see Fig. 9.2a) along either $x$- or $y$-direction (peak current densities of ~$10^7$ A/cm$^2$, repetition rate of 1 Hz; compare with Fig. 9.1b). The following MHz-pulse-writing scheme is applied: First, 30 writing pulses (see Fig. 9.2c) are sent along the $x$-direction. After a break of ~30 s, 30 further writing pulses are sent along the $y$-direction, followed by another 30-s break. This procedure is repeated for several

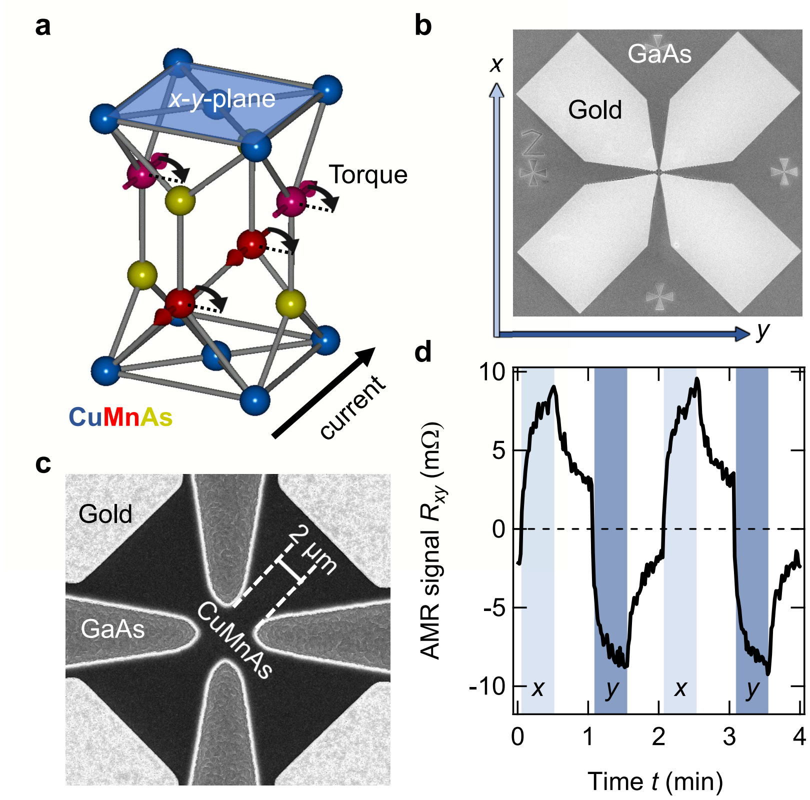

**Figure 9.1.: Antiferromagnetic memory device and megahertz-writing-pulse operation.** **a**, Unit cell of the tetragonal antiferromagnet CuMnAs and Néel spin-orbit torque. The two compensating magnetic manganese sublattices (red and purple spheres) are inversion partners. The Néel vector is oriented in the $x$-$y$-plane. If a charge current is passed through CuMnAs in the $x$-$y$-plane, its crystal symmetry and the spin-orbit interaction induce a nonequilibrium spin polarization of opposite sign at the two magnetic sublattices exerting an identical torque on them (see curved arrows). This favors a Néel-vector orientation in $x - y$-plane and perpendicular to the current direction. **b**, Optical microscopy image (area of $700 \times 700\,\mu\text{m}^2$) showing the antiferromagnetic memory device. Gold pads (light gray areas) are used to contact the CuMnAs in the central region. The GaAs substrate is shown in dark gray. **c**, Detailed electron microscope image of the central device region of 2-µm-width. **d**, Electrical switching of CuMnAs. The electrical switching is accomplished by sending trains of MHz pulses (see Fig. 9.2c) through the device (repetition rate of 1 Hz, current density of $\sim 10^7\,\text{A/cm}^2$). Each sequence consists of 30 individual pulses. The resulting change in the anisotropic resistance (AMR) is monitored by the transverse resistivity $R_{xy}$ (read-out rate of 1 Hz). Alternating the writing-current direction between $x$- and $y$-directed (light and dark blue shaded areas, respectively; compare with **b**), reorients a part of the magnetic moments and changes the AMR signal. When the current is switched off (white areas), the AMR signal slightly relaxes. Reproducible switching is achieved with successive iterations, where each switching operation exhibits a typical integration-like behavior.

times. The transverse resistance $R_{xy}$ is measured using weak electrical probe pulses at a repetition rate of 1 Hz.

The resulting AMR signal (Fig. 9.2d) clearly shows a repetitive step-like behavior representing the reproducible reorientation of the Néel vector. Note that a slight relaxation of the AMR signal is observed when the writing pulses are switched off. These switching characteristics have already been observed in previous studies [Ole17a].

## 9.3. Preliminary results

To test the feasibility of the antiferromagnetic memory for future high-speed applications, we next replace the electrical contact-based MHz writing pulses by free-space THz pulses (see Figs. 9.2a and b).

The THz transients are derived from optical rectification of amplified laser pulses (central wavelength of 800 nm, pulse energy of 4 mJ, pulse duration of 350 fs , repetition rate of 1 kHz; see Section 3.1) in a 1.3 mol% MgO-doped stoichiometric $LiNbO_3$ crystal using the tilted-pulse-front scheme [Hir11], delivering a central frequency of ~1 THz and a peak electric field of ~300 kV/cm at the sample position (see Fig. 9.2d). The linearly-polarized THz electric field drives charge currents in the plane of the antiferromagnetic device whose direction can be conveniently controlled by the THz polarization set by a wire-grid polarizer.

**Comparing MHz- and THz-pulse writing of an antiferromagnetic memory device.** Figures 9.2e-h show a direct comparison of MHz- and THz-pulse writing of the CuMnAs-based memory device. Most importantly, we see a change in the AMR signal by illuminating the AFM with a train of THz pulses (Fig. 9.2f). By closely matching writing and read-out rates (1 Hz for the MHz pulses and ~100 Hz for the THz pulses), we can resolve the AMR-signal change induced by single pulses. Remarkably, MHz and THz schemes both show very similar time evolutions of the AMR read-out signal (see Figs. 9.2e and f). As evident from Fig. 9.2f, already the first THz pulse is responsible for a large part of the AMR-signal change.

Next, we rotate the THz-pulse polarization by 90° (see Fig. 9.2b) and apply a similar writing scheme as for the MHz pulses, but with a closely-matched writing-pulse and read-out repetition rate at ~100 Hz. Figures 9.2g and h show very similar AMR-signal evolutions, regardless of whether MHz- or THz-writing pulses are used. This indicates that the antiferromagnetic memory device remains functional even with THz-writing pulses. For more details see [Ole17b].

## 9.4. Future directions

In summary, our preliminary findings strongly suggest that the current-induced NSOT writing mechanism in AFMs is operative at THz speeds. Further calibration measurements show that a similar energy is needed to write the same amount of information (change in transverse AMR signal) in the CuMnAs-based device with THz and MHz pulses (not shown). This highlights the large potential of AFMs for THz spintronics. However, these experiments do not allow deriving the actual switching dynamics of the Néel vector, crucial for any high-speed application. Future studies, utilizing additionally an ultrafast read-out might complete the envisioned THz antiferromagnetic memory device.

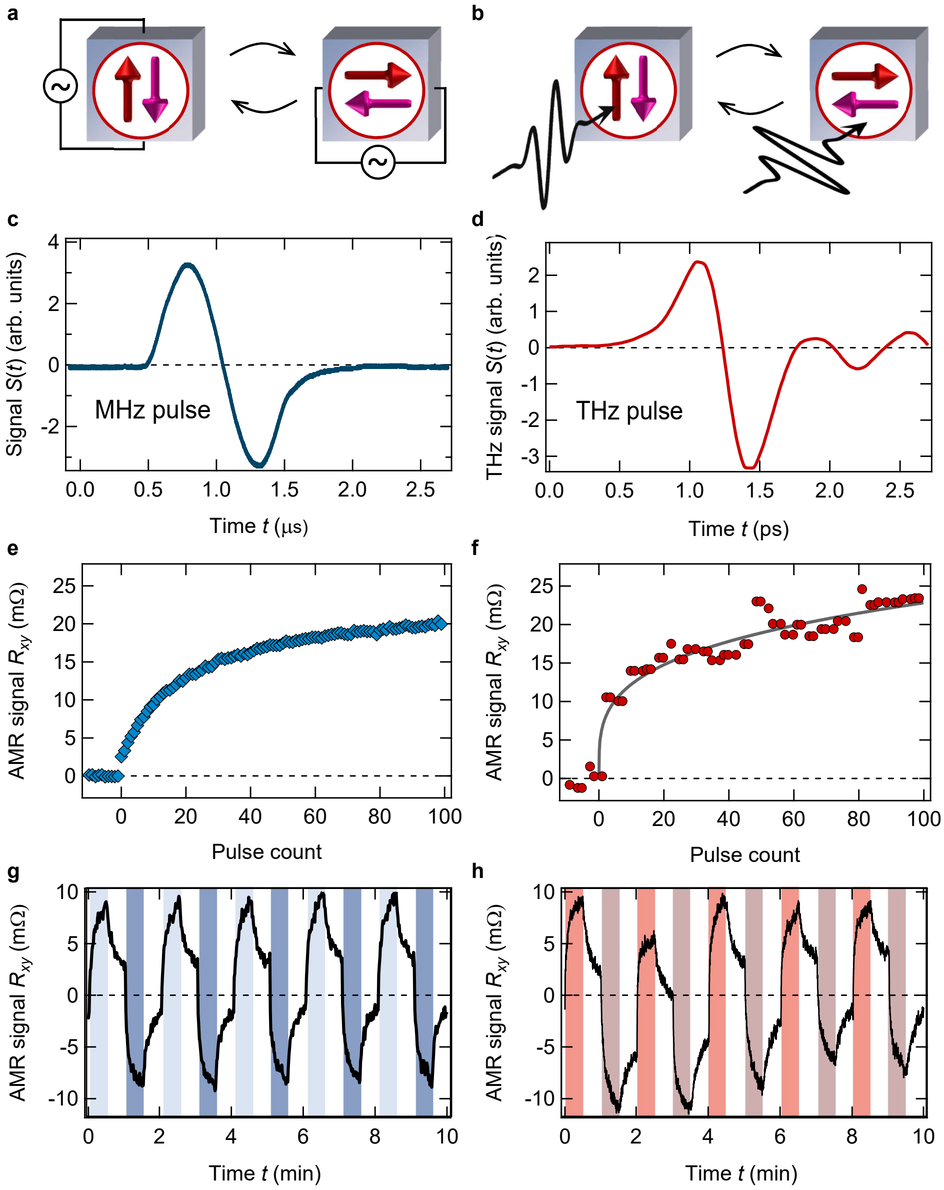

**Figure 9.2.: MHz- and THz-pulse writing of an antiferromagnetic memory device. a**, Schematic of the MHz-pulse writing scheme. Changing between two perpendicular current directions leads to a corresponding reorientation of the Néel vector **b**, Schematic of the THz-pulse writing scheme. Same as in **a** but employing free-space THz pulses. Here, the favored Néel-vector orientation is determined by the linear-polarization direction of the THz-writing pulses. **c**, MHz pulse used for the electrical-contact-based writing scheme (repetition rate of 1 Hz, current density of ~$10^7$ A/cm$^2$ **d**, THz pulse used for the all-optical writing scheme (repetition rate of ~100 Hz, electric field at the sample position of ~300 kV/cm). **e**, Anisotropic-magneto-resistance (AMR) signal measured by the transverse resistance change $R_{xy}$ as a function of the read-pulse count (rate of 1 Hz) for MHz pulses constantly applied along one axis. **f**, Same as in **e** but employing linearly-polarized free-space THz transients as shown in part **d**. The read-out rate is adapted to ~100 Hz. The gray curve is a guide to the eye. **g**, AMR-signal changes for successive switching operations of the antiferromagnetic memory device employing the same writing scheme as in Fig. 9.1d (see also text). Light- and dark-blue-shaded areas represent MHz-pulse trains of perpendicular current directions. **h**, Same as in **g** but employing the all-optical THz-pulse writing scheme. Light- and dark-red-shaded areas represent THz-pulse trains with perpendicular linear THz polarizations. White areas in **g** and **h** mark periods without any writing pulse.

# 10. Summary

In this work, we advance concepts to explore spin-dependent phenomena in spintronic nanostructures in the THz range. Spin-to-charge conversion (anomalous and spin Hall effects) and spincaloritronic schemes (spin-dependent and spin Seebeck effect) are investigated at highest frequencies. To this end, we test the ultimate speed of these spintronic phenomena and reveal the underlying ultrafast physical processes. Concerning the spin Seebeck effect, we elucidate the close connection between carrier multiplication and the rise of the spin Seebeck current. In terms of the spin-dependent Seebeck effect, preliminary results suggest that an ultrafast-heating mechanism is of crucial importance. Eventually, we explore new THz spintronic functionalities to launch magnon pulses into magnetic insulators, to switch antiferromagnetic memory devices with ultrashort THz pulses, and to construct an efficient spintronic THz emitter.

In detail, this thesis follows a systematic route from spin-to-charge conversion over heat-driven spin currents to terahertz spin control:

**Terahertz anomalous Hall effect.** First, we study the anomalous Hall effect from DC to 40 THz in technologically relevant metals (see Chapter 4). We find an anomalous Hall angle as large as 2 % virtually independent of frequency. In our understanding, this surprising result arises from the large disorder in the studied thin films, strongly broadening the spectral anomalous Hall response. Our results imply the feasibility of spin-dependent Hall effects at THz speeds, including the closely related spin Hall effect.

These findings are highly relevant for future high-speed spintronic devices such as the currently developed spin-orbit torque magnetic random-access memory [Pre15]. Future studies at low temperatures or in cleaner samples may provide further insights into spin-orbit interaction at THz frequencies [Kim10, Wei11]. Finally, extending this scheme to nonmagnetic materials might enable a direct study of the spin Hall effect by, for instance, employing transient spin polarizations [Wer11, Pri15].

**Spintronic terahertz emitter.** Based on these promising results, we develop a conceptually new spintronic THz emitter outperforming standard table-top THz sources (see Chapter 5). It consists of a nanometer-thin heterostructure containing magnetic and strongly spin-orbit-coupled metals. After photoexcitation with femtosecond optical laser pulses, a combination of the ultrafast spin-dependent Seebeck effect with the inverse spin Hall effect causes the emission of a THz transient. Remarkably, it covers the range from 1 to 30 THz without any spectral gaps due to the featureless refractive index of metals and the short metal-electron lifetimes.

In principle, the emitter functionality is not limited to a specific pump wavelength, thus enabling broad applications. The spintronic THz source not only facilitates linear THz spectroscopy but it can also generate strong THz pulses with field strengths of up to 300 kV/cm enabling nonlinear control over THz resonances in the hard-to-access 5-10 THz range (see Chapter 6). These findings are an example for a straightforward implementation of THz spintronic phenomena into a useful device that is readily appreciated by the broad THz community [Hui17a, Wu17, Yan16, Tor17, Sas17, Li17, Zha17a]. We anticipate improvements of the emitter concept driven by material science [Dem16, Pai14] or by entirely new spintronic phenomena [Les16, Ikh17]. These developments might also enable an efficient spintronic THz detector in the future.

**Spintronic characterization by terahertz emission.** Such progress might be fostered by a convenient spintronic characterization tool with high sample throughput. In this regard, THz-emission spectroscopy is shown to be a promising approach for an all-optical and fast determination of spintronic parameters in heterostructures consisting of normal (see Chapter 5 and Ref. [Cra17]) and magnetic metals (see Chapter 7). The ease of use (no need for microstructuring) and the potential interface sensitivity of this approach complement the spintronic workbench.

Future studies will aim at a more microscopic understanding of the spin-current-generation mechanism in metallic heterostructures [Mue15, Fog17, Bat10], finally allowing for the extraction of absolute spin Hall angles, the enhancement of ultrafast spin currents to eventually control remote layers [Liu12a], and the development of even more efficient spintronic THz emitters.

**Terahertz spin Seebeck effect.** To identify elementary steps in the ultrafast spin-current generation, we first turn to less complex structures: we study the spin current from a magnetic insulator (rather than a metal) into a spin-orbit-coupled metal (see Chapter 8). Surprisingly, we find a spin-Seebeck-current rise time of only ~100 fs. Based on our modeling, this time scale arises from the quasi-instantaneous response of the metal electron spins (<5 fs) deflecting the insulator magnetic moments without inertia. The measured dynamics support the notion that electrons impinging on the metal/insulator interface drive the ultrafast spin Seebeck dynamics. As more electron-hole pairs lead to more scattering (resulting in more torque), the spin Seebeck current monitors the carrier multiplication during the thermalization of the metal electrons.

Our approach might enable spin-noise spectroscopy at buried interfaces [Sin16] with high sensitivity to the local magnetic texture and the detailed spin couplings at interfaces. Moreover, ultrafast heating of a metal layer provides a convenient scheme to launch incoherent magnon pulses into an insulator. These might be useful for ultrafast magnonics and enable control over remote magnetic layers.

**Terahertz writing of an antiferromagnetic memory device.** Finally, we turn from THz probing to the even more exciting THz driving of spin dynamics. We present preliminary results of writing information to an antiferromagnetic memory cell with ultrashort THz pulses. Our findings suggest that the current-induced Néel-spin-orbit-torque switching mechanism remains operative in the THz range for antiferromagnets. Future studies, will aim at a read-out at ultrafast speeds to complete the envisioned THz antiferromagnetic memory device.

In summary, this work demonstrates that combining the two fields of THz spectroscopy and spintronics leads to novel insights and applications. We hope that our results and the presented schemes provide a means to deepen the understanding of spin dynamics at highest speeds.

# A. Appendix

## A.1. Fourier transformation

The Fourier transformation of a function $f\left(t\right)$ is given by

$$f\left(\omega\right)=\frac{1}{\sqrt{2\pi}}\int\mathrm{d}t\,f\left(t\right)\mathrm{e}^{\mathrm{i}\omega t}. \tag{A.1}$$

The inverse Fourier transformation of the function $f\left(\omega\right)$ is given by

$$f\left(t\right)=\frac{1}{\sqrt{2\pi}}\int\mathrm{d}\omega\,f\left(\omega\right)\mathrm{e}^{-\mathrm{i}\omega t}. \tag{A.2}$$

## A.2. Convolution

The convolution of two functions $\left(b*c\right)\left(t\right)$ is defined as

$$\left(b*c\right)\left(t\right):=\frac{1}{\sqrt{2\pi}}\int_{-\infty}^{\infty}\mathrm{d}t'\,b\left(t-t'\right)c\left(t'\right)=\left(c*b\right)\left(t\right). \tag{A.3}$$

## A.3. Dynamic model of the spin Seebeck effect

It should be noted that, apart from the numerical implementation, the following model has been derived to the largest extent by T. Kampfrath (Department of Physical Chemistry, Fritz Haber Institute of the Max Planck Society, 14195 Berlin, Germany) with valuable help of P. W. Brouwer (Department of Physics, Freie Universität Berlin, 14195 Berlin, Germany).

According to Fig. 8.5b, interfacial F and N layers of thickness $a$ each are coupled by nearest-neighbor sd-type exchange interaction. We divide the interfacial plane in N cells of size $a^3$, and consider the total electron spin $\boldsymbol{S}_j^{\mathrm{F}}$ and $\boldsymbol{S}_j^{\mathrm{N}}$ contained in an F cell and N cell with index $j$, respectively. The expectation value of $\boldsymbol{S}_j^{\mathrm{F}}$ is related to the F magnetization $\boldsymbol{M}$ by $\left\langle\boldsymbol{S}_j^{\mathrm{F}}\right\rangle\propto a^3\boldsymbol{M}$.

According to ab initio simulations [Jia11], coupling between F and N spins is given by the sd-exchange-like Hamiltonian [Ada13, Uch10, Sil79, Kaj10] $H_{\mathrm{sd}}=J_{\mathrm{sd}}\sum\boldsymbol{S}_j^{\mathrm{F}}\cdot$

$\boldsymbol{S}_j^{\mathrm{N}}/\hbar^2$. Therefore, each $\boldsymbol{S}_j^{\mathrm{N}}$ applies the torque $\boldsymbol{S}_j^{\mathrm{F}} \times J_{sd}\boldsymbol{S}_j^{\mathrm{N}}$ on the adjacent $\boldsymbol{S}_j^{\mathrm{F}}$. Accordingly, the total $H_{\mathrm{sd}}$-related torque exerted by N on F is given the sum over all cells $j$. By taking the expectation value, we obtain the average spin current density

$$\boldsymbol{j}_s = -\frac{J_{\mathrm{sd}}}{Na^2\hbar^2}\sum_j \left\langle \boldsymbol{S}_j^{\mathrm{F}} \times \boldsymbol{S}_j^{\mathrm{N}} \right\rangle \tag{A.4}$$

flowing from F to N where $Na^2$ is the coupled interface area. Note that the tensor of the spin current density is given by the tensor product $\boldsymbol{j}_s \otimes \boldsymbol{n}$ where $\boldsymbol{n}$ is the normal unit vector of the F/N interface. We now split the random observable $\boldsymbol{S}_j^{\mathrm{F}} = \left\langle \boldsymbol{S}_j^{\mathrm{F}} \right\rangle + \boldsymbol{s}_j^{\mathrm{F}} + \Delta\boldsymbol{s}_j^{\mathrm{F}}$ in three contributions: its mean value $\left\langle \boldsymbol{S}_j^{\mathrm{F}} \right\rangle \propto a^3\boldsymbol{M}$ and its fluctuating part $\boldsymbol{s}_j^{\mathrm{F}}$, both taken in the absence of interfacial coupling. In contrast, $\Delta\boldsymbol{s}_j^{\mathrm{F}}$ quantifies the modification due to sd-exchange-coupling to the N layer. By applying an analogous splitting to $\boldsymbol{S}_j^{\mathrm{N}}$, the spin current becomes

$$\boldsymbol{j}_s = \boldsymbol{j}_s^{\mathrm{N}} + \boldsymbol{j}_s^{\mathrm{F}} = \frac{J_{\mathrm{sd}}}{Na^2\hbar^2}\sum_j \left\langle \boldsymbol{s}_j^{\mathrm{N}} \times \Delta\boldsymbol{s}_j^{\mathrm{F}} - \boldsymbol{s}_j^{\mathrm{F}} \times \Delta\boldsymbol{s}_j^{\mathrm{N}} \right\rangle. \tag{A.5}$$

It has contributions $\boldsymbol{j}_s^{\mathrm{N}}$ and $\boldsymbol{j}_s^{\mathrm{F}}$ arising from spin fluctuations in N and F, respectively, which cancel in equilibrium. We approximate $\Delta\boldsymbol{s}_j^{\mathrm{F}}$ to first order in $J_{\mathrm{sd}}$, that is, by the linear response given by the spatiotemporal convolution [Šim03]

$$\Delta\boldsymbol{s}_j^{\mathrm{F}} = J_{\mathrm{sd}}\sum_{j'}\int \mathrm{d}t'\, \underline{\chi}^{\mathrm{F}}\left(\boldsymbol{r}_j - \boldsymbol{r}_{j'}, t-t'\right)\boldsymbol{s}_{j'}^{\mathrm{N}}\left(t'\right). \tag{A.6}$$

Here, $\underline{\chi}^{\mathrm{F}}\left(\boldsymbol{r},t\right) = \left(\chi_{ii'}^{\mathrm{F}}\left(\boldsymbol{r},t\right)\right)$ is the spin susceptibility tensor of F in matrix notation. An analogous expression holds for $\Delta\boldsymbol{s}_j^{\mathrm{N}}$ with respect to $\underline{\chi}^{\mathrm{N}}\left(\boldsymbol{r}_j - \boldsymbol{r}_{j'}, t-t'\right)\boldsymbol{s}_{j'}^{\mathrm{F}}\left(t'\right)$. We furthermore assume that spins of different cells have negligible correlation, for instance $\left\langle \boldsymbol{s}_j^{\mathrm{N}}\left(t\right)\boldsymbol{s}_i^{\mathrm{N}}\left(t'\right)\right\rangle \propto \delta_{ji}$. By substituting $\Delta\boldsymbol{s}_j^{\mathrm{N}}$ and $\Delta\boldsymbol{s}_j^{\mathrm{F}}$ in Eq. A.5, we obtain

$$\begin{aligned} \boldsymbol{j}_s\left(t\right) =& \boldsymbol{j}_s^{\mathrm{N}} + \boldsymbol{j}_s^{\mathrm{F}} & \text{(A.7)} \\ =& \frac{J_{\mathrm{sd}}}{a^2\hbar^2}\int \mathrm{d}t' \left[\left\langle \boldsymbol{s}^{\mathrm{N}}\left(t\right) \times \underline{\chi}^{\mathrm{F}}\left(t-t'\right)\boldsymbol{s}^{\mathrm{N}}\left(t'\right)\right\rangle - \left\langle \boldsymbol{s}^{\mathrm{F}}\left(t\right) \times \underline{\chi}^{\mathrm{N}}\left(t-t'\right)\boldsymbol{s}^{\mathrm{F}}\left(t'\right)\right\rangle\right], & \text{(A.8)} \end{aligned}$$

where $\boldsymbol{s}^{\mathrm{N}} = \boldsymbol{s}_j^{\mathrm{N}}$ and $\boldsymbol{s}^{\mathrm{F}} = \boldsymbol{s}_j^{\mathrm{F}}$ are the spin of any conjoined F and N cells, respectively, say at $j = j' = 1$. The $\underline{\chi}^{\mathrm{F}}\left(\boldsymbol{r}_j - \boldsymbol{r}_{j'} = 0, t\right)$ and $\underline{\chi}^{\mathrm{N}}\left(\boldsymbol{r}_j - \boldsymbol{r}_{j'} = 0, t\right)$ can be interpreted as the spin susceptibility of any F and N cell, respectively. Therefore, we arrive at the picture of a single pair of coupled F-N cells as considered in the main text.

In Eq. A.8, the difference of the two terms reflects the competition between the torques arising from the fluctuations of the N-cell and F-cell spins. For example, the first term can be understood as follows: the fluctuating exchange field $J_{\mathrm{sd}}\boldsymbol{s}^{\mathrm{N}}\left(t\right)$ due to N exerts torque on the magnetic moment $\Delta\boldsymbol{s}^{\mathrm{F}} = J_{\mathrm{sd}}\int \mathrm{d}t'\,\underline{\chi}^{\mathrm{F}}\left(t-t'\right)\boldsymbol{s}^{\mathrm{N}}\left(t'\right)$ which it has induced in F before. As this torque scales quadratically with the noise

$\boldsymbol{s}^{\mathrm{N}}$, it does not vanish, provided $\Delta\boldsymbol{s}^{\mathrm{F}}(t)$ results from an earlier time $t'$ that lies inside the correlation window of the N-cell spin. The last statement becomes more apparent when we explicitly write out the matrix and vector products in Eq. A.8. Consequently, the component $j_{\mathrm{s}} := j_{\mathrm{s}x}$ of the spin current density polarized along the sample magnetization (see Fig. 8.1) is found to be

$$j_{\mathrm{s}}(t) = \frac{J_{\mathrm{sd}}}{a^2\hbar^2}\sum_{ijk}\epsilon_{xjk}\int \mathrm{d}t' \left[\chi^{\mathrm{F}}_{kl}(t-t')\left\langle s^{\mathrm{N}}_j(t)\, s^{\mathrm{N}}_l(t')\right\rangle - \chi^{\mathrm{N}}_{kl}(t-t')\left\langle s^{\mathrm{F}}_j(t)\, s^{\mathrm{F}}_l(t')\right\rangle\right], \tag{A.9}$$

where $\epsilon_{xjk}$ denotes the Levi-Civita symbol. The first term of Eq. A.9 quantifies the torque due to N-cell spin fluctuations and depends critically on the spin correlation function $\left\langle s^{\mathrm{N}}_j(t)\, s^{\mathrm{N}}_l(t')\right\rangle$ which typically peaks sharply around time $t = t'$. Any temperature change of the N spins will lead to a (possibly delayed) modification of the spin correlation function and, therefore, a spin current response whose time-dependence is determined by the spin susceptibility $\chi^{\mathrm{F}}_{kl}(t)$ of the ferromagnet F. An analogous interpretation applies to the second term.

Note that Eq. A.9 is valid for all kinds of magnetic insulators F, including anti-ferromagnets. If N is isotropic (as in the case of Pt), one has $\left\langle s^{\mathrm{N}}_j(t)\, s^{\mathrm{N}}_l(t')\right\rangle \propto \delta_{jl}\left\langle s^{\mathrm{N}}_z(t)\, s^{\mathrm{N}}_z(t')\right\rangle$, and the first term of Eq. A.9 turns into Eq. 8.2 in Chapter 8.

**From fluctuations to temperatures.** To relate the correlation functions in Eq. A.9 to temperatures in F and N, we consider the Kubo form of the fluctuation-dissipation theorem in the classical limit [Kub66],

$$\left\langle s^{\mathrm{N}}_i(t)\, s^{\mathrm{N}}_j(t')\right\rangle/\hbar^2 = k_{\mathrm{B}}T^{\mathrm{N}} \cdot \left(\bar{\Theta} * \chi^{\mathrm{N}}_{ij} - \bar{\Theta} * \bar{\chi}^{\mathrm{N}}_{ij}\right)(t-t'), \tag{A.10}$$

where $\Theta$ is the Heaviside step function. The overbar denotes time inversion, that is, $\bar{f}(t) = f(-t)$, and $*$ denotes convolution (see App. A.2). Note that strictly this equation refers to equilibrium and cannot be applied to the situation of our experiment (see Chapter 8) where the temperature of N (and F) is generally time-dependent.

To derive a fluctuation-dissipation theorem for a nonstationary system, we make use of the Langevin theory [Kub66, Bal79, Atx16, Ell15] in which the N-cell spin is assumed to be coupled to a bath (or thermostat) of time-dependent temperature $T^{\mathrm{N}}(t)$. In this framework [Kub66, Bal79], the spin fluctuations $\boldsymbol{s}^{\mathrm{N}}(t)$ arise from a random magnetic field $\boldsymbol{r}^{\mathrm{N}}(t)$, with vanishing ensemble average $\left\langle \boldsymbol{r}^{\mathrm{N}}(t)\right\rangle$, the bath applies to the spin system. Assuming $\boldsymbol{r}^{\mathrm{N}}$ has no memory, the intensity of the spin fluctuations is directly proportional to the instantaneous bath temperature,

$$\left\langle r^{\mathrm{N}}_i(t)\, r^{\mathrm{N}}_j(t')\right\rangle = A^{\mathrm{N}}k_{\mathrm{B}}T^{\mathrm{N}}(t)\,\delta_{ij}\delta(t-t'), \tag{A.11}$$

where the constant $A^{\mathrm{N}}$ quantifies how strongly the N bath and the N spins are coupled. By using linear response, $\boldsymbol{s}^{\mathrm{N}} = \underline{\chi}^{\mathrm{N}} * \boldsymbol{r}^{\mathrm{N}}$, and writing out the convolution (see App. A.2), we obtain the spin-spin correlation function for a time-dependent bath temperature $T^{\mathrm{N}}$,

$$\left\langle s_i^{\mathrm{N}}(t)\, s_j^{\mathrm{N}}(t')\right\rangle / \hbar^2 = A^{\mathrm{N}} k_{\mathrm{B}} \sum_m \int \mathrm{d}\tau\, \chi_{im}^{\mathrm{N}}(t-\tau)\, \chi_{jm}^{\mathrm{N}}(t'-\tau)\, T^{\mathrm{N}}(\tau)\,. \tag{A.12}$$

This relationship shows that the temporal structure of the spin susceptibility $\chi_{ij}^{\mathrm{N}}$ of N determines how quickly the system adapts to a sudden change in $T^{\mathrm{N}}$. In the case of time-independent $T^{\mathrm{N}}$, Eq. A.12 reduces to the familiar Langevin-version of the fluctuation-dissipation theorem [Kub66, Bal79]. Comparison with the Kubo-type fluctuation-dissipation theorem (Eq. A.10) yields

$$\bar{\Theta} * \left(\chi_{jl}^{\mathrm{N}} - \bar{\chi}_{lj}^{\mathrm{N}}\right) = A^{\mathrm{N}} \sum_m \chi_{jm}^{\mathrm{N}} * \chi_{lm}^{\mathrm{N}}. \tag{A.13}$$

This constraint on the spin susceptibility function can be used to determine the constant $A^{\mathrm{N}}$. Completely analogous equations are obtained for the F-cell spin. We now substitute Eq. A.12 and its analog for F into Eq. A.10 to obtain

$$j_s(t) = \left(\kappa^{\mathrm{F}} * T^{\mathrm{F}} - \kappa^{\mathrm{N}} * T^{\mathrm{N}}\right)(t)\,, \tag{A.14}$$

with the response functions

$$\kappa^{\mathrm{N}}(t) = \frac{k_{\mathrm{B}} J_{\mathrm{sd}}^2 A^{\mathrm{N}}}{a^2} \sum_{jklm} \epsilon_{zjk} \chi_{jm}^{\mathrm{N}}(t) \cdot \left(\chi_{kl}^{\mathrm{F}} * \chi_{lm}^{\mathrm{N}}\right)(t) \tag{A.15}$$

and completely analogously

$$\kappa^{\mathrm{F}}(t) = \frac{k_{\mathrm{B}} J_{\mathrm{sd}}^2 A^{\mathrm{F}}}{a^2} \sum_{jklm} \epsilon_{zjk} \chi_{jm}^{\mathrm{F}}(t) \cdot \left(\chi_{kl}^{\mathrm{N}} * \chi_{lm}^{\mathrm{F}}\right)(t)\,. \tag{A.16}$$

Equations A.14, A.15, and A.16 can be considered as time-dependent generalization of the static constitutive relation (Eq. 8.1) of the interfacial SSE. It can be shown that in the static limit of time-independent temperatures, Eq. A.14 reduces to Eq. 8.1, that is, $j_s = \mathcal{K} \cdot \left(T^{\mathrm{F}} - T^{\mathrm{N}}\right)$, where $\mathcal{K} = \int \mathrm{d}t\, \kappa^{\mathrm{N}}(t) = \int \mathrm{d}t\, \kappa^{\mathrm{F}}(t)$. The proof makes use of Eqs. A.15, A.13 and A.16, Parseval's theorem, and the causality of the spin susceptibilities of F and N.

For an isotropic nonmagnetic metal N with $\chi_{ij}^{\mathrm{N}}(t) = \delta_{ij} \chi^{\mathrm{N}}(t)$, Eq. A.15 implies the somewhat simpler relationship

$$\kappa^{\mathrm{N}} = \frac{k_{\mathrm{B}} J_{\mathrm{sd}}^2 A^{\mathrm{N}}}{a^2} \chi^{\mathrm{N}} \cdot \left[\left(\chi_{yz}^{\mathrm{F}} - \chi_{zy}^{\mathrm{F}}\right) * \chi^{\mathrm{N}}\right]. \tag{A.17}$$

For the second response function, we obtain

$$\kappa^{\mathrm{F}}(t) = \frac{k_{\mathrm{B}} J_{\mathrm{sd}}^2 A^{\mathrm{F}}}{a^2} \sum_m \left[\chi_{ym}^{\mathrm{F}} \cdot \left(\chi^{\mathrm{N}} * \chi_{xm}^{\mathrm{F}}\right) - \chi_{xm}^{\mathrm{F}} \cdot \left(\chi^{\mathrm{N}} * \chi_{ym}^{\mathrm{F}}\right)\right]. \tag{A.18}$$

**Nonthermal electron distribution.** Our previous considerations (Eqs. A.11 and A.12) presume a thermal bath with temperature $T^{\mathrm{N}}$. To reveal the nature of the bath and to also account for the nonthermal state of the N electrons directly after laser excitation, we extend our model of the N layer. As the fluctuation of the N-cell spin is assumed to arise predominantly from electrons entering and leaving the N cell [Tse05, Žut11, Ber96, Sti02], we model the dynamics of the N-cell spin as the sum of random events $l$,

$$s_z^{\mathrm{N}}(t) = \hbar \sum_l \sigma_l p(t - t_l). \tag{A.19}$$

In each event, an electron with spin $z$-component $\sigma_l$ and $\langle \sigma_l \rangle = 0$ enters the N cell at time $t_l$. The electron propagation into and out of the cell is captured by the function $p(t)$ whose width is on the order of $\tau^{\mathrm{N}}$, the mean time it takes an electron to traverse the interfacial metal layer. By neglecting correlations between different events $l$ and between $\sigma_l$ and $t_l$, Eq. A.19 leads to the spin correlation function $\left\langle s_z^{\mathrm{N}}(t)\, s_z^{\mathrm{N}}(t')\right\rangle \propto \sum_l \langle p(t-t_l)\, p(t'-t_l)\rangle$. The sum over all $t_l$ can be rewritten as an integral over an auxiliary time $\tau$ and yields

$$\left\langle s_z^{\mathrm{N}}(t)\, s_z^{\mathrm{N}}(t')\right\rangle \propto \int \mathrm{d}\tau\, p(t-\tau)\, p(t'-\tau)\, \Gamma(\tau), \tag{A.20}$$

where $\Gamma(\tau)\,\mathrm{d}\tau$ is the number of events in the time interval $[\tau, \tau + \mathrm{d}\tau]$.

Remarkably, Eq. A.20 has the same structure as Eq. A.12. To work out this analogy even further, we note that $\Gamma(\tau)$ equals the rate at which N electrons with a given energy $\varepsilon$ are elastically backscattered at the F/N interface (Fig. 8.5b-e). More precisely, they are scattered from Bloch states (see Section 2.2) $k$ with negative (incident) group velocity $v_{kz}$ to states $k'$ with positive (outgoing) $v_{k'z}$. According to Fermi's Golden Rule [All87], the scattering rate is

$$\Gamma(t) \propto \sum_{kk'} |M_{kk'}|^2\, n_k(t) \cdot [1 - n_{k'}(t)]\, \delta(\varepsilon_{k'} - \varepsilon_k). \tag{A.21}$$

We now assume diffuse scattering, constant matrix elements $M_{kk'}$ and isotropic electronic occupation numbers $n_k(t) = n(\varepsilon_k, t)$ where $\varepsilon_k$ denotes the band structure (see Section 2.2). As a consequence, Eq. A.21 simplifies to $\Gamma(t) \propto \int \mathrm{d}\varepsilon\, D(\varepsilon)^2\, n(\varepsilon, t) \cdot [1 - n(\varepsilon, t)]$ where $D(\varepsilon) \propto \sum_k \delta(\varepsilon - \varepsilon_k)$ is the electronic density of states [All87]. Since for Pt, $D(\varepsilon)$ is approximately constant around the Fermi energy [Lin08], Eq. A.21 finally yields

$$\Gamma(t) \propto k_{\mathrm{B}} \widetilde{T}_{\mathrm{e}}^{\mathrm{N}}(t) = \int \mathrm{d}\varepsilon\, n(\varepsilon, t) \cdot [1 - n(\varepsilon, t)], \tag{A.22}$$

where $\widetilde{T}_{\mathrm{e}}^{\mathrm{N}}(t)$ is the instantaneous generalized electron temperature, consistent with Eq. 8.3 of the main text.

In the case of a thermal electron distribution, $n(\varepsilon, t)$ equals a Fermi function (see Section 2.2), and $\Gamma(t)$ becomes proportional to the instantaneous electronic temperature $T_{\mathrm{e}}^{\mathrm{N}}(t)$. Consequently, comparison of Eq. A.20 to Eq. A.12 identifies the bath temperature $T^{\mathrm{N}}(t)$ of the Langevin model with $T_{\mathrm{e}}^{\mathrm{N}}(t)$, the temperature of the electronic orbital degrees of freedom of the N layer. This reasoning even applies to the nonthermal case and leads us to set $T^{\mathrm{N}}(t) = \widetilde{T}_{\mathrm{e}}^{\mathrm{N}}(t)$, thereby extending Eq. A.12 to nonthermal electron distributions.

Similar considerations can be applied to the correlation function of the F-cell spin, if we wish to go beyond the Langevin-type result of Eq. A.12. According to Eq. A.25 and Ref. [Rez14], the spin current $\boldsymbol{j}_{\mathrm{s}}^{\mathrm{F}}(t)$ due to F-cell spin fluctuations can be expressed by the occupation numbers of all magnon modes, including nonthermal populations. However, since in our experiment the pump-induced changes of the YIG layer are negligible, we do not consider this aspect further.

**Numerical implementation and estimates.** Our numerical calculations are based on Eqs. A.17 and A.18. For the N layer, we assume $\chi^{\mathrm{N}}(t) = \chi_{\mathrm{DC}}^{\mathrm{N}}\Theta(t)\exp\left(-t/\tau^{\mathrm{N}}\right)$ where $\tau^{\mathrm{N}} = 3.5\,\mathrm{fs}$ and $1\,\mathrm{fs}$, as determined by using the Fermi velocity of Pt [Ket68] and Cu [Ash98], respectively. The N-cell DC spin susceptibility $\chi_{\mathrm{DC}}^{\mathrm{N}}$ is related to the paramagnetic susceptibility $\widetilde{\chi}_{\mathrm{DC}}^{\mathrm{N}}$ of Pt [Clo64, Fra75] and Cu [Mor13] through $\chi_{\mathrm{DC}}^{\mathrm{N}} = a^3\widetilde{\chi}_{\mathrm{DC}}^{\mathrm{N}}/\mu_0 g_{\mathrm{e}}^2\mu_{\mathrm{B}}^2$ where $\mu_0$ is the vacuum permeability, $g_{\mathrm{e}} \approx -2$, and $\mu_{\mathrm{B}}$ is the Bohr magneton. The factor $a^3$ is required since $\chi_0^{\mathrm{N}}$ refers to the integrated N-cell volume whereas $\widetilde{\chi}_0^{\mathrm{N}}$ is given per volume. The factor $\mu_0 g_{\mathrm{e}}^2\mu_{\mathrm{B}}^2$ accounts for the different units used in the definition of $\widetilde{\chi}_0^{\mathrm{N}}$ and $\chi_0^{\mathrm{N}}$.

For F=YIG, we determine the $\underline{\chi}^{\mathrm{F}}$ tensor by the Kubo formula (Eq. A.10) using the equilibrium spin correlation functions $\left\langle s_j^{\mathrm{F}}(t)\, s_l^{\mathrm{F}}(t')\right\rangle = \left\langle s_j^{\mathrm{F}}(t-t')\, s_l^{\mathrm{F}}(0)\right\rangle$ as an input. These functions are calculated by atomistic spin-dynamics simulations [Bar16, Ell15, Atx16] in which ~$10^6$ $\mathrm{Fe}^{3+}$ spins are propagated classically according to the YIG spin Hamiltonian plus a thermal noise field provided by a thermostat with temperature 300 K. Trajectories $\boldsymbol{s}^{\mathrm{F}}(t)$ are obtained by summing all 20 $\mathrm{Fe}^{3+}$ spins of a selected YIG unit cell. Note that this summation is approximately tantamount to summing up magnon amplitudes over all wave vectors and magnon branches [Bar16]. The ensemble average is obtained by averaging the product $s_j^{\mathrm{F}}(t-t')\, s_l^{\mathrm{F}}(0)$ over many trajectories.

As a cross check, we also estimate the order of magnitude of $\mathcal{K} = \int \mathrm{d}t\, \kappa^{\mathrm{N}}(t)$ with $\kappa$ given by Eq. A.17. This formula can be simplified using Eq. A.13 and yields the spin Seebeck coefficient

$$\mathcal{K} = \int \mathrm{d}t\, \chi^{\mathrm{N}}(t) \cdot \left[\Theta * \left(\chi_{yz}^{\mathrm{F}} - \chi_{zy}^{\mathrm{F}}\right)\right](t)\,. \tag{A.23}$$

For our estimate, we use the analytical $\chi^{\mathrm{N}}(t)$ from above. Concerning the transverse susceptibility of F, we solve the equation of motion $\hbar\Delta\dot{\boldsymbol{s}}^{\mathrm{F}} = \left\langle \boldsymbol{S}^{\mathrm{F}}\right\rangle \times J_{\mathrm{sd}}\boldsymbol{s}^{\mathrm{N}}$, compare to $\Delta\boldsymbol{s}^{\mathrm{F}} = \underline{\chi}^{\mathrm{F}} * J_{\mathrm{sd}}\boldsymbol{s}^{\mathrm{N}}$ and find $\chi_{yz}^{\mathrm{F}} - \chi_{zy}^{\mathrm{F}} = \Theta(t) \cdot 2\left|\left\langle \boldsymbol{S}^{\mathrm{F}}\right\rangle\right|/\hbar^2$ where $\left|\left\langle \boldsymbol{S}^{\mathrm{F}}\right\rangle\right| \approx 7\hbar$ is the total spin of the YIG unit cell at room temperature. We obtain

$$\mathcal{K} = \frac{2k_{\mathrm{B}}J_{\mathrm{sd}}^2\left|\left\langle \boldsymbol{S}^{\mathrm{F}}\right\rangle\right|\chi_{\mathrm{DC}}^{\mathrm{N}}\tau^{\mathrm{N}}}{a^2\hbar^2}, \tag{A.24}$$

which allows us to estimate $J_{\mathrm{sd}} \approx 4\,\mathrm{meV}$ using Eq. 8.1 and considering the peak of the measured $j_{\mathrm{s}}(t)$ (Fig. 8.5a).

Assuming that $J_{\mathrm{sd}}$ is the same for YIG/Pt and YIG/Cu and using Eq. A.24, we find that the spin Seebeck coefficient K of YIG/Cu is a factor of about 0.5 smaller than that of YIG/Pt because of the different spin susceptibility (see above). This difference in K provides a further reason for our observation that the YIG/Cu/Pt sample delivers a factor of 6 smaller THz-emission signal than YIG/Pt (see Fig. 8.2e).

Note that our equations for the SSE current are formulated in terms of the constant $J_{\mathrm{sd}}$ that quantifies the coupling strength of electron spins at the F/N interface [Ada13]. To connect to works [Bur13, Wei13] that formulate the SSE in terms of the spin-mixing conductance $g^{\uparrow\downarrow}$, we consider the current $\boldsymbol{j}_{\mathrm{s}}^{\mathrm{F}}$ arising from the fluctuations of the F spins. Assuming an isotropic susceptibility of the N-cell spins and approximating $\boldsymbol{s}^{\mathrm{F}}(t')$ by $\boldsymbol{s}^{\mathrm{F}}(t) + \dot{\boldsymbol{s}}^{\mathrm{F}}(t)(t'-t)$ in Eq. A.8 yields

$$\boldsymbol{j}_{\mathrm{s}}^{\mathrm{F}}(t) = \left\langle \boldsymbol{s}^{\mathrm{F}}(t) \times \dot{\boldsymbol{s}}^{\mathrm{F}}(t) \right\rangle \frac{J_{\mathrm{sd}}^2}{a^2\hbar^2} \int \mathrm{d}t'\, \chi^{\mathrm{N}}(t')\, t'. \tag{A.25}$$

This relationship agrees with the familiar result for thermal spin pumping, which is typically written as $\left\langle \boldsymbol{s}^{\mathrm{F}}(t) \times \dot{\boldsymbol{s}}^{\mathrm{F}}(t) \right\rangle \hbar\, \mathrm{Re}g^{\uparrow\downarrow}/4\pi \left|\left\langle \boldsymbol{S}^{\mathrm{F}} \right\rangle\right|^2$ (Ref. [Tse05]). Comparison of the prefactors in both equations yields

$$\mathrm{Re}g^{\uparrow\downarrow} = \frac{4\pi \left|\left\langle \boldsymbol{S}^{\mathrm{F}} \right\rangle\right|^2 J_{\mathrm{sd}}^2 \chi_{\mathrm{DC}}^{\mathrm{N}}}{\hbar^3 a^2} \int \mathrm{d}t'\, \chi^{\mathrm{N}}(t')\, t'. \tag{A.26}$$

By modeling $\chi^{\mathrm{N}}$ as detailed above and evaluating the integral, we obtain $\mathrm{Re}g^{\uparrow\downarrow} = 4\pi \left|\left\langle \boldsymbol{S}^{\mathrm{F}} \right\rangle\right|^2 J_{\mathrm{sd}}^2 \chi_{\mathrm{DC}}^{\mathrm{N}} \tau^{\mathrm{N}}/\hbar^3 a^2 \approx 2.4 \cdot 10^{18}\,\mathrm{m}^{-2}$, in good agreement with calculated [Jia11] and measured values [Bur13, Wei13].

# Bibliography

[Ada13] H. Adachi, K.-I. Uchida, E. Saitoh, & S. Maekawa. *Theory of the spin Seebeck effect.* Reports on Progress in Physics **76**, 3, (2013) 036501.

[Aes97] M. Aeschlimann, M. Bauer, S. Pawlik, W. Weber, R. Burgermeister, D. Oberli, & H. Siegmann. *Ultrafast spin-dependent electron dynamics in fcc Co.* Physical review letters **79**, 25, (1997) 5158.

[Agr14] M. Agrawal, V. Vasyuchka, A. Serga, A. Kirihara, P. Pirro, T. Langner, M. Jungfleisch, A. Chumak, E. T. Papaioannou, & B. Hillebrands. *Role of bulk-magnon transport in the temporal evolution of the longitudinal spin-Seebeck effect.* Physical Review B **89**, 22, (2014) 224414.

[Ale17] A. Alekhin, I. Razdolski, N. Ilin, J. P. Meyburg, D. Diesing, V. Roddatis, I. Rungger, M. Stamenova, S. Sanvito, U. Bovensiepen, *et al. Femtosecond spin current pulses generated by the nonthermal spin-dependent Seebeck effect and interacting with ferromagnets in spin valves.* Physical Review Letters **119**, 1, (2017) 017202.

[All87] P. B. Allen. *Theory of thermal relaxation of electrons in metals.* Physical review letters **59**, 13, (1987) 1460.

[All12] L. Allen & J. H. Eberly. *Optical resonance and two-level atoms.* Courier Corporation, 2012.

[An12] Z. An, F. Liu, Y. Lin, & C. Liu. *The universal definition of spin current.* Scientific reports **2**, (2012) 388.

[Apo14] V. Apostolopoulos & M. Barnes. *THz emitters based on the photo-Dember effect.* Journal of Physics D: Applied Physics **47**, 37, (2014) 374002.

[Ash98] N. W. Ashcroft, N. D. Mermin, & S. Rodriguez. *Solid state physics.* American Association of Physics Teachers, 1998.

[Atx16] U. Atxitia, D. Hinzke, & U. Nowak. *Fundamentals and applications of the Landau–Lifshitz–Bloch equation.* Journal of Physics D: Applied Physics **50**, 3, (2016) 033003.

[Awa16] N. Awari, S. Kovalev, C. Fowley, K. Rode, R. Gallardo, Y.-C. Lau, D. Betto, N. Thiyagarajah, B. Green, O. Yildirim, *et al. Narrow-band tunable terahertz emission from ferrimagnetic* $Mn_{3-x}Ga$ *thin films.* Applied Physics Letters **109**, 3, (2016) 032403.

[Bai88] M. N. Baibich, J. M. Broto, A. Fert, F. N. Van Dau, F. Petroff, P. Etienne, G. Creuzet, A. Friederich, & J. Chazelas. *Giant magnetoresistance of (001) Fe/(001) Cr magnetic superlattices.* Physical review letters **61**, 21, (1988) 2472.

[Bal79] V. Balakrishnan. *Fluctuation-dissipation theorems from the generalised Langevin equation.* Pramana **12**, 4, (1979) 301.

[Bar05] T. Bartel, P. Gaal, K. Reimann, M. Woerner, & T. Elsaesser. *Generation of single-cycle THz transients with high electric-field amplitudes.* Optics Letters **30**, 20, (2005) 2805.

[Bar16] J. Barker & G. E. Bauer. *Thermal spin dynamics of yttrium iron garnet.* Physical review letters **117**, 21, (2016) 217201.

[Bar17] J. M. Bartell, C. L. Jermain, S. V. Aradhya, J. T. Brangham, F. Yang, D. C. Ralph, & G. D. Fuchs. *Imaging Magnetization Structure and Dynamics in Ultrathin $Y_3Fe_5O_{12}$/Pt Bilayers with High Sensitivity Using the Time-Resolved Longitudinal Spin Seebeck Effect.* Physical Review Applied **7**, 4, (2017) 044004.

[Bat10] M. Battiato, K. Carva, & P. M. Oppeneer. *Superdiffusive spin transport as a mechanism of ultrafast demagnetization.* Physical review letters **105**, 2, (2010) 027203.

[Bau12] G. E. Bauer, E. Saitoh, & B. J. Van Wees. *Spin caloritronics.* Nature materials **11**, 5, (2012) 391.

[Bau15] S. Baumann, F. Donati, S. Stepanow, S. Rusponi, W. Paul, S. Gangopadhyay, I. Rau, G. Pacchioni, L. Gragnaniello, M. Pivetta, *et al.* *Origin of perpendicular magnetic anisotropy and large orbital moment in Fe atoms on MgO.* Physical review letters **115**, 23, (2015) 237202.

[Bea98] E. Beaurepaire, M. Maret, V. Halté, J.-C. Merle, A. Daunois, & J.-Y. Bigot. *Spin dynamics in $CoPt_3$ alloy films: a magnetic phase transition in the femtosecond time scale.* Physical Review B **58**, 18, (1998) 12134.

[Ber96] L. Berger. *Emission of spin waves by a magnetic multilayer traversed by a current.* Physical Review B **54**, 13, (1996) 9353.

[Ber13] C. Berry, N. Wang, M. Hashemi, M. Unlu, & M. Jarrahi. *Significant performance enhancement in photoconductive terahertz optoelectronics by incorporating plasmonic contact electrodes.* Nature communications **4**, (2013) 1622.

[Bin89] G. Binasch, P. Grünberg, F. Saurenbach, & W. Zinn. *Enhanced magnetoresistance in layered magnetic structures with antiferromagnetic interlayer exchange.* Physical review B **39**, 7, (1989) 4828.

[Bla11] F. Blanchard, G. Sharma, L. Razzari, X. Ropagnol, H.-C. Bandulet, F. Vidal, R. Morandotti, J.-C. Kieffer, T. Ozaki, H. Tiedje, *et al.* *Gen-*

*eration of intense terahertz radiation via optical methods.* IEEE Journal of Selected Topics in Quantum Electronics **17**, 1, (2011) 5.

[Blu03] S. Blundell. *Magnetism in condensed matter.* AAPT, 2003.

[Boc73] V. Bochkarev, V. Buravikhin, V. Sukhomlin, & V. Egorov. *Hall effect and electrical properties of films obtained from* $DyCo_5$ *compound.* Izvestiya Vysshikh Uchebnykh Zavedenij, Fizika 145–148.

[Boo14] S. R. Boona, R. C. Myers, & J. P. Heremans. *Spin caloritronics.* Energy & Environmental Science **7**, 3, (2014) 885.

[Bos16] D. Bossini, S. Dal Conte, Y. Hashimoto, A. Secchi, R. Pisarev, T. Rasing, G. Cerullo, & A. Kimel. *Macrospin dynamics in antiferromagnets triggered by sub-20 femtosecond injection of nanomagnons.* Nature communications **7**.

[Bou11] O. Boulle, G. Malinowski, & M. Kläui. *Current-induced domain wall motion in nanoscale ferromagnetic elements.* Materials Science and Engineering: R: Reports **72**, 9, (2011) 159.

[Boy03] R. W. Boyd. *Nonlinear optics.* Academic press, 2003.

[Bra16a] L. Braun. *Electron and Phonon Dynamics in Topological Insulators at THz Frequencies.* Dissertation, Freie Universität Berlin (2016).

[Bra16b] L. Braun, G. Mussler, A. Hruban, M. Konczykowski, T. Schumann, M. Wolf, M. Münzenberg, L. Perfetti, & T. Kampfrath. *Ultrafast photocurrents at the surface of the three-dimensional topological insulator* $Bi_2Se_3$. Nature communications **7**, (2016) 13259.

[Bru08] F. D. Brunner, O.-P. Kwon, S.-J. Kwon, M. Jazbinšek, A. Schneider, & P. Günter. *A hydrogen-bonded organic nonlinear optical crystal for high-efficiency terahertz generation and detection.* Optics express **16**, 21, (2008) 16496.

[Brü12] E. Bründermann, H.-W. Hübers, & M. F. Kimmitt. *Terahertz techniques*, Bd. 151. Springer, 2012.

[Buc15] F. Buccheri & X.-C. Zhang. *Terahertz emission from laser-induced microplasma in ambient air.* Optica **2**, 4, (2015) 366.

[Bur13] C. Burrowes & B. Heinrich. *Spin Pumping at Ytrium Iron Garnet Interfaces.* In *Magnonics.* Springer, 2013 129–141.

[Caf05] A. P. Caffrey, P. E. Hopkins, J. M. Klopf, & P. M. Norris. *Thin film non-noble transition metal thermophysical properties.* Microscale Thermophysical Engineering **9**, 4, (2005) 365.

[Cat12] G. Cataldo, J. A. Beall, H.-M. Cho, B. McAndrew, M. D. Niemack, & E. J. Wollack. *Infrared dielectric properties of low-stress silicon nitride.* Optics letters **37**, 20, (2012) 4200.

[Cha74] G. Chantry, J. Fleming, E. A. Nicol, H. Willis, M. Cudby, & F. Boerio. *The far infra-red spectrum of crystalline polytetrafluoroethylene.* Polymer **15**, 2, (1974) 69.

[Cha07a] W. L. Chan, J. Deibel, & D. M. Mittleman. *Imaging with terahertz radiation.* Reports on progress in physics **70**, 8, (2007) 1325.

[Cha07b] C. Chappert, A. Fert, & F. N. Van Dau. *The emergence of spin electronics in data storage.* Nature materials **6**, 11, (2007) 813.

[Cha16] C.-Z. Chang & M. Li. *Quantum anomalous Hall effect in time-reversal-symmetry breaking topological insulators.* Journal of Physics: Condensed Matter **28**, 12, (2016) 123002.

[Che93] V. Cherepanov, I. Kolokolov, & V. L'vov. *The saga of YIG: spectra, thermodynamics, interaction and relaxation of magnons in a complex magnet.* Physics reports **229**, 3, (1993) 81.

[Cho13] L. Chotorlishvili, Z. Toklikishvili, V. Dugaev, J. Barnaś, S. Trimper, & J. Berakdar. *Fokker-Planck approach to the theory of the magnon-driven spin Seebeck effect.* Physical Review B **88**, 14, (2013) 144429.

[Chu07] E. M. Chudnovsky. *Theory of spin Hall effect: Extension of the Drude model.* Physical review letters **99**, 20, (2007) 206601.

[Chu15] A. Chumak, V. Vasyuchka, A. Serga, & B. Hillebrands. *Magnon spintronics.* Nature Physics **11**, 6, (2015) 453.

[Clo64] A. Clogston, V. Jaccarino, & Y. Yafet. *Interpretation of Knight shifts and susceptibilities of transition metals: Platinum.* Physical Review **134**, 3A, (1964) A650.

[Coc13] T. L. Cocker, V. Jelic, M. Gupta, S. J. Molesky, J. A. Burgess, G. De Los Reyes, L. V. Titova, Y. Y. Tsui, M. R. Freeman, & F. A. Hegmann. *An ultrafast terahertz scanning tunnelling microscope.* Nature Photonics **7**, 8, (2013) 620.

[Coc16] T. L. Cocker, D. Peller, P. Yu, J. Repp, & R. Huber. *Tracking the ultrafast motion of a single molecule by femtosecond orbital imaging.* Nature **539**, 7628, (2016) 263.

[Cor14] M. Cornet, J. Degert, E. Abraham, & E. Freysz. *Terahertz Kerr effect in gallium phosphide crystal.* JOSA B **31**, 7, (2014) 1648.

[Cot86] M. G. Cottam & D. J. Lockwood. *Light scattering in magnetic solids.* Wiley New York (NY), 1986.

[Cra17] J. Cramer, T. Seifert, A. Kronenberg, F. Fuhrmann, G. Jakob, M. Jourdan, T. Kampfrath, & M. Kläui. *Complex THz and DC inverse spin Hall effect in YIG/Cu$_{1-x}$Ir$_x$ bilayers across a wide concentration range.* arXiv preprint arXiv:1709.01890 .

[Cze11] F. Czeschka, L. Dreher, M. Brandt, M. Weiler, M. Althammer, I.-M. Imort, G. Reiss, A. Thomas, W. Schoch, W. Limmer, *et al. Scaling behavior of the spin pumping effect in ferromagnet-platinum bilayers.* Physical review letters **107**, 4, (2011) 046601.

[DA11] J. A. Del Alamo. *Nanometre-scale electronics with III-V compound semiconductors.* Nature **479**, 7373, (2011) 317.

[D'A14] F. D'Angelo, Z. Mics, M. Bonn, & D. Turchinovich. *Ultra-broadband THz time-domain spectroscopy of common polymers using THz air photonics.* Optics express **22**, 10, (2014) 12475.

[Dai04] J. Dai, J. Zhang, W. Zhang, & D. Grischkowsky. *Terahertz time-domain spectroscopy characterization of the far-infrared absorption and index of refraction of high-resistivity, float-zone silicon.* JOSA B **21**, 7, (2004) 1379.

[Dem16] K.-U. Demasius, T. Phung, W. Zhang, B. P. Hughes, S.-H. Yang, A. Kellock, W. Han, A. Pushp, & S. S. Parkin. *Enhanced spin–orbit torques by oxygen incorporation in tungsten films.* Nature communications **7**, (2016) 10644.

[Dhe67] P. Dheer. *Galvanomagnetic effects in iron whiskers.* Physical Review **156**, 2, (1967) 637.

[Dhi17] S. Dhillon, M. Vitiello, E. Linfield, A. Davies, M. C. Hoffmann, J. Booske, C. Paoloni, M. Gensch, P. Weightman, G. Williams, *et al. The 2017 terahertz science and technology roadmap.* Journal of Physics D: Applied Physics **50**, 4, (2017) 043001.

[DP92] P. d. V. Du Plessis & T. Germishuyse. *Electrical resistivity of some $RCo_3$ compounds.* Journal of Magnetism and Magnetic Materials **104**, (1992) 1349.

[Du14] C. Du, H. Wang, F. Yang, & P. C. Hammel. *Enhancement of pure spin currents in spin pumping $Y_3Fe_5O_{12}$/Cu/metal trilayers through spin conductance matching.* Physical Review Applied **1**, 4, (2014) 044004.

[Duv96] L. Duvillaret, F. Garet, & J.-L. Coutaz. *A reliable method for extraction of material parameters in terahertz time-domain spectroscopy.* IEEE Journal of selected topics in quantum electronics **2**, 3, (1996) 739.

[Ell15] M. O. Ellis, R. F. Evans, T. A. Ostler, J. Barker, U. Atxitia, O. Chubykalo-Fesenko, & R. W. Chantrell. *The Landau–Lifshitz equation in atomistic models.* Low Temperature Physics **41**, 9, (2015) 705.

[Ell16] D. Ellsworth, L. Lu, J. Lan, H. Chang, P. Li, Z. Wang, J. Hu, B. Johnson, Y. Bian, J. Xiao, *et al. Photo-spin-voltaic effect.* Nature Physics **12**, 9, (2016) 861.

[Els15] T. Elsaesser, K. Reimann, & M. Woerner. *Focus: Phase-resolved nonlinear terahertz spectroscopy-From charge dynamics in solids to molecular* *excitations in liquids.* The Journal of chemical physics **142**, 21, (2015) 212301.

[Eva14] R. F. Evans, W. J. Fan, P. Chureemart, T. A. Ostler, M. O. Ellis, & R. W. Chantrell. *Atomistic spin model simulations of magnetic nanomaterials.* Journal of Physics: Condensed Matter **26**, 10, (2014) 103202.

[Fan10] R. Fan, C. Kinane, T. Charlton, R. Dorner, M. Ali, M. de Vries, R. Brydson, C. Marrows, B. Hickey, D. Arena, *et al. Ferromagnetism at the interfaces of antiferromagnetic FeRh epilayers.* Physical Review B **82**, 18, (2010) 184418.

[Fer02a] B. Ferguson & Z. Xi-Cheng. *Materials for terahertz science and technology.* Nature materials **1**, 1, (2002) 26.

[Fer02b] M. E. Fermann, A. Galvanauskas, & G. Sucha. *Ultrafast lasers: Technology and applications*, Bd. 80. CRC Press, 2002.

[Fog17] A. Fognini, T. Michlmayr, A. Vaterlaus, & Y. Acremann. *Laser-induced ultrafast spin current pulses: a thermodynamic approach.* Journal of Physics: Condensed Matter **29**, 21, (2017) 214002.

[Fra75] F. Fradin, D. Koelling, A. Freeman, & T. Watson-Yang. *Calculation of the electronic structure and related physical properties of platinum.* Physical Review B **12**, 12, (1975) 5570.

[Fre10] F. Freimuth, S. Blügel, & Y. Mokrousov. *Anisotropic spin Hall effect from first principles.* Physical review letters **105**, 24, (2010) 246602.

[Fre17] R. Freeman, A. Zholud, Z. Dun, H. Zhou, & S. Urazhdin. *Intrinsic and extrinsic contributions to spin scattering in Pt.* arXiv preprint arXiv:1707.05330 .

[Fuc38] K. Fuchs. *The conductivity of thin metallic films according to the electron theory of metals.* In *Mathematical Proceedings of the Cambridge Philosophical Society*, Bd. 34. Cambridge University Press, 1938 100–108.

[Fül16] J. Fülöp, G. Polónyi, B. Monoszlai, G. Andriukaitis, T. Balciunas, A. Pugzlys, G. Arthur, A. Baltuska, & J. Hebling. *Highly efficient scalable monolithic semiconductor terahertz pulse source.* Optica **3**, 10, (2016) 1075.

[Gal99] G. Gallot & D. Grischkowsky. *Electro-optic detection of terahertz radiation.* JOSA B **16**, 8, (1999) 1204.

[Gam11] E. G. Gamaly. *Femtosecond Laser-Matter Interaction: Theory, Experiments and Applications.* CRC Press, 2011.

[Gan06] S. Ganichev & W. Prettl. *Intense terahertz excitation of semiconductors*, Bd. 14. Oxford University Press on Demand, 2006.

[Gep12] S. Geprägs, S. Meyer, S. Altmannshofer, M. Opel, F. Wilhelm, A. Rogalev, R. Gross, & S. T. Goennenwein. *Investigation of induced Pt magnetic polarization in Pt/$Y_3Fe_5O_{12}$ bilayers.* Applied Physics Letters **101**, 26, (2012) 262407.

[GI57] R. Glover III & M. Tinkham. *Conductivity of Superconducting Films for Photon Energies between 0.3 and 40 $k_BT_c$.* Physical Review **108**, 2, (1957) 243.

[Gil04] T. L. Gilbert. *A phenomenological theory of damping in ferromagnetic materials.* IEEE Transactions on Magnetics **40**, 6, (2004) 3443.

[Gra82] D. E. Gray. *American institute of physics handbook.* McGraw-Hill, 1982.

[Gre89] F. J. Greidanus & S. Klahn. *Magneto-Optical Recording and Data Storage Materials.* Angewandte Chemie International Edition **28**, 2, (1989) 235.

[Gre16] B. Green, S. Kovalev, V. Asgekar, G. Geloni, U. Lehnert, T. Golz, M. Kuntzsch, C. Bauer, J. Hauser, J. Voigtlaender, *et al.* *High-field high-repetition-rate sources for the coherent THz control of matter.* Scientific reports **6**.

[Gri90] D. Grischkowsky, S. Keiding, M. Van Exter, & C. Fattinger. *Far-infrared time-domain spectroscopy with terahertz beams of dielectrics and semiconductors.* JOSA B **7**, 10, (1990) 2006.

[Hal14] P. Hale, J. Madeo, C. Chin, S. Dhillon, J. Mangeney, J. Tignon, & K. Dani. *20 THz broadband generation using semi-insulating GaAs interdigitated photoconductive antennas.* Optics express **22**, 21, (2014) 26358.

[Har83] M. Hartmann & T. R. McGuire. *Relationship between Faraday Rotation and Hall Effect in Amorphous Rare-Earth-Transition-Metal Alloys.* Physical review letters **51**, 13, (1983) 1194.

[Hau09] T. Hauet, F. Montaigne, M. Hehn, Y. Henry, & S. Mangin. *Magnetoresistance in an amorphous exchange-coupled bilayer.* Physical Review B **79**, 22, (2009) 224435.

[Hau11] C. P. Hauri, C. Ruchert, C. Vicario, & F. Ardana. *Strong-field single-cycle THz pulses generated in an organic crystal.* Applied Physics Letters **99**, 16, (2011) 161116.

[Hel12] T. Helgaker, S. Coriani, P. Jørgensen, K. Kristensen, J. Olsen, & K. Ruud. *Recent advances in wave function-based methods of molecular-property calculations.* Chemical reviews **112**, 1, (2012) 543.

[Hér06] J. Héroux, Y. Ino, M. Kuwata-Gonokami, Y. Hashimoto, & S. Katsumoto. *Terahertz radiation emission from GaMnAs.* Applied physics letters **88**, 22, (2006) 221110.

[Hir11] H. Hirori, A. Doi, F. Blanchard, & K. Tanaka. *Single-cycle terahertz pulses with amplitudes exceeding 1 MV/cm generated by optical rectification in $LiNbO_3$.* Applied Physics Letters **98**, 9, (2011) 091106.

[Hof09] M. C. Hoffmann, N. C. Brandt, H. Y. Hwang, K.-L. Yeh, & K. A. Nelson. *Terahertz kerr effect.* Applied Physics Letters **95**, 23, (2009) 231105.

[Hof12] M. C. Hoffmann. *Nonlinear terahertz spectroscopy.* In *Terahertz Spectroscopy and Imaging.* Springer, 2012 355–388.

[Hof13] A. Hoffmann. *Spin Hall effects in metals.* IEEE transactions on magnetics **49**, 10, (2013) 5172.

[Hoh00] J. Hohlfeld, S.-S. Wellershoff, J. Güdde, U. Conrad, V. Jähnke, & E. Matthias. *Electron and lattice dynamics following optical excitation of metals.* Chemical Physics **251**, 1, (2000) 237.

[Hon85] S. Honda, M. Nawate, M. Ohkoshi, & T. Kusuda. *Hall effect and magnetic properties in GdFe and CoCr sputtered films.* Journal of Applied Physics **57**, 8, (1985) 3204.

[Hub00] R. Huber, A. Brodschelm, F. Tauser, & A. Leitenstorfer. *Generation and field-resolved detection of femtosecond electromagnetic pulses tunable up to 41 THz.* Applied Physics Letters **76**, 22, (2000) 3191.

[Hui15] T. Huisman, R. Mikhaylovskiy, A. Telegin, Y. P. Sukhorukov, A. Granovsky, S. Naumov, T. Rasing, & A. Kimel. *Terahertz magneto-optics in the ferromagnetic semiconductor* $HgCdCr_2Se_4$. Applied Physics Letters **106**, 13, (2015) 132411.

[Hui16a] T. J. Huisman & T. Rasing. *THz Emission Spectroscopy for THz Spintronics.* Journal of the Physical Society of Japan **86**, 1, (2016) 011009.

[Hui16b] T. Huisman, R. Mikhaylovskiy, J. Costa, F. Freimuth, E. Paz, J. Ventura, P. Freitas, S. Blugel, Y. Mokrousov, T. Rasing, *et al. Femtosecond control of electric currents in metallic ferromagnetic heterostructures.* Nature Nanotechnology **11**, 5, (2016) 455.

[Hui17a] T. Huisman, C. Ciccarelli, A. Tsukamoto, R. Mikhaylovskiy, T. Rasing, & A. Kimel. *Spin-photo-currents generated by femtosecond laser pulses in a ferrimagnetic GdFeCo/Pt bilayer.* Applied Physics Letters **110**, 7, (2017) 072402.

[Hui17b] T. Huisman, R. Mikhaylovskiy, T. Rasing, A. Kimel, A. Tsukamoto, B. de Ronde, L. Ma, W. Fan, & S. Zhou. *Sub-100-ps dynamics of the anomalous Hall effect at terahertz frequencies.* Physical Review B **95**, 9, (2017) 094418.

[Hwa15] H. Y. Hwang, S. Fleischer, N. C. Brandt, B. G. Perkins Jr, M. Liu, K. Fan, A. Sternbach, X. Zhang, R. D. Averitt, & K. A. Nelson. *A review of non-linear terahertz spectroscopy with ultrashort tabletop-laser pulses.* Journal of Modern Optics **62**, 18, (2015) 1447.

[Ike10] S. Ikeda, K. Miura, H. Yamamoto, K. Mizunuma, H. Gan, M. Endo, S. Kanai, J. Hayakawa, F. Matsukura, & H. Ohno. *A perpendicular-*

*anisotropy CoFeB-MgO magnetic tunnel junction.* Nature materials **9**, 9, (2010) 721.

[Ikh17] M. Ikhlas, T. Tomita, T. Koretsune, M.-T. Suzuki, D. Nishio-Hamane, R. Arita, Y. Otani, & S. Nakatsuji. *Large anomalous Nernst effect at room temperature in a chiral antiferromagnet.* Nature Physics **13**, (2017) 1085.

[Inf17] Infraspecs. *See http://www.infraspecs.de/html/ir_polarizer_ p02.html for the polarizer transmission function* (2017).

[Ino08] S. Inoue, H. Y. Y. Ko, & T. Suzuki. *Magnetic properties of single-crystalline FeRh alloy thin films.* IEEE Transactions on Magnetics **44**, 11, (2008) 2875.

[Jen37] F. A. Jenkins & H. E. White. *Fundamentals of optics.* Tata McGraw-Hill Education, 1937.

[Jia11] X. Jia, K. Liu, K. Xia, & G. E. Bauer. *Spin transfer torque on magnetic insulators.* EPL (Europhysics Letters) **96**, 1, (2011) 17005.

[Jia15] W. Jiang, P. Upadhyaya, W. Zhang, G. Yu, M. B. Jungfleisch, F. Y. Fradin, J. E. Pearson, Y. Tserkovnyak, K. L. Wang, O. Heinonen, *et al. Blowing magnetic skyrmion bubbles.* Science **349**, 6245, (2015) 283.

[Jia16a] M. Jiang, X. Chen, X. Zhou, B. Cui, Y. Yan, H. Wu, F. Pan, & C. Song. *Electrochemical control of the phase transition of ultrathin FeRh films.* Applied Physics Letters **108**, 20, (2016) 202404.

[Jia16b] M. Jiang, X. Chen, X. Zhou, Y. Wang, F. Pan, & C. Song. *Influence of film composition on the transition temperature of FeRh films.* Journal of Crystal Growth **438**, (2016) 19.

[Jin15] Z. Jin, A. Tkach, F. Casper, V. Spetter, H. Grimm, A. Thomas, T. Kampfrath, M. Bonn, M. Kläui, & D. Turchinovich. *Accessing the fundamentals of magnetotransport in metals with terahertz probes.* Nature Physics **11**, 9, (2015) 761.

[Joh85] M. Johnson & R. H. Silsbee. *Interfacial charge-spin coupling: Injection and detection of spin magnetization in metals.* Physical Review Letters **55**, 17, (1985) 1790.

[Jul75] M. Julliere. *Tunneling between ferromagnetic films.* Physics letters A **54**, 3, (1975) 225.

[Jun16] T. Jungwirth, X. Marti, P. Wadley, & J. Wunderlich. *Antiferromagnetic spintronics.* Nature nanotechnology **11**, 3, (2016) 231.

[Kad05] F. Kadlec, P. Kužel, & J.-L. Coutaz. *Study of terahertz radiation generated by optical rectification on thin gold films.* Optics letters **30**, 11, (2005) 1402.

[Kai99] R. Kaindl, F. Eickemeyer, M. Woerner, & T. Elsaesser. *Broadband phase-matched difference frequency mixing of femtosecond pulses in GaSe: Experiment and theory.* Applied Physics Letters **75**, 8, (1999) 1060.

[Kaj10] Y. Kajiwara, K. Harii, S. Takahashi, J. Ohe, K. Uchida, M. Mizuguchi, H. Umezawa, H. Kawai, K. Ando, K. Takanashi, *et al. Transmission of electrical signals by spin-wave interconversion in a magnetic insulator.* Nature **464**, 7286, (2010) 262.

[Kal12] S. Kaltenborn, Y.-H. Zhu, & H. C. Schneider. *Wave-diffusion theory of spin transport in metals after ultrashort-pulse excitation.* Physical Review B **85**, 23, (2012) 235101.

[Kam06] T. Kampfrath. *Charge-Carrier Dynamics in Solids and Gases Observed by Time-Resolved Terahertz Spectroscopy.* Dissertation, Freie Universität Berlin (2006).

[Kam07] T. Kampfrath, J. Nötzold, & M. Wolf. *Sampling of broadband terahertz pulses with thick electro-optic crystals.* Applied physics letters **90**, 23, (2007) 231113.

[Kam11] T. Kampfrath, A. Sell, G. Klatt, A. Pashkin, S. Mährlein, T. Dekorsy, M. Wolf, M. Fiebig, A. Leitenstorfer, & R. Huber. *Coherent terahertz control of antiferromagnetic spin waves.* Nature Photonics **5**, 1, (2011) 31.

[Kam13a] T. Kampfrath, M. Battiato, P. Maldonado, G. Eilers, J. Nötzold, S. Mährlein, V. Zbarsky, F. Freimuth, Y. Mokrousov, S. Blügel, *et al. Terahertz spin current pulses controlled by magnetic heterostructures.* Nature nanotechnology **8**, 4, (2013) 256.

[Kam13b] T. Kampfrath, K. Tanaka, & K. A. Nelson. *Resonant and nonresonant control over matter and light by intense terahertz transients.* Nature Photonics **7**, 9, (2013) 680.

[Kar54] R. Karplus & J. Luttinger. *Hall effect in ferromagnetics.* Physical Review **95**, 5, (1954) 1154.

[Kat10] I. Katayama, R. Akai, M. Bito, H. Shimosato, K. Miyamoto, H. Ito, & M. Ashida. *Ultrabroadband terahertz generation using 4-N, N-dimethylamino-4'-N'-methyl-stilbazolium tosylate single crystals.* Applied Physics Letters **97**, 2, (2010) 021105.

[Keh15] A. Kehlberger, U. Ritzmann, D. Hinzke, E.-J. Guo, J. Cramer, G. Jakob, M. C. Onbasli, D. H. Kim, C. A. Ross, M. B. Jungfleisch, *et al. Length scale of the spin Seebeck effect.* Physical review letters **115**, 9, (2015) 096602.

[Ken15] A. D. Kent & D. C. Worledge. *A new spin on magnetic memories.* Nature nanotechnology **10**, 3, (2015) 187.

[Ket68] J. Ketterson, L. Windmiller, S. Hörnfeldt, & F. Mueller. *Fermi velocity and Fermi radius in platinum.* Solid State Communications **6**, 12, (1968) 851.

[Kik13] T. Kikkawa, K. Uchida, Y. Shiomi, Z. Qiu, D. Hou, D. Tian, H. Nakayama, X.-F. Jin, & E. Saitoh. *Longitudinal spin Seebeck effect free from the proximity Nernst effect.* Physical review letters **110**, 6, (2013) 067207.

[Kim07] M.-H. Kim, G. Acbas, M.-H. Yang, I. Ohkubo, H. Christen, D. Mandrus, M. Scarpulla, O. Dubon, Z. Schlesinger, P. Khalifah, *et al. Determination of the infrared complex magnetoconductivity tensor in itinerant ferromagnets from Faraday and Kerr measurements.* Physical Review B **75**, 21, (2007) 214416.

[Kim09] A. Kimel, B. Ivanov, R. Pisarev, P. Usachev, A. Kirilyuk, & T. Rasing. *Inertia-driven spin switching in antiferromagnets.* Nature Physics **5**, 10, (2009) 727.

[Kim10] M.-H. Kim, G. Acbas, M.-H. Yang, M. Eginligil, P. Khalifah, I. Ohkubo, H. Christen, D. Mandrus, Z. Fang, & J. Cerne. *Infrared anomalous Hall effect in* $SrRuO_3$*: Exploring evidence for crossover to intrinsic behavior.* Physical Review B **81**, 23, (2010) 235218.

[Kim12] K.-Y. Kim, J. H. Glownia, A. J. Taylor, & G. Rodriguez. *High-power broadband terahertz generation via two-color photoionization in gases.* IEEE Journal of Quantum Electronics **48**, 6, (2012) 797.

[Kim13] M.-H. Kim, T. Tanaka, C. Ellis, A. Mukherjee, G. Acbas, I. Ohkubo, H. Christen, D. Mandrus, H. Kontani, & J. Cerne. *Infrared anomalous Hall effect in* $Ca_xSr_{1-x}RuO_3$ *films.* Physical Review B **88**, 15, (2013) 155101.

[Kim17] J. Kimling, G.-M. Choi, J. T. Brangham, T. Matalla-Wagner, T. Huebner, T. Kuschel, F. Yang, & D. G. Cahill. *Picosecond spin Seebeck effect.* Physical review letters **118**, 5, (2017) 057201.

[Kir10] A. Kirilyuk, A. V. Kimel, & T. Rasing. *Ultrafast optical manipulation of magnetic order.* Reviews of Modern Physics **82**, 3, (2010) 2731.

[Kir13] A. Kirilyuk, A. V. Kimel, & T. Rasing. *Laser-induced magnetization dynamics and reversal in ferrimagnetic alloys.* Reports on progress in physics **76**, 2, (2013) 026501.

[Kit05] C. Kittel. *Introduction to solid state physics.* Wiley, 2005.

[Kla10] G. Klatt, F. Hilser, W. Qiao, M. Beck, R. Gebs, A. Bartels, K. Huska, U. Lemmer, G. Bastian, M. B. Johnston, *et al. Terahertz emission from lateral photo-Dember currents.* Optics express **18**, 5, (2010) 4939.

[KO11] T. Kleine-Ostmann & T. Nagatsuma. *A review on terahertz communications research.* Journal of Infrared, Millimeter, and Terahertz Waves **32**, 2, (2011) 143.

[Kon09] H. Kontani, T. Tanaka, D. Hirashima, K. Yamada, & J. Inoue. *Giant orbital Hall effect in transition metals: Origin of large spin and anomalous Hall effects.* Physical review letters **102**, 1, (2009) 016601.

[Koo10] B. Koopmans, G. Malinowski, F. Dalla Longa, D. Steiauf, M. Fähnle, T. Roth, M. Cinchetti, & M. Aeschlimann. *Explaining the paradoxical diversity of ultrafast laser-induced demagnetization.* Nature materials **9**, 3, (2010) 259.

[Kou62] J. Kouvel & C. Hartelius. *Anomalous magnetic moments and transformations in the ordered alloy FeRh.* Journal of Applied Physics **33**, 3, (1962) 1343.

[Kub57] R. Kubo. *Statistical-mechanical theory of irreversible processes. I. General theory and simple applications to magnetic and conduction problems.* Journal of the Physical Society of Japan **12**, 6, (1957) 570.

[Kub66] R. Kubo. *The fluctuation-dissipation theorem.* Reports on progress in physics **29**, 1, (1966) 255.

[Lak11] M. Lakshmanan. *The fascinating world of the Landau–Lifshitz–Gilbert equation: an overview.* Philosophical Transactions of the Royal Society of London A: Mathematical, Physical and Engineering Sciences **369**, 1939, (2011) 1280.

[Lal03] P. Lalanne & M. Hutley. *Artificial media optical properties-subwavelength scale.* Encyclopedia of optical engineering **1**, (2003) 62.

[Lam08] N. Laman & D. Grischkowsky. *Terahertz conductivity of thin metal films.* Applied Physics Letters **93**, 5, (2008) 051105.

[Lan58] L. D. Landau & E. M. Lifshitz. *Quantum mechanics: non-relativistic theory.* Pergamon, 1958.

[LaR15] J. L. LaRue, T. Katayama, A. Lindenberg, A. S. Fisher, H. Öström, A. Nilsson, & H. Ogasawara. *THz-pulse-induced selective catalytic CO oxidation on Ru.* Physical review letters **115**, 3, (2015) 036103.

[Lee07] Y. Lee, J. Hayakawa, S. Ikeda, F. Matsukura, & H. Ohno. *Effect of electrode composition on the tunnel magnetoresistance of pseudo-spin-valve magnetic tunnel junction with a MgO tunnel barrier.* Applied Physics Letters **90**, 21, (2007) 212507.

[Lei99a] A. Leitenstorfer, S. Hunsche, J. Shah, M. Nuss, & W. Knox. *Detectors and sources for ultrabroadband electro-optic sampling: Experiment and theory.* Applied physics letters **74**, 11, (1999) 1516.

[Lei99b] A. Leitenstorfer, S. Hunsche, J. Shah, M. Nuss, & W. Knox. *Femtosecond charge transport in polar semiconductors.* Physical review letters **82**, 25, (1999) 5140.

[Lei02] C. Lei, M. Bauer, K. Read, R. Tobey, Y. Liu, T. Popmintchev, M. Murnane, & H. Kapteyn. *Hot-electron-driven charge transfer processes on $O_2$/Pt (111) surface probed by ultrafast extreme-ultraviolet pulses.* Physical Review B **66**, 24, (2002) 245420.

[Len11] B. Lenk, H. Ulrichs, F. Garbs, & M. Münzenberg. *The building blocks of magnonics.* Physics Reports **507**, 4, (2011) 107.

[Les16] E. Lesne, Y. Fu, S. Oyarzun, J. Rojas-Sánchez, D. Vaz, H. Naganuma, G. Sicoli, J.-P. Attané, M. Jamet, E. Jacquet, *et al. Highly efficient and tunable spin-to-charge conversion through Rashba coupling at oxide interfaces.* Nature Materials **15**, 12, (2016) 1261.

[Leu15] J. C. Leutenantsmeyer, V. Zbarsky, M. von der Ehe, S. Wittrock, P. Peretzki, H. Schuhmann, A. Thomas, K. Rott, G. Reiss, T. H. Kim, *et al. Spin-transfer torque switching at ultra low current densities.* Materials Transactions **56**, 9, (2015) 1323.

[Li17] G. Li, R. Mikhaylovskiy, K. Grishunin, D. Costa, T. Rasing, & A. Kimel. *Laser induced THz emission from femtosecond photocurrents in Co/ZnO/Pt and Co/Cu/Pt multilayers.* arXiv preprint arXiv:1711.08342 .

[Lia15] X. Liang, X. Xu, R. Zheng, Z. A. Lum, & J. Qiu. *Optical constant of CoFeB thin film measured with the interference enhancement method.* Applied Optics **54**, 7, (2015) 1557.

[Lin08] Z. Lin, L. V. Zhigilei, & V. Celli. *Electron-phonon coupling and electron heat capacity of metals under conditions of strong electron-phonon nonequilibrium.* Physical Review B **77**, 7, (2008) 075133.

[Liu12a] L. Liu, C.-F. Pai, Y. Li, H. Tseng, D. Ralph, & R. Buhrman. *Spin-torque switching with the giant spin Hall effect of tantalum.* Science **336**, 6081, (2012) 555.

[Liu12b] M. Liu, H. Y. Hwang, H. Tao, A. C. Strikwerda, K. Fan, G. R. Keiser, A. J. Sternbach, K. G. West, S. Kittiwatanakul, J. Lu, *et al. Terahertz-field-induced insulator-to-metal transition in vanadium dioxide metamaterial.* Nature **487**, 7407, (2012) 345.

[Liu17] B. Liu, H. Bromberger, A. Cartella, T. Gebert, M. Först, & A. Cavalleri. *Generation of narrowband, high-intensity, carrier-envelope phase-stable pulses tunable between 4 and 18 THz.* Optics letters **42**, 1, (2017) 129.

[Lu14] X. Lu & X.-C. Zhang. *Investigation of ultra-broadband terahertz time-domain spectroscopy with terahertz wave gas photonics.* Frontiers of Optoelectronics **7**, 2, (2014) 121.

[Mae17a] S. Maehrlein, I. Radu, P. Maldonado, A. Paarmann, M. Gensch, A. M. Kalashnikova, R. V. Pisarev, M. Wolf, P. M. Oppeneer, J. Barker, *et al. Revealing spin-phonon interaction in ferrimagnetic insulators by ultrafast lattice excitation.* arXiv preprint arXiv:1710.02700 .

[Mae17b] S. Maekawa, S. O. Valenzuela, E. Saitoh, & T. Kimura. *Spin current*, Bd. 22. Oxford University Press, 2017.

[Mäh16] S. Mährlein, M. Wolf, & K. Franke. *Nonlinear Terahertz Phononics: A Novel Route to Controlling Matter.* Dissertation, Freie Universität Berlin (2016).

[Man09] A. Manchon & S. Zhang. *Theory of spin torque due to spin-orbit coupling.* Physical Review B **79**, 9, (2009) 094422.

[Man12] A. Mann, J. Walowski, M. Münzenberg, S. Maat, M. J. Carey, J. R. Childress, C. Mewes, D. Ebke, V. Drewello, G. Reiss, *et al. Insights into ultrafast demagnetization in pseudogap half-metals.* Physical Review X **2**, 4, (2012) 041008.

[Man14] S. Mangin, M. Gottwald, C. Lambert, D. Steil, V. Uhlir, L. Pang, M. Hehn, S. Alebrand, M. Cinchetti, G. Malinowski, *et al. Engineered materials for all-optical helicity-dependent magnetic switching.* Nature materials **13**, 3, (2014) 286.

[Man15] A. Manchon, H. C. Koo, J. Nitta, S. Frolov, & R. Duine. *New perspectives for Rashba spin-orbit coupling.* Nature materials **14**, 9, (2015) 871.

[Mat14] R. Matsunaga, N. Tsuji, H. Fujita, A. Sugioka, K. Makise, Y. Uzawa, H. Terai, Z. Wang, H. Aoki, & R. Shimano. *Light-induced collective pseudospin precession resonating with Higgs mode in a superconductor.* Science **345**, 6201, (2014) 1145.

[Mil12] D. L. Mills. *Nonlinear optics: basic concepts.* Springer Science & Business Media, 2012.

[Mit99] D. Mittleman, M. Gupta, R. Neelamani, R. Baraniuk, J. Rudd, & M. Koch. *Recent advances in terahertz imaging.* Applied Physics B **68**, 6, (1999) 1085.

[Miy07] T. Miyasato, N. Abe, T. Fujii, A. Asamitsu, S. Onoda, Y. Onose, N. Nagaosa, & Y. Tokura. *Crossover behavior of the anomalous Hall effect and anomalous Nernst effect in itinerant ferromagnets.* Physical review letters **99**, 8, (2007) 086602.

[Moh06] P. Mohn. *Magnetism in the solid state: an introduction*, Bd. 134. Springer Science & Business Media, 2006.

[Mon16] R. Mondal, M. Berritta, & P. M. Oppeneer. *Relativistic theory of spin relaxation mechanisms in the Landau-Lifshitz-Gilbert equation of spin dynamics.* Physical Review B **94**, 14, (2016) 144419.

[Mor13] V. L. Moruzzi, J. F. Janak, & A. R. Williams. *Calculated electronic properties of metals.* Elsevier, 2013.

[Mos10] O. Mosendz, J. Pearson, F. Fradin, G. Bauer, S. Bader, & A. Hoffmann. *Quantifying spin Hall angles from spin pumping: Experiments and theory.* Physical review letters **104**, 4, (2010) 046601.

[Mot29] N. F. Mott. *The scattering of fast electrons by atomic nuclei.* Proceedings of the Royal Society of London. Series A, Containing Papers of a Mathematical and Physical Character **124**, 794, (1929) 425.

[Mue15] B. Mueller & B. Rethfeld. *Ultrafast magnetization dynamics driven by equilibration of temperatures and chemical potentials.* In *Ultrafast Magnetism I.* Springer, 2015 65–68.

[Nag10] N. Nagaosa, J. Sinova, S. Onoda, A. MacDonald, & N. Ong. *Anomalous hall effect.* Reviews of modern physics **82**, 2, (2010) 1539.

[Nak13] H. Nakayama, M. Althammer, Y.-T. Chen, K. Uchida, Y. Kajiwara, D. Kikuchi, T. Ohtani, S. Geprägs, M. Opel, S. Takahashi, *et al. Spin Hall magnetoresistance induced by a nonequilibrium proximity effect.* Physical review letters **110**, 20, (2013) 206601.

[Nen16] D. M. Nenno, S. Kaltenborn, & H. C. Schneider. *Boltzmann transport calculation of collinear spin transport on short timescales.* Physical Review B **94**, 11, (2016) 115102.

[Nic16] D. Nicoletti & A. Cavalleri. *Nonlinear light–matter interaction at terahertz frequencies.* Advances in Optics and Photonics **8**, 3, (2016) 401.

[Nol09] W. Nolting & A. Ramakanth. *Quantum theory of magnetism.* Springer Science & Business Media, 2009.

[Nov16] T. Nova, A. Cartella, A. Cantaluppi, M. Först, D. Bossini, R. Mikhaylovskiy, A. Kimel, R. Merlin, & A. Cavalleri. *An effective magnetic field from optically driven phonons.* Nature Physics **13**, (2016) 132.

[Oh14] T. Oh, Y. Yoo, Y. You, & K. Kim. *Generation of strong terahertz fields exceeding 8 MV/cm at 1 kHz and real-time beam profiling.* Applied Physics Letters **105**, 4, (2014) 041103.

[Ole17a] K. Olejník, V. Schuler, X. Marti, V. Novák, Z. Kašpar, P. Wadley, R. Campion, K. Edmonds, B. Gallagher, J. Garces, *et al. Antiferromagnetic CuMnAs multi-level memory cell with microelectronic compatibility.* Nature communications **8**, (2017) 15434.

[Ole17b] K. Olejnik, T. Seifert, Z. Kaspar, V. Novak, P. Wadley, R. Campion, M. Baumgartner, P. Gambardella, P. Nemec, J. Wunderlich, *et al. THz electrical writing speed in an antiferromagnetic memory.* arXiv preprint arXiv:1711.08444 .

[Ong06] N. Ong & W. LEE. *Geometry and the Anomalous Hall Effect in Ferromagnets.* In *Foundations of Quantum Mechanics in the Light of New Technology ISQM-Tokyo'05.* 2006 121–126.

[Opp91] P. Oppeneer, J. Sticht, & F. Herman. *Theory of the Magneto-Optical Properties of Transition Metals and Rare Earth Compounds.* Journal of the Magnetics Society of Japan **15**, 1, (1991) 73.

[Ord88] M. A. Ordal, R. J. Bell, R. W. Alexander, L. A. Newquist, & M. R. Querry. *Optical properties of Al, Fe, Ti, Ta, W, and Mo at submillimeter wavelengths.* Applied optics **27**, 6, (1988) 1203.

[Orn10] J. Orna, P. Algarabel, L. Morellón, J. Pardo, J. de Teresa, R. L. Antón, F. Bartolomé, L. García, J. Bartolomé, J. Cezar, *et al.* *Origin of the giant magnetic moment in epitaxial $Fe_3O_4$ thin films.* Physical Review B **81**, 14, (2010) 144420.

[Pai14] C.-F. Pai, M.-H. Nguyen, C. Belvin, L. H. Vilela-Leão, D. Ralph, & R. Buhrman. *Enhancement of perpendicular magnetic anisotropy and transmission of spin-Hall-effect-induced spin currents by a Hf spacer layer in W/Hf/CoFeB/MgO layer structures.* Applied Physics Letters **104**, 8, (2014) 082407.

[Pal09] P. Paluskar, R. Lavrijsen, M. Sicot, J. Kohlhepp, H. Swagten, & B. Koopmans. *Correlation between magnetism and spin-dependent transport in CoFeB alloys.* Physical review letters **102**, 1, (2009) 016602.

[Pas13] A. Pashkin, A. Sell, T. Kampfrath, & R. Huber. *Electric and magnetic terahertz nonlinearities resolved on the sub-cycle scale.* New Journal of Physics **15**, 6, (2013) 065003.

[Pei12] K.-E. Peiponen, A. Zeitler, & M. Kuwata-Gonokami. *Terahertz spectroscopy and imaging*, Bd. 171. Springer, 2012.

[Pim05] A. Pimenov, S. Tachos, T. Rudolf, A. Loidl, D. Schrupp, M. Sing, R. Claessen, & V. Brabers. *Terahertz conductivity at the Verwey transition in magnetite.* Physical Review B **72**, 3, (2005) 035131.

[Pol11] D. Polyushkin, E. Hendry, E. Stone, & W. Barnes. *THz generation from plasmonic nanoparticle arrays.* Nano letters **11**, 11, (2011) 4718.

[Pre15] G. Prenat, K. Jabeur, G. Di Pendina, O. Boulle, & G. Gaudin. *Beyond STT-MRAM, spin orbit torque RAM SOT-MRAM for high speed and high reliability applications.* In *Spintronics-based Computing.* Springer, 2015 145–157.

[Pre16] F. Pressacco, V. Uhlíř, M. Gatti, A. Bendounan, E. E. Fullerton, & F. Sirotti. *Stable room-temperature ferromagnetic phase at the FeRh (100) surface.* Scientific reports **6**, (2016) 22383.

[Pri95] G. A. Prinz. *Spin-polarized transport.* Physics today **48**, (1995) 58.

[Pri15] S. Priyadarshi, K. Pierz, & M. Bieler. *Detection of the anomalous velocity with subpicosecond time resolution in semiconductor nanostructures.* Physical review letters **115**, 25, (2015) 257401.

[Qui12] F. Quirin, M. Vattilana, U. Shymanovich, A.-E. El-Kamhawy, A. Tarasevitch, J. Hohlfeld, D. von der Linde, & K. Sokolowski-Tinten. *Structural dynamics in FeRh during a laser-induced metamagnetic phase transition.* Physical Review B **85**, 2, (2012) 020103.

[Rad11] I. Radu, K. Vahaplar, C. Stamm, T. Kachel, N. Pontius, H. Dürr, T. Ostler, J. Barker, R. Evans, R. Chantrell, *et al.* *Transient ferromagnetic-like state mediating ultrafast reversal of antiferromagnetically coupled spins.* Nature **472**, 7342, (2011) 205.

[Rad12] F. Radu, R. Abrudan, I. Radu, D. Schmitz, & H. Zabel. *Perpendicular exchange bias in ferrimagnetic spin valves.* Nature communications **3**, (2012) 715.

[Ram08] R. Ramos, S. Arora, & I. Shvets. *Anomalous anisotropic magnetoresistance in epitaxial $Fe_3O_4$ thin films on MgO (001).* Physical Review B **78**, 21, (2008) 214402.

[Ram11] G. Ramakrishnan & P. C. Planken. *Percolation-enhanced generation of terahertz pulses by optical rectification on ultrathin gold films.* Optics letters **36**, 13, (2011) 2572.

[Ram14] G. Ramanandan, G. Ramakrishnan, N. Kumar, A. Adam, & P. Planken. *Emission of terahertz pulses from nanostructured metal surfaces.* Journal of Physics D: Applied Physics **47**, 37, (2014) 374003.

[Raz17] I. Razdolski, A. Alekhin, N. Ilin, J. Meyburg, V. Roddatis, D. Diesing, U. Bovensiepen, & A. Melnikov. *Nanoscale interface confinement of ultrafast spin transfer torque driving non-uniform spin dynamics.* Nature communications **8**, (2017) 15007.

[Rei07] K. Reimann. *Table-top sources of ultrashort THz pulses.* Reports on Progress in Physics **70**, 10, (2007) 1597.

[Rez14] S. Rezende, R. Rodríguez-Suárez, R. Cunha, A. Rodrigues, F. Machado, G. F. Guerra, J. L. Ortiz, & A. Azevedo. *Magnon spin-current theory for the longitudinal spin-Seebeck effect.* Physical Review B **89**, 1, (2014) 014416.

[Ric94] A. Rice, Y. Jin, X. Ma, X.-C. Zhang, D. Bliss, J. Larkin, & M. Alexander. *Terahertz optical rectification from (110)-zinc-blende crystals.* Applied physics letters **64**, 11, (1994) 1324.

[Rüc17] A. Rückriegel & P. Kopietz. *Spin currents, spin torques, and the concept of spin superfluidity.* Physical Review B **95**, 10, (2017) 104436.

[Rus67] E. E. Russell & E. E. Bell. *Measurement of the optical constants of crystal quartz in the far infrared with the asymmetric Fourier-transform method.* JOSA **57**, 3, (1967) 341.

[Sai06] E. Saitoh, M. Ueda, H. Miyajima, & G. Tatara. *Conversion of spin current into charge current at room temperature: Inverse spin-Hall effect.* Applied Physics Letters **88**, 18, (2006) 182509.

[Sai16] V. Saidl, M. Brajer, L. Horák, H. Reichlová, K. Výborný, M. Veis, T. Janda, F. Trojánek, M. Maryško, I. Fina, *et al. Investigation of magneto-structural phase transition in FeRh by reflectivity and transmittance measurements in visible and near-infrared spectral region.* New Journal of Physics **18**, 8, (2016) 083017.

[Saj14] M. Sajadi, M. Wolf, & T. Kampfrath. *Terahertz field enhancement via coherent superposition of the pulse sequences after a single optical-rectification crystal.* Applied Physics Letters **104**, 9, (2014) 091118.

[Saj15] M. Sajadi, M. Wolf, & T. Kampfrath. *Terahertz-field-induced optical birefringence in common window and substrate materials.* Optics express **23**, 22, (2015) 28985.

[Saj17] M. Sajadi, M. Wolf, & T. Kampfrath. *Transient birefringence of liquids induced by terahertz electric-field torque on permanent molecular dipoles.* Nature communications **8**.

[Sak95] J. J. Sakurai & E. D. Commins. *Modern quantum mechanics, revised edition.* AAPT, 1995.

[San14] Y. Sano, I. Kawayama, M. Tabata, K. Salek, H. Murakami, M. Wang, R. Vajtai, P. Ajayan, J. Kono, & M. Tonouchi. *Imaging molecular adsorption and desorption dynamics on graphene using terahertz emission spectroscopy.* Scientific reports **4**.

[San17] D. Sander, S. Valenzuela, D. Makarov, C. Marrows, E. Fullerton, P. Fischer, J. McCord, P. Vavassori, S. Mangin, P. Pirro, *et al. The 2017 Magnetism Roadmap.* J. Phys. D: Appl. Phys **50**, 363001, (2017) 363001.

[Sas17] Y. Sasaki, K. Suzuki, & S. Mizukami. *Annealing effect on laser pulse-induced THz wave emission in Ta/CoFeB/MgO films.* Applied Physics Letters **111**, 10, (2017) 102401.

[Sch09] A. Schneider. *Beam-size effects in electro-optic sampling of terahertz pulses.* Optics letters **34**, 7, (2009) 1054.

[Sch14] A. Schellekens, K. Kuiper, R. De Wit, & B. Koopmans. *Ultrafast spin-transfer torque driven by femtosecond pulsed-laser excitation.* Nature communications **5**, (2014) 4333.

[Sch16] M. Schreier, F. Kramer, H. Huebl, S. Geprägs, R. Gross, S. T. Goennenwein, T. Noack, T. Langner, A. A. Serga, B. Hillebrands, *et al. Spin*

*Seebeck effect at microwave frequencies.* Physical Review B **93**, 22, (2016) 224430.

[See11] K. Seemann, F. Freimuth, H. Zhang, S. Blügel, Y. Mokrousov, D. Bürgler, & C. Schneider. *Origin of the planar Hall effect in nanocrystalline* $Co_{60}Fe_{20}B_{20}$. Physical review letters **107**, 8, (2011) 086603.

[Sei16] T. Seifert, S. Jaiswal, U. Martens, J. Hannegan, L. Braun, P. Maldonado, F. Freimuth, A. Kronenberg, J. Henrizi, I. Radu, *et al. Efficient metallic spintronic emitters of ultrabroadband terahertz radiation.* Nature photonics **10**, 7, (2016) 483.

[Sei17a] T. Seifert, S. Jaiswal, J. Barker, I. Razdolski, J. Cramer, O. Gueckstock, S. Watanabe, C. Ciccarelli, A. Melnikov, G. Jakob, *et al. Launching magnons at the terahertz speed of the spin Seebeck effect.* arXiv preprint arXiv:1709.00768 .

[Sei17b] T. Seifert, S. Jaiswal, M. Sajadi, G. Jakob, S. Winnerl, M. Wolf, M. Kläui, & T. Kampfrath. *Ultrabroadband single-cycle terahertz pulses with peak fields of 300 kV* $cm^{-1}$ *from a metallic spintronic emitter.* Applied Physics Letters **110**, 25, (2017) 252402.

[Sei17c] T. Seifert, U. Martens, S. Günther, M. Schoen, F. Radu, X. Chen, I. Lucas, R. Ramos, M. Aguirre, P. Algarabel, *et al. Terahertz spin currents and inverse spin Hall effect in thin-film heterostructures containing complex magnetic compounds.* In *SPIN*. World Scientific, 2017 1740010.

[Sel08] A. Sell, A. Leitenstorfer, & R. Huber. *Phase-locked generation and field-resolved detection of widely tunable terahertz pulses with amplitudes exceeding 100 MV/cm.* Optics letters **33**, 23, (2008) 2767.

[Sha04] J. Shan & T. F. Heinz. *Terahertz radiation from semiconductors.* Ultrafast Dynamical Processes in Semiconductors 2083–2083.

[Sha15] M. Shalaby & C. P. Hauri. *Demonstration of a low-frequency three-dimensional terahertz bullet with extreme brightness.* Nature Communications **6**, (2015) ncomms6976.

[She03] Y. Shen, P. Upadhya, E. Linfield, H. Beere, & A. Davies. *Ultrabroadband terahertz radiation from low-temperature-grown GaAs photoconductive emitters.* Applied physics letters **83**, 15, (2003) 3117.

[Shi11] R. Shimano, Y. Ikebe, K. Takahashi, M. Kawasaki, N. Nagaosa, & Y. Tokura. *Terahertz Faraday rotation induced by an anomalous Hall effect in the itinerant ferromagnet* $SrRuO_3$. Europhysics Letters **95**, 1, (2011) 17002.

[Sil79] R. Silsbee, A. Janossy, & P. Monod. *Coupling between ferromagnetic and conduction-spin-resonance modes at a ferromagnetic-normal-metal interface.* Physical Review B **19**, 9, (1979) 4382.

[Šim03] E. Šimánek & B. Heinrich. *Gilbert damping in magnetic multilayers.* Physical Review B **67**, 14, (2003) 144418.

[Sin15] J. Sinova, S. O. Valenzuela, J. Wunderlich, C. Back, & T. Jungwirth. *Spin hall effects.* Reviews of Modern Physics **87**, 4, (2015) 1213.

[Sin16] N. A. Sinitsyn & Y. V. Pershin. *The theory of spin noise spectroscopy: a review.* Reports on Progress in Physics **79**, 10, (2016) 106501.

[Spi61] W. Spitzer & D. Kleinman. *Infrared lattice bands of quartz.* Physical Review **121**, 5, (1961) 1324.

[Sta07] C. Stanciu, F. Hansteen, A. Kimel, A. Kirilyuk, A. Tsukamoto, A. Itoh, & T. Rasing. *All-optical magnetic recording with circularly polarized light.* Physical review letters **99**, 4, (2007) 047601.

[Sti02] M. D. Stiles & A. Zangwill. *Anatomy of spin-transfer torque.* Physical Review B **66**, 1, (2002) 014407.

[Sto85] T. Stobiecki, K. Kowalski, & Z. Obuszko. *Charge transfer and Hall effect in amorphous GdCo, GdCoMo and GdFe films.* Physica B+ C **130**, 1-3, (1985) 94.

[Stö07] J. Stöhr & H. C. Siegmann. *Magnetism: from fundamentals to nanoscale dynamics*, Bd. 152. Springer Science & Business Media, 2007.

[Sun05] Q.-f. Sun & X. Xie. *Definition of the spin current: The angular spin current and its physical consequences.* Physical Review B **72**, 24, (2005) 245305.

[Suz15] I. Suzuki, T. Naito, M. Itoh, & T. Taniyama. *Barkhausen-like antiferromagnetic to ferromagnetic phase transition driven by spin polarized current.* Applied Physics Letters **107**, 8, (2015) 082408.

[Sve15] V. Sverdlov & S. Selberherr. *Silicon spintronics: Progress and challenges.* Physics Reports **585**, (2015) 1.

[Swa84] L. Swartzendruber. *The Fe-Rh (Iron-Rhodium) system.* Journal of Phase Equilibria **5**, 5, (1984) 456.

[Tho07] M. D. Thomson, M. Kreft, T. Löffter, & H. G. Roskos. *Broadband THz emission from gas plasmas induced by femtosecond optical pulses: From fundamentals to applications.* Laser & photonics reviews **1**, 4, (2007) 349.

[Ton07] M. Tonouchi. *Cutting-edge terahertz technology.* Nature photonics **1**, 2, (2007) 97.

[Tor17] G. Torosyan, S. Keller, L. Scheuer, R. Beigang, & E. T. Papaioannou. *Efficient Spintronic Terahertz Emitters Based on Epitaxial Grown Fe/Pt Layer Structures.* arXiv preprint arXiv:1707.08894 .

[Tse05] Y. Tserkovnyak, A. Brataas, G. E. Bauer, & B. I. Halperin. *Nonlocal magnetization dynamics in ferromagnetic heterostructures.* Reviews of Modern Physics **77**, 4, (2005) 1375.

[Tsu83] T. Tsushima & M. Ohokoshi. *Spin reorientation in $DyCo_5$.* Journal of magnetism and magnetic materials **31**, (1983) 197.

[Tve15] E. G. Tveten, A. Brataas, & Y. Tserkovnyak. *Electron-magnon scattering in magnetic heterostructures far out of equilibrium.* Physical Review B **92**, 18, (2015) 180412.

[Uch08] K. Uchida, S. Takahashi, K. Harii, J. Ieda, W. Koshibae, K. Ando, S. Maekawa, & E. Saitoh. *Observation of the spin Seebeck effect.* Nature **455**, 7214, (2008) 778.

[Uch10] K. Uchida, J. Xiao, H. Adachi, J. Ohe, S. Takahashi, J. Ieda, T. Ota, Y. Kajiwara, H. Umezawa, H. Kawai, *et al. Spin Seebeck insulator.* Nature materials **9**, 11, (2010) 894.

[Uch14] K. Uchida, T. Kikkawa, A. Miura, J. Shiomi, & E. Saitoh. *Quantitative temperature dependence of longitudinal spin Seebeck effect at high temperatures.* Physical Review X **4**, 4, (2014) 041023.

[Uhl25] G. E. Uhlenbeck & S. Goudsmit. *Ersetzung der Hypothese vom unmechanischen Zwang durch eine Forderung bezüglich des inneren Verhaltens jedes einzelnen Elektrons.* Naturwissenschaften **13**, 47, (1925) 953.

[Ulb11] R. Ulbricht, E. Hendry, J. Shan, T. F. Heinz, & M. Bonn. *Carrier dynamics in semiconductors studied with time-resolved terahertz spectroscopy.* Reviews of Modern Physics **83**, 2, (2011) 543.

[Ver41] E. Verwey & P. Haayman. *Electronic conductivity and transition point of magnetite ("$Fe_3O_4$").* Physica **8**, 9, (1941) 979.

[Vic13] C. Vicario, C. Ruchert, F. Ardana-Lamas, P. M. Derlet, B. Tudu, J. Luning, & C. P. Hauri. *Off-resonant magnetization dynamics phase-locked to an intense phase-stable terahertz transient.* Nature Photonics **7**, 9, (2013) 720.

[Vic15] C. Vicario, M. Jazbinsek, A. Ovchinnikov, O. Chefonov, S. Ashitkov, M. Agranat, & C. Hauri. *High efficiency THz generation in DSTMS, DAST and OH1 pumped by Cr: forsterite laser.* Optics express **23**, 4, (2015) 4573.

[Wad16] P. Wadley, B. Howells, J. Železnỳ, C. Andrews, V. Hills, R. P. Campion, V. Novák, K. Olejník, F. Maccherozzi, S. Dhesi, *et al. Electrical switching of an antiferromagnet.* Science **351**, 6273, (2016) 587.

[Wal16] J. Walowski & M. Münzenberg. *Perspective: Ultrafast magnetism and THz spintronics.* Journal of Applied Physics **120**, 14, (2016) 140901.

[Wan13] W. Wang, J.-M. Mariot, M. Richter, O. Heckmann, W. Ndiaye, P. De Padova, A. Taleb-Ibrahimi, P. Le Fevre, F. Bertran, F. Bondino, *et al. Fe $t_{2g}$ band dispersion and spin polarization in thin films of $Fe_3O_4$ (0 0 1)/MgO (0 0 1): Half-metallicity of magnetite revisited.* Physical Review B **87**, 8, (2013) 085118.

[Wan15] S. Wang, L. Zou, X. Zhang, J. Cai, S. Wang, B. Shen, & J. Sun. *Spin Seebeck effect and spin Hall magnetoresistance at high temperatures for a Pt/yttrium iron garnet hybrid structure.* Nanoscale **7**, 42, (2015) 17812.

[Wei11] J. Weischenberg, F. Freimuth, J. Sinova, S. Blügel, & Y. Mokrousov. *Ab initio theory of the scattering-independent anomalous Hall effect.* Physical review letters **107**, 10, (2011) 106601.

[Wei13] M. Weiler, M. Althammer, M. Schreier, J. Lotze, M. Pernpeintner, S. Meyer, H. Huebl, R. Gross, A. Kamra, J. Xiao, *et al.* *Experimental test of the spin mixing interface conductivity concept.* Physical review letters **111**, 17, (2013) 176601.

[Wei14] D. Wei, M. Obstbaum, M. Ribow, C. H. Back, & G. Woltersdorf. *Spin Hall voltages from ac and dc spin currents.* Nature communications **5**.

[Wel07] G. H. Welsh, N. T. Hunt, & K. Wynne. *Terahertz-pulse emission through laser excitation of surface plasmons in a metal grating.* Physical review letters **98**, 2, (2007) 026803.

[Wer11] L. K. Werake, B. A. Ruzicka, & H. Zhao. *Observation of intrinsic inverse spin Hall effect.* Physical review letters **106**, 10, (2011) 107205.

[Whi72] R. M. White. *Quantum theory of magnetism.* Springer, 1972.

[Wie12] S. Wienholdt, D. Hinzke, & U. Nowak. *THz switching of antiferromagnets and ferrimagnets.* Physical review letters **108**, 24, (2012) 247207.

[Win12] S. Winnerl. *Scalable microstructured photoconductive terahertz emitters.* Journal of Infrared, Millimeter, and Terahertz Waves **33**, 4, (2012) 431.

[Wol01] S. Wolf, D. Awschalom, R. Buhrman, J. Daughton, S. Von Molnar, M. Roukes, A. Y. Chtchelkanova, & D. Treger. *Spintronics: a spin-based electronics vision for the future.* Science **294**, 5546, (2001) 1488.

[Wu97] Q. Wu & X.-C. Zhang. *Free-space electro-optics sampling of mid-infrared pulses.* Applied physics letters **71**, 10, (1997) 1285.

[Wu13] S. Wu, T. Zhu, X. Yang, & S. Chen. *The anomalous Hall effect in the perpendicular Ta/CoFeB/MgO thin films.* Journal of Applied Physics **113**, 17, (2013) 17C717.

[Wu17] Y. Wu, M. Elyasi, X. Qiu, M. Chen, Y. Liu, L. Ke, & H. Yang. *High-Performance THz Emitters Based on Ferromagnetic/Nonmagnetic Heterostructures.* Advanced Materials **29**, 4.

[Wun05] J. Wunderlich, B. Kaestner, J. Sinova, & T. Jungwirth. *Experimental observation of the spin-Hall effect in a two-dimensional spin-orbit coupled semiconductor system.* Physical review letters **94**, 4, (2005) 047204.

[Xia10] J. Xiao, G. E. Bauer, K.-I. Uchida, E. Saitoh, S. Maekawa, *et al.* *Theory of magnon-driven spin Seebeck effect.* Physical Review B **81**, 21, (2010) 214418.

[Yan84] A. Yanase & K. Siratori. *Band structure in the high temperature phase of* $Fe_3O_4$. Journal of the Physical Society of Japan **53**, 1, (1984) 312.

[Yan16] D. Yang, J. Liang, C. Zhou, L. Sun, R. Zheng, S. Luo, Y. Wu, & J. Qi. *Powerful and tunable THz emitters based on the Fe/Pt magnetic heterostructure.* Advanced Optical Materials **4**, 12, (2016) 1944.

[Yao04] Y. Yao, L. Kleinman, A. MacDonald, J. Sinova, T. Jungwirth, D.-s. Wang, E. Wang, & Q. Niu. *First principles calculation of anomalous Hall conductivity in ferromagnetic bcc Fe.* Physical review letters **92**, 3, (2004) 037204.

[Yas05] T. Yasui, T. Yasuda, K.-I. Sawanaka, & T. Araki. *Terahertz paintmeter for noncontact monitoring of thickness and drying progress in paint film.* Applied Optics **44**, 32, (2005) 6849.

[Yeh05] P. Yeh. *Optical waves in layered media*, Bd. 61. Wiley-Interscience, 2005.

[Zak90] J. Zak, E. Moog, C. Liu, & S. Bader. *Universal approach to magneto-optics.* Journal of Magnetism and Magnetic Materials **89**, 1-2, (1990) 107.

[Zei07] J. A. Zeitler, P. F. Taday, D. A. Newnham, M. Pepper, K. C. Gordon, & T. Rades. *Terahertz pulsed spectroscopy and imaging in the pharmaceutical setting - a review.* Journal of Pharmacy and Pharmacology **59**, 2, (2007) 209.

[Žel14] J. Železnỳ, H. Gao, K. Vỳbornỳ, J. Zemen, J. Mašek, A. Manchon, J. Wunderlich, J. Sinova, & T. Jungwirth. *Relativistic Néel-order fields induced by electrical current in antiferromagnets.* Physical review letters **113**, 15, (2014) 157201.

[Zha10] X.-C. Zhang & J. Xu. *Introduction to THz wave photonics*, Bd. 29. Springer, 2010.

[Zha15] L. Zhang, K. Mu, Y. Zhou, H. Wang, C. Zhang, & X.-C. Zhang. *High-power THz to IR emission by femtosecond laser irradiation of random 2D metallic nanostructures.* Scientific reports **5**.

[Zha17a] S. Zhang, Z. Jin, X. Liu, W. Zhao, X. Lin, C. Jing, & G. Ma. *Photoinduced terahertz radiation and negative conductivity dynamics in Heusler alloy* $Co_2MnSn$ *film.* Optics Letters **42**, 16, (2017) 3080.

[Zha17b] X. C. Zhang, A. Shkurinov, & Y. Zhang. *Extreme terahertz science.* Nature Photonics **11**, 1, (2017) 16.

[Zhe05] X. Zheng, A. Sinyukov, & L. M. Hayden. *Broadband and gap-free response of a terahertz system based on a poled polymer emitter-sensor pair.* Applied Physics Letters **87**, 8, (2005) 081115.

[Zhe06] X. Zheng, C. V. McLaughlin, M. R. Leahy-Hoppa, A. M. Sinyukov, & L. M. Hayden. *Modeling a broadband terahertz system based on an electro-optic polymer emitter-sensor pair.* JOSA B **23**, 7, (2006) 1338.

[Zhe07] X. Zheng, C. V. McLaughlin, P. Cunningham, & L. M. Hayden. *Organic broadband terahertz sources and sensors.* Journal of Nanoelectronics and Optoelectronics **2**, 1, (2007) 58.

[Zhu06] V. Zhukov, E. Chulkov, & P. Echenique. *Lifetimes and inelastic mean free path of low-energy excited electrons in Fe, Ni, Pt, and Au: Ab initio GW+ T calculations.* Physical Review B **73**, 12, (2006) 125105.

[Zie00] M. Ziese & H. Blythe. *Magnetoresistance of magnetite.* Journal of Physics: Condensed Matter **12**, 1, (2000) 13.

[Zou13] W. Zouaghi, M. Thomson, K. Rabia, R. Hahn, V. Blank, & H. Roskos. *Broadband terahertz spectroscopy: principles, fundamental research and potential for industrial applications.* European Journal of Physics **34**, 6, (2013) 179.

[Žut04] I. Žutić, J. Fabian, & S. D. Sarma. *Spintronics: Fundamentals and applications.* Reviews of modern physics **76**, 2, (2004) 323.

[Žut11] I. Žutić & H. Dery. *Spintronics: Taming spin currents.* Nature materials **10**, 9, (2011) 647.

# List of publications

## Publications within this thesis

**T. Seifert**, S. Jaiswal, J. Barker, I. Razdolski, J. Cramer, O. Gueckstock, S. Maehrlein, L. Nadvornik S. Watanabe, C. Ciccarelli, A. Melnikov, G. Jakob, M. Münzenberg, S.T.B. Goennenwein, G. Woltersdorf, P.W. Brouwer, M. Wolf, M. Kläui, and T. Kampfrath, "Launching magnons at terahertz speed with the spin Seebeck effect", *ArXiv*, *1709.00768*, submitted to: *Nature Communications*, (2017).

K. Olejnik, **T. Seifert**, Z. Kaspar, V. Novak, P. Wadley, R. P. Campion, M. Baumgartner, P. Gambardella, P. Nemec, J. Wunderlich, J. Sinova, P. Kuzel, M. Müller, T. Kampfrath, and T. Jungwirth, "THz electrical writing speed in an antiferromagnetic memory", submitted to: *Scientific Advances*, (2017).

J. Cramer, **T. Seifert**, A. Kronenberg, F. Fuhrmann, G. Jakob, M. Jourdan, T. Kampfrath, and M. Kläui, "Complex THz and DC inverse spin Hall effect in YIG/Cu$_{1-x}$Ir$_x$ bilayers across a wide concentration range", *ArXiv*, *1709.01890*, submitted to: *Nano Letters*, (2017).

**T. Seifert**, U. Martens, S. Günther, M. A. W. Schoen, F. Radu, X. Z. Chen, I. Lucas, R. Ramos, M. H. Aguirre, P. A. Algarabel, A. Anadón, H. Körner, J. Walowski, C. Back, M. R. Ibarra, L. Morellón, E. Saitoh, M. Wolf, C. Song, K. Uchida, M. Münzenberg, I. Radu, and T. Kampfrath, "Terahertz spin currents and inverse spin Hall effect in thin-film heterostructures containing complex magnetic compounds", *SPIN*, Vol. **7**, Issue *3*, (2017), pp. *1740010*.

**T. Seifert**, S. Jaiswal, M. Sajadi, G. Jakob, S. Winnerl, M. Wolf, M. Kläui, and T. Kampfrath, "Ultrabroadband single-cycle terahertz pulses with peak fields of 300 kV cm$^{-1}$ from a metallic spintronic emitter", *Applied Physics Letters*, Vol. **110**, Issue *25*, (2017), pp. *252402*.

**T. Seifert**, S. Jaiswal, U. Martens, J. Hannegan, L. Braun, P. Maldonado, F. Freimuth, A. Kronenberg, J. Henrizi, I. Radu, E. Beaurepaire, Y. Mokrousov, P. M. Oppeneer, M. Jourdan, G. Jakob, D. Turchinovich, L. M. Hayden, M. Wolf, M. Münzenberg, M. Kläui, and T.Kampfrath, "Efficient metallic spintronic emitters of ultrabroadband terahertz radiation", *Nature Photonics*, Vol. **10**, Issue *7*, (2016), pp. *483-488*.

## Publications concerning other topics

A. Veamatahau, B. Jiang, **T. Seifert**, S. Makuta, K. Latham, M. Kanehara, T. Teranishi, and Y. Tachibana, "Origin of surface trap states in CdS quantum dots: relationship between size dependent photoluminescence and sulfur vacancy trap states", *Physical Chemistry Chemical Physics*, Vol. **17**, Issue *4*, (2015), pp. *2850-2858*.

R. Henze, **T. Seifert**, J. Ward, and O. Benson, "Tuning whispering gallery modes using internal aerostatic pressure", *Optics Letters*, Vol. **36**, Issue *23*, (2011), pp. *4536-4538*.

# Academic curriculum vitae

For reasons of data protection, the curriculum vitae is not included in the online version

# Danksagung

An dieser Stelle möchte ich allen Menschen danken, die mich im Verlauf meiner Promotion auf verschiedenste Weisen unterstützt haben. Speziell geht mein Dank an:

Tobias Kampfrath für seine unerschütterliche und ansteckende Begeisterung für Physik, für seine Zeit und Hingabe als Mentor und für das Schaffen einer absolut angenehmen und produktiven Atmosphäre in der Terahertz-Forschungsgruppe;

Martin Wolf für das Ermöglichen meiner Arbeit am Fritz-Haber-Institut in einer höchst professionellen Umgebung und für sein Engagement als Zweitgutachter meiner Doktorarbeit;

den Mitgliedern der Terahertz-Forschungsgruppe - besonders Sebastian, Julius, Mohsen, Oliver and Lukas - für ihre große Unterstützung und die schöne Zeit, nicht nur im Labor, sondern auch bei etlichen Fabeckstraßen-Feiern;

der guten Seele des hilflosen Doktoranden - Reinhard Franke - für das Aushelfen in unzähligen Situationen;

den Kollegen vom Elektroniklabor, durch deren Hilfe und Können viele Experimente erst ermöglicht wurden - nicht zuletzt Viktor Platschkowski, dessen Enthusiasmus und Hilfsbereitschaft uns allen in Erinnerung bleiben wird;

der Forschungsgruppe um Tomas Jungwirth - besonders Kamil Olejnik - für spannende Experimente an Antiferromagneten;

den vielen Menschen, die Proben für uns hergestellt haben, besonders Samridh und Joel aus der mainzer Forschungsgruppe um Mathias Kläui, Ulrike und Jakob aus der Forschungsgruppe aus Greifswald um Markus Münzenberg sowie Ilie Radu vom Helmholtzt-Zentrum Berlin;

meinen Freunden für die schöne gemeinsame Zeit abseits des Labors und einfach dafür, dass sie da sind, wenn man sie braucht;

meinen Eltern, meiner Oma, meinem Onkel, und meinem Bruder für deren Unterstützung, Rat und Rückhalt, ohne die diese Arbeit nicht möglich gewesen wäre;

Nora - danke, dass es dich in meinem Leben gibt und du mir hilfst, nicht das wirklich Wichtige aus den Augen zu verlieren.

## Selbstständigkeitserklärung gemäß der Promotionsordnung

Sämtliche verwendeten Hilfsmittel, Hilfen und Quellen sind an der entsprechenden Stelle angegeben. Ich versichere, dass ich auf dieser Grundlage diese Arbeit selbstständig verfasst habe. Diese Arbeit wurde bisher weder in gleicher noch ähnlicher Form einer anderen Prüfungskommission vorgelegt oder veröffentlicht.

Berlin, den

Tom S. Seifert